Stony Brook University

MICROMECHANICS OF FAILURE IN POROUS CARBONATE AND VOLCANIC ROCKS

A Dissertation Presented

by

Wei Zhu

To

The Graduate School

in Partial Fulfillment of the

Requirements

for the Degree of

Doctor of Philosophy

in

Geosciences

Stony Brook University

August 2010

Stony Brook University
The Graduate School

Wei Zhu

We, the dissertation committee for the above candidate for the
Doctor of Philosophy degree, hereby recommend
acceptance of this dissertation.

Teng-fong Wong – Dissertation Advisor
Professor, Department of Geosciences, Stony Brook University

Donald J. Weidner - Chairperson of Defense
Distinguished Professor, Department of Geosciences, Stony Brook University

Troy Rasbury
Associate Professor, Department of Geosciences, Stony Brook University

Christiane Stidham
Lecturer, Department of Geosciences, Stony Brook University

Patrick Baud
Professor, Laboratoire de Géophysique Expérimentale EOST Strasbourg

This dissertation is accepted by the Graduate School

Lawrence Martin
Dean of the Graduate School

Abstract of the Dissertation

MICROMECHANICS OF FAILURE IN POROUS CARBONATE AND VOLCANIC ROCKS

by

Wei Zhu

Doctor of Philosophy

in

Geosciences

Stony Brook University

2010

Laboratory experiments, microstructural observations and micromechanical modeling were conducted to investigate the micromechanics on porous carbonate and volcanic rocks. A suite of limestones, two blocks of Alban Hills tuff and three blocks of Mt. Etna basalt samples were chosen to study.

Microstructural observations illustrate that pore collapse first initiates at the larger pores, and microcracking dominates the deformation around the pore surface in porous limestones. To capture these micromechanical processes, we developed a model treating the limestone as a dual porosity medium, with the total porosity partitioned between macroporosity and microporosity. While inelastic compaction is associated with pore collapse in limestones, development of dilatancy and brittle faulting was observed to relate to the initiation and propagation of stress-induced cracks in a compact rock. The Coulomb criterion is used extensively for describing the macroscopic development of shear fracture in a brittle rock. To gain insights into the physics of the Coulomb criterion,

we derived analytic approximations for the empirical failure parameters with reference to the sliding wing crack model.

Uniaxial and conventional triaxial experiments have been conducted on Alban Hills tuff and Mt. Etna basalt at room temperature. The phenomenological behaviors were observed to be qualitatively similar to that in a porous sedimentary rock. Synthesizing published data, we observe a systematic trend for both uniaxial compressive strength and pore collapse pressure of nonwelded tuff to decrease with increasing porosity. To interpret the compaction behavior in tuff, we extended the cataclastic pore collapse model originally formulated for a porous carbonate rock to a dual porosity medium made up of macropores and micropores or microcracks. Microstructural observations of the intact material of Mt. Etna basalt revealed the presence of thin cracks (probably formed during the rapid cooling of the lava) and quasi-spherical voids formed during degassing. The effects of water, phenocryst and porosity on mechanical behaviors of Etna basalt were systematically investigated. Micromechanical models were employed to elucidate the micromechanics of brittle failure and inelastic compaction.

Table of Contents

List of Figures

List of Tables

Acknowledgements

This work would not have been possible with out many people who helped and supported me along the way. I am most grateful to my advisor Teng-fong Wong, for his continuous support in my Ph. D. study. He introduced me to the world of rock mechanics. He has enlightened me through his wide knowledge and guided me to see science with opened eyes. He sets a great example on how to do science with positive attitude.

I appreciate the guidance from Patrick Baud as well, who mentored me the experimental techniques in lab. The encouragement and insightful discussions from him were highly valuable to my research. I also would like to thank my committee members Donald J. Weidner, Troy Rasbury and Christiane Stidham for their stimulating suggestions and comments.

I would like to express my thanks to people in my lab including: Laurent Louis, Veronika Vajdova, Cecilia Cheung, Josephine Durand, Yutao Ji, and especially my former lab mates Sheryl Tembe and Natalie Tzu-mo Chen, who helped me and shared their experience unselfishly.

Lastly, my deepest thanks goes to my family. My parents always have faith in me. They stand by me and give me strength at all times. I am especially thankful for my husband's endurance for my long working hours. His encouragements together with home cooking meals surely cheered me up when I feel frustrated. I am grateful for all the supports and unconditional love from my family members.

Publications

Zhu, W., P. Baud and T.-F. Wong (2010), Micromechanics of cataclastic pore collapse in limestone, *Journal of Geophysical Research*, 115, B04405, doi:10.1029/2009JB006610

Vajdova, V., **W. Zhu**, T-M.N. Chen and T.-F. Wong (2010), Micromechanics of brittle faulting and cataclastic flow in Tavel limestone, *Journal of Structural Geology*, in press

Zhu, W., P. Baud and T.-F. Wong (2010), Micromechanical basis for the Coulomb failure parameters, *Earth and Planetary Science Letters*, submitted

Wong, T.-F. and **W. Zhu** (2007), Weak elastic anisotropy in a cracked rock, *Geological Society of London*, Special Publications, 284, 207-220. doi: 10.1144/SP284.14

Tembe, S., V. Vajdova, T.-F. Wong and **W. Zhu** (2006), Initiation and propagation of strain localization in circumferentially notched samples of two porous sandstones, *Journal of Geophysical Research*, 111, B02409, doi:10.1029/2005JB003611

Zhu, W., P. Baud, S. Vinciguerra and T.-F. Wong, Micromechanics of brittle faulting and cataclastic flow in Alban Hills tuff, in preparation

Zhu, W., P. Baud, S. Vinciguerra and T.-F. Wong, Brittle faulting and cataclastic flow in Mt. Etna basalt, in preparation

Chapter 1

Introduction

Brittle-ductile transition in rocks is associated with a broad spectrum of deformation mechanisms and failure modes. The deformation mechanism has significant influence on the failure mode and microstructure preserved in naturally deformed rocks, state of stress in the lithosphere, spatiotemporal evolution of stress and deformation during the earthquake cycle, and coupling of crustal deformation and fluid transport. It is now recognized that each failure mode has distinct characteristics of stress-strain behavior and porosity evolution. Laboratory investigations under controlled conditions can provide useful insights into how these variable influence the failure mode and mechanics of the brittle-ductile transition.

Previous studies have underscored that the failure mode of a rock is intimately related to the porosity and how it changes in response to an applied stress. On one hand, dilatancy is universally observed as a precursor to the inception of shear localization in

the brittle faulting regime [*Brace*, 1978]. On the other hand, plastic flow (associated with crystal plasticity and diffusive mass transfer) does not involve any volumetric change [*Paterson and Wong*, 2005]. In the transitional regime of cataclastic flow (associated with homogeneously distributed microcracking), the scenario is more complicated since the pore space may dilate or compact in response to an applied stress field.

More than half of the Earth's oil reserves are found in carbonate rocks. Extraction of fluid from a reservoir reduces the pore pressure and thus increases the effective stress, which can impact the stress field and hydromechanical properties, possibly leading to inelastic deformation and failure manifested by phenomena such as surface subsidence, well failure and induced seismicity [*Boutéca et al*., 1996; *Segall,* 1989; *Fredrich et al*., 2000*; Wong et al*., 2004]. In a sedimentary basin, mechanical compaction can lead to irreversible reduction of the porosity, thus providing a physical mechanism of diagenesis especially during early and intermediate burial [*Pettijohn*, 1975; *Choquette and James*, 1986].

Laboratory studies in the past have elucidated the phenomenology and micromechanics of the brittle-ductile transition in porous sandstones [*Wong et al*., 1997]. Limestone is a common crustal rock that like sandstones, represents some of the best aquifers and hydrocarbon reservoirs. Notwithstanding the similarities in phenomenological behaviors, the micromechanics of compaction are quite different in clastic and carbonate rocks. *Zhang et al*. [1990] formulated a Hertzian fracture mechanics model to interpret the micromechanical process of inelastic compaction in sandstones. The model predicts that the compactive yield stress of porous sandstone would scale inversely with porosity and grain size, which is in basic agreement with experimental

observations [*Wong et al*., 1997]. For limestones, a micromechanical model that can capture aspects of the inelastic compaction failure process is the plastic pore collapse model [e.g., *Curran and Carroll*, 1979]. Baud *et al*. [2000] observed that the yield cap of relatively compact Solnhofen limestone can be interpreted using such a model, with pore collapse induced by crystal plasticity processes such as dislocation slip and deformation twinning. However, this plastic pore collapse model was pointed to be very limited when predicting the compactive yield behaviors of more porous limestone [*Vajdova et al*., 2004]. In Chapter 2, we indicated the major discrepancies with this model on porous limestones based on our microstructural observations. To capture the aspects of cataclastic pore collapse we developed a micromechanical model treating the limestone as a dual porosity medium, with the total porosity partitioned between macroporosity and microporosity. The pore structures were illustrated; the micromechanism of inelastic compaction was analyzed, and the theoretical predictions were compared with microstructural observations in Chapter 2.

While pore collapse seems to dominate the inelastic compaction in porous limestones, the development of dilatancy and brittle faulting in a compact rock were observed to relate to the initiation and propagation of stress-induced microcracks [*Tapponier and Brace*, 1976; *Kranz*, 1983]. The Coulomb criterion is used extensively for describing the macroscopic development of shear fracture in a brittle rock, and yet the micromechanical basis for the Coulomb failure parameters remains obscure. To gain insights into the physics of the Coulomb criterion, in Chapter 3 we derived analytic approximations for the empirical failure parameters with reference to the sliding wing crack model. These expressions clarify the dependence of the uniaxial compressive strength on

micromechanical parameters including the fracture toughness, friction coefficient, crack dimension and density.

An understanding of how tuff deforms and fails is of importance in the mechanics of volcanic eruption, as well as geotechnical and seismic applications related to the integrity of tuff structures and repositories. While the engineering and physical properties have been widely investigated [*Nimick et al*., 1985; *Avar and Hudyma*, 2007; *Moon*, 1993], not much is known about the failure modes and mechanical properties in tuff samples. In Chapter 4 we have obtained two blocks of tuff samples from Alban Hills, Italy The phenomenological behavior was observed to be qualitatively similar to that in a porous sedimentary rock. To interpret the compaction behavior in tuff, we extended the cataclastic pore collapse model presented in Chapter 2 to a dual porosity medium made up of macropores and micropores or microcracks.

Besides pyroclastic tuffs, we also investigated basalt samples obtained from Mt. Etna volcano district in Italy. While the tuffs undergo a transition in failure mode from brittle to cataclastic regime with relatively small increase of confining pressures, dilatancy and brittle faulting seem to dominate the failure behavior on Etna basalt up to a relatively high confining presure. A recent study by *Adelinet et al*. [2010] has shown that the Iceland basalt can be characterized by a dual porosity of cracks and equant pores. The bimodal porosity of basalt is similar to those of porous limetstone and tuffs. Whether the micromechanical models presented in previous chapters are applicable to Etna basalt would be guided by systematic microstructural observations. In Chapter 5, we studied three blocks of Mt. Etna basalt samples. A series of experiments were conducted to illustrate the phenomenological behaviors of our basalt samples. Microstructure of intact

and deformed samples was studied under optical microscope and scanning electron microscopes (SEM). The effects of water, phenocryst and porosity on mechanical behaviors of Etna basalt were systematically investigated. Micromechanical models were employed based on microstructural observations.

The major conclusions and suggestions for future work are presented in Chapter 6.

The four major chapters are intended to be read as separate units. Chapter 2 has been accepted as a paper with the same title by *Wei Zhu*, *Patrick Baud* and *Teng-fong Wong* in *Journal of Geophysical Research*. Although not included in the dissertation, a detailed study in Tavel limestone that adopted the same micromechanical model has been accepted in *Journal of Structural Geology* with the title of Micromechanics of brittle faulting and cataclastic flow in Tavel limestone by *Veronika Vajdova*, *Wei Zhu*, *Tzu-Mo Natalie Chen and Teng-fong Wong*. Chapter 3 has been submitted with the same title to *Earth and Planetary Science Letters* by *Wei Zhu, Patrick Baud and Teng-fong Wong*. Chapter 4 and Chapter 5 are in preparation for submission.

References

Adelinet, M., J. Fortin, Y. Guéguen, A. Schubnel, and L. Geoffroy (2010), Frequency and fluid effects on elastic properties of basalt: Experimental investigations, *Geophys. Res. Lett.*, *37*(2), L02303, doi: 10.1029/2009gl041660.

Avar, B., and N. Hudyma (2007), Observations on the influence of lithophysae on elastic (Young's) modulus and uniaxial compressive strength of Topopah Spring Tuff at Yucca Mountain, Nevada, USA, *Int J Rock Mech Min*, *44*(2), 266-270.

Baud, P., A. Schubnel, and T. Wong (2000), Dilatancy, compaction, and failure mode in Solnhofen limestone, *Journal of Geophysical Research*, *105*(B8), 19289-19303, doi: 10.1029/2000JB900133.

Boutéca, M., J. P. Sarda, and F. Schneider (1996), Subsidence induced by the production of fluids, *Rev I Fr Petrol*, *51*(3), 349-379.

Brace, W. (1978), Volume changes during fracture and frictional sliding: a review, *Pure and Applied Geophysics*, *116*(4), 603-614.

Choquette, P. W., and N. P. James (1986), Diagenesis in limestones - the deep burial environment, *Geosciences Canada*, *14*, 3-35.

Curran, J., and M. Carroll (1979), Shear stress enhancement of void compaction, *Journal of Geophysical Research*, *84*, 1105–1112, doi: 10.1029/JB084iB03p01105.

Fredrich, J. T., J. G. Arguello, G. L. Deitrick, and E. P. de Rouffignac (2000), Geomechanical modeling of reservoir compaction, surface subsidence, and casing damage at the Belridge diatomite field, *Spe Reserv Eval Eng*, *3*(4), 348-359.

Kranz, R. L. (1983), Microcracks in rocks, a review, *Tectonophysics*, *100*, 449-480.

Moon, V. (1993), Geotechnical characteristics of ignimbrite: A soft pyroclastic rock type, *Engineering Geology*, *35*(1-2), 33-48.

Nimick, F. B., R. H. Price, R. G. Van Buskirk, and J. R. Goodell (1985), Uniaxial and triaxial compression test series on Topopah Spring Tuff from USW G-4, Yucca Mountain, Nevada*Rep. SAND--84-1101*.

Paterson, M., and T. Wong (2005), *Experimental rock deformation--The brittle field, 2nd Edition*, 348 pp., Springer-Verlag, New York.

Pettijohn, F. J. (1975), *Sedimentary Rocks*, 628 pp., Harper & Row, New York.

Segall, P. (1989), Earthquakes Triggered by Fluid Extraction, *Geology*, *17*(10), 942-946.

Tapponier, P., and W. F. Brace (1976), Development of stress-induced microcracks in Westerly granite, *Int. J. Rock Mech. Min. Sci. & Geomech. Abstr*, *13*, 103-112.

Vajdova, V., P. Baud, and T. Wong (2004), Compaction, dilatancy, and failure in porous carbonate rocks, *Journal of Geophysical Research*, *109*, B05204, doi: 10.109/2003JB002508.

Wong, T.-F., C. David, and W. Zhu (1997), The transition from brittle faulting to cataclastic flow in porous sandstones: Mechanical deformation, *Journal of Geophysical Research*, *102*, 3009-3025, doi: 10.1029/96JB03281.

Wong, T.-f., C. David, and B. Menéndez (2004), Mechanical compaction, in *Mechanics of Fluid-Saturated Rocks*, edited by Y. Guéguen and M. Boutéca pp. 55-114, Elsevier Academic Press, Amsterdam.

Zhang, J. X., T. F. Wong, and D. M. Davis (1990), Micromechanics of Pressure-Induced Grain Crushing in Porous Rocks, *Journal of Geophysical Research*, *95*, 341-352, doi: 10.1029/JB095iB01p00341.

Chapter 2

Micromechanics of cataclastic pore collapse in limestone

Abstract

The analysis of compactant failure in carbonate formations hinges upon a fundamental understanding of the mechanics of inelastic compaction. Microstructural observations indicate that pore collapse in a limestone initiates at the larger pores, and microcracking dominates the deformation in the periphery of a collapsed pore. To capture these micromechanical processes, we developed a model treating the limestone as a dual porosity medium, with the total porosity partitioned between macroporosity and microporosity. The representative volume element is made up of a large pore which is surrounded by an effective medium containing the microporosity. Cataclastic yielding of this effective medium obeys the Mohr-Coulomb or Drucker-Prager criterion, with failure parameters dependent on porosity and pore size. An analytic approximation was derived

for the unconfined compressive strength associated with failure due to the propagation and coalescence of pore-emanated cracks. For hydrostatic loading, identical theoretical results for the pore collapse pressure were obtained using the Mohr-Coulomb or Drucker-Prager criterion. For nonhydrostatic loading, the stress state at the onset of shear-enhanced compaction was predicted to fall on a linear cap according to the Mohr-Coulomb criterion. In contrast, nonlinear caps in qualitative agreement with laboratory data were predicted using the Drucker-Prager criterion. Our micromechanical model implies that the effective medium is significantly stronger and relatively pressure-insensitive in comparison to the bulk sample.

1. Introduction

In response to an applied stress field or pore pressure change, the pore space of a rock may either compact or dilate. In the first scenario, mechanical compaction can cause irreversible reduction of the porosity, and thus provide a physical mechanism of diagenesis, especially during early and intermediate burial [*Pettijohn*, 1975; *Choquette and James*, 1986]. In a reservoir or aquifer, extraction of fluid reduces the pore pressure and thus increases the effective stress, which can impact the stress field and hydromechanical properties, possibly leading to inelastic deformation and failure manifested by phenomena such as surface subsidence, well failure and induced seismicity [*Boutéca et al*., 1996; *Segall*, 1989; *Fredrich et al*., 2000; *Wong et al.*, 2004].

Useful insights into the mechanics of these sedimentary, tectonic and geotechnical processes can be gained from the laboratory investigation of inelastic compaction and failure mode of porous sedimentary rocks under controlled conditions. Such rock

mechanics studies have demonstrated that from a phenomenological point of view, the mechanical compaction behaviors in clastic and carbonate rocks are qualitatively similar [*Wong et al*., 1997; *Vajdova et al*., 2004; *Bemer et al*., 2004; *Baud et al*., 2006; *Baud et al*., 2009]. Under hydrostatic loading, compaction is primarily elastic up to a critical pressure, beyond which porosity decreases irreversibly with increasing pressure. Under nonhydrostatic loading, initiation of inelastic compaction would develop at a mean stress that is lower than the critical pressure under hydrostatic loading. At the initiation of inelastic compaction, the mean stress value typically decreases with increasing differential stress, and in terms of the first and second stress invariants these yield points map out a compactant failure "cap" in the stress space.

Notwithstanding these similarities in phenomenological behavior, the micromechanics of compaction is quite different in clastic and carbonate rocks. In a clastic rock such as sandstone, inelastic compaction in a laboratory sample derives primarily from grain crushing initiated by the stress concentrations at grain contacts, that induce intragranular cracks to radiate in a conical pattern towards the interior of the impinging grains [e.g., *Menéndez et al*., 1996]. This micromechanical process can be analyzed by a Hertzian fracture mechanics model [*Zhang et al*., 1990], which predicts that the compactive yield stress of porous sandstone would scale inversely with porosity and grain size, in basic agreement with experimental observations [*Wong et al*., 1997].

In contrast, microstructural observations have shown that inelastic compaction in limestone is associated with pore collapse, that seems to initiate from stress concentrations at the surface of an equant pore, which induce a ring of localized damage in its periphery. A micromechanical model that can capture aspects of this failure process

is the plastic pore collapse model, which has been developed in several different contexts by *Bhatt et al*. [1975], *Gurson* [1977], and *Curran and Carroll* [1979]. For the relatively compact Solnhofen limestone, *Baud et al*. [2000] observed that its yield cap can be interpreted using *Curran and Carroll's* [1979] model of the collapse of spherical pores induced by crystal plasticity processes such as dislocation slip and deformation twinning operative in the proximity of the pore surface. In this scenario, a concentric shell of plastic deformation would develop and transform the pore geometry from spherical to ellipsoidal with an overall decrease in volume.

However, *Vajdova et al.* [2004] concluded that the agreement of this plastic pore collapse model with the compactive yield behaviors of more porous limestones is quite limited. Microstructural observations to be reported in this study indicate at least two major discrepancies with the *Curran and Carroll* [1979] model assuming crystal plasticity. First, pore collapse seems to first initiate at the larger pores, while the theoretical model predicts that it is equally likely for collapse to initiate from a large or a small pore. Second, cataclasis and microcracking (rather than crystal plasticity) seem to be the dominant deformation mechanisms in the proximity of a pore that has collapsed. Relatively intense cracking would develop with a concentric halo surrounding the pore, and comminuted fragments may spall and fall into the void. In this study, we will refer to this scenario as "cataclastic pore collapse".

The objective of this study is to develop a micromechanical model that can capture such a cataclastic pore collapse process associated with inelastic compaction in limestone. Motivated by microstructural observations, the pore size distribution of a limestone will be treated as bimodal, with the larger pores constituting the "macroporosity" and the

smaller ones the "microporosity". Hence the limestone represents a dual porosity medium, that yields first at the large pores, each of which is surrounded by an effective medium containing the microporosity. Cataclastic yielding (in the form of brittle failure) of this effective medium obeys the Mohr-Coulomb or Drucker-Prager criterion, with failure parameters that are dependent on the porosity and pore size according to *Sammis and Ashby's* [1986] micromechanical model for compressive failure induced by pore-emanated cracking. Prediction of this cataclastic pore collapse model will be compared with experimental data on the inelastic yield behavior of several porous limestones.

2. Phenomenology of Inelastic Compaction in Porous Limestone

We show in Figure 2.1a the hydrostatic compression data for four nominally dry limestone samples. Petrophysical data of the limestones are compiled in Table 2.1. The convention is adopted that compressive stresses and compactive strains (i.e. shortening and porosity decrease) are positive. At relatively low pressures a nonlinear "toe" may be observed initially in the hydrostat [*Vajdova et al*., 2004], which can be attributed to the elastic closure of microcrack porosity. The hydrostatic response then became relatively linear, and for the most compact Solnhofen limestone this linear trend persisted up to the maximum pressure in the experiment. In contrast, the hydrostats of the other three limestones became nonlinear again at pressures above the critical values P^* marked in Figure 2.1a. This critical pressure is identified with an inflection point in the hydrostat, which marks the onset of inelastic compaction associated with pore collapse [*Vajdova et al*., 2004]. Presumably the critical pressure for Solnhofen limestone is higher than the maximum pressure (of 450 MPa) attained by *Baud et al*. [2000] in their experiment. We

compile in Table 2.1 the critical pressures of a number of porous limestones. There is an overall trend for P^* to decrease with increasing porosity.

To illustrate the inelastic compaction behavior under nonhydrostatic loading, we show in Figure 2.1b data for the mean stress as a function of volumetric strain in five conventional triaxial compression experiments on the Tavel limestone, at confining pressure ranging from 50 MPa to 240 MPa [*Vajdova et al*., 2004]. In each of these experiments, the volumetric strain evolved over three distinct stages with the progressive increase of differential stress (and mean stress). In the first stage, the triaxial compression curves basically coincided with the hydrostat up to a critical stress state (indicated by C^* for the curve at 100 MPa confining pressure). In the second stage at stress levels beyond C^*, there was an accelerated decrease in volume in comparison to the hydrostat, which implies that the deviatoric stress field provided significant inelastic contribution to the compactive strain. This phenomenon of "shear-enhanced compaction" persisted until the volumetric strain switched from compaction to a third stage of dilation. This transition from compactive to dilatant cataclastic flow occurred at the critical stress state $C^{*\prime}$, as indicated in Figure 2.1b for the experiment at 100 MPa confining pressure.

We plotted in Figure 2.1c the critical stress states (differential stress and mean stress) at the onset of shear-enhanced compaction for Solnhofen [*Baud et al*., 2000], Majella [*Baud et al*., 2009], Tavel and Indiana [*Vajdova et al*., 2004] limestones with porosities ranging from 3% to 30%. The C^* data map out compactive yield caps that are approximately elliptical in shape, with major and minor axes that expand with decreasing porosity.

3. Dual Porosity and Stress-Induced Damage in Limestone

The mechanical and transport properties of a porous rock are sensitively dependent on the porosity and its geometric attributes. Carbonate rocks are widely recognized to have pore geometry that is significantly more complex than other sedimentary rocks such as siliciclastics [C*hoquette and Pray*, 1970; *Lucia*, 1995; *Lønøy*, 2006]. One of the reasons for the geometric complexity is that depositional environment and diagenesis exerts significant genetic influence over the development of texture and fabric of a carbonate rock [*Folk*, 1980], which can in turn modify both the size and connectivity of the pore space in a relatively rapid and drastic manner. The pore size in a carbonate rock may span over a very broad range, with a distribution that is often bimodal, including a significant subset of microporosity that cannot be resolved under an optical microscope [*Pittman*, 1971].

In a comprehensive classification widely adopted in carbonate petrography, *Choquette and Pray* [1970] proposed as many as 7 "fabric-selective" porosity types, including interparticle, intraparticle and intercrystalline pores. Since then, many researchers have argued that if one strives to arrive at a realistic prediction of permeability as a function of porosity in carbonate rocks, then further refinement of the classification is necessary [e.g., *Lucia*, 1995]. Indeed *Lønøy* [2006] recently developed a pore system that incorporates 20 pore-type classes.

In contrast, the question of how different porosity types can influence the development of mechanical failure in a carbonate rock has not been investigated systematically in rock mechanics. The conventional approach is to treat the porosity as a single entity, and an empirical relation for the compressive failure stress as a function of porosity is derived

from mechanical data on the brittle strength or compactive yield stress [e.g. *Hugman and Friedman*, 1979; *Bemer et al*., 2004]. Such an approach seems reasonable in the absence of systematic observations on the micromechanics of compressive failure. Recently we conducted a comprehensive study of the deformation microstructure in Tavel, Indiana and Majella limestones (Table 2.1), which indicate that at least two porosity types with quite distinct failure mechanisms should be specified in a micromechanical model for cataclastic pore collapse. Since details of the microstructural data will be provided in future publications, here we will only present observations that are pertinent to formulation of our dual porosity compaction model.

3.1. Pore Size Distribution in Three Limestones

Figure 2.2a illustrates the pore structure of Indiana limestone observed under an optical microscope. It is an allochemical limestone, with porosity ranging from 14.6% to 16.2% [*Vajdova et al*., 2004]. The allochems include skeletal debris and ooliths, which occur as elongate features that typically align sub-parallel to sedimentary bedding. The allochems are commonly coated with micritic cement around their rims, and the interparticle porosity is made up of relatively large pores (areas with lightest color in Figure 2.2a). Some of these pores are partially filled with blocky calcite corresponding to sparry cement. The grain size of Indiana limestone ranges from < 5 μm for the micrites to >300 μm for the allochems. The interparticle pores with relatively large diameters in this allochemical limestone correspond to the macroporosity. In addition, intercrystalline and intraparticle porosities also occur as micropores within the allochems and cement. *Choquette and Pray* [1970] defined micropores in a carbonate rock to be voids with average diameter <1/16 mm, and scanning electron microscope (SEM) observations have

shown that the microporosity includes many submicron pores [*Pittman*, 1971; *Anselmetti et al*., 1998].

3.1.1. Macroporosity

To characterize the pore size statistics, a petrographical thin section of an Indiana limestone sample was scanned using an Epson Perfection™ V700 photo scanner. As shown in Figure 2.2b, at a resolution of 1800 dpi or higher the scanner can resolve the macroporosity as effectively as an optical microscope, with the advantage that it can cover the whole area of the thin section, thus circumventing the need to assemble a mosaic of numerous optical micrographs. The macropores were identified using a gray-scale thresholding approach, and the binarized image was then analyzed using ImageJ, a public domain image processing program developed at the National Institutes of Health. The area of each individual pore was determined, and the equivalent diameter of a circle with the same area was evaluated. From geometric probability theory, it can be demonstrated that the areal porosity (sum of the pore areas normalized by the total area of a random section) can be used to estimate the porosity (void volume normalized by the total volume) of the sample if it is isotropic. If the pores can be idealized as spherical, then the area observed in the thin section is expected to be mostly smaller than the great circle area of the pore that was intercepted. Hence the equivalent diameters we evaluated from intercept areas measured on a thin-section represent lower bounds. For a system of monodisperse spherical pores with radius r, it can be proved that the mean intercept area is $(2/3)\pi r^2$, which implies that the pore diameter inferred from intercept area would be underestimated by a factor of $\sqrt{1.5}=1.225$ [*Underwood*, 1970].

At 1800 dpi or higher, the pixel size of the scanned image is on the order of 10 μm or less. However, the resolution of such observations on a petrographic thin section is conventionally taken to be limited by its thickness (~33 μm). Figure 2.3a shows the size distribution of the macropores with equivalent diameter >33 μm in Indiana limestone. The pore size ranges over one order of magnitude, with a maximum diameter of 621 μm. The areal macroporosity evaluated from binarized image is 5.2%, which is significantly smaller than the total porosity of 16.5% that we inferred from density of the cylindrical sample (assuming a calcite grain density of 2710 kg/m^3.) In unpublished work of *Vajdova, Baud, Wu and Wong* (Micromechanics of inelastic compaction in two allochemical limestones, to be submitted to Journal of Structural Geology), the pores and allochems were mapped manually in selected area of the thin section under an optical microscope and imaging software was then used to determine their areal fractions. The porosity so inferred from this independent measurement is in basic agreement with what was determined from the scanned image. They also determined the mean value of the allochems to be 350 μm, comparable to some of the larger macropores. The macropore size distribution is skewed and somewhat resembles a log-normal distribution. If we did not truncate the smaller pores with diameters <33 μm, the number of the smallest pores would be significantly larger and the size distribution then peaks at the smallest values, even though the areal porosity would only increase by a very small amount of 0.3% to 5.5%.

For comparison, we also show in Figure 2.3a the pore diameter distribution in an Indiana limestone sample that had been hydrostatically compacted to beyond P^*, resulting in a permanent porosity reduction of 2.8%. The areal macroporosity evaluated

from the binarized image is 3.4%, and comparison of the pore size distributions of the undeformed and compacted samples shows an overall reduction in n_A, the number of pores per unit area. This implies that collapse of the macropores contributed a significant proportion of the inelastic compaction.

We used the same approach to characterize the pore size distribution in Majella limestone (Figure 2.3b), an allochemical limestone that can also be classified as a grainstone made up of fragments of rudists (ranging in size from 50 to 400 μm and occupying ~50% of the rock volume) that are embedded in a matrix of sparry calcite and silica cement [*Tondi et al*., 2006]. Our sample has a total porosity of 30% (Table 2.1). In *Choquette and Pray's* [1970] classification this rudist limestone is considered to be made up of interparticle and intercrystalline macropores, which were classified collectively as "intergranular" by *Anselmetti et al*. [1998]. Our analysis of the scanned image of the Majella limestone shows that the macropore size ranges over one order of magnitude, with an areal macroporosity of 11.4% (for pores with diameter >33 μm) and maximum equivalent diameter of 475 μm (that is comparable to the rudist dimension).

We also characterized the pore size distribution in Tavel limestone (Figure 2.3c), a micritic limestone with composition dominated by calcite with a small amount (<10%) of quartz [*Vajdova et al*., 2004]. This limestone is relatively homogeneous, with small number of sparry grains (~11% in volume) embedded in a microcrystalline matrix. The micrite has an average diameter of ~ 5 μm, whereas the sparry grains are coarser, with an average diameter of 25 μm. Voids occur mostly as micropores within the microcrystalline matrix, and there is a small number of larger pores which can be resolved under an optical microscope at higher magnifications. The data in Figure 2.3c were obtained by

image analysis of such optical micrographs on selected areas of a Tavel limestone with a total porosity of 11.0% (Table 2.1). These macropores contribute a relatively small porosity of 0.8% to the total. Our data for this Tavel limestone sample show that its macropores are smaller than those in the two allochemical limestones by an order of magnitude, with diameters ranging from 3 to 30 μm (Figure 2.3c). We should, however, note that in other Tavel limestone samples isolated pores with diameters up to 100 μm were observed. In *Choquette and Pray's* [1970] classification, the macroporosity and microporosity in such a compact micritic limestone are considered to be predominately intercrystalline.

3.1.2. Microporosity

Micropores in a carbonate rock are distributed as intercrystalline and intraparticle porosities within the allochems and cements [*Pittman*, 1971]. Many of these equant voids are submicron in size, as illustrated by our SEM observation on a Tavel limestone sample (Figure 2.4a). For comparison, we include on the right showing micropores ranging in size from <1 μm to ~10 μm in the more porous Indiana limestone. Hence a significant fraction of these micropores cannot be resolved or characterized quantitatively using a refined imaging tool such as X-ray micro-computed tomography [*Knackstedt et al*., 2009], unless one resorts to manual measurement under the SEM over a relatively large area which can be very time-consuming.

The microporosity Φ_m will be defined as the difference between total porosity Φ (inferred from bulk density of the dry limestone sample) and the macroporosity Φ_M (inferred from image analysis as shown in Figures 2.3a, 2.3b and 2.3c), so that $\Phi = \Phi_M + \Phi_m$. Figure 2.4b summarizes the partitioning between macroporosity and

microporosity in the three limestones we studied. The data show that notwithstanding the very different textures and porosities, the porosity partitioning in these limestones is similar in that the microporosity represents a very significant fraction of the total porosity. According to Figure 2.4b, the ratio Φ_m / Φ between microporosity and total porosity has relatively high values of 0.68, 0.62 and 0.92 for Indiana, Majella and Tavel limestones, respectively. Our definition of these two types of porosity is analogous to that of *Baechle et al*. [2008], who also reported relatively high proportions of microporosity in 26 carbonate samples.

The bimodal characteristics of carbonate porosity can sometimes be inferred from mercury injection measurements [*Keith and Pittman*, 1983]. To interpret the capillary pressure data of such measurements, one typically considers a conceptual model of pore space that is made up of pores (that occupy most of the volume) connected by throats (that are of negligible volume but control the percolation and fluid transport), with the implication that the mercury injection capillary pressure is inversely proportional to throat size according to the Young-Laplace equation [*Dullien*, 1992]. If indeed the throat and pore sizes are correlated as first observed by *Wardlaw et al*. [1987] for Indiana limestone, then mercury intrusion data can be used to indirectly infer the pore size distribution of interest in our micromechanical model. For example, a ratio of ~2-11 between the pore and throat diameters have been inferred from mercury injection and microstructural data on several carbonate and clastic rocks. [*Churcher et al*., 1991;*Wardlaw et al*., 1988].

We compile in Figure 2.4c the mercury injection measurements for Indiana [*Churcher et al*., 1991] and Majella [*Baud et al*, 2009] limestones, showing the cumulative

percentage of pore space injected by mercury as a function of the capillary pressure (and the corresponding effective throat diameter). The data of *Baud et al*. [2009] for the relative distribution of pore space as a function of throat diameter were integrated to arrive at the curve in Figure 2.4c. The throat diameter was calculated from the capillary pressure using the Young-Laplace equation, using surface tension and contact angle values of 480 N/m and 140°, respectively.

The data suggest that the throat size distribution in both limestones are bimodal: for Indiana limestone, two inflection points (marked by the arrows in Figure 2.4c) corresponding to threshold throat diameters of ~0.9 μm and 100 μm can be identified, and similarly there are two inflection points on the Majella limestone curve corresponding to throat diameters of 1 μm and 20 μm. The mercury injection data therefore imply that the macropores in Indiana limestone are larger than those in Majella limestone, in agreement with our microstructural data (Figures 2.3a and 2.3b).

3.2. Cataclastic Damage Associated With Shear Localization and Shear-Enhanced Compaction

To contrast the damage associated with brittle and ductile failure modes in limestone, we present in Figure 2.5 backscattered SEM observations on failed samples of Tavel and Indiana limestones. A Tavel limestone sample (with initial porosity of 13.6%) was deformed under uniaxial compression. After attaining a peak stress of 106 MPa, the sample underwent strain softening and developed a shear band at ~30^{o} with respect to σ_1, the maximum principal stress. Figure 2.5a shows an incipient shear band (enclosed within the white rectangle) that had developed in the proximity of the through-going shear band. Numerous stress-induced microcracks sub-parallel to σ_1 had emanated from the large as

well as small pores. Some of these pore-emanated cracks have coalesced, but the overall pattern of shear localization seems to be controlled by cracking related to several macopores with diameters of 10 μm or more. This intensely damaged zone is contrasted with the relatively undamaged areas on its right.

Another Tavel limestone was hydrostatically compressed to an additional 60 MPa beyond the critical pressure P^* (180 MPa). Macropores at various stages of collapse were observed in this sample. Figure 2.5b shows a macropore which has a relatively circular cross-section with a diameter of ~20 μm, that is surrounded by a halo of cataclastic damage. A concentric rim of relatively intense damage has extended over a thickness of ~2 μm. While the spatial distribution of damage is circumferentially symmetric, its intensity decays with radial distance, such that the micritic matrix seems relatively undeformed beyond a thickness of ~6 μm.

A Tavel limestone sample (with initial porosity of 10.4%) was deformed triaxially at a confining pressure of 150 MPa. Significant shear-enhanced compaction was observed, and the sample was unloaded just after reaching the critical stress state $C^{*'}$ (Figure 2.1b). Figure 2.5c shows the collapse of one of the largest macropores in this compacted sample. Intensive cataclastic damage was observed near the surface, especially around the equator with numerous pore-emanated cracks sub-parallel to σ_1. Many of these microcracks had coalesced in a pattern akin to what we observed in the uniaxially compressed sample (Figure 2.5a). More comprehensive microstructural observations on Tavel limestone will be presented by *Vajdova, Zhu, Chen and Wong* (Micromechanics of brittle faulting and cataclastic flow in Tavel limestone, accepted by Journal of Structural Geology).

An Indiana limestone sample (with initial porosity of 17.9%) was deformed triaxially at a confining pressure of 20 MPa. Significant shear-enhanced compaction was observed, and the sample was unloaded just beyond $C^{*'}$. Figure 2.5d shows the collapse of a macropore in this compacted sample. Cataclastic damage qualitatively similar to that in Tavel limestone (Figure 2.5c) was observed to develop primarily in the cement, while the allochems remain relatively intact.

4. A Micromechanical Model for the Initiation of Cataclastic Pore Collapse

Motivated by our microstructural observations, we formulated a dual porosity model to analyze the micromechanics of failure. In a micromechanical model it is often necessary to make certain assumptions so as to render the mathematics tractable. Similar to previous models of plastic pore collapse [*Bhatt et al*., 1975; *Gurson*, 1977; *Curran and Carroll*, 1979], we will idealize the pores as spherical in shape. As illustrated in Figure 2.6a, the representative volume element is made up of a macropore of radius a (comparable to data presented in Figure 2.3) surrounded by an effective medium made up numerous micropores of radius a^* (comparable to those shown in Figure 2.4a). The macropore size is relatively small in comparison to the linear dimension b of the representative volume element, so that we have $b >> a > a^*$.

The effective medium is isotropic and initially elastic until it yields when stress concentration at the spherical surface reaches a threshold. For hydrostatic loading, relatively simple results are available. If the remote stress field (Figure 2.6b) is such that

the three principal stresses are equal and compressive ($S_1 = S_2 = S_3 = P_c$), then the local principal stresses in the vicinity of the pore is given by [*Timoshenko and Goodier*, 1951]

$$\sigma_{\rho\rho} = P_c \frac{(1 - a^3/\rho^3)}{(1 - a^3/b^3)}. \tag{1a}$$

$$\sigma_{\theta\theta} = \sigma_{\psi\psi} = P_c \frac{(1 + a^3/(2\rho^3))}{(1 - a^3/b^3)}. \tag{1b}$$

where a spherical coordinate system (ρ, θ, ψ) has been adopted, with ρ denoting the radial distance from the center of the sphere. The stresses decay rapidly with radial distance, and if the representative volume element is sufficiently large so that $b>>a$, the local stresses can be approximated by

$$\sigma_{\rho\rho} = P_c \left(1 - \frac{a^3}{\rho^3}\right). \tag{2a}$$

$$\sigma_{\theta\theta} = \sigma_{\psi\psi} = P_c \left(1 + \frac{a^3}{2\rho^3}\right) \tag{2b}$$

As the remotely applied pressure increases, a point will be reached when the elastic limit is exceeded. This will first occur at the spherical surface ($\rho = a$), where the principal stresses are simply given by:

$$\sigma_{\rho\rho} = 0. \tag{3a}$$

$$\sigma_{\theta\theta} = \sigma_{\psi\psi} = \frac{3P_c}{2} \tag{3b}$$

In the following discussion, we will refer to a stress state with the minimum principal stress equal to zero as "unconfined compression". Accordingly the local stress field in the proximity of the pore surface as given by (3a) and (3b) corresponds to unconfined compression. Another example of unconfined compression is when the intermediate

principal stress also vanishes, which corresponds to uniaxial compression. If the brittle failure criterion is given by the Mohr-Coulomb relation (which is independent of the intermediate principal stress), then the uniaxial compressive strength and unconfined compressive strength are predicted to be identical.

Failure in such an unconfined stress state is expected to be brittle. Hence, the macroscopic and microscopic failure modes are fundamentally different. The macroscopic failure is compactant and ductile, involving the collapse of macropores distributed throughout the volume. In contrast, the micromechanical failure is brittle, involving a pore-scale failure mode that is possibly analogous to the crack coalescence process shown in Figure 2.5a, but with an important difference. In our dual porosity model, the brittle failure occurs in an effective medium that is made up solely of micropores, without any involvement of the macropores. In contrast, the macropores seem to play a dominant role in the bulk failure of the Tavel limestone sample (Figure 2.5b).

4.1. Pore-emanated Cracking Model for Brittle Failure: An Analytic Approximation

To analyze the micromechanics of brittle failure in unconfined compression, we adopted *Sammis and Ashby's* [1986] pore-emanated cracking model. The 2-dimensional model considers an elastic medium permeated by circular holes of uniform radius r (Figure 2.7a). Implicit in this model is the assumption that the failure behavior is independent of the intermediate principal stress. In particular, results derived here for uniaxial compression is expected to be also applicable to a generic unconfined compressive state. As the applied stress σ increases, a point is reached when the stress intensity factor of a small crack on the circular surface attains the critical value K_{IC}, at

which point wing cracks would propagate to a distance ℓ parallel to the stress direction (Figure 2.7b). As the wing cracks propagate to longer distances, they interact with one another to induce an additional tensile stress intensity (Figure 2.7c), ultimately leading to an instability with coalescence of the pore-emanated cracks.

Summing up the contributions from external loading and crack interaction, *Sammis and Ashby* [1986] arrived at this expression for the stress intensity factor at the wing crack tip:

$$K_I = \sigma\sqrt{\pi r}\left[\frac{1.1\sqrt{L}}{(1+L)^{3.3}} + \frac{\sqrt{2}}{\pi}\sqrt{\Phi(1+L)}\right] \tag{4a}$$

where the normalized crack length is $L = \ell / r$. The crack propagates whenever the stress intensity factor equals the fracture toughness: $K_I = K_{IC}$, and accordingly the stress as a function of crack extension is given by

$$\sigma(L) = \frac{K_{IC}}{\sqrt{\pi r}}\left[\frac{1.1\sqrt{L}}{(1+L)^{3.3}} + \frac{\sqrt{2}}{\pi}\sqrt{\Phi(1+L)}\right]^{-1} \tag{4b}$$

A necessary condition for an instability (and stress drop) to develop is for $d\sigma / dL = 0$, when the pore-emanated crack has propagated to a critical normalized length L_{cr}. With some algebra it can be shown that this critical length is related to the porosity Φ according to

$$\Phi = 2\pi^2 (1+L_{cr})\left[\frac{3.63\sqrt{L_{cr}}}{(1+L_{cr})^4} - \frac{0.55}{\sqrt{L_{cr}}(1+L_{cr})^{3.3}}\right]^2 \tag{5}$$

The peak stress so attained is $\sigma(L_{cr})$, corresponding to the unconfined compressive strength σ_u.

Figure 2.8 shows the normalized unconfined compressive strength $\sigma_u / (K_{IC} / \sqrt{\pi r})$ as a function of porosity Φ, and it can be seen that the empirically fitted power law $1.325\Phi^{-0.414}$ (with a correlation coefficient of 0.999) basically coincides with points calculated using (4b) and (5). Thus, we have arrived at an analytic approximation for the unconfined compressive strength according to *Sammis and Ashby's* [1986] pore-emanated cracking model

$$\sigma_u = \frac{1.325}{\Phi^{0.414}} \frac{K_{IC}}{\sqrt{\pi r}} \tag{6}$$

We compiled in Table 2.1 data for the unconfined compressive strength of micritic and allochemical limestones (made up of 80% or more calcite) with porosities ranging up to 30%. The laboratory data are compared with theoretical predictions of the *Sammis and Ashby* [1986] model in Figure 2.9. The data seem to fall into two groups. Data for compact micritic limestones (with porosity < 15%) can be bracketed by the two theoretical curves for $K_{IC} / \sqrt{\pi r} = 35$ and 75 MPa, whereas data for allochemical and porous micritic limestones can be bracketed by the two theoretical curves for $K_{IC} / \sqrt{\pi r} = 5$ and 22 MPa. Because this parameter depends on the inverse square root of pore size, these curves that bracket the data would actually correspond to a very broad range of pore size. If we assume a K_{IC} value of 0.2 MPa $m^{1/2}$ based on fracture mechanics measurements on calcite [*Atkinson and Meredith*, 1987], then the pore-emanated cracking model together with the unconfined strength data imply that the compact micritic limestones have average pore size of r = 2-10 μm and the allochemical and porous micritic limestones have average pore size of r = 26-500 μm.

A “lithographic” limestone such as Solnhofen and the more porous Tavel limestone are examples of a compact micritic limestone that is primarily made up of lithified microcrystalline calcite, with grain size typical in the μm-range [*Folk*, 1980]. Our analysis suggests that the average size of the pores involved in brittle failure of these compact limestones also falls in the μm-range, and is comparable to the macropore size in Tavel limestone (Figure 2.3c). The data in Figure 2.9 for the high-porosity micritic limestones are for the Pillar limestone, which is a relatively unconsolidated micritic mudstone [*Lézin et al*., 2009], which is likely to have significantly larger pores. Their inferred pore sizes are comparable to those of the allochemical limestones, which fall in the range of our macroporosity data for Indiana (Figure 2.3a) and Majella (Figure 2.3b) limestones.

More general results for biaxial loading were also derived by *Ashby and Sammis* [1986], but their model predicts that the confinement can inhibit brittle failure at a lateral stress level that is lower than experimental observations [*Wong*, 1990]. The analysis here is not subject to this limitation since we will only use the results for uniaxial loading. Incorporating two basic microstructural variables (porosity and average pore size) and the fracture toughness, our analytic approximation seems to capture the overall trend for the unconfined compressive strength as a function of porosity of porous limestones. While a 3-dimensional model incorporating pore size statistics is definitely desirable, more detailed and finer microstructural data should be acquired first to place realistic constraints on the additional parameters in such a more elaborate model.

4.2. Cataclastic Pore Collapse Induced by Hydrostatic Compression

If indeed the pore-emanated cracking model can be applied to brittle failure in the effective medium surrounding a macropore (Figure 2.6a), then the unconfined compressive strength σ_u^* is given by

$$\sigma_u^* = \frac{1.325}{\Phi_*^{0.414}} \frac{K_{IC}}{\sqrt{\pi a*}} \tag{7a}$$

where Φ_* and $a*$ denote the porosity and average radius of the micropores embedded in the effective medium. If volume of the representative element (Figure 2.6a) is V_T, then the volumes of the macropore and micropores are $V_T\Phi_M$ and $V_T\Phi_m$, respectively. The volume of the effective medium surrounding the macropore is $V_T(1-\Phi_M)$, and accordingly its porosity is

$$\Phi_* = \frac{\Phi_m}{1-\Phi_M} \approx \Phi_m \tag{7b}$$

Our data for three limestones (Figure 2.4b) show the macroporosity Φ_M to be less than around 11%, hence the microporosity Φ_m provides an upper bound and close approximation for the porosity Φ_* of the effective medium.

Brittle failure in the effective medium initiates when the local stresses given by (3a) and (3b) satisfy the failure criterion. Here we will consider two such criteria. The first is the Mohr-Coulomb criterion, which can be expressed in terms of the maximum and minimum principal stresses as

$$\sigma_1 = \frac{2c\cos\phi}{(1-\sin\phi)} + \frac{(1+\sin\phi)}{(1-\sin\phi)}\sigma_3 \tag{8a}$$

where c and ϕ denote the cohesion and angle of internal friction, respectively. This criterion is independent of the intermediate principal stress, and when the material is subjected to an unconfined stress state with $\sigma_3 = 0$, failure occurs when $\sigma_1 = \sigma_u^* = 2c\cos\phi/(1-\sin\phi)$. Accordingly, the Mohr-Coulomb criterion can also be written as

$$\sigma_1 = \sigma_u^* + \frac{(1+\sin\phi)}{(1-\sin\phi)}\sigma_3 \tag{8b}$$

We will also consider the Drucker-Prager yield criterion, which provides a smooth failure envelope in the stress space. There are several alternative approaches one can use to express this criterion in terms of the Mohr-Coulomb parameters c and ϕ [*Davis and Selvadurai*, 2002]. Here we will follow *Curran and Carroll* [1979] to use

$$\sqrt{J_2} = \frac{2\sin\phi}{(3+\sin\phi)} I_1 + \frac{6c\cos\phi}{(3+\sin\phi)} \tag{9a}$$

where the two stress invariants are related to the principal stresses by $I_1 = \sigma_1 + \sigma_2 + \sigma_3$ and $J_2 = [(\sigma_1-\sigma_2)^2 + (\sigma_2-\sigma_3)^2 + (\sigma_3-\sigma_1)^2]/6$. When subjected to an unconfined stress state with $\sigma_3 = 0$, this form of the Drucker-Prager criterion predicts that failure would occur when $\sigma_1 = \sigma_2 = \sigma_u^* = 2c\cos\phi/(1-\sin\phi)$, identical to the Mohr-Coulomb prediction. With this result, the Drucker-Prager criterion can be written as

$$\sqrt{J_2} = \frac{2\sin\phi}{(3+\sin\phi)} I_1 + \frac{3(1-\sin\phi)}{(3+\sin\phi)}\sigma_u^* \tag{9b}$$

When the representative volume element is subjected to a remotely applied hydrostatic pressure, yielding initiates at the macropore surface when the local stresses given by (3a) and (3b) satisfy either of the two yield criteria. Cataclastic damage will first localize in a

concentric halo, akin to that shown in Figure 2.5b. In term of the principal stresses, this stress field is given by $\sigma_1 = \sigma_2 = 3P_c/2$ and $\sigma_3 = 0$, which on substituting into (8b) or (9b) give an identical prediction for the critical pressure for cataclastic yield, namely, $P_c = P^* = (2/3)\sigma_u^*$. This marks the onset of hydrostatically induced pore collapse which, according to the pore-emanated cracking model (7a), would occur at a critical pressure

$$P^* = \frac{2}{3}\sigma_u^* = \frac{0.883}{\Phi_*^{0.414}} \frac{K_{IC}}{\sqrt{\pi a^*}} = \frac{0.883}{\Phi^{0.414}} S^* \tag{10}$$

with

$$S^* = \frac{K_{IC}}{(\Phi_*/\Phi)^{0.414}\sqrt{\pi a^*}} .$$

Hence our micromechanical model for cataclastic pore collapse predicts that while there is an overall decrease of the critical pressure with increasing porosity, the yield stress is also dependent on the parameter S^* which characterizes the cooperative effect of micropore size, fracture toughness and partitioning of microporosity and macroporosity. Unlike the unconfined compressive strength, only limited data are available on P^*. We compile in Figure 2.10 laboratory data for micritic and allochemical limestones (made up of 90% or more calcite) with porosities ranging up to 30%. To help us define the overall trend, we also include data for chalk (with porosities ranging from 38% to 45%) that were compiled by *Vajdova et al*. [2004]. For the Solnhofen limestone (with 3% porosity) we only have a lower bound of 450 MPa (Figure 2.1a), the highest pressure attained in the hydrostatic compression experiment of *Baud et al*. [2000]. By extrapolation of C^* data on the cap (Figure 2.1c), we estimate the critical pressure of this highly compact micritic limestone to be $P^* \approx 550$ MPa, corresponding to the tip of the arrow attached to this data point in Figure 2.10.

The data fall between two limiting curves accordingly to (10). The two samples with lowest porosities (Solnhofen and Tavel limestones) lie on the upper curve corresponding to S^* = 130 MPa. Since $\pi a^* = (K_{IC}/S^*)^2(\Phi/\Phi_*)^{0.828}$, the micropore diameter for this upper limit can be estimated to be $a^* \geq (K_{IC}/S^*)^2/\pi = 0.6$ μm, assuming as before a K_{IC} value of 0.2 MPa $m^{1/2}$. If S^*= 130 MPa, the predicted P^* for porosity down to 3% is 490 MPa, which implies that the local stresses at the spherical pore are $\sigma_1 = \sigma_2 = 3P^*/2 =$ 735 MPa. While microcracks may nucleate from the submicron pores under such a high stress, there is also a possibility that crystal plasticity processes become dominant. As noted by *Baud et al*. [2000], this local stress concentration corresponds to a resolved shear stress of 425 MPa, which is more than double that required to activate all dislocation slip systems (and twinning) of calcite.

The P^* data for samples with porosities beyond ~23% fall on a plateau given by the lower limit S^*= 20 MPa, which implies that $a^* \geq$ 32 μm. We only have microstructural data for one limestone in this porous end-member, namely, the Majella limestone with a total porosity of 30% (Figure 2.3b). Our data indicate that a pore diameter of 64 μm is approaching the lower range of the macropores, and in this sense may represent an upper limit on the size of the micropores. To test the prediction of this model, it would be useful to conduct more systematic measurements of size statistics of micropores in such porous carbonate rocks.

Between the upper and lower limits, the inferred value of S^* decreases rapidly by a factor of 6.5 with porosity increasing by a factor of 2 or so (Figure 2.10). This significant decrease follows an overall trend that seems independent of whether the limestone is a

micritic or allochemical. Since changes in the porosity partitioning factor Φ_* / Φ is unlikely to be large enough to result in this decrease, a significant part of this decrease is probably related to corresponding increase in micropore size from submicron to tens of micron. In Figure 2.11 we plot the inferred values of S^* as a function of total porosity Φ. It can bee seen that the data can be fitted empirically by this linear relation:

$$S^* = 130 \text{ MPa} \qquad \text{for} \quad \Phi \le 0.10 , \tag{11a}$$

$$S^* = \frac{K_{IC}}{(\Phi_* / \Phi)^{0.414} \sqrt{\pi a^*}} = A - B\Phi \quad \text{for } 0.10 \le \Phi \le 0.23 , \tag{11b}$$

$$S^* = 20 \text{ MPa} \qquad \text{for} \quad \Phi \ge 0.23 \tag{11c}$$

where the coefficients A=227.7 MPa and B=966.1 MPa. The values of P^* predicted by the micromechanical model (10) in conjunction with the empirical relation (11) are plotted as the dashed curves in Figure 2.10.

Given the geometric complexity of the pore space in carbonate rocks and the interplay of both fracture mechanics and microstructural parameters in the parameter S^*, one would not have expected it to have such an apparently simple dependence on the total porosity Φ. In the absence of more comprehensive data on pore size statistics and deeper understanding of its relationship to carbonate diagenesis, the linear relation (11) is solely based on empirical data and to what extent it can be generalized to sedimentary settings would require more systematic investigations in the future.

4.3. Cataclastic Pore Collapse Under Conventional Triaxial Compression

Under nonhydrostatic loading, the results are more complicated, with fundamentally different predictions accordingly to whether the Mohr-Coulomb or Drucker-Prager yield criterion was adopted. We consider a remote stress field $S_1 > S_2 = S_3$ applied to the

representative volume element (Figure 2.6a), corresponding to a conventional triaxial compression test in the laboratory. With reference to a cylindrical coordinate system (ρ, θ, *z*), the local principal stresses along the equator of the sphere (at *z*=0 and ρ=*a*) are given by [*Timoshenko and Goodier*, 1951]

$$\sigma_1 = \sigma_{zz} = \frac{3}{2}\left[\frac{(9-5\nu)}{(7-5\nu)}(S_1 - S_3) + S_3\right], \tag{12a}$$

$$\sigma_2 = \sigma_{\theta\theta} = \frac{3}{2}\left[\frac{(5\nu-1)}{(7-5\nu)}(S_1 - S_3) + S_3\right], \tag{12b}$$

$$\sigma_3 = \sigma_{\rho\rho} = 0\,. \tag{12c}$$

For the Mohr-Coulomb criterion, we can substitute (12a) and (12c) into (8b) to arrive at the following result for the critical stress state *C** at the onset of shear-enhanced compaction:

$$S_1 - S_3 = \frac{(7-5\nu)}{(9-5\nu)}\left(\frac{2}{3}\sigma_u^* - S_3\right) = \frac{(7-5\nu)}{(9-5\nu)}\left(P^* - S_3\right) \tag{13a}$$

where ν denotes Poisson's ratio of the effective medium. If we define $P = (S_1 + 2S_3)/3$ and $Q = S_1 - S_3$, then the stress state *C** can also be expressed as

$$Q = \frac{3(7-5\nu)}{10(2-\nu)}\left(P^* - P\right). \tag{13b}$$

This predicts that a plot of *Q* versus *P* falls on a straight line with a slope that falls on a narrow range of 0.9-1.05 for ν =0-0.5. However, this amazingly simple prediction of a linear yield envelope is in discrepancy with laboratory observations (Figure 2.1c). In recent years, a number of studies have been conducted to investigate the inelastic compaction behavior of porous siliciclastic and carbonate rocks [e.g., *Wong et al*., 1997; *Vajdova et al*., 2004; *Bemer et al*., 2004; *Baud et al*., 2006; *Baud et al*., 2009]. To our

knowledge, most of the data for the onset of inelastic compaction fall on yield caps that are approximately elliptical in shape, except for an isolated study on Bleurswiller sandstone [*Fortin et al*., 2006] which shows an apparently linear cap. Our analysis here implies that the intermediate principal stress (12b) cannot be neglected in analyzing the development of cataclastic pore collapse.

We next consider the Drucker-Prager criterion by substituting all three principal stresses from equation (12) into (9b). After some algebra, we arrived at this quadratic relation between the mean stress P and differential stress Q at the onset of shear-enhanced compaction:

$$\begin{aligned}&(\alpha-\beta^2\gamma^2)Q^2+[(3\beta-4\beta\gamma^2)P-2\beta\gamma(1-2\gamma)P^*]Q\\&+(1-2\gamma)(P-P^*)[(1+2\gamma)P+(1-2\gamma)P^*]=0\end{aligned}. \tag{14}$$

with $\alpha=100(7-13\nu+7\nu^2)/[9(7-5\nu)^2]$, $\beta=10(1+\nu)/[9(7-5\nu)]$ and $\gamma=2\sin\phi/(3+\sin\phi)$.

In Figure 2.12 we replot the laboratory data in Figure 2.1c, with the differential stress and mean stress at the onset of shear-enhanced compaction normalized by the critical pressure for pore collapse from hydrostatic compression experiments (except for the Solnhofen limestone for which we estimated a P^* value of 550 MPa). Yield stress data for the normalized stresses Q/P^* and P/P^* of the four porous limestones fall on caps very close to one another. A similar behavior was observed for porous sandstones when the yield stresses were normalized by P^* [*Wong et al.*, 1997].

For comparison, we also show the theoretical predictions of (12b) and (13) according to the Mohr-Coulomb and Drucker-Prager criteria, respectively. The solid curves are all for a Poisson's ratio of 0.2. The dotted and dash-dotted curves are for Poisson's ratio

equal to the limiting values of 0 and 0.5 (and ϕ=0). Overall the effect of Poisson's ratio on the cap is relatively small.

Nonlinear caps in qualitative agreement with laboratory data are predicted using the Drucker-Prager yield criterion. The cap expands with decreasing friction angle ϕ (Figure 2.12). The highest differential stresses are associated with the cap for ϕ=0 (corresponding to the von Mises criterion), which shows the best quantitative agreement with experimental data, albeit at somewhat lower levels. For this limiting case, the differential stress Q as a function of the mean stress P is given by:

$$\frac{Q}{P^*} = \frac{3}{20}\frac{(7-5\nu)}{(7-13\nu+7\nu^2)}\left[\sqrt{4(7-13\nu+7\nu^2)-27\left(\frac{(1-\nu)P}{P^*}\right)^2}-(1+\nu)\left(\frac{P}{P^*}\right)\right]. \qquad (15)$$

with the pore collapse pressure P^* as a function of porosity given by (10) and (11).

From what is known about the pressure sensitivity of brittle failure, one would expect the internal friction angle to be greater than 0. Indeed *Bemer et al*.[2004] analyzed low-pressure data for limestone and concluded that the angle ϕ falls in the range of 10^o-45^o, with an apparent trend for its value to increase with decreasing porosity. Fitting the brittle strength data of Solnhofen [*Baud et al*., 2000], Tavel [*Vajdova et al*., 2004], and Indiana [*Ramamurthy*, 2001] limestones, we determined friction angles of 34^o, 25^o, and 25^o, respectively.

However, one should bear in mind that in the context of our model, mechanical response in the effective medium made up of micropores with size ranging from submicron to tens of micron is not identical to that in the bulk sample involving larger macropores. The effective medium is significantly stronger, with an unconfined strength σ_u^* (=1.5P^*) that is typically higher than the bulk sample by a factor of 2-3 (Table 2.1). It

should be noted that seismic velocity data for carbonate rocks show that samples with relatively high microporosity fractions have lower velocities, with the implication that the rock acts as a dual porosity medium with macropores surrounded by a relatively compliant effective medium made up of micropores [*Baechle et al*., 2008]. In addition to lowering the elastic stiffness, our analysis here indicates that brittle failure in such an effective medium with numerous micropores would have a pressure sensitivity significantly lower than that of the bulk sample. To be consistent with the experimentally determined yield caps, our micromechanical model would require the effective medium to fail as a cohesive and pressure insensitive material.

5. Summary and Discussion

We have presented a micromechanical model for cataclastic pore collapse as a mechanism of inelastic compaction in porous limestone. Motivated by microstructural observations, the pore size distribution was treated as bimodal, with the total porosity partitioned between macroporosity and microporosity. Our data for three limestones indicate that the macropores constitute 0.38 or less of the total porosity. Our microstructural observations in these three limestones show that pore collapse tends to first initiate at the larger pores, accompanied by significant cataclasis and microcracking. Accordingly the limestone was modeled as a dual porosity medium, that yields first at the large pores, each of which is surrounded by an effective medium containing the microporosity. Cataclastic yielding (in the form of unconfined compressive failure) of this effective medium obeys the Mohr-Coulomb or Drucker-Prager criterion, with failure

parameters that are dependent on the porosity and pore size according to *Sammis and Ashby's* [1986] micromechanical model for pore-emanated cracking.

We derived an analytic expression for the uniaxial compressive strength associated with failure due to the propagation and coalescence of pore-emanated cracks. This model predicts that the strength is proportional to the inverse square root of the pore size and decreases with increasing porosity following a power law. When laboratory data on unconfined strength were interpreted with this model, two distinct ranges of pore sizes were identified to be active in the failure process. While compact micritic limestones (with porosities <15%) were inferred to have average pore size of 2-10 μm, allochemical and porous micritic limestones have average pore size of 26-500 μm. These values are comparable to microstructural data on macropore dimensions.

The analytic approximation was then used to evaluate the unconfined compressive strength of the effective medium, with the assumption that it was made up micropores of smaller dimensions. For hydrostatic loading, identical theoretical results for the pore collapse pressure P^* were obtained using the Mohr-Coulomb or Drucker-Prager criterion. The critical pressure P^* is predicted to decrease with increasing porosity following a power law, and to increase linearly with a parameter S^* which characterizes the interplay of micropore size, fracture toughness and partitioning of microporosity and macroporosity. Comparison with laboratory data suggests an upper and lower limits of 130 MPa and 20 MPa for S^*. Between these limits, the inferred value of S^* was observed to decrease linearly with increasing porosity.

For nonhydrostatic loading, our micromechanical model provided very different predictions depending on which yield criterion was employed. For the Mohr-Coulomb

criterion, the stress state at the onset of shear-enhanced compaction was predicted to fall on a linear cap. In contrast, nonlinear caps in qualitative agreement with laboratory data were obtained using the Drucker-Prager criterion. The cap is predicted to expand with decreasing friction angle, and in particular the cap for $\phi=0$ (corresponding to the von Mises criterion) shows the best quantitative agreement with experimental data. To be comparable to laboratory data, our micromechanical model implies that the effective medium (solely made up of micropores) is significantly stronger and relatively pressure-insensitve in comparison to the bulk sample (made up of both macropores and micropores).

Our dual porosity model captures a number of micromechanical processes, which cannot be described in a plastic pore collapse model that assumes a single type of porosity. However, since microporosity has been introduced as a distinct entity embedded in the effective medium, predictions of the micromechanical model hinge on geometric and mechanical attributes of the micropores which are difficult to quantify. A technique such as mercury injection porosimetry characterizes the throat dimensions, which can only provide lower bounds on the pore size. Notwithstanding its limitations, it provides an indirect proxy of the bimodal pore geometry (Figure 2.4c). While more refined microstructural observations can elucidate some of the geometric attributes, it is unclear at this point how the mechanical attributes (including the elastic and failure parameters) can be characterized experimentally. Useful insights can possibly be gained from theoretical models and numerical simulations on multi-scale failure development in such a porous medium. Our model focuses on pore-emanated cracking, thus ignoring the role of pre-existing microcracks and their interactions with the micropores, which should be

accounted for if one were to develop a more comprehensive model. It would also be useful to numerically study how the yield cap would evolve with the progressive development of pore collapse, as well as how sensitive it is to macropore geometry.

Our model was developed explicitly for a porous limestone under nominally dry condition. To extend our results to a saturated condition, chemical effects often pervasive in a carbonate rock needs to be isolated from the mechanical effect. There is a paucity of data on either effects related to compactant failure in carbonate rocks. For brittle failure of Tavel limestone, a systematic study of *Vincké et al*. [1998] concluded that the peak stresses for dry and saturated samples (at several pore pressures) follow Terzaghi's effective stress principle, and if indeed the principle also applies to the development of cataclastic pore collapse, then the results derived here can be generalized to saturated limestone samples under drained conditions by using effective stresses as the variables.

We have limited our applications here to porous limestones with relatively high calcite content. Laboratory data indicate that the brittle strength of a carbonate rock would increase with increasing dolomite and quartz contents [*Hugman and Friedman*, 1979]. There are limited data on the effect of these mineral contents on compactive yield stresses of carbonate rocks, and it is possible to extend the micromechanical model for application to these carbonate rocks. It should also be noted that limestones we consider by no means encompass the full spectrum of pore geometry complexity. In particular, our representative volume element is overly simplistic for a carbonate rock with moldic porosity, for which the effective medium surrounding the macropores has geometric attributes significantly more complex than the concentric spheres we used. Seismic velocity measurements indicate that these limestones have relatively high elastic

stiffnesses [*Eberli et al*., 2003]. Other rock types (such as tuff) seem to also have bimodal porosity similar to limestones, and it would also be of interest to test whether our model may be applicable with appropriate choice of fracture toughness.

Acknowledgments

We are grateful to Veronika Vajdova, whose systematic microstructural observations provide the driving force for this study. Lily Wu conducted the pore size measurements, and Jim Quinn assisted us with SEM measurements. Jerome Fortin kindly provided the Chauvigny limestone data in Figure 2.1a. We have benefited from discussions over the years with Phil Choquette, Hubert King, Bill Meyers, Dave Olgaard, Troy Rasbury and Veronika Vajdova. Geog Dresen, Yves Guéguen and the associate editor provided comprehensive reviews and many useful suggestions. This research was partially supported by funds from ExxonMobil Research and Engineering Company.

References

Anselmetti, F. S., S. Luthi, and G. P. Eberli (1998), Quantitative characterization of carbonate pore systems by digital image analysis, *AAPG Bulletin*, *82*, 1815-1836.

Atkinson, B. K., and P. G. Meredith (1987), Experimental fracture mechanics data for rocks and minerals, in *Fracture Mechanics of Rock*, edited by B. K. Atkinson, pp. 477-525, Academic Press, London.

Baechle, G. T., A. Colpaert, G. P. Eberli, and R. J. Weger (2008), Effects of microporosity on sonic velocity in carbonate rocks, *The Leading Edge*, 1012-1018.

Baud, P., A. Schubnel, and T.-f. Wong (2000), Dilatancy, compaction and failure mode in Solnhofen limestone, *J. Geophys. Res.*, *195*, 19289-19303.

Baud, P., S. Vinciguerra, C. David, A. Cavallo, E. Walker, and T. Reuschle (2009), Compaction and failure in high porosity carbonates: mechanical data and microstructural observations, *Pure Appl. Geophys.*, *166*, 869-898..

Baud, P., V. a. Vajdova, and T.-f. Wong (2006), Shear-enhanced compaction and strain localization: Inelastic deformation and constitutive modeling of four porous sandstones, *J. Geophys. Res.*, *111*, B12401, doi: 10.1029/2005JB004101.

Bemer, E., O. Vincké, and P. Longuemare (2004), Geomechanical log deduced from porosity and mineralogical content, *Oil & Gas Sci. Tech. - Rev. IFP*, *59*, 405-426.

Bhatt, J. J., M. M. Carroll, and J. F. Schatz (1975), A spherical model calculation for volumetric response of porous rocks, *J. Appl. Mech.*, *42*, 363-368.

Boutéca, M., J.-P. Sarda, and F. Schneider (1996), Subsidence induced by the production of fluids, *Rev. Inst. Franc. Petr.*, *51*, 349-379.

Choquette, P. W., and L. C. Pray (1970), Geologic nomenclature and classification of porosity in sedimentary carbonates, *AAPG Bulletin*, *54*, 207-250.

Choquette, P. W., and N. P. James (1986), Diagenesis in limestones - the deep burial environment, *Geosciences Canada*, *14*, 3-35.

Churcher, P. L., P. R. French, J. C. Sham and L. L. Schramm (1991), Rock properties of Berea sandstone, Baker dolomite, and Indiana limestone, *Society of Petroleum Engineers*, SPE 21044.

Curran, J. H., and M. M. Carroll (1979), Shear stress enhancement of void compaction, *J. Geophys. Res.*, *84*, 1105-1112.

Dautriat, J., N. Gland, A. Dimanov, S. Youssef, and O. Vizika (2007), Anisotropic permeabilities evolution of reservoir rocks under pressure: New experimental and numerical approaches, *http://www.earth-prints.org/bitstream/2122/2703/1/dautriat.pdf*.

Davis, R. O., and A. P. S. Selvadurai (2002), *Plasticity and Geomechanics*, 287 pp., Cambridge University Press, Cambridge, UK.

Dullien, F. A. L. (1992), *Porous Media: Fluid Transport and Pore Structure. (2nd ed.)*, Academic Press, San Diego.

Eberli, G. P., G. T. Baechle, F. S. Anselmetti, and M. L. Incze (2003), Factors controlling elastic properties in carbonate sediments and rocks, *The Leading Edge*, 654-666.

Fabre, D., and J. Gustkiewicz (1997), Poroelastic properties of limestones and sandstones under hydrostatic conditions, *Int. J. Rock Mech. Min. Sci.*, *34*, 127-134.

Folk, R. L. (1980), *Petrology of Sedimentary Rocks*, 184 pp., Hemphill, Austin.

Fortin, J., S. Stanchits, G. Dresen, and Y. Guéguen (2006), Acoustic emission and velocities associated with the formation of compaction bands in sandstone, *J. Geophys. Res.*, *111*, B10203, doi:10.1029/2005JB003854.

Fredrich, J. T., G. L. Deitrick, J. G. Arguello, and E. P. deRouffignac (2000), Geomechanical modeling of reservoir compaction, surface subsidence, and casing damage at the Belridge diatomite field, *SPE Res. Eval. & Eng.*, *3*, 348-359.

Gurson, A. L. (1977), Continuum theory of ductile rupture by void nucleation and growth: Part I - Yield criteria and flow rules for porous ductile media, *J. Eng. Mat. Tech.*, *99*, 2-15.

Handin, J., and R. V. J. Hager (1957), Experimental deformation of sedimentary rocks under confining pressure: tests at room emperature on dry samples, *AAPG Bulletin*, *41*, 1-50.

Hugman, R. H. H., and M. Friedman (1979), Effects of texture and composition on mechanical behavior of experimentally deformed carbonate rocks, *AAPG Bulletin*, *63*, 1478-1489.

Keith, B. D. and E. D. Pittman (1983), Bimodal porosity in oolitic reservoir: effect on productivity and log response, Rodessa Limestone (Lower Cretaceous), East Texas Basin, *AAPG Bulletin*, *67*, 1391-1399.

Knackstedt, M. A., S. Latham, M. Madadi, A. Sheppard, and T. Varslot (2009), Digital rock physics: 3D imaging of core material and correlations to acoustic and flow properties, *The Leading Edge*, *January*, 28-33.

Lézin, C., F. Odonne, G. J. Massonnat, and G. Escadeillas (2009), Dependence of joint spacing on rock properties in carbonate strata, *AAPG Bulletin*, *93*, 271-290.

Lion, M., M. Skoczylasa, and B. Ledesert (2005), Effects of heating on the hydraulic and poroelastic properties of bourgogne limestone, *Int. J. Rock Mech. Min. Sci.*, *42*, 508-520.

Lønøy, A. (2006), Making sense of carbonate pore systems, *AAPG Bulletin*, *90*, 1381-1405.

Lucia, F. J. (1995), Rock-fabric/petrophysical classification of carbonate pore space for reservoir characterization, *AAPG Bulletin*, *79*, 1275-1300.

Menéndez, B., W. Zhu, and T.-f. Wong (1996), Micromechanics of brittle faulting and cataclastic flow in Berea sandstone, *J. Struct. Geol.*, *18*, 1-16.

Pettijohn, F. J. (1975), *Sedimentary Rocks, 3rd ed.*, 628 pp., Harper & Row, New York.

Pittman, E. D. (1971), Microporosity in carbonate rocks, *AAPG Bulletin*, *55*, 1873-1878.

Ramamurthy, T. (2001), Shear strength response of some geological materials in triaxial compression, *Int. J. Rock Mech. Min. Sci.*, *38*, 683-697.

Sammis, C. G., and M. F. Ashby (1986), The failure of brittle porous solids under compressive stress states, *Acta metall.*, *34*, 511-526.

Segall, P. (1989), Earthquakes triggered by fluid extraction, *Geology*, *17*, 942-946.

Timoshenko, S., and J. N. Goodier (1951), *Theory of Elasticity*, 567 pp., McGraw Hill, New York.

Tondi, E., M. Antonellini, A. Aydin, L. Marchegiani, and G. Cello (2006), The role of deformation bands, stylolites and sheared stylolites in fault development in carbonate grainstones of Majella Mountain, Italy, *J. Struct. Geol.*, *28*, 376-391.

Underwood, E. E. (1970), *Quantitative Stereology*, 274 pp., Addison Wesley, Reading.

Vajdova, V., P. Baud, and T.-f. Wong (2004), Compaction, dilatancy and failure in porous carbonate rocks, *J. Geophys. Res.*, *109*, B05204, doi:10.1029/2003JB002508.

Vincké, O., M. J. Boutéca, J. M. Piau, and D. Fourmaintraux (1998), Study of the effective stress at failure, in *Poromechanics, A Tribute to Maurice A. Biot*, edited by J.-F. Thimus, Y. Abousleiman, A. H.-D. Cheng, O. Coussy and E. Detournay, pp. 635-639, A. A. Balkema, Rotterdam.

Wardlaw, N. C., Y. Li and D. Forbes (1987), Pore-Throat size correlation from capillary pressure curves, *Transport in Porous Media*, *2*, 597-614.

Wardlaw, N. C., M. McKellar and Y. Li (1988), Pore and throat size distributions determined by mercury porosimetry and by direct observation, *Carbonates and Evaporites*, *3*, 1-15.

Wong, T.-f. (1990), Mechanical compaction and the brittle-ductile transition in porous sandstones, in *Deformation Mechanisms, Rheology and Tectonics*, edited by R. J. Knipe and R. H. Rutter, pp. 111-122, Geol. Society Special Publication Vol. 54, London.

Wong, T.-f., C. David, and B. Menéndez (2004), Mechanical compaction, in *Mechanics of Fluid-Saturated Rocks*, edited by Y. Guéguen and M. Boutéca, pp. 55-114, Elsevier Academic Press, Amsterdam.

Wong, T.-f., C. David, and W. Zhu (1997), The transition from brittle faulting to cataclastic flow in porous sandstones: Mechanical deformation, *J. Geophys. Res.*, *102*, 3009-3025.

Zhang, J., T.-f. Wong, and D. M. Davis (1990), Micromechanics of pressure-induced grain crushing in porous rocks, *J. Geophys. Res.*, *95*, 341-352.

Notation

a	radius of a macropore surrounded by an effective medium, μm
a^*	radius of micropores embedded in an effective medium, μm
b	linear dimension of the representative volume element, μm
c	cohesive strength, MPa
C^*	critical stress state for onset of shear-enhanced compaction, MPa
$C^{*'}$	critical stress state for transition from shear-enhanced compaction to dilatancy, MPa
I_1	first stress invariant, MPa
J_2	second stress invariant, MPa^2
K_I	(mode I) stress intensity factor, $MPa \cdot m^{1/2}$
K_{IC}	fracture toughness (critical stress intensity factor), $MPa \cdot m^{1/2}$
ℓ	length of pore-emanated crack, μm
L	crack length normalized by pore radius
L_{cr}	critical normalized crack length
n_A	number of pores per unit area, mm^{-2}
P^*	critical pressure for pore collapse, MPa
P_c	confining pressure, MPa
r	uniform radius of circular holes in *Sammis and Ashby's* [1986] model, μm
$S_{1,2,3}$	remote principal stresses, MPa
V_T	volume of the representative element, μm^3
ϕ	angle of internal friction, degree
Φ	total porosity, %
Φ_m	microporosity, %
Φ_M	macroporosity, %
Φ_*	porosity of the effective medium, %
ρ	radial distance from the center of the spherical pore
σ_1	maximum principal stress, MPa
$\sigma_{\rho,\theta,\psi}$	local principal stresses in the vicinity of the pore, MPa
σ_u	unconfined compressive strength of bulk medium, MPa
σ_u^*	unconfined compressive strength of effective medium, MPa
ν	Poisson's ratio

Table 2.1 Unconfined compressive strength and pore collapse pressure of porous limestone

Limestone	Porosity %	Unconfined Compressive Strength σ_u MPa	Pore Collapse Pressure *P** MPa	References*
Micritic				
Solnhofen	1.7	320	-	
	3.0	-	>450 (~550)	
	3.7	369	-	
	4.1	275	-	
	5.5	280	-	
	5.5	320	-	
Bouye (M)	7.49	158.9	-	*Lézin et al.* [2009]
Bouye (W1)	8.1	147.2	-	*Lézin et al.* [2009]
Bouye (M3)	8.82	142.5	-	*Lézin et al.* [2009]
Tavel	10.4	180	290	
Tavel	13.6	105	180	this study
Pillar (Bed2brac)	20.3	17.12	-	*Lézin et al.* [2009]
Pillar (Mud1)	21.7	24.5	-	*Lézin et al.* [2009]
Pillar (Mud2)	21.9	21.87	-	*Lézin et al.* [2009]
Allochemical				
Madison (R61-16)	0.55	208	-	*Hugman and Friedman* [1979]
Madison (T-69)	2.03	46	-	*Hugman and Friedman* [1979]
Mariana	13	40	-	*Handin and Hager* [1957]
Chauvigny	17	-	120	*J. Fortin* (personal comm.)
	17.4	-	140	
	17.7	41	-	*Fabre and Gustkiewics* [1997]
Indiana	19.4	41	-	
	18, 20	-	60	
	8.43	80	-	*Hugman and Friedman* [1979]
Lavoux	21.8	30.4	30	*Fabre and Gustkiewics* [1997]
Anstrude	23.2	43.2	-	*Lion et al.* [2005]
Estaillades	27	-	30	*Dautriat et al.* [2007]
Majella	30	15.9	26.5	*Baud et al*. [2009], this study

* Reference sources are listed only if the data were not among those included in the compilations of *Baud et al*. (2000) and *Vajdova et al*. [2004].

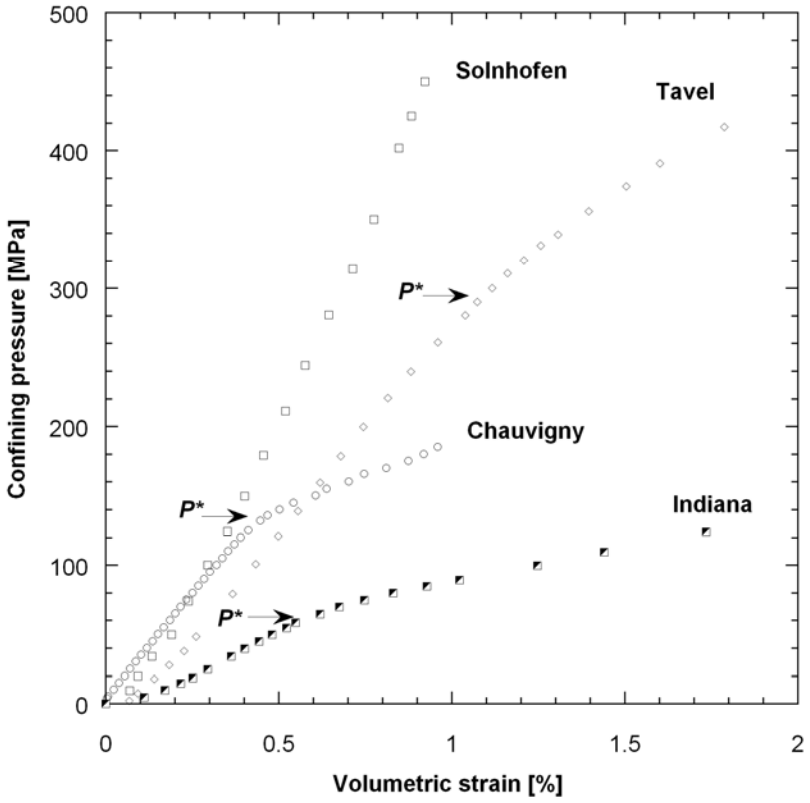

Figure 2.1a: Volumetric strain versus confining pressure for nominally dry samples of Solnhofen [*Baud et al*., 2000], Chauvigny [*J. Fortin*, private communication 2009], Tavel and Indiana [*Vajdova et al*., 2004] limestones. Critical pressures for pore collapse *P** are indicated by arrows.

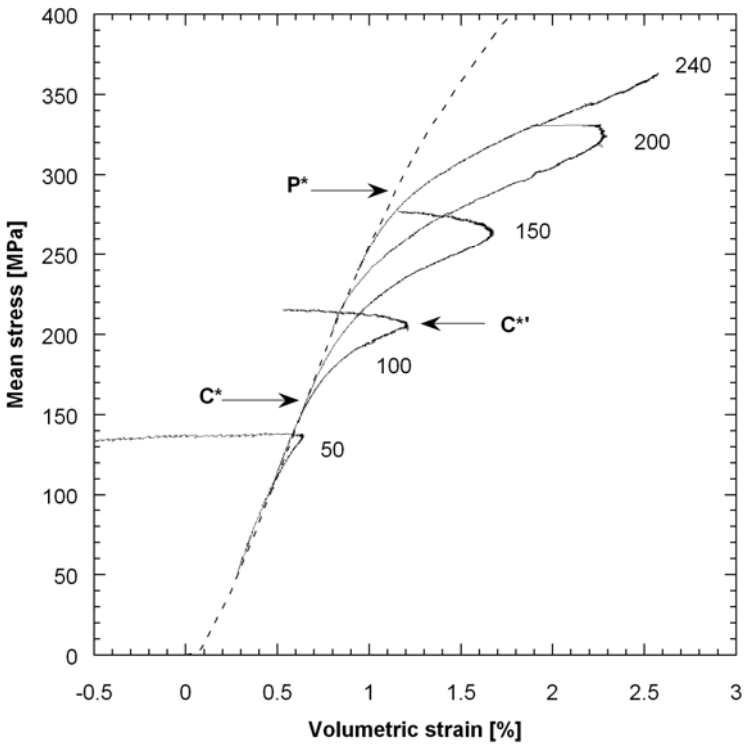

Figure 2.1b: Volumetric strain versus mean stress for triaxial compression of Tavel limestone [*Vajdova et al*., 2004]. The confining pressure (in MPa) is indicated on each curve. For reference, the hydrostat is shown by the dashed line. The critical stress states for onset of shear-enhanced compaction (*C**) and transition from shear-enhanced compaction to dilatancy (*C*'*) are indicated by arrows for the experiment conducted at 100 MPa confining pressure.

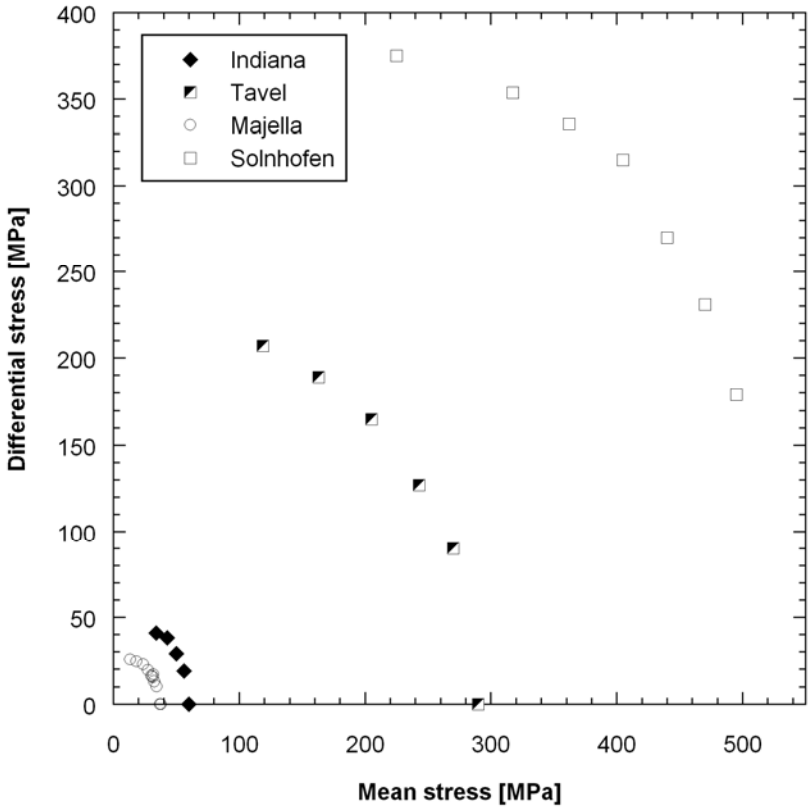

Figure 2.1c: Compactive yield caps for onset of shear-enhanced compaction in the *P* (mean stress) and *Q* (differential stress) space for four limestones. The critical stress (*C**) data are from *Vajdova et al*. [2004] and *Baud et al*. [2009].

(a)

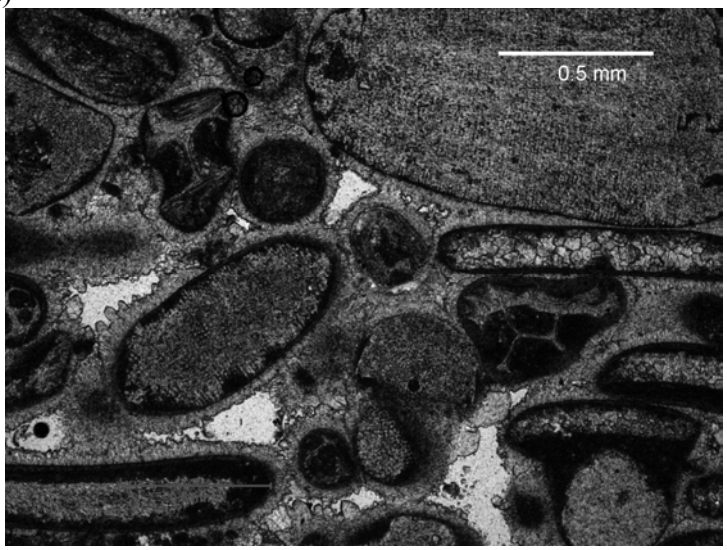

(b)

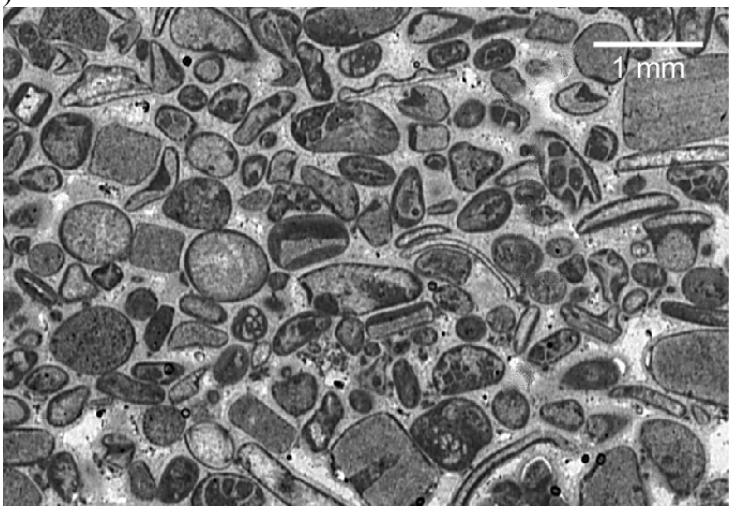

Figure 2.2: (a) Optical micrograph of intact Indiana limestone sample. The allochems are coated with micritic cement around their rims. The lightest phase represents pore space. (b) Scanned image of intact Indiana limestone sample at a resolution of 2400 dpi.

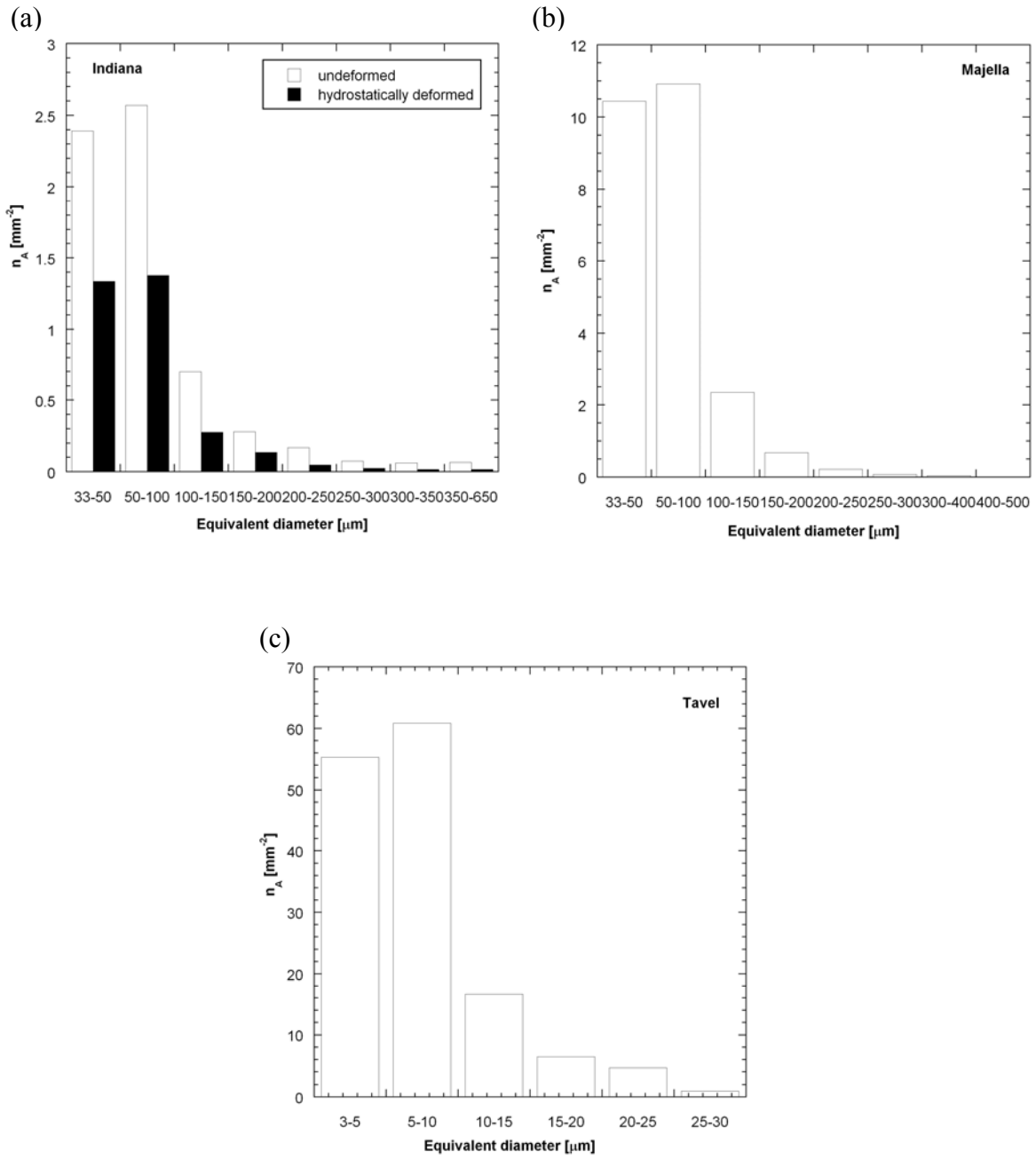

Figure 2.3: Pore size distributions of (a) undeformed and hydrostatically compacted Indiana limestone samples. The number of pores per unit area is plotted versus equivalent diameter. Only data for diameters greater than 33 μm are shown. The deformed sample was compacted to beyond the critical pressure P^*. (b) Majella limestone sample for equivalent diameter greater than 33 μm, and (c) Tavel limestone sample for pores that can be resolved under optical microscope at relatively high magnification.

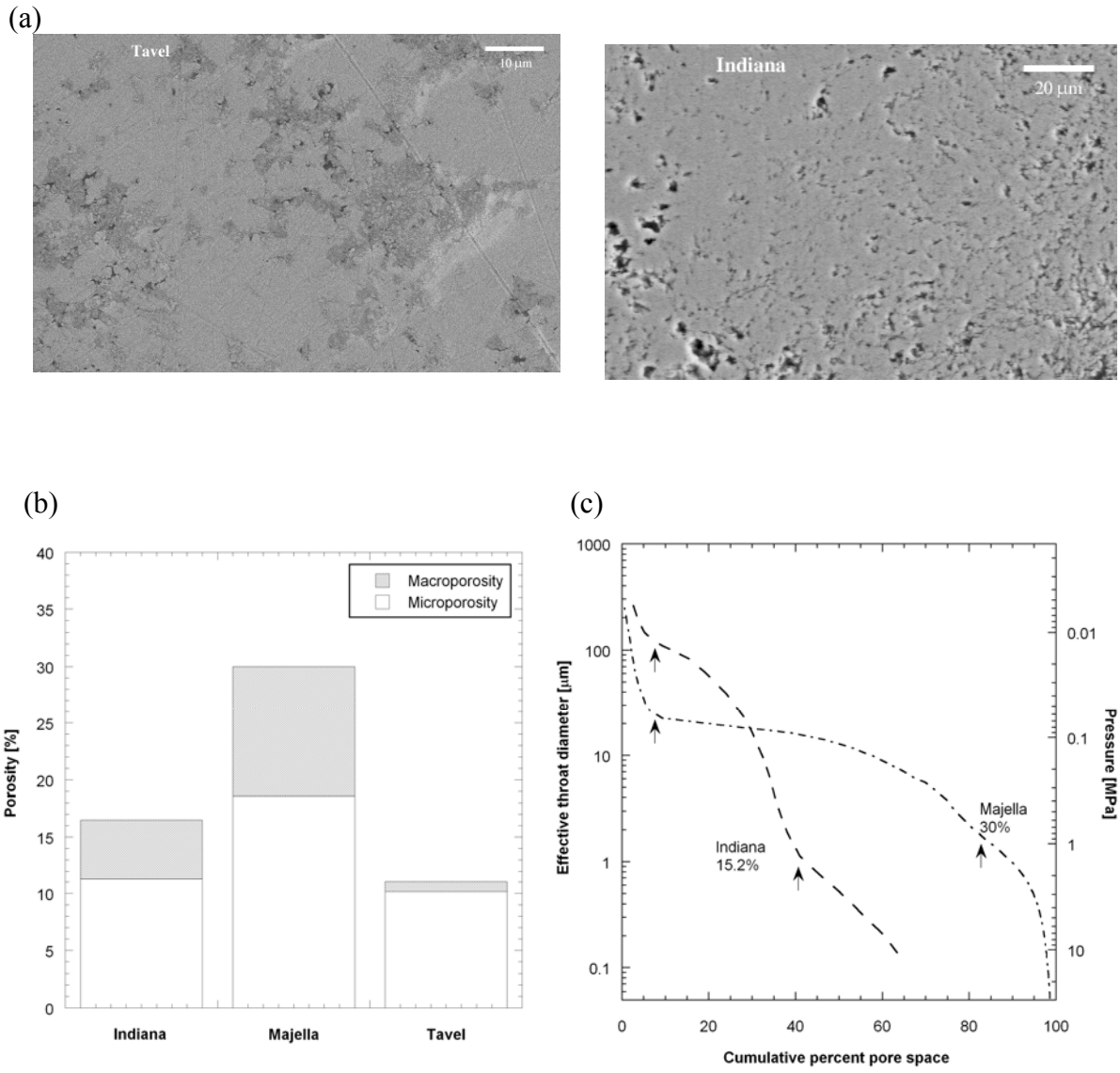

Figure 2.4: (a) Backscattered SEM images of micropores (darker areas) in two limestone samples. The left frame is from a Tavel limestone sample stressed to just beyond the onset of dilatancy, showing micropores embedded in the micritic matrix. The right frame is from a relatively undeformed allochem in a hydrostatically compacted Indiana limestone sample. (b) Partitioning of microporosity and macroporosity in Indiana, Majella and Tavel limestones. (c) Bimodal throat size distributions of Indiana and Majella limestones inferred from mercury injection tests by *Churcher et al*. [1991] and *Baud et al*. [2009], respectively. The effective throat diameter and capillary pressure are plotted versus cumulative percent pore space injected by mercury. Arrows mark inflection points corresponding to threshold throat diameters.

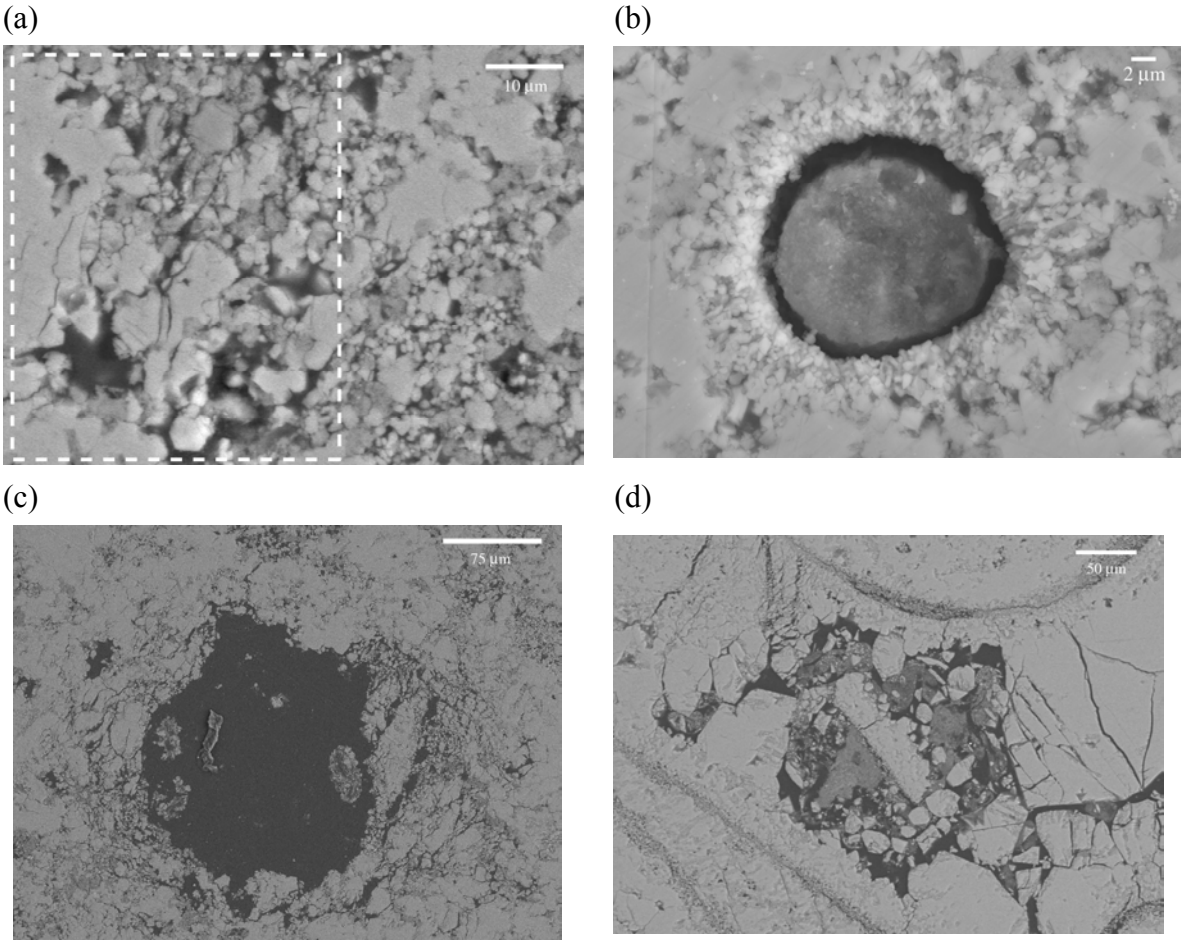

Figure 2.5: Backscattered SEM images of deformed limestone samples. (a) A Tavel limestone sample that failed in uniaxial compression. Area within the white rectangle shows an incipient shear band developed in the proximity of the through-going shear band. Direction of σ_1 is vertical. (b) A hydrostatically compacted Tavel limestone sample. A macropore surrounded by a halo of cataclastic damage was observed. The diameter of the macropore is ~ 20µm, the concentric rim of particularly intense damage extended over a thickness of ~2µm. (c) A Tavel limestone sample deformed triaxially at a confining pressure of 150 MPa. Intensive cataclastic damage was observed near the surface of a large macropore that has collapsed, especially around the equator with numerous pore-emanated cracks sub-parallel to σ_1 (vertical direction). (d) An Indiana limestone sample deformed triaxially at a confining pressure of 20 MPa. Collapse of a macropore is shown in the figure. Direction of σ_1 is vertical.

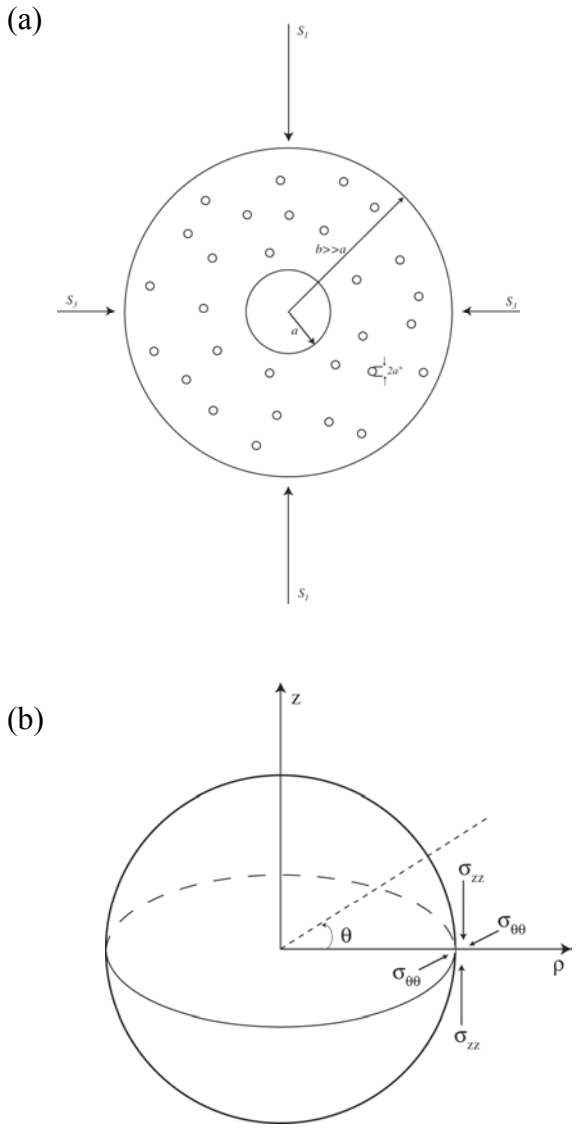

Figure 2.6: (a) Schematic diagram of a representative volume element of radius *b*. A macropore of radius *a* is surrounded by an effective medium made up of many micropores of radius a^*. Remote principal stresses are represented by S_1, S_2 and S_3. (b) Local stress field at the vicinity of the macropore. The local principal stresses σ_{zz} and $\sigma_{\theta\theta}$ act along the axial and azimuthal directions, respectively. Because of the boundary conditions in the pore surface, the radial stress is zero.

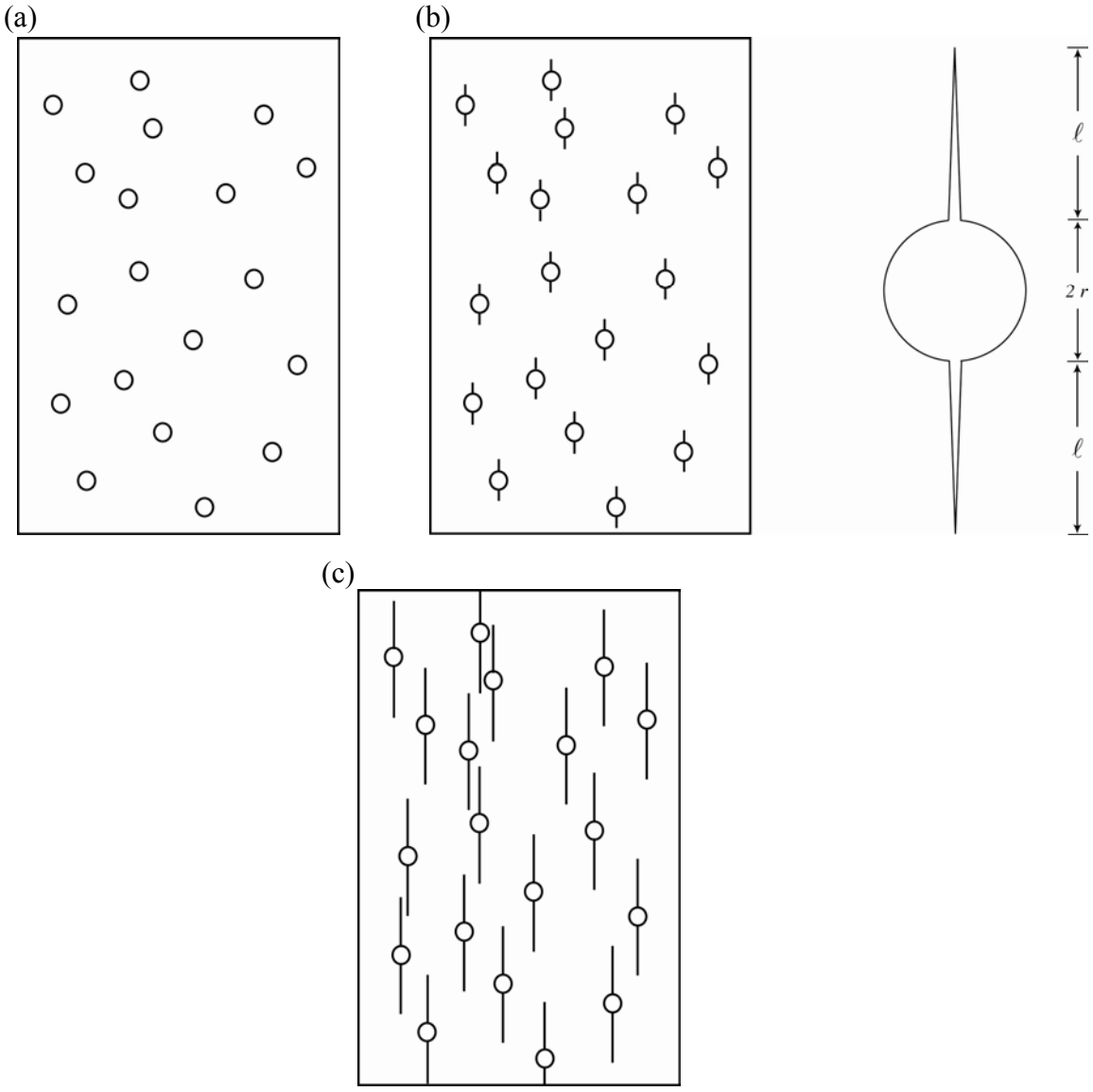

Figure 2.7: *Sammis & Ashby's* [1986] pore-emanated cracking model. (a) A 2-dimensional elastic medium is permeated by circular holes of uniform radius *r*. (b) Cracks emanate from circular pores when subjected to remotely applied axial stress. The stress-induced cracks have propagated to a length . (c) Propagation and coalescence of pore-emanated cracks lead to instability and macroscopic failure.

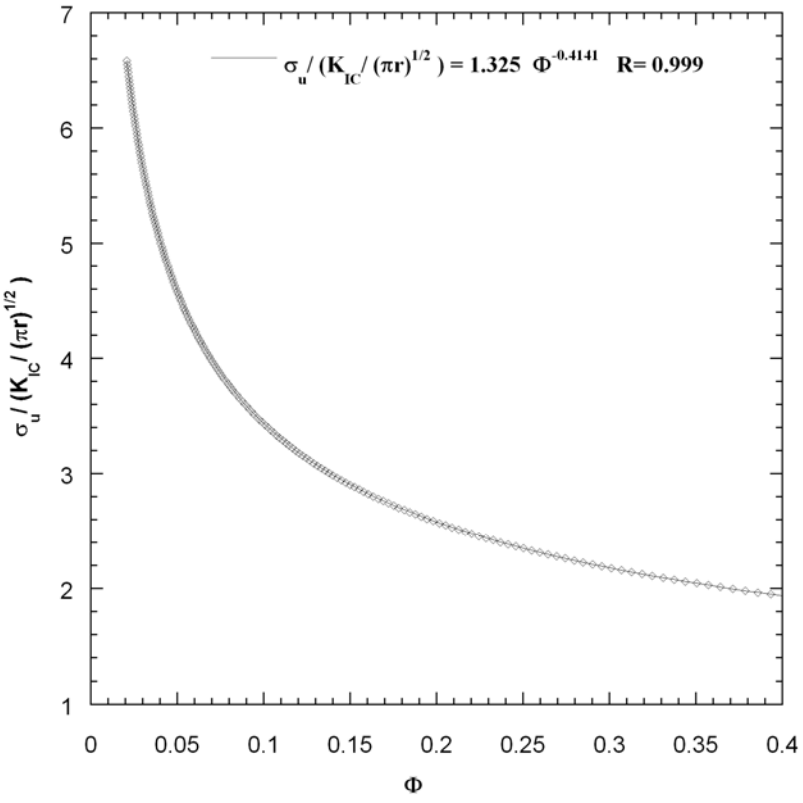

Figure 2.8: Theoretical predictions of normalized unconfined compressive strength as a function of porosity according to (4b) and (5) are shown as diamond symbols. The solid curve corresponds to the power law (6) obtained by regression, with a correlation coefficient of 0.999.

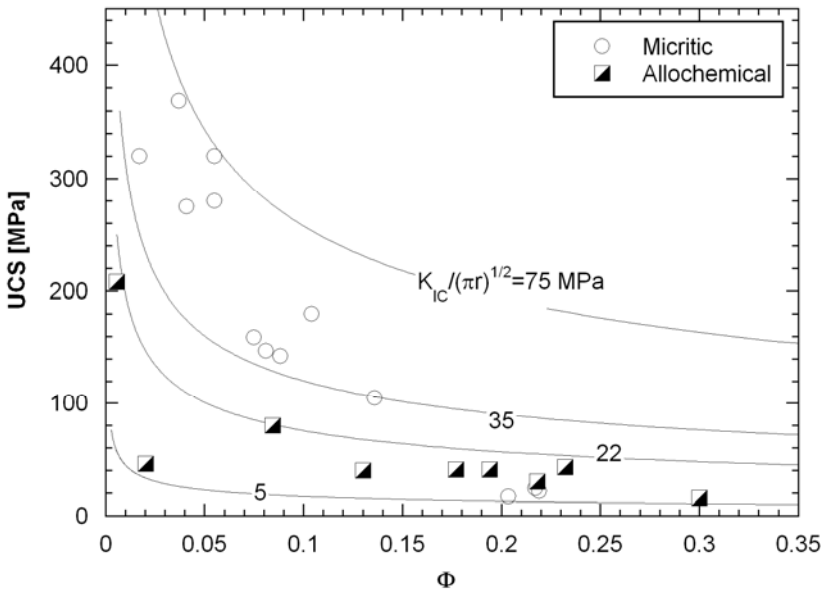

Figure 2.9: Comparison of theoretical predictions with laboratory data on unconfined compressive strength (UCS) of micritic and allochemical limestones. Theoretical curves of UCS as a function of porosity for four different values of are plotted. Experimental data (Table 2.1) of micritic and allochemical limestones are shown as circles and squares, respectively.

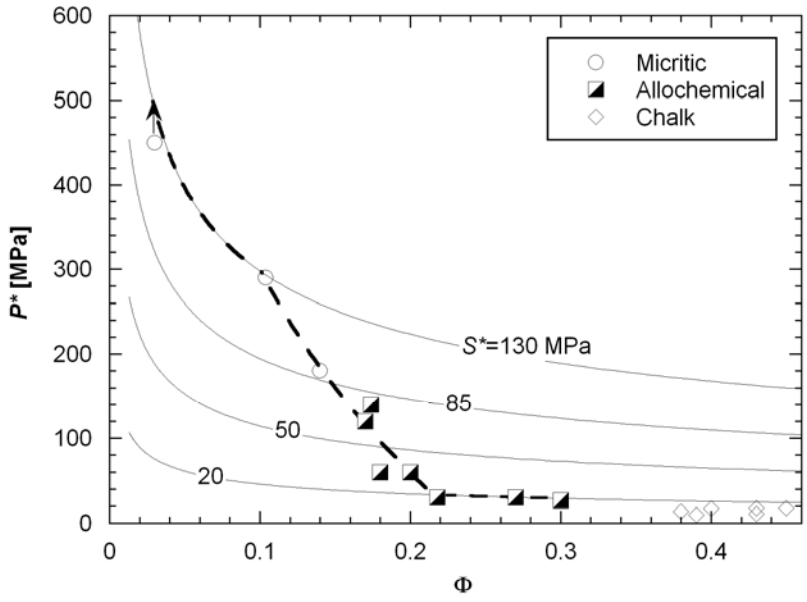

Figure 2.10: Comparison of theoretical predictions with laboratory data on critical pressures for pore collapse (P^*) of limestones. Theoretical curves of P^* as a function of porosity for four different values of S^* (10) are plotted. Experimental data (Table 2.1) of micritic, allochemical limestones and chalk are shown as circles, squares and diamonds, respectively. They are bounded by upper and lower limits of S^*=130 MPa and S^*=20 MPa. The dashed curve with three segments corresponds to S^* given by the empirical equation (11).

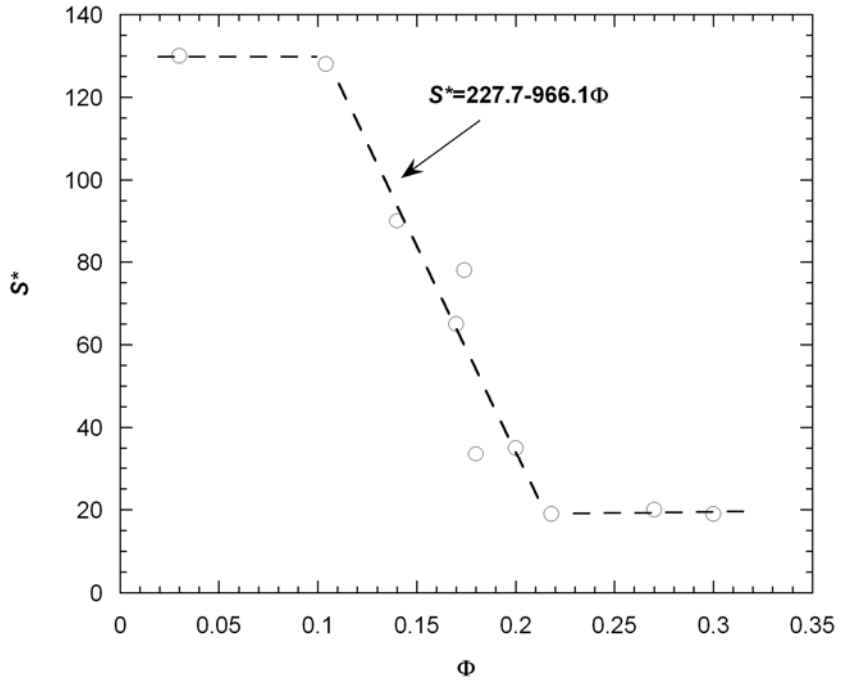

Figure 2.11: Inferred value of *S** versus total porosity. The empirical relation (11) is shown by a dashed curve with three segments.

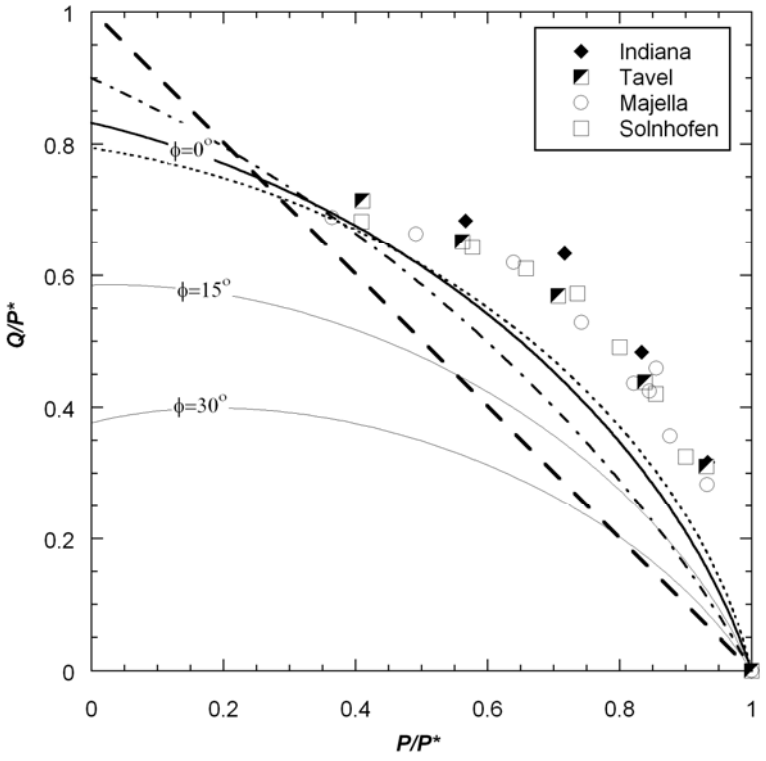

Figure 2.12: Differential stress (Q) and mean stress (P) at the onset of shear-enhanced compaction normalized by the pore collapse pressure P^*. The four limestones are identical to those in Figure 2.1c. Solid curves and dashed line represent theoretical predictions according to Drucker-Prager and Mohr-Coulomb criteria with ν=0.2, respectively. The angle of internal friction ϕ is marked on each of the Drucker-Prager curves. The dotted and dash-dotted curves are for ϕ=0, with Poisson's ratio ν=0 and ν=0.5, respectively.

Chapter 3

Micromechanical basis for the Coulomb failure parameters

Abstract

The Coulomb criterion is used extensively for describing the macroscopic development of shear fracture in a brittle rock, and yet the micromechanical basis for the Coulomb failure parameters remains obscure. To gain insights into the physics of the Coulomb criterion, we derived analytic approximations for the empirical failure parameters with reference to the sliding wing crack model. These expressions clarify the dependence of the uniaxial compressive strength on micromechanical parameters including the fracture toughness, friction coefficient, crack dimension and density. The internal friction coefficient can be approximated as related linearly to the friction coefficient of the sliding crack, and the difference between the two coefficients has a logarithmic dependence on the square root of the crack density.

1. Introduction

In 1776 Coulomb proposed the simplest and arguably the most important criterion for the macroscopic development of shear fracture in a brittle rock. This linear relation has been found to be applicable to geomaterials over a broad range of pressures, and it is adopted widely in geological and geotechnical applications (*Goodman*, 1989; *Paterson and Wong*, 2005; *Jaeger et al.*, 2007). Nevertheless, there have been misunderstandings as to whether Coulomb was indeed the first to formulate this important failure criterion and what exactly he proposed. Many of the historical errors in the geological and geophysical literature were rectified by *Handin* (1969), who also highlighted several questions on the physics of the Coulomb criterion that remain obscure.

The fracture of a brittle rock is characterized by the Coulomb criterion using two empirical parameters, commonly known as the "cohesive (shear) strength" and "coefficient of internal friction" (*Paterson and Wong*, 2005; *Jaeger et al.*, 2007). There has been significant confusion with respect to the latter parameter. Indeed Coulomb himself drew an analogy of his concept of internal friction with Amonton's law of friction, thus implying that the coefficient of internal friction corresponds directly to that for frictional sliding on a physical surface. As elaborated by *Handin* (1969), this is a misconception since no sliding surface exists in the intact body until cohesion is broken. "In cohesive material, internal friction is a fictitious quantity that cannot be measured directly. …It is not the post-fracture friction associated with sliding on new surfaces in broken material. Neither is it equivalent to the frictional resistance to slip on artificial rock surfaces."

For an incohesive granular material such as sand, the coefficient of internal friction is typically higher than the friction coefficient for sliding between the individual grains, and the difference between the two coefficients is related to microstructural attributes including porosity, particle shape and grain size distribution (*Holtz and Kovacs*, 1981; *Mitchell,* 1993). In a cohesive rock the coefficient of internal friction has been observed to attain a value that may exceed unity (*Handin*, 1969; *Paterson and Wong*, 2005; *Jaeger et al.*, 2007), and is usually greater than the frictional coefficient for sliding on pre-existing fracture surfaces which typically has a value small than unity (*Byerlee*, 1978). Presumably the difference between the two coefficients for a given rock is related to microstructural parameters that control the micromechanics of fracture in a brittle rock. The micromechanical basis for the Coulomb failure parameters can be established only if a realistic model for the damage mechanics of brittle fracture has been developed.

A model that can capture many of the key micromechanical processes associated with the onset and development of dilatancy and compressive failure in rock is the sliding wing crack model, which has been analyzed in numerous theoretical studies (e.g., *Horii and Nemat-Nasser*, 1986; *Ashby and Sammis*, 1990; *Kemeny and Cook*, 1991). The model identifies a number of micromechanical parameters (including the friction coefficient for sliding on a preexisting crack, crack density, crack dimension and fracture toughness) that exert significant influence on the development of brittle fracture. The primary objective of this study is to gain insights into the physics of the Coulomb criterion by connecting the Coulomb failure parameters with these micromechanical parameters with reference to the sliding wing crack model.

2. Onset of Dilatancy and Development of Brittle Fracture

In Figure 3.1 we use *Brace's* (1964) data for Frederick diabase to illustrate application of the Coulomb criterion. In this paper, we will adopt the convention that compression is positive, and denote the maximum and minimum principal stresses by σ_1 and σ_3, respectively. Four nominally dry samples were deformed in conventional triaxial compression at confining pressures ranging from room pressure to 318 MPa. Each of the diabase samples failed by development of a macroscopic shear fracture after attaining a peak differential stress. The Mohr circle that corresponds to the stress state at the peak σ_1 value and the fixed confining pressure (σ_3) is plotted in Figure 3.1a. It can be seen that the failure envelope can be approximated by a line that is tangential to the four Mohr circles, which corresponds to the linear Coulomb criterion relating the shear traction τ to the normal traction σ_n:

$$\tau = \tau_o + \sigma_n \tan\varphi \tag{1}$$

The slope of the tangent is the coefficient of internal friction $\mu_i = \tan\varphi$. The intercept τ_0 corresponds to the cohesive (shear) strength. It is implicitly assumed in the Coulomb criterion that the shear failure would ultimately develop along a planar fracture at an angle $(\pi/4 - \varphi/2)$ with respect to σ_1.

Alternatively we can plot directly the principal stresses (Figure 3.1b), which also fall on a linear trend given by the equation:

$$\sigma_1 = \sigma_u + k\,\sigma_3 \tag{2}$$

This straight line in the principal stress space has an intercept that corresponds to the uniaxial compressive strength σ_u. The slope *k* corresponds to the coefficient of passive

stress in Rankine's theory of earth pressure (*Lambe and Whitman*, 1969). These two parameters can be expressed in terms of the Coulomb failure parameters:

$$\sigma_u = 2\tau_o \left(\sqrt{\mu_i^2 + 1} + \mu_i \right) \tag{3a}$$

$$k = \left(\sqrt{\mu_i^2 + 1} + \mu_i \right)^2 \tag{3b}$$

For a saturated rock deformed under drained condition, the mechanical effect of pore pressure is such that Coulomb criterion in the form of either (1) or (2) would still apply if the principal stresses and normal stresses are replaced by the Terzaghi effective stresses, given by subtracting the pore pressure from the stresses (*Handin et al*., 1963; *Brace and Martin*, 1968).

In the brittle faulting regime, inelastic deformation accompanied by dilatancy is typically observed prior to the attainment of the peak stress. The stress level at the onset of dilatancy, commonly designated C' following *Brace, Paulding and Scholz* (1966), is usually observed to be between 1/3 and 2/3 of the macroscopic fracture stress. There is significant uncertainty associated with picking this critical stress level from mechanical data (*Hadley*, 1973). Nevertheless, laboratory data indicate that the principal stresses at the onset of dilatancy for a given rock often follow an approximately linear trend (*Paterson and Wong*, 2005), as illustrated in Figure 3.2a and 3.2b for compact and porous rocks, respectively. Microstructural observations have shown that the development of dilatancy at and beyond C' are related to the initiation and propagation of stress-induced cracks (*Tapponier and Brace*, 1976; *Kranz*, 1983). Both intragranular and intergranular cracking have been observed to propagation preferentially along orientations sub-parallel to the maximum principal stress σ_1.

3. The Sliding Wing Crack Model

While the stress-induced cracking is delocalized in the pre-peak stage, the damage development becomes localized along a macroscopic shear band with the attainment of the peak stress and development of strain softening (*Wong*, 1982; *Moore and Lockner*, 1995; *Menéndez et al*., 1996). A conceptual model widely used to analyze such micromechanical processes is the "sliding wing crack" (e.g. *Horii and Nemat-Nasser*, 1986; *Ashby and Sammis*, 1990; *Kemeny and Cook*, 1991). The model considers the growth of "wing cracks" that initiate from tensile stress concentration at the tips of pre-existing cracks undergoing frictional slip. The fracture mechanics is such that increasing the deviatoric stresses causes the wing crack to propagate along a curved path and ultimately reach a stable orientation parallel to the direction of σ_1 (Figure 3.3a). With the accumulation of such anisotropic damage distributed throughout the rock, it will ultimately attain a critical state at which the multiplicity of cracks coalesce to develop a shear band (Figure 3.3b).

The sliding wing crack has some advantages of analytical tractability and it captures a vital aspect of mean stress dependence through introducing friction on the sliding crack. However, it should be noted that this model is only one of a range of possible models which can describe the generation of growing cracks initiated at grain-scale heterogeneities in the rock (*Kemeny and Cook*, 1991). *Nemat-Nasser* (1985) has suggested that since there are common features to all these models, the essential aspects might be represented by a generic model.

3.1. Initiation of Wing Cracks

The sliding wing crack model considers sources of tensile stress concentration that are located at the tips of pre-existing cracks (with initial length $2c$ and oriented at angle γ to σ_1). The applied stresses induce a shear traction on the crack plane and, if this resolved shear traction is sufficiently high to overcome the frictional resistance across the closed crack, frictional slip results in tensile stress concentrations at the two tips which may induce "wing cracks" to nucleate and extend out of the initial plane of the main sliding crack (Figure 3.3a). The driving force is characterized by the mode-I stress intensity factor K_I at the tip of the putative wing crack. With increased loading, it will attain the critical value K_{IC}, at which point a wing crack nucleates and propagates along a curved path to ultimately reach a stable orientation parallel to the direction of σ_1.

If the onset of dilatancy C' is identified with the initiation of wing cracks and if the rock is assumed to contain randomly oriented cracks, then the wing cracks should first nucleate from those sliding cracks oriented at $\gamma = \frac{1}{2}\tan^{-1}(1/\mu)$, where μ is the frictional coefficient for sliding along the main crack. From linear elastic fracture mechanics (*Cotterell and Rice*, 1980; *Horii and Nemat-Nasser*, 1986; *Ashby and Sammis*, 1990), the principal stresses at the onset of dilatancy is inferred to be

$$\sigma_1 = \left[\frac{\sqrt{1+\mu^2}+\mu}{\sqrt{1+\mu^2}-\mu}\right]\sigma_3 + \left[\frac{\sqrt{3}}{\sqrt{1+\mu^2}-\mu}\right]\frac{K_{IC}}{\sqrt{\pi c}} \tag{4}$$

Mechanical data for the critical stress state C' at the onset of dilatancy (Figure 3.2) can be fitted with this linear relation to infer values of μ and $K_{IC}/\sqrt{\pi c}$. Using this approach, *Ashby and Sammis* (1990) analyzed the mechanical data of nine rock types to

obtain values of μ ranging from 0.55 to 0.64. For the Four-mile gneiss with relatively strong mica foliation, *Rawling et al.* (2002) inferred lower values of μ ranging from 0.2 to 0.3. If the wing crack initiates from an intragranular location, it is appropriate to assume a K_{IC} value comparable to fracture mechanics measurements on the minerals that form the rock. However, a somewhat lower K_{IC} value is expected for intergranular cracking along a grain boundary, usually considered to be weaker than the intact mineral.

3.2. Propagation and Coalescence of Wing Cracks

As the density of wing cracks increases, they coalesce to form a macroscopic shear band in the strain softening stage (Figure 3.3b). To analyze the peak stress data, we here adopt *Ashby and Sammis'* (1990) 2-dimensional damage mechanics model for mathematical convenience. The evolution of damage is characterized by the parameter $D = \pi(\ell + c\cos\gamma)^2 n_A$, where ℓ is the length of the wing crack, and n_A is the number of sliding cracks per unit area initially present. Before wing cracks nucleate, the length $\ell = 0$ and therefore the initial damage is given by $D_o = \pi(c\cos\gamma)^2 n_A$, a non-dimensional quantity that is sensitively dependent on the number and dimension of the sliding cracks. It should be noted that the initial damage D_o is directly proportional to the "crack density" parameter ($\varepsilon_o = c^2 n_A$) introduced by *Walsh* (1965) and *Budiansky and O'Connell* (1976) for analyzing the elastic moduli of a cracked solid.

With the progressive propagation and interaction of the wing cracks, the principal stresses evolve with damage in accordance with equation (17) of *Ashby and Sammis* (1990):

$$\sigma_1 = \left[C_1 + \frac{C_4\ (\sqrt{D/D_o} - 1)}{1 + \sqrt{\pi D_o}\ \dfrac{\sqrt{D/D_o} - 1}{1 - \sqrt{D}}} \right] \sigma_3 + \frac{\sqrt{\sqrt{D/D_o} - 1 + 0.1/\cos\gamma}}{1 + \sqrt{\pi D_o}\ \dfrac{\sqrt{D/D_o} - 1}{1 - \sqrt{D}}} \frac{C_4}{\sqrt{\cos\gamma}} \frac{K_C}{\sqrt{\pi c}} \qquad (5)$$

where $C_1 = (\sqrt{1+\mu^2} + \mu)/(\sqrt{1+\mu^2} - \mu)$ and $C_4 = \sqrt{30}\cos\gamma/(\sqrt{1+\mu^2} - \mu)$. The operative micromechanical processes are expected to be complex, involving intragranular, intergranular and transgranular cracking and possibly a hybrid of modes I, II and III. Hence it is likely that the critical stress intensity factor would have a value significantly higher than the K_{IC} value for mode-I cracking in the minerals. Accordingly we use a different notation K_C for this fracture toughness. Following previous studies (*Horii and Nemat-Nasser*, 1986; *Ashby and Sammis*, 1990; *Fredrich et al.*, 1990), a value of $\gamma = 45^o$ was assumed in equations (5) for all our calculations presented here.

Figure 3.4a illustrates the evolution of stress with damage evolution, for a friction coefficient μ=0.7, initial damage $D_o = 0.12$ and $K_C/\sqrt{\pi c}$ = 65 MPa. Five fixed values of σ_3 are considered. The evolution of σ_1 with accumulation of damage *D* is qualitatively similar, in that the attainment of a peak stress is followed by strain softening. The peak σ_1 value as a function of σ_3 falls on a linear trend (Figure 3.4b). Calculations using different values of initial damage and friction give qualitatively similar results, in that the peak stress values fall on a linear failure envelope :

$$\sigma_1 = a(\mu, D_o)\ \sigma_3 + b(\mu, D_o)\ \frac{K_C}{\sqrt{\pi c}} \qquad (6)$$

Comparing equation (6) with equations (1) and (2), it can be seen that in the context of the sliding wing crack model, the uniaxial compressive strength σ_u and cohesive shear

strength τ_o are proportional to $K_C/\sqrt{\pi c}$ and dependent on both μ and D_o. Furthermore, the internal friction coefficient μ_i depends on not only the friction coefficient μ but also the initial damage D_o.

As presented here, the sliding wing crack model involves four micromechanical parameters: μ, D_o, $K_{IC}/\sqrt{\pi c}$ and $K_C/\sqrt{\pi c}$. These parameters can be inferred by fitting mechanical data on the onset of dilatancy and peak stress to equations (4) and (6), respectively. Linear regression of the former provides constraints on μ and $K_{IC}/\sqrt{\pi c}$. However, the fitting exercise can be quite cumbersome for the latter in the absence of analytic expressions for the coefficients *a* and *b* in equation (6). An optimal fit can be obtained only by repeated trials over the parameter space of D_o and $K_C/\sqrt{\pi c}$. This approach is illustrated in Figure 3.5 using mechanical data from conventional triaxial compression tests on Etna basalt (block EB_III) that were acquired recently by *Zhu et al*. (in preparation, 2010). The saturated samples were deformed under drained condition at a pore pressure p_p fixed at 10MPa. Figure 3.5a shows the effective mean stress $(\sigma_1+2\sigma_3)/3-p_p$ as a function of porosity change in five experiments at effective pressures σ_3-p_p ranging from 10 MPa to 150 MPa. Data from a hydrostatic compression experiment are shown as the dashed curve. Following the procedure outlined by *Wong et al*. (1997), the onset of dilatancy is identified as the point C' on the triaxial compression curve beyond which the nonhydrostatic loading induced a porosity enhancement relative to pure hydrostatic loading at the same effective mean stress. The C' and peak stress data are then plotted in Figure 3.5b, and the four micromechanical

parameters we obtained by fitting two straight lines through the data are listed in Table 3.1.

Using the same approach, we obtained these four micromechanical parameters for a total of ten sets of mechanical data for which both the C' and peak stress values are available over a sufficiently wide range of pressures (Table 3.1). Inferred values of the friction coefficient fall in the range of 0.26 to 0.71, comparable to measurements on common minerals (*Horn and Deere*, 1962) and values previously inferred by *Ashby and Sammis* (1990). The initial damage parameter spans a narrower range between 0.13 and 0.36. Our inferred values of the normalized fracture toughness $K_C / \sqrt{\pi c}$ for ultimate failure are greater than the corresponding values of $K_{IC} / \sqrt{\pi c}$ for wing crack initiation, by as much as a factor of 5 in the case of the basalt EB_I. Following *Ashby and Sammis* (1990), most previous studies (e.g. *Baud et al.*, 2000; *Rawling et al.*, 2002) did not differentiate between the two critical stress intensity factors, even though they implicitly placed more weight on the peak stress data and therefore their inferred values were closer to the $K_C / \sqrt{\pi c}$ parameter we defined here. Given the systematic difference between the values inferred from the C' and peak stress data, we concluded that it is more appropriate to specify two distinct fracture toughness parameters for the two different stages of inelastic deformation and failure.

4. Micromechanics of Uniaxial Compressive Failure and Internal Friction

To elucidate the micromechanical basis of the Coulomb failure parameters, we will next obtain analytic approximations for the uniaxial compressive strength σ_u and internal

friction coefficient $\mu_i = \tan\varphi$ as functions of the micromechanical parameters μ, D_o and $K_C / \sqrt{\pi c}$ according to the sliding wing crack model. Related expressions for the cohesive shear strength τ_o and Rankine coefficient *k* can then be obtained using equation (3).

4.1. Analytic Approximation for the Uniaxial Compressive Strength

For uniaxial compressive loading, $\sigma_3 = 0$ and hence equation (4) can be simplified as:

$$\sigma_1 = \left(\frac{\sqrt{30\cos\gamma(\sqrt{D/D_0} - \alpha)}}{1 + \sqrt{\pi D_0}\,\dfrac{\sqrt{D/D_0} - 1}{1 - \sqrt{D}}} \right) \frac{K_C}{[\sqrt{1+\mu^2} - \mu]\sqrt{\pi c}} \tag{7}$$

where $\alpha = 1 - 0.1/\cos\gamma$. A necessary condition for an instability (and strain softening) to develop is for $d\sigma_1 / dD = 0$, which implies that

$$D(1-\sqrt{\pi}) + \sqrt{D}(3\sqrt{D_0\pi} - \sqrt{\pi} - 2) + [1 + (2\alpha - 1)\sqrt{D_0\pi} - 2\alpha D_0\sqrt{\pi}] = 0 \tag{8}$$

Once the initial damage D_o has been specified, the critical value of the damage parameter *D* at which instability develops can be obtained as a positive root of the above equation. Substituting this critical value into equation (7), the stress σ_1 so attained would correspond to the unconfined compressive strength σ_u, which is predicted to scale with $K_C / [(\sqrt{1+\mu^2} - \mu)\sqrt{\pi c}]$

Using this approach we calculated the normalized unconfined compressive strength as a function of initial damage parameter D_0, plotted as open symbols in Figure 3.6. The predicted values can be empirically fitted by a power law (with a correlation coefficient of 0.999) shown as the dashed curve in Figure 3.6. Thus, this provides an analytic

approximation for the unconfined compressive strength according to the sliding wing crack model:

$$\sigma_u = \frac{1.346}{\sqrt{1+\mu^2}-\mu}\,\frac{K_C}{\sqrt{\pi c}}\,D_0^{-0.256} \tag{9}$$

4.2. Dependence of Internal Friction on Friction Coefficient of the Sliding Crack and Initial Damage

Our derivation of an analytic approximation for the internal friction coefficient was guided by the contour plot of constant μ_i values in the parameter space of friction coefficient μ and initial damage D_o. We first fixed values of μ and D_o and then using a procedure analogous to that shown in Figure 3.4a, we calculated via equation (5) the normalized stress $\sigma_1/(K_c/\sqrt{\pi c})$ as a function of damage *D* at a fixed normalized stress $\sigma_3/(K_c/\sqrt{\pi c})$. The normalized peak stress was picked from the curve, and the process repeated for several other values of $\sigma_3/(K_c/\sqrt{\pi c})$. Analogous to Figure 3.4b, the peak stress data were then fitted with the linear relation (6), from which the slope $a(\mu, D_o)$ was determined. This represents the Rankine coefficient *k*, and using equation (3b) we then calculated the corresponding internal friction coefficient $\mu_i(\mu, D_o)$ which were plotted in Figure 3.7 as solid contour lines.

This contour plot can be used a graphical tool for inferring the initial damage, as illustrated by the data points in Figure 3.7 for the rocks compiled in Table 3.1. Mechanical data from triaxial compression experiments were used to infer values of μ (from linear regression of C' data) and $\mu_i = \tan\varphi$ (from linear regression of peak stress data). These two values uniquely locate its position on the contour plots, and the

corresponding value of D_o can immediately be read off from the horizontal axis, without resorting to additional numerical calculations.

An interesting feature of the curvilinear contours is that they are approximately parallel to one another. Furthermore, adjacent contours (in increments of $\Delta\mu_i = 0.1$) have roughly the same vertical spacing corresponding to $\Delta\mu \approx 0.1$. This suggests that an approximately linear relation exists between the internal friction coefficient $\mu_i = \tan\varphi$ and the friction coefficient μ, with a slope close to unity. Indeed if we plot the calculated values of μ_i as a function of μ (for a fixed initial damage D_o), they fall on a linear trend with a slope ranging from 0.91 to 0.99 for D_o between 0.12 and 0.7 (Figure 3.8a). This implies an analytic approximation for the internal friction coefficient in the form of $\mu_i = A(D_o) + B(D_o)\,\mu$.

By linear regression, the intercepts *A* and slopes *B* of the calculated values in Figure 3.8a were evaluated and then plotted as functions of D_o in Figure 3.8b and 8c, respectively. We observed that these two sets of values can be fitted empirically by a logarithmic relation $A = -0.062 - 0.501 \log D_o$ and a linear relation $B = 0.895 + 0.142 D_o$, respectively. The empirical relations are shown as the dashed curves in the figures, which are in excellent agreement with the calculated values for D_o ranging from 0.1 to 0.7. Incorporating these results, we thus arrive at an analytic approximation for the internal friction coefficient according to the sliding wing crack model:

$$\mu_i = \tan\varphi = -0.062 - 0.501 \log D_o + (0.895 + 0.142 D_o)\,\mu \qquad (10)$$

In Table 3.2 we compiled values of the Coulomb failure parameters and micromechanical parameters inferred using the analytic approximations, which are in

good agreement with those in Table 3.1 obtained by direct numerical calculations. We also plotted as dashed lines the contours for $\mu_i = \tan\varphi$ according to the approximation (10). It can be seen that they are in very good agreement with the solid lines from direct numerical calculations.

5. Discussion

With reference to the sliding wing crack model, we have derived analytic approximations for the Coulomb failure parameters as functions of four micromechanical parameters, thus clarifying the physics underlying the empirical failure criterion for macroscopic failure. Our results are expected to apply to a brittle rock with a pore space that is dominated by microcracks. As reviewed by *Kemeny and Cook* (1991), there are several other types of micromechanical model proposed for brittle failure, with reference to tensile stress concentrations induced by cylindrical pores (*Sammis and Ashby*, 1986), elastic mismatch (*Dey and Wang*, 1981), elastic contact of impinging grains (*Zhang et al.*, 1990), and dislocation pile-up (*Wong*, 1990)**.** However, since there are common features to all these models (*Nemat-Nasser*, 1985), it is possible that some of our results derived herein may be generalized to other rocks with different pore space characteristics.

According to equation (9), the uniaxial compressive strength scales with $K_C/[(\sqrt{1+\mu^2}-\mu)\sqrt{\pi c}]$ and it increases with decreasing D_o. For rocks with similar composition and porosity such that they have comparable values for the three micromechanical parameters K_C, μ and D_o, our analysis suggests that σ_u would scale with $1/\sqrt{c}$. It is plausible that the sliding crack dimension *c* scales with the average grain size (*Fredrich et al.*, 1990), in which case one expects the uniaxial compressive strength

to scale with the inverse square root of the grain size. Indeed this type of "Hall-Petch relation" has been observed in several rock types (e.g. *Brace*, 1961; *Wong et al.*, 1990).

As reviewed by *Chang et al.* (2006), numerous attempts have been made to correlate the uniaxial compressive strength and seismic velocities (or elastic moduli) with mixed success. If indeed such a correlation can be established, then borehole geophysics data on velocity can be used to infer the strength. Assuming a linear correlation, *Hickman and Zoback* (2004) inferred from velocity log data at the SAFOD pilot hole the uniaxial compressive strength and in situ stresses as functions of depth. Equation (9) shows that for comparable values of $K_C / [(\sqrt{1+\mu^2} - \mu)\sqrt{\pi c}]$, the strength σ_u depends on the initial damage D_o according to a power law with an exponent of -0.256. The parameter D_o is directly proportional to the "crack density" ε_o, which is the pore space parameter that exerts significant influence over the elastic moduli and sonic speeds of a cracked solid (*Walsh*, 1965; *Budiansky and O'Connell*, 1976; *Mavko et al.*, 1998). Hence our analysis suggests that an empirical correlation between a seismic speed and the uniaxial compressive strength in a suite of rock may exist only if the average crack length, fracture toughness and friction coefficient are such that the parameter $K_C / [(\sqrt{1+\mu^2} - \mu)\sqrt{\pi c}]$ is comparable.

For the internal friction coefficient μ_i, equation (10) shows that it has a linear dependence on the friction coefficient μ. The influence of μ may explain the significant difference in internal friction between San Marcos gabbro and Westerly granite (Tables 3.1 and 3.2), two compact rocks with relatively low inferred values of D_o. The former

has a significantly larger proportion of mica which is expected to reduce the frictional resistance along some the sliding cracks (*Rawling et al.*, 2002).

As for the dependence on the initial damage, we note that (10) can be approximated as $\mu_i = \tan\varphi \approx -0.06 - \log\sqrt{D_o} + (0.90 + 0.14 D_o)\,\mu$, which implies that the internal friction coefficient has a logarithmic dependence on the square root of the initial damage D_o. Our analysis shows that typically $\mu_i \geq \mu$, with the difference $\mu_i - \mu$ increasing with decreasing D_o. The difference between the coefficients μ_i and μ is higher in a rock with relatively small amount of initial damage, which is often a compact crystalline rock. There seems to be a weak correlation between the porosity and inferred D_o values. The initial damage of a compact rock such as Westerly granite and San Marcos gabbro is inferred to be smaller than that for a porous sedimentary rock such as Berea sandstone and Indiana limestone (Tables 3.1 and 3.2; Figure 3.7). However, if we consider the Bentheim, Vosges and Berea sandstones of comparable porosities, their inferred D_o values span over a broad range. This is not unexpected since D_o is sensitively dependent on crack dimension, and even if two rocks have the same porosity, the damage parameter can be significantly higher in the one with relatively long preexisting cracks. Evaluation of this important micromechanical parameter can be performed by either detailed microstructural observations or indirect inference from measurements of elastic moduli or sonic speeds.

Acknowledgments

That we need specify two different critical stress intensity factors for the sliding wing crack model was motivated by related research of Emmanuelle Klein when she visited

the Stony Brook laboratory some time ago. This research was partially supported by funds from ExxonMobil Research and Engineering Company.

References

Ashby, M.F., Sammis, C.G., 1990. The damage mechanics of brittle solids in compression, Pure and Appl. Geophys., 133, 489-521.

Baud, P., Zhu, W., Wong, T.-f., 2000. Failure mode and weakening effect of water on sandstone, J. Geophys. Res., 105, 16371-16390.

Brace, W.F., 1961. Dependence of fracture strength of rocks on grain size, in Proc. 4th Symposium on Rock Mechanics, pp. 99-103, Penn. State Univ., Min. Ind. Exp. Sta. Bull. No.76.

Brace, W.F., 1964. Brittle fracture of rocks, in State of Stress in the Earth's Crust, edited by W.J. Judd, pp. 111-178, Elsevier, New York.

Brace, W.F., Martin, R.G.I., 1968. A test of the law of effective stress for crystalline rocks of low porosity, Int. J. Rock Mech. Min. Sci., 5, 415-426.

Brace, W.F., Paulding, B., Scholz, C.H., 1966. Dilatancy in the fracture of crystalline rocks, J. Geophys. Res., 71, 3939-3954.

Budiansky, B., O'Connell, R.J., 1976. Elastic moduli of a cracked solid, Int. J. Solids Struct., 12, 81-97.

Byerlee, J.D., 1978. Friction of rocks, Pure Appl. Geophys., 116, 615-626.

Chang, C., Zoback, M.D., Khaksar, A., 2006. Empirical relations between rock strength and physical properties in sedimentary rocks, J. Petrol. Sci. Eng., 51, 223-237.

Cotterell, B., Rice, J.R., 1980. Slightly curved or kinked cracks, Int. J. Fracture, 16, 155-169.

Dey, T., Wang, C.Y., 1981. Some mechanisms of microcrack growth and interaction in compressive rock failure, Int. J. Rock Mech. Min. Sci., 18, 199-210.

Fredrich, J., Evans, B., Wong, T.-f., 1990. Effects of grain size on brittle and semi-brittle strength: implications for micromechanical modelling of failure in compression, J. Geophys. Res., 95, 10907-10920.

Goodman, R.E., 1989. Introduction to Rock Mechanics, 2nd ed., 2 ed., 562 pp., John Wiley and Sons, NY.

Hadley, K., 1973. Laboratory investigation of dilatancy and motion on fault surfaces at low confining pressures, in Proc. Conf. Tectonic Problems of the San Andreas Fault System, edited by R. L. Kovach and A. Nur, pp. 427-435.

Handin, J., 1969. On the Coulomb-Mohr failure criterion, J. Geophys. Res., 74, 5343-5348.

Handin, J., Hager, R.V., Friedman, M., Feather, J.N., 1963. Experimental deformation of sedimentary rock under confining pressure: pore pressure effects, Bull. Am. Asso. Petrol. Geol., 47, 717-755.

Hickman, S., Zoback, M.D., 2004. Stress orientations and magnitudes in the SAFOD pilot hole, Geophys. Res. Lett., 31, L15S12, doi:10.1029/2004GL020043.

Holtz, R.D., Kovacs, W.D., 1981. Introduction to Geotechnical Engineering, 733 pp., Prentice-Hall, Englewood Cliffs, NJ.

Horii, H., Nemat-Nasser, S., 1986. Brittle failure in compression: splitting, faulting and brittle-ductile transition, Phil. Trans. Royal Soc. London, 319, 337-374.

Horn, H.M., Deere, D.U., 1962. Frictional Characteristics of minerals, Geotechnique, 12, 319-335.

Jaeger, J.C., Cook, N.G.W., Zimmerman, R.W., 2007. Fundamentals of Rock Mechanics, 4th ed., 475 pp., Blackwell, Oxford.

Kemeny, J.M., Cook, N.G.W., 1991. Micromechanics of deformation in rocks, in Toughening Mechanisms in Quasi-Brittle Materials, edited by S. P. Shah, pp. 155-188, Klewer Academic.

Klein, E., 2002. Micromécanique des Roches Granulaires Poreuses: Expérimentation et Modélisation, 158 pp, Université Louis Pasteur de Strabourg, Strasbourg, France.

Kranz, R.L., 1983. Microcracks in rocks, a review, Tectonophysics, *100*, 449-480.

Lambe, T.W., Whitman, R.V., 1969. Soil Mechanics, 553 pp., John Wiley, NY.

Mavko, G., Mukerji, T., Dvorkin, J., 1998. The Rock Physics Handbook: Tools for Seismic Analysis in Porous Media, 329 pp., Cambridge University Press, Cambridge.

Menéndez, B., Zhu, W., Wong, T.-f., 1996. Micromechanics of brittle faulting and cataclastic flow in Berea sandstone, J. Struct. Geol., 18, 1-16.

Mitchell, J.K., 1993. Fundamentals of Soil Behavior, 2nd Edition, 437 pp., John Wiley, NY.

Moore, D.E., Lockner, D.A, 1995. The role of microcracking in shear-fracture propagation in granite, J. Struct. Geol., 17, 95-114.

Nemat-Nasser, S., 1985. Discussion of geometric probability approach to the characterization and analysis of microcracking in rocks, Mech. Mater., 4, 277-281.

Paterson, M.S., Wong, T.-f., 2005. Experimental Rock Deformation - The Brittle Field, 2nd Edition, 348 pp., Spinger-Verlag, New York.

Rawling, G.C., Baud, P., Wong, T.-f., 2002. Dilatancy, brittle strength and anisotropy of foliated rocks: Experimental deformation and micromechanical modeling, J. Geophys. Res., 107, 2234, doi:10.1029/2001JB000472.

Sammis, C.G., Ashby, M.F., 1986. The failure of brittle porous solids under compressive stress states, Acta metall., 34, 511-526.

Tapponier, P., Brace, W.F., 1976. Development of stress-induced microcracks in Westerly granite, Int. J. Rock Mech. Min. Sci., 13, 103-112.

Walsh, J.B., 1965. The effect of cracks on the uniaxial elastic compression of rocks, J. Geophys. Res., 70, 399-411.

Wong, R.H.C., Chau, K.T., Wang, P., 1996. Microcracking and grain size effect in Yuen Long marbles, Int. J. Rock Mech. Min. Sci., 33, 479-485.

Wong, T.-f., 1982. Micromechanics of faulting in Westerly granite, Int. J. Rock Mech. Min. Sci., 19, 49-64.

Wong, T.-f., 1990. A note on the propagation behavior of a crack nucleated by a dislocation pile-up, J. Geophys. Res., 95, 8639-8646.

Wong, T.-f., David, C., Zhu, W., 1997. The transition from brittle faulting to cataclastic flow in porous sandstones: Mechanical deformation, J. Geophys. Res., 102, 3009-3025.

Vajdova, V., Baud, P., Wong, T.-f., 2004. Compaction, dilatancy and failure in porous carbonate rocks, J. Geophys. Res., 109, B05204, doi:10.1029/2003JB002508.

Zhang, J., Wong, T.-f., Davis, D.M., 1990. Micromechanics of pressure-induced grain crushing in porous rocks, J. Geophys. Res., 95, 341-352.

Table 3.1. Petrophysical properties and micromechanical parameters inferred from sliding wing crack model

Rock Type	Average Grain Size, mm	Porosity %	μ	D_0	$K_{IC}/\sqrt{\pi c}$ MPa	$K_c/\sqrt{\pi c}$ MPa	References
Westerly granite	0.750	0.009	0.71	0.13	31.00	70	*Brace et al.* (1966)
San Marcos gabbro	2.000	0.2	0.26	0.14	87.88	160	*Hadley* (1973)
EB_I basalt	-	5.0	0.50	0.14	14.38	82	*Zhu et al*., in preparation
EB_III basalt	-	5.0	0.65	0.18	2.04	55	*Zhu et al*., in preparation
Bentheim sandstone	0.210	23.0	0.67	0.21	8.11	19	*Klein* (2002)
Wertheim sandstone	0.205	13.0	0.63	0.18	4.75	26	*Klein* (2002)
Vosges sandstone	0.140	23.0	0.58	0.31	3.40	18	*Klein* (2002)
Berea sandstone (wet)	0.170	21.0	0.52	0.36	6.10	31	*Baud et al.* (2000)
Indiana limestone	0.300	15.6	0.33	0.36	77.00	85	*Vajdova et al*. (2004)
Tavel limestone	0.005	10.4	0.35	0.31	13.00	17	*Vajdova et al*. (2004)

Table 3.2. Coulomb failure parameters from rock mechanics experiments and micromechanical parameters inferred from analytic approximation for sliding wing crack model

Rock Type	μ	tanφ	τ_0	D_0	$K_c/\sqrt{\pi c}$, MPa
Westerly Granite	0.70	1.02	61.07	0.133	68.79
San Marcos gabbro	0.26	0.61	117.05	0.14	144.30
EB_I basalt	0.50	0.81	68.02	0.14	80.24
EB_III basalt	0.65	0.91	46.36	0.18	55.07
Bentheim sandstone	0.67	0.89	15.51	0.22	18.55
Wertheim sandstone	0.63	0.86	22.14	0.21	26.52
Vosges sandstone	0.58	0.73	13.31	0.32	16.73
Berea sandstone (wet)	0.52	0.65	22.78	0.36	29.24
Indiana limestone	0.33	0.47	62.98	0.36	82.16
Tavel limestone	0.35	0.52	12.61	0.31	16.21

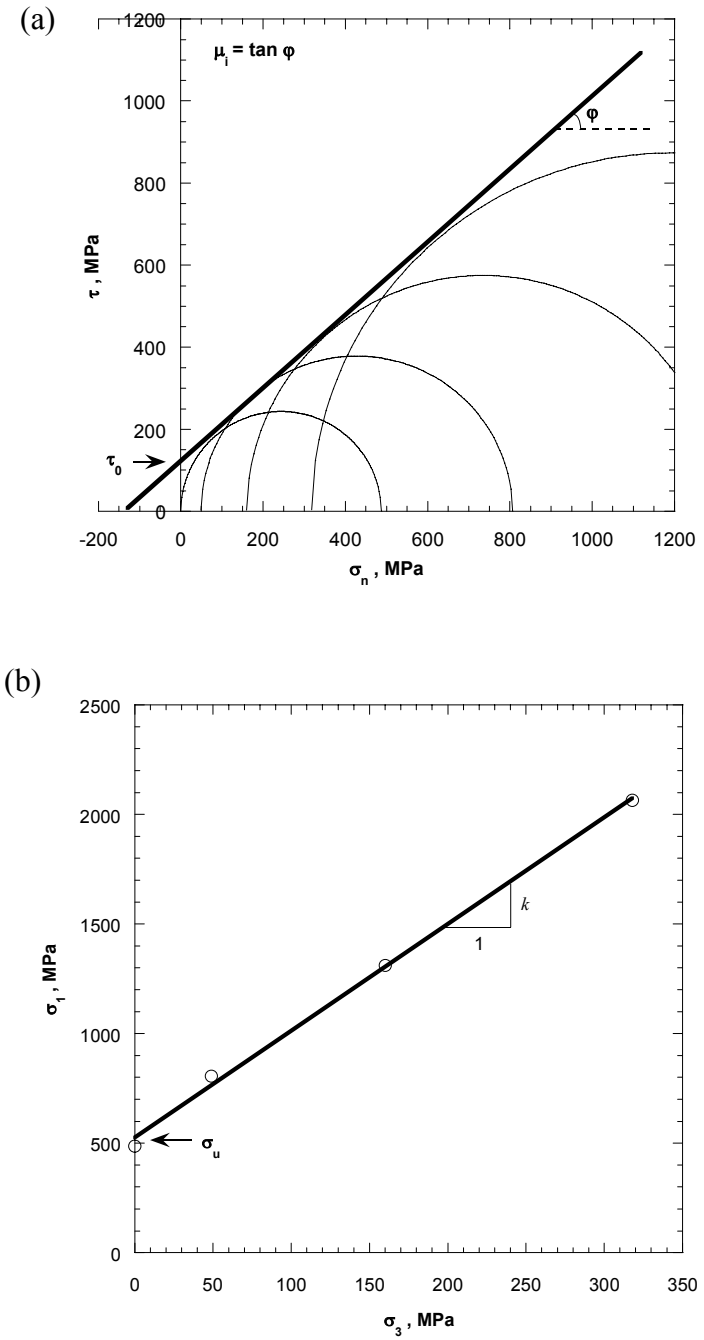

Figure 3.1. Peak stresses associated with brittle fracture in nominally dry samples of Frederick diabase in four conventional triaxial compression tests (*Brace*, 1964), plotted in the form of (a) Mohr circles, and (b) maximum principal stress as a function of minimum principal stress. The cohesive strength τ_0, angle of internal friction φ, uniaxial compressive strength σ_u and Rankine coefficient *k* are indicated.

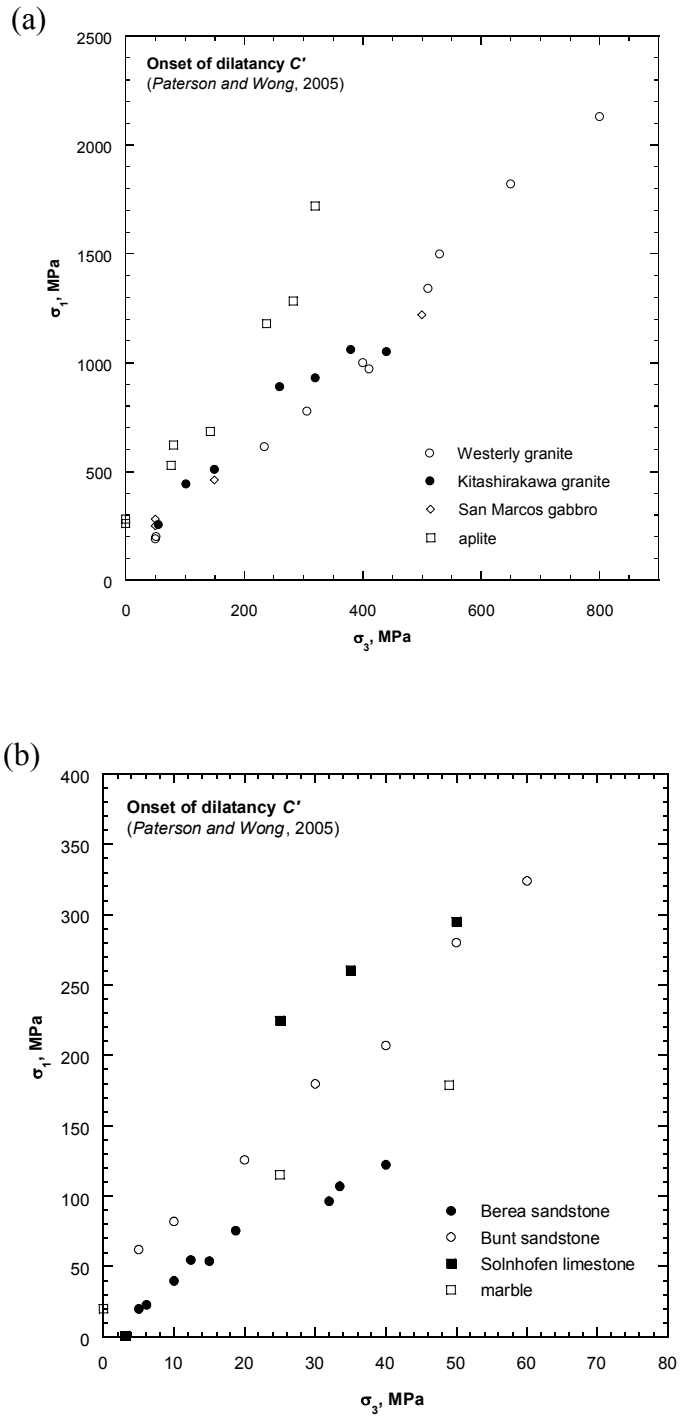

Figure 3.2. Maximum and minimum principal stresses at the onset of dilatancy *C'* in (a) compact, and (b) porous rocks (after *Paterson and Wong*, 2005).

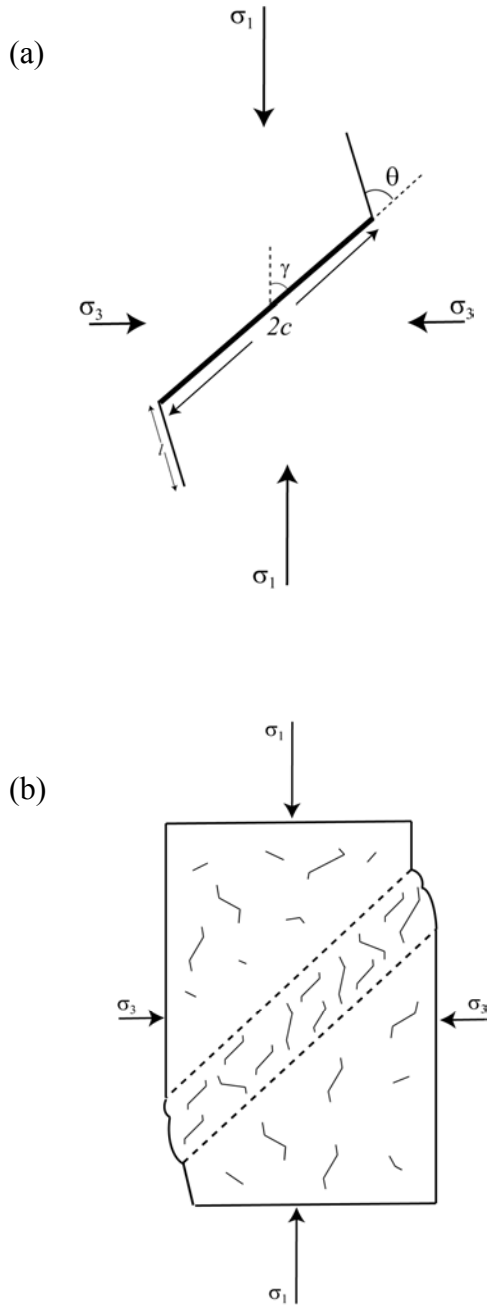

Figure 3.3. (a) Sliding wing crack model for the development of dilatancy and instability in the brittle faulting regime. Directions of the maximum and minimum principal stresses are indicated. The sliding and wing cracks are at angles of γ and θ with respect to the σ_1 direction, respectively.
(b) Schematic diagram of a failed sample. Directions of the maximum and minimum principal stresses are shown. A macroscopic shear fault across the sample has developed by the coalescence of sliding wing cracks.

(a)

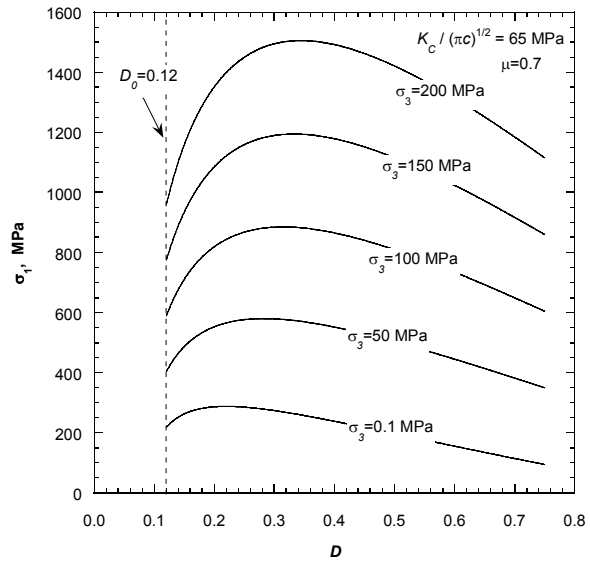

(b)

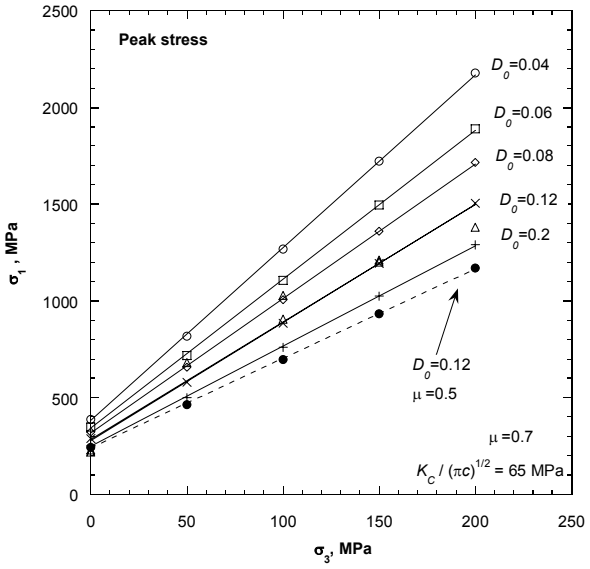

Figure 3.4. (a) Maximum principal stress as a function of the damage parameter D according to (5) for initial damage D_0=0.12, friction coefficient μ=0.7 and normalized fracture toughness $K_c/(\pi c)^{1/2}$ = 65 MPa. The curves for five different minimum principal stresses ranging from 0.1 MPa to 200 MPa are shown. (b) The solid lines connect peak values of the maximum principal stress versus the minimum principal stresses for five different values of initial damage D_o with fixed values of friction coefficient μ=0.7 and normalized fracture toughness $K_c/(\pi c)^{1/2}$ = 65 MPa. For comparison the dashed line is for fixed values of μ=0.5 and D_0=0.12.

(a)

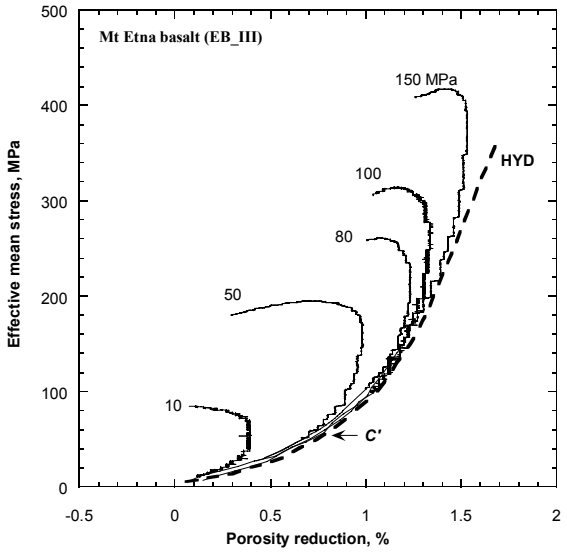

(b)

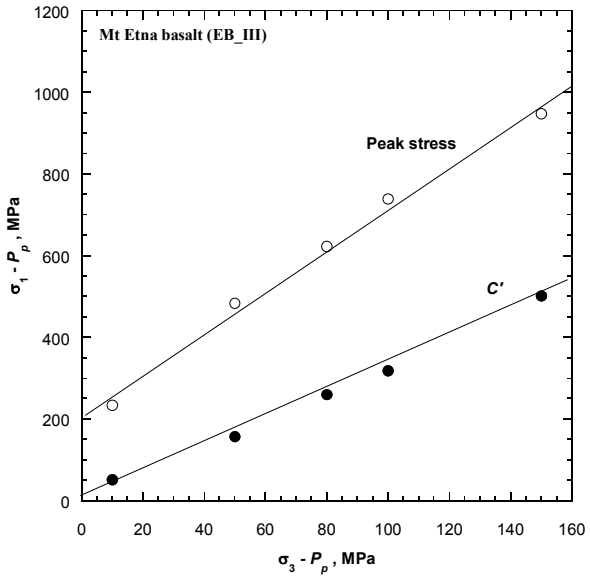

Figure 3.5. Experimental data for EB_III block of Mt Etna basalt samples deformed in the brittle faulting regime (*Zhu et al*., in preparation). (a) Effective mean stress as a function of porosity reduction in five conventional triaxial compression experiments, with effective pressure fixed at values as indicated. For reference the hydrostat is plotted as the dashed line. The onset of dilatancy *C'* at effective pressure of 50 MPa is marked by the arrow. (b) Values for peak stress (open circles) and onset of dilatancy *C'* (solid circles) determined from mechanical data in (a) are plotted in effective principal stress space.

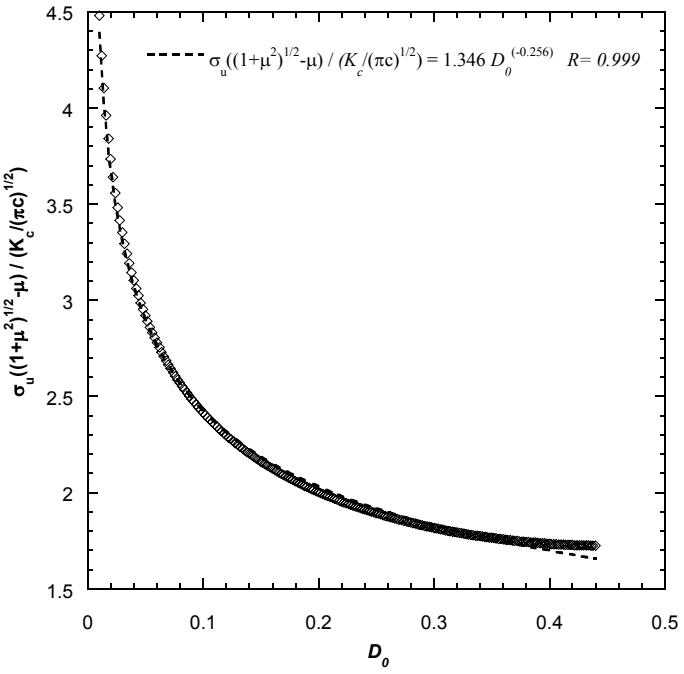

Figure 3.6. The open symbols represent theoretical predictions of the normalized unconfined compressive strength as a function of initial damage according to the sliding wing crack model. The dashed curve corresponds to the power law (9) obtained by regression, with a correlation coefficient of 0.999.

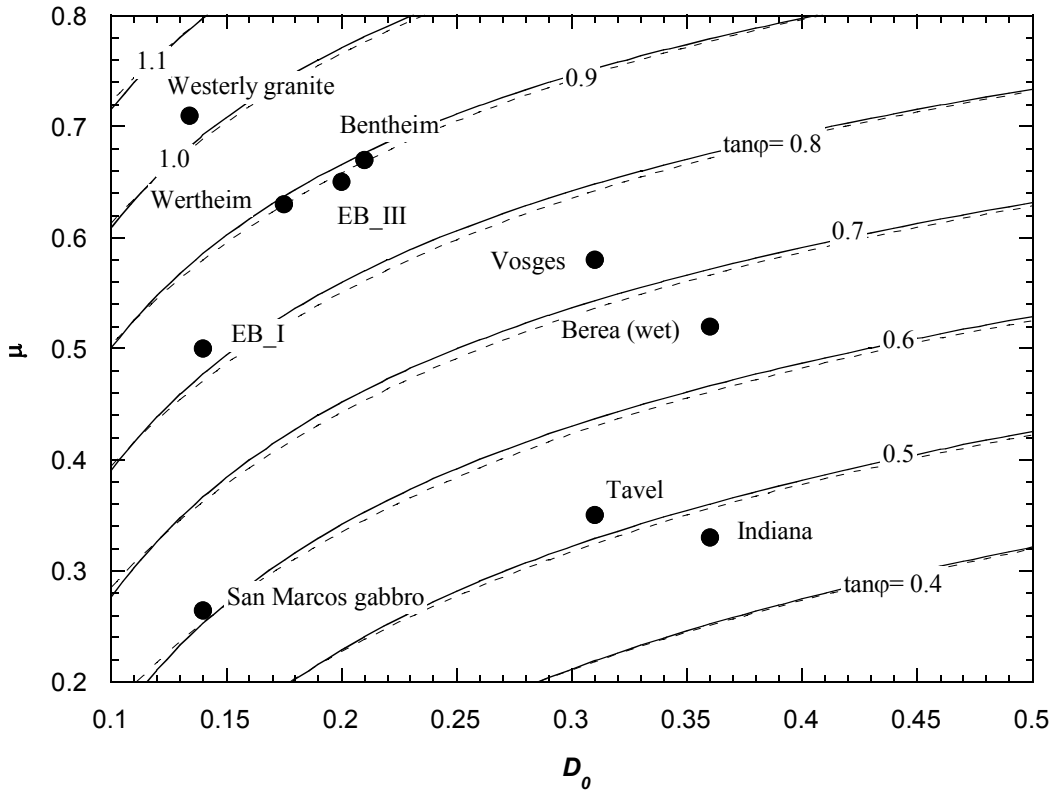

Figure 3.7. The solid lines represent contours of equal coefficient of internal friction (μ_i = tan φ) in the space of friction coefficient μ and initial damage D_0 according to the sliding wing crack model. Experimental data and inferred values of these three parameters for ten rocks (compiled in Table 3.1) are plotted. For comparison, the analytic approximation according to (10) is plotted as dashed contour lines.

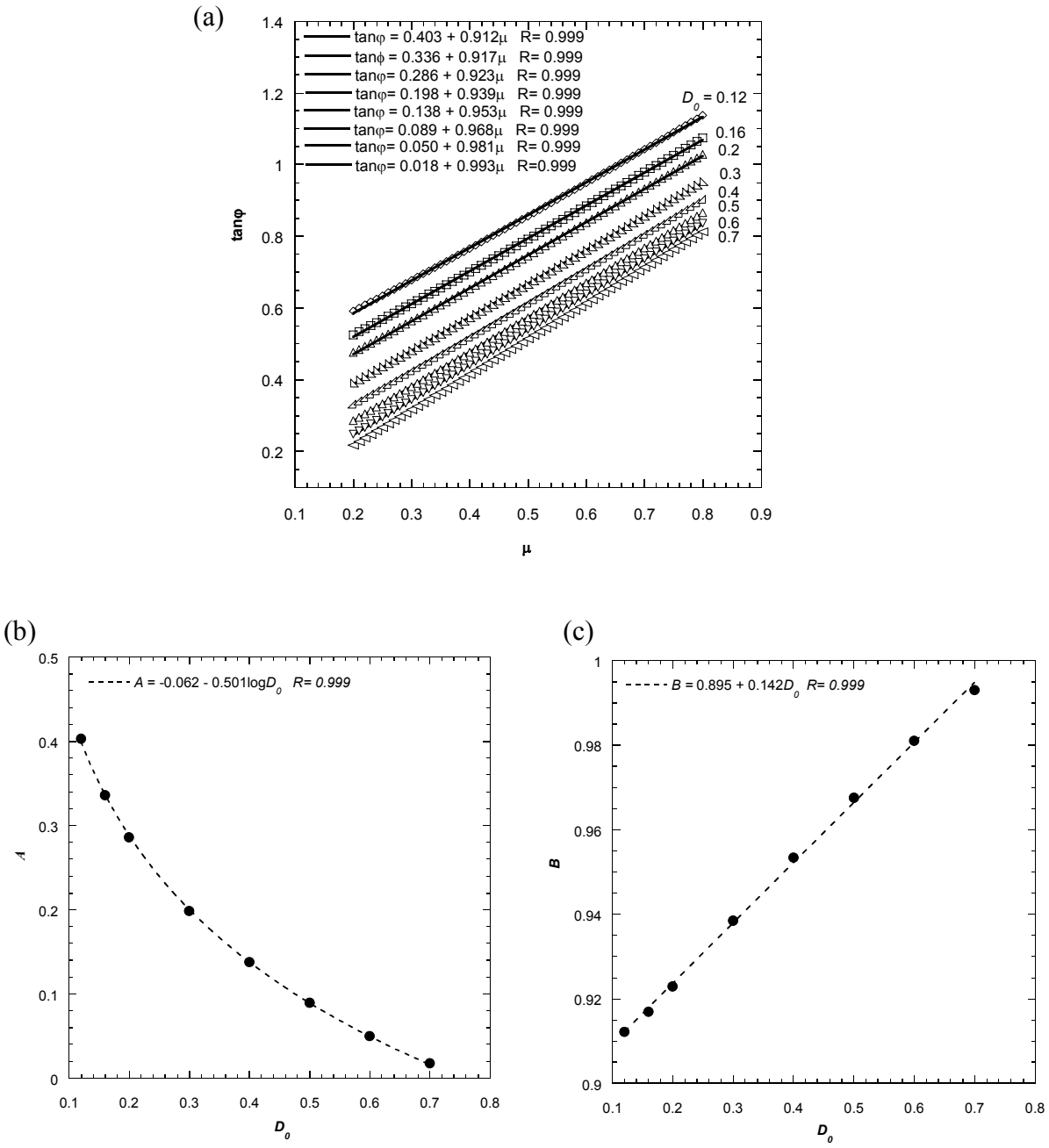

Figure 3.8. (a) The open symbols represent theoretical predictions of the sliding wing crack model for the internal friction coefficient ($\mu_i = \tan \varphi$) as a function of friction coefficient μ of the sliding crack for fixed values of initial damage D_0 as indicated. The calculated values fall on linear trends (with a correlation coefficient of 0.999), with slopes ranging from 0.91 to 0.99. The linear relations obtained by regression are listed. (b) The intercept A and (c) slope B determined from calculations similar to those in (a) are plotted as functions of initial damage D_0. The solid symbols correspond to predictions of the sliding wing crack model for the intercept and slope, which can be fitted empirically by the dashed curves with a correlation coefficient of 0.999, corresponding to a logarithmic and linear relation, respectively.

Chapter 4

Micromechanics of brittle faulting and cataclastic flow in Alban Hills tuff

Abstract

An understanding of how tuff deforms and fails is of importance in the mechanics of volcanic eruption, as well as geotechnical and seismic applications related to the integrity of tuff structures and repositories. Previous rock mechanics studies have focused on the brittle strength. We conducted mechanical tests on nominally dry and water-saturated tuff samples retrieved from the Colli Albani drilling project, in conjunction with systematic microstructural observations on the deformed samples so as to elucidate the micromechanics of brittle failure and inelastic compaction. The phenomenological behavior was observed to be qualitatively similar to that in a porous sedimentary rock. Synthesizing published data, we observe a systematic trend for both uniaxial compressive strength and pore collapse pressure of nonwelded tuff to decrease with increasing

porosity. To interpret the compaction behavior in tuff, we extended the cataclastic pore collapse model originally formulated for a porous carbonate rock to a dual porosity medium made up of macropores and micropores or microcracks.

1. Introduction

Tuffs are consolidated pyroclastic or volcaniclastic rocks. Since they are the products of explosive volcanic eruptions, tuff deposits may disperse widely and blanket vast areas (~10^2-10^3 km^2) in a considerable thickness (~100 m). There are 41 large industrial cities in 24 nations (including two megacities) that are underlain or partly underlain by tuffs [*Heiken*, 2006]. Since the ejected pyroclasts and volcaniclastic could subsequently be welded and cemented to different degrees, they form consolidated rocks that span a broad spectrum of porosity and mechanical strength. At one extreme, the well-consolidated tuffs are sufficiently strong that they have been used for the construction of buildings and structures for thousands of years [*Funiciello et al*., 2006].

A proposed repository for high-level nuclear waste in the USA is located in a tuff formation in Yucca Mountain, Nevada [*Long and Ewing,* 2004]. A challenging seismological question for this repository is estimation of the physical limit on extremely large ground motion associated with earthquake hazards [*Andrews et al.*, 2007]. *Andrews* [2007] recently suggested that since this estimate is sensitively dependent on how the porous tuff yields in compaction, pertinent mechanical data are required to constrain realistically the modeling of ground motion [*Lockner and Morrow*, 2008]. Hence it is important to have a fundamental understanding of the mechanical and hydraulic

properties of tuffs, which can provide useful insights and constraints on the physics of volcanic eruption, as well as geotechnical and seismic applications related to the integrity of tuff structures and repositories.

Previous rock mechanics studies of tuff have focused on the brittle strength, and most are site specific. A common observation is that tuff strength can be highly variable at a given site. In her comprehensive study of ignimbrite (a pyroclastic deposit or "ash flow tuff") in New Zealand, *Moon* [1993] observed very rapid vertical variations in uniaxial compressive strength, by as much as two orders of magnitude in core samples retrieved within one vertical section. While there is an overall trend for the strength to decrease with increasing porosity, other microstructural attributes (including the nature of welding, microcrack density, as well as the presence of lithophysae, pumice and clay minerals) seem to also exert important influence [*Price and Bauer*, 1985; *Moon*, 1993; *Schultz and Li*, 1995; *Evans and Bradbury*, 2004; *Avar and Hudyma*, 2007].

Possibly because of its material complexity and mechanical variability, there is a paucity of microstructural observations on the damage development associated with brittle failure in tuff. In the absence of such observations, it is very difficult to place any constraints on the micromechanics of brittle failure in tuff and to assess whether some of the existing damage mechanics models (primarily developed for application to compact crystalline rocks or porous sedimentary rocks) are applicable to tuff. A first objective of this study is therefore to conduct mechanical tests on tuff samples retrieved from the Colli Albani (Rome, Italy) drilling project [*Mariucci et al*., 2008], in conjunction with systematic microstructural observations on the deformed samples so as to elucidate the micromechanics of brittle failure. We deformed samples from two blocks of tuff, with

average porosity of 32% and 35%, respectively. Both nominally dry and water-saturated samples were studied.

Partly because of its relative high porosity, tuff undergoes a transition in failure mode from brittle fracture to cataclastic flow with increasing confinement at room temperature. In this study we conducted conventional triaxial compression experiments over a sufficiently broad range of pressure so that this phenomenon of low-temperature brittle-ductile transition can be observed. The macroscopic mechanical behavior (involving shear-enhanced compaction and strain hardening) was observed to be qualitatively similar to that in a porous sedimentary rock such as sandstone [*Wong et al*., 1997] or limestone [*Vajdova et al*., 2004].

Notwithstanding the similarities in their phenomenological behaviors, the micromechanics of compaction in clastic and carbonate rocks have recently been demonstrated to be quite different. In a clastic rock such as sandstone, inelastic compaction in a laboratory sample derives primarily from grain crushing initiated by the stress concentrations at grain contacts, that induce intragranular cracks to radiate in a conical pattern towards the interior of the impinging grains [*Menéndez et al*., 1996]. In contrast, microstructural observations have shown that inelastic compaction in limestone is associated with pore collapse, that seems to initiate from stress concentrations at the surface of an equant pore, which induce a ring of localized damage in its periphery [*Zhu et al*., 2010a]. Whether these two fundamentally different micromechanical processes are at all relevant to tuff compaction is a question that can be addressed only if systematic microstructural observations have been conducted on the deformed samples. Accordingly a second objective of this study is to investigate the phenomenology and micromechanics

of inelastic compaction and cataclastic flow in the Alban Hills tuff. Synthesizing our data with other published mechanical data, we assess to what extent the micromechanical processes associated with brittle fracture and compactive cataclastic flow in tuff can be analyzed with some of the existing damage mechanics models.

2. Experimental Procedure

2.1. Alban Hills Volcanic Complex

The geologic foundation of Rome is mostly composed of tuffs from the Colli Albani (Alban Hills) volcanic field in the southeastern part of the present city, and to a less extent, from the Sabatini field in the northwest. Alban Hills is part of a chain of mainly explosive volcanic districts and small eruptive centers that developed along the Tyrrhenian margin of central Italy over a distance of ~200 km since the Middle Pleistocene. Extensional faults associated with the Apenninic orogeny and subsequent opening of the Tyrrhenian Sea follow a regional trend along the NW-SE direction, which is intersected by a local N-S, right-lateral fault system developed behind the Olevano-Antrodoco thrust front [*de Rita and Giampaolo*, 2006; *Vinciguerra et al*., 2009]. Recent seismic swarms and hydrothermal activity at the Alban Hills volcanic complex have triggered the interest to gain a deeper understanding of the volcanic and seismic hazards it may pose to Rome and its vicinity. A scientific drilling project involving a 350 m borehole was accordingly undertaken to elucidate the inner structure of this volcanic field [*Mariucci et al*., 2008].

The volcanic history of Alban Hills may be roughly divided into three main phases, that were separated by two periods of dormancy with durations on the order of 10^3 years. The early Tuscolano-Artemisio Phase (~561-366 ka) with five large pyroclastic eruptions

was the most explosive and voluminous (with cumulative volume on the order of 10 km^3). The second Faete Phase (~308-250 ka) was less energetic, and the Late Hydromagmatic Phase (~200-36 ka) was dominated by pyroclastic surges. The main lithology penetrated by the Colli Albani drilling project was the tuff deposited during the Tuscolano-Artemision Phase, which exhibited a wide variability in grain-size and cohesion [*Mariucci et al*., 2008]. Since the nonwelded tuff was primarily deposited by pyroclastic flow, it can also be categorized as an ignimbrite.

2.2. Sample Material and Preparation

Figure 4.1 (after *Vincigerra et al*., 2009) illustrates schematically the stratigraphy of volcanic units encountered by the Colli Albani borehole. One of our ignimbrite blocks was retrieved from ~137m in the Tufo Pisolitico di Trigoria unit. During the Archaic period Tufo Pisolitico was the primary building stone for the infrastructure of Rome [*de Rita and Giampaolo*, 2006]. Our block is from an interval 12.4 m thick that was described by *Mariucci et al*. [2008] as "light gray, indurate, matrix-supported, coarse-ash deposit with leucite, mm-to-cm-sized gray scoria clasts and sedimentary lithics, accretionary lapilli, enriched in carbonate lithics in the base".

Our second block was retrieved from a depth of ~107 m in the Tufo del Palatino unit, within an interval 22.2 m thick that was described by *Mariucci et al*. [2008] as "dark gray, massive, indurate, matrix-supported, coarse-ash, with leucite and clinopyroxene, abundant mm-to-cm-sized gray and yellow scoria clasts, lava and sedimentary lithics". While the compositions of the two blocks are quite similar, there is an overall trend for the Tufo Pisolitico block to be more porous than the Tufo del Palatino block. In this paper, samples from these two blocks will be denoted by PI and PA, respectively.

Hydrostatic and triaxial compression experiments were performed on nominally dry and water-saturated samples. The PA samples were all deformed in the Stony Brook laboratory, as were two PI samples that were hydrostatically compacted. Nonhydrostatic deformation experiments on the PI tuff were performed in the Institut de Physique du Globe de Strasbourg. A total of 11 PA and 7 PI tuff samples were deformed, and petrographic thin sections of 9 of these deformed samples were prepared for microstructural observations. Before a deformation experiment in wet conditions, the connected porosity of a sample was measured by water saturation (Table 4.1*).* Additional porosity measurements were performed on one sample of each block using a gas pycnometer (Accupyc 1330). The connected porosity was in both cases about 0.5% higher than the previous measurements performed by water saturation. The non connected porosity was estimated to be in both cases less than 0.2%

The Stony Brook and Strasbourg laboratories followed similar sample preparation and experimental protocol. However, dimensions of the cylindrical specimens were different: in Stony Brook the specimens had initial diameter of 18.4 mm and length of 38.2 mm, whereas those in Strasbourg had diameter of 20 mm and length 40mm length. For a wet experiment the sample was first dried in vacuum at 80°C for 48 hours, then saturated with deionized water. Each sample was jacketed with a thin copper foil of thickness 0.05 mm and placed between two steel end-plugs, one of which has a piezoelectric transducer (PZT-7, 5.0-mm diameter, 1-MHz longitudinal resonant frequency) on its flat surface, and the other one has a concentric hole for fluid access to the pore pressure system. Heat-shrink polyolefine tubing was used to separate the sample from confining pressure medium (kerosene). For a nominally dry test the sample was dried in vacuum at 80°C for

several days. Electric resistance strain gages (TML type PFL-10-11) were attached to the copper jacket to measure the axial and transverse strains. The strain gages were easily broken due to pore collapse near the sample surface. To circumvent the problem, we followed the procedure of *Vajdova et al*. [2004]: after the sample had been pressurized to 5 MPa, the larger surface pores were filled with a high-viscosity epoxy. The sample was then jacketed with copper foil, and a small hydrostatic pressure was applied to "season" the copper jacket before two strain gages were glued to its surface in orthogonal directions.

2.3. Mechanical Deformation

The jacketed samples were deformed in the conventional triaxial configuration at room temperature. The triaxial experiments were conducted at confining pressures ranging from 5 MPa to 45 MPa for nominally dry samples and from 5 MPa to 30 MPa for saturated samples. One dry sample of each block was also deformed without any confinement. The confining pressure was monitored by a strain gage pressure transducer to accuracy of 0.1 MPa, and during triaxial loading it was held constant to within 1%. The axial load was measured with an external load cell with an accuracy of 1 kN. The axial displacement was servo-controlled at a fixed rate (corresponding to a nominal strain rate of 1.2×10^{-5} s^{-1}).

Experiments on the saturated samples were conducted at a fixed pore pressure of 10 MPa, and the strain rate was sufficiently slow for the deformation to be under fully drained conditions. Adjustment of a pressure generator kept the pore pressure constant, and the pore volume change was recorded by monitoring the piston displacement of the pressure generator with a displacement transducer (DCDT). The porosity change was

calculated from the ratio of the pore volume change to the initial bulk volume of the sample. The displacement was measured outside the pressure vessel with a DCDT mounted between the moving piston and the fixed upper platen. For dry experiments, the volumetric strain was calculated using the relation $\varepsilon_V = \varepsilon_{\parallel} + 2\varepsilon_{\perp}$, where $\varepsilon_{\parallel}$ and $\varepsilon_{\perp}$ are the strains measured in the axial and transverse directions, respectively.

The load, displacement, and strain gage signals were acquired by a 16-bit A/D converter at a sampling rate of 1 s^{-1} with resolutions of 0.3 MPa, 1 μm and 10^{-5}, respectively. Uncertainty in strain was estimated to be 2 x 10^{-4} (when calculated from the DCDT signal) and 10^{-5} (when measured directly by the strain gages). Acoustic emission activity can be monitored by the piezoelectric transducer attached to the sample. However, since the activity in our tuff samples was not significant, we did not use the any of the acoustic emission data in this study.

2.4. Microstructural Analysis

Microstructure of the two intact and seven deformed samples was studied under optical microscope and scanning electron microscopes (SEM) on thin-sections. Optical microscopy was performed using a Nikon optical polarizing microscope. For SEM observations, the gold-coated thin-sections were studied at Stony Brook using a LEO 1550 microscope with a voltage up to 10 KV. Additional observations on the undeformed samples were performed at INGV Rome using a thermal field emission SEM (FESEM), with an accelerating voltage of 10kV and an electric current of 12 ηA. FESEM images have been collected using the back-scattered electron (BSE) mode at magnification 50 to 5000. All SEM micrographs presented here were acquired in the backscattered electron mode.

To characterize the pore size statistics of an undeformed tuff sample, the thin section of T0_PA (from the Tufo del Palatino block) was scanned using an Epson Perfection™ V700 photo scanner at a resolution of 3200 dpi. Our experience has been that the scanner can resolve the macroporosity as effectively as an optical microscope, with the advantage that it can cover the whole area of the thin section, thus circumventing the need to assemble a mosaic of numerous optical micrographs [*Zhu et al*., 2010a]. The macropores were identified using a brightness (grey-scale) thresholding approach [*Russ*, 1990], and the binarized image was then analyzed using the ImageJ, a public domain image processing program developed at the National Institute of Health. The area of each individual pore was determined, and the equivalent diameter of a circle with the same area was evaluated.

3. Mechanical Data

Table 4.1 summarizes the deformation history of all tuff samples in this study. The convention is adopted that compressive stresses and compactive strains (i.e. shortening and porosity decrease) are positive. The maximum and minimum principal stresses will be denoted by σ_1 and σ_3, respectively. The dry and wet experiments are denoted by the letters "Td" and "Tw", respectively. Hence, Td2_PI corresponds to number 2 of a series of four triaxial compression experiments on nominally dry samples of the Tufo Pisolitico block. The letter "u" and "h' indicate uniaxial compression and hydrostatic tests, respectively. Hence, Twh1_PA corresponds to the first of two hydrostatic compression tests on saturated samples of the Tufo del Palatino block.

The brittle-ductile transition in a porous ignimbrite is illustrated by the mechanical data for dry Tufo Pisolitico samples at confining pressure ranging from room pressure to 45 MPa (Figure 4.2a). In uniaxial compression, the sample Tdu_PI attained a peak stress and then failed by strain softening. At a confining pressure of 5 MPa, the sample Td1_PI attained a peak stress significantly higher than the uniaxial compressive strength, after which it strain softened and the stress dropped stably to attain a residual level. This sample failed by development of a shear bands oriented at ~30^{o} to σ_1. At confining pressure of 10 MPa, the sample Td2_PI attained a peak stress and quickly decayed to a plateau. At more elevated pressures, the samples Td3_PI and Td4_PI both showed strain hardening, with differential stress increasing monotonically with increasing strain. Strain localization was not observed in these samples that failed by cataclastic flow.

The mechanical data and failure modes for dry samples from the Tufo de Palatino block are qualitatively similar (Figure 4.2b), but probably due to the lower porosities, the stresses involved were higher than those for corresponding experiments on Tufo Pisolitico (Figure 4.2a).

Mechanical data for saturated samples of Tufo de Palatino (Figure 4.2c) indicated significant weakening of the porous tuffs in the presence of water. At an effective pressure (confining pressure minus pore pressure) of 5 MPa, the peak stress (near the plateau) was about half of that for a dry sample that failed by brittle faulting. Strain localization was not obvious in the failed sample Tw1_PA, implying that the brittle-ductile transition in a wet sample would occur at a lower effective pressure. The significant water-weakening effect we observed in the Alban Hills tuffs is comparable to that reported in previous studies on tuffs from Yucca Mountain [*Martin et al.*, 1994; 1995]

To illustrate the development of inelastic volume change, we show in Figure 4.3 data for the development of mean stress $(\sigma_1 + 2\sigma_3)/3$ and effective mean stress (mean stress minus pore pressure) with volumetric strain for the Tufo del Palatino samples. The triaxial and hydrostatic compression data are shown as solid and dashed curves, respectively. An inflection point (marked by *P** in Figures 4.3a and 4.3b) can be identified in each of the hydrostats, which is interpreted to be associated with the onset of pore collapse analogous to hydrostatic compression behavior in porous sandstones [*Zhang et al*., 1990] and carbonate rocks [*Vajdova et al*., 2004]. In the cataclastic flow regime, the triaxial compression curve for a given effective pressure basically coincided with the hydrostat up to a critical stress state *C** (as indicated in Figures 4.3a and 4.3b for the experiment at 30 MPa effective pressure), beyond which there was an accelerated increase in porosity reduction in comparison to the hydrostat. This implies that the deviatoric stress field provided significant inelastic contribution to the compactive strain, a phenomenon called "shear-enhanced compaction" that initiated at yield stress level *C** [*Wong et al*., 1997]. Our data for Tufo de Palatino show lower values for the critical pressure *P** for onset of pore collapse and critical stress *C** for onset of shear-enhanced compaction in the presence of water.

4. Microstructural Observations

Observed under the optical microscope, our undeformed Alban Hills tuffs include a small number of lithic clasts and pumices (up to cm in scale) embedded in a fine-grained glassy matrix. Figure 4.4a shows one such pumice containing numerous relatively large pores. Figure 4.4b shows the interior of a lapilli with lower degree of vesculation, which

should probably be classified as a scoria. Figure 4.4c shows a shard with relatively straight edges and sharp corners, characteristic of an ignimbrite that is nonwelded. Figure 4.4d shows another scoria clast, containing numerous pores with dimensions up to 100 μm.

4.1. Macropores, Micropores and Microcracks

It should be emphasized that equant pores of many different scales were observed in the Alban Hills tuff samples. In parallel, a complex network of fine microcracks may also exist. Figure 4.4e shows an area in the matrix with large pores (~100 μm) and many smaller ones (~10 μm), and Figure 4.4f shows another area with pores mostly in the 10 μm range. However, when we zoomed into the sub-area inside the white dashed rectangle, we were able to resolve numerous μm-sized pores. Furthermore we also observed a complicated complex of elongated microcracks with different degrees of connectivity. While some appear to have been healed, many of the microcracks seem open with a finite aperture.

To characterize the partitioning of porosity among these features, we followed the approach of *Zhu et al*. [2010a] to evaluate the macroporosity (defined to be that part of the total porosity associated with equant pores with equivalent diameter >33 μm) by analyzing a scanned image of the thin section T0_PA. In Figure 4.5a we show a binarized image scanned at 3200 dpi of an area of this sample. Porosity is shown as dark areas (with very low brightness level). There are isolated area with irregular shape that could be grains plucked out during the preparation of thin section. Using the ImageJ software, the area of each individual pore was determined, and the equivalent diameter of a circle with the same area was evaluated. At 3200 dpi, the pixel size of the scanned image is less

than 10 μm. Since the resolution of such observations on a petrographic thin section is conventionally taken to be limited by its thickness (~33 μm), we only included those pores with equivalent diameter >33 μm in the histogram shown in Figure 4.5b. The size distribution of macropores ranges over one order of magnitude, with a maximum diameter of 794 μm. The areal macroporosity evaluated from our binarized image is 11.7% for our Alban Hills tuff, which is about 1/3 the total porosity of 32% (Table 4.1). This represents an upper bound, since it may include areas associated with plucked grains.

We define "microporosity" to be the difference between total porosity and macroporosity. Figure 4.5c summarizes the partitioning between macroporosity and microporosity in our tuff sample, and for comparison values for two limestones determined by *Zhu et al*. [2010a] using an identical approach. Our data show that the porosity partitioning in Alban Hills tuff is very similar to that in a limestone, in which the microporosity represents a very significant fraction of the total porosity. The ratio between microporosity and total porosity has relatively high values of 0.63, 0.62 and 0.68 for Tufo del Palatino, Majella limestone and Indiana limestone, respectively.

In spite of this similarity, there is a qualitative difference in the microporosity in tuff and limestone, in that the former includes a very significant number of microcracks (Figure 4.4f). However, since microcrack porosity depends not only on the number but also the aperture, a dense population of microcracks typically contributes very little towards the porosity. Accordingly the microporosity inferred from our measurements is expected to derive mostly from equant micropores (Figures 4.4e and 4.4f).

4.2. Brittle Faulting

The uniaxially compressed samples Tdu_PA and Tdu_PI both failed by the development of a through-going shear band at ~30^o with respect to σ_1. In the failed sample Tdu_PA, we observed a shear zone ~ 0.1 mm wide. Stress-induced microcracks sub-parallel to σ_1 were observed to have emanated from relatively large pores embedded in the matrix (Figure 4.6a). In contrast, such wing cracks were not observed in relation to macropores in a pumice (Figure 4.6b).

The sample Td1_PA failed in the brittle faulting regime (Figure 4.2b). Intense microcracking had developed in the vicinity of the shear bands that had developed in the failed sample (Figure 4.6c). Numerous stress-induced cracks subparallel to σ_1 had coalesced. Figure 4.6d shows a macropore embedded in the matrix, with numerous microcracks aligned subparallel to σ_1 that had emanated from the macropore and coalesced with each other. Figure 4.6e shows the path along which shear localization had developed, which seems to have bypassed the lithic clasts by traversing along their boundaries. A similar observation was reported by *Evans and Bradbury* [2004], who found in naturally deformed samples of the Bishop tuff that the fracture paths seem to lie preferentially along the boundaries of phenocrysts, lapilli and lithic clasts.

4.3. Inelastic Compaction

Damage in the inelastically compacted samples is primarily associated with pore collapse. The sample Twh1_PA was hydrostatically compressed to an additional 70 MPa beyond the critical pressure *P** (Figure 4.3a). Macropores at various stages of collapse were observed in this sample. It should be noted that for such a relatively weak pyroclastic rock, it is unavoidable that some grains would be plucked out when one

prepares a thin-section. Hence, care should be taken not to interpret by mistake such a plucked grain as a collapsed pore, which should retain fragments either attached to the pore periphery or spalled into the pore interior.

We show in Figure 4.7a the collapse of a macropore in matrix with a diameter of ~300 μm. Intensive cataclastic damage was observed near the surface with numerous microcracks surrounding the macropore. Pore-emanated cracks have extended a distance around 100 μm. The area beyond the damage zone seems to be relatively undeformed. Figure 4.7b shows a collapsed pore in the matrix with a diameter around 60μm. The micropore observed is about 5 times smaller than the macropore. Stress-induced microcracks coalesced around the pore surface. The intensive damage zone has propagated radially by ~50 μm.

The sample Tw4_PA was triaxially compressed to beyond the compactive yield stress C^* at a confining pressure of 30 MPa (Figure 4.3a). The development of shear-enhanced compaction was manifested by pervasive collapse of macropores. We show in Figure 4.7c a collapsed macropore within the matrix with a diameter of ~250 μm. Intensive damage was observed around the pore surface. Stress-induced microcracks had extended and coalesced with each other, which led to a thin layer of crushed grains in the periphery of the macropore. The damage zone has extended radially by ~60 μm and the area beyond remained intact. Besides macropores, collapse of some of the larger micropores was also observed in the triaxially compacted sample. Figure 4.7d shows a micropore with a diameter of ~90 μm. Microcracks had emanated from the micropore and coalesced around the pore circumference. In Figure 4.7e we show the cataclastic damage of pore

collapse in sample Tw4_PA. Crushed grains had spalled and fallen into the interior of the macropore while the matrix seems relatively undeformed.

5. Discussion

The development of dilatancy and micromechanics of brittle faulting in compact crystalline rocks and porous siliciclastic rocks have been extensively investigated [*Paterson and Wong*, 2005]. Our observations here have shown that the brittle faulting process in a porous tuff is similar in many respects. Shear localization does not develop until the post-failure stage after the peak stress has been attained. The post-peak deformation is stabilized by increasing pressure. The tuff contains numerous preexisting microcracks which can readily nucleate stress-induced damage. Very high densities of microcracking are observed within the shear zones.

However, there seem to be at least two important differences. First, the pore space in our Alban Hills tuff has numerous pores which, according to our microstructural observations, assume a significant role in the nucleation of stress-induced microcracks. In this respect, it is somewhat similar to recent observations in porous limestones [*Zhu et al*., 2010a; *Vajdova et al*., 2010], in which a key mechanism for brittle faulting is pore-emanated cracking. Second, the water-weakening we observed here for Alban Hills tuffs (Table 4.1) and *Martin et al.* [1994; 1995] reported for Yucca Mountain tuffs is significantly stronger than that observed in a siliciclastic rock or compact crystalline rock [*Baud et al*., 2000; *Paterson and Wong*, 2005].

As for inelastic compaction and cataclastic flow, our observations indicate that the phenomenology in a porous tuff is qualitatively similar to that in a siliciclastic [*Wong et*

al., 1997] or carbonate [*Vajdova et al*., 2004] rock. Notwithstanding these similarities, our observations also underscore that the micromechanics in tuff is very different from that in a clastic rock such as sandstone, which involves primarily grain crushing initiated by the stress concentrations at grain contacts [*Menéndez et al*., 1996]. In some respects, the behavior in tuff is qualitatively similar to that documented recently in porous limestones [*Zhu et al*., 2010a; *Vajdova et al*., 2010], which typically involves pore collapse that initiates from stress concentrations at the periphery of the larger pores. Similar partitioning between macroporosity and microporosity was also observed (Figure 4.5c). Given these apparent similarities, a first question we would like to address is whether and to what extent some of the micromechanical models applicable to porous limestone can be extended to porous tuff. This requires a synthesis of our mechanical data with other published data.

5.1. Uniaxial Compressive Strength of Nonwelded and Welded Tuffs

5.1.1. Welded Tuff

Previous rock mechanics studies of tuff have mostly focused on the uniaxial compressive strength (UCS) as a geotechnical property. In particular, tuff samples from both outcrops and boreholes in Yucca Mountain, Nevada have been investigated extensively [*Nimick et al*., 1985; *Martin et al*., 1995; *Schultz and Li*, 1995; *Lockner and Morrow*, 2008; *Avar and Hudyma*, 2006]. The two primary units at the proposed repository site are Paintbrush and Calico Hills. The former unit has a wide range of welding characteristics (from nonwelded to densely welded), and the comprehensive investigations of *Martin et al*. [1994, 1995] concluded that no apparent correlations between porosity and the UCS were observed on welded Paintbrush tuff. A similar

conclusion was reached by *Mogi* [1964] who investigated three welded tuffs from Japan, and by *Moon* [1993] who investigated a large variety of ignimbrites from New Zealand. This prompted us to analyze the UCS data of welded and nonwelded tuffs separately.

The compiled UCS data on welded tuff are plotted as a function of total porosity in Figure 4.8a. At a given porosity, the UCS has been observed to vary by as much as one order of magnitude. To explain the very large scatter, it has been suggested that other microstructural attributes (including the nature of welding, microcrack density, as well as the presence of lithophysae, pumice and clay minerals) all exert important influence on the strength of a welded tuff, [*Price and Bauer*, 1985; *Moon*, 1993; *Avar and Hudyma*, 2007].

5.1.2. Nonwelded Tuff

For comparison we compiled in Figure 4.8b the UCS data for nonwelded tuffs with porosities ranging from 0.3% to 57.1%. Our Tufo Pisolitico and Tufo del Palatino samples are considered to be nonwelded. In Yucca Mountain, the tuff from the Calico Hills unit is also classified as non-welded ignimbrites [*Martin et al*., 1995; *Schultz and Li*, 1995; *Lockner and Morrow*, 2008]. We included the data of *Aversa and Evangelista* [1998] for the Neapolitan fine-grained tuff, a highly porous ignimbrite deposited in the Phlegrean field in Naples. In addition, a large data set on UCS of relatively compact tuffs (non-welded volcanic breccia with porosities <10%) from Hong Kong have been published [*HK Geotechnical Office*, 1990; *Dobson and Nakagawa*, 2005].

The data of the nonwelded tuffs indicate a more systematic correlation between the UCS and total porosity. In light of this apparent correlation and our microstructural observations, we will first attempt to interpret this trend using the pore-emanated

cracking model of *Sammis and Ashby* [1986]. The 2-dimensional damage mechanics model considers an elastic medium permeated by circular holes of uniform radius *r*. As the applied stress increases, a point is reached when the stress intensity factor of a small crack on the circular surface attains the critical value K_{IC}, at which point wing cracks would propagate to a certain distance parallel to the σ_1 direction. As the wing cracks propagate to longer distances with increasing stress, they interact with one another to induce an additional tensile stress intensity, ultimately leading to an instability with coalescence of the pore-emanated cracks.

For uniaxial compression, *Zhu et al*. [2010a] have recently obtained an analytic estimate of the UCS according to this pore-emanated cracking model for brittle failure:

$$\sigma_u = \frac{1.325}{\Phi^{0.414}} \frac{K_{IC}}{\sqrt{\pi r}} \tag{1}$$

where Φ denotes the total porosity. The UCS data for nonwelded tuff are compared with this analytic approximation in Figure 4.8b. Except for some extremely weak tuffs at the high porosity end, most of the data can be bracketed by the two theoretical curves corresponding to $K_{IC}/\sqrt{\pi r}$ = 5 and 35 MPa. If the pore-emanated cracking initiates intragranularly within a lithic clast, an estimate of K_{IC} can be made based on experimental measurements on common silicate minerals. For feldspars, the measured values are ~0.3 MPa $m^{1/2}$ and can be higher (but not by order of magnitude) in other silicate minerals such as quartz and olivine. In a glass experimental measurements are also higher. However, if the wing crack grows along a grain boundary (along scoria or lithic clasts), K_{IC} is expected to be lower, possibly by a factor of 2 or so [*Atkinson and Meredith*, 1987].

If we were to assume K_{IC} = 0.3 MPa $m^{1/2}$, then according to equation (1) the laboratory data for UCS of nonwelded tuffs are bracketed by average macropore size ranging from r = 23 μm to 1.15 mm. Specific to our Tufo del Palatino sample (Tdu_PA), the inferred pore diameter is $2r$ = 238 μm, which is comparable to our microstructural observations on the macropore size (Figure 4.4e). This indicates that it is viable for the larger pores in the tuff to provide stress concentration sites for wing cracks to initiate and coalesce, leading to brittle failure as analyzed in the damage mechanics model of *Sammis and Ashby* [1986].

However, it should be noted that the Tufo Pisolitico sample (Tdu_PI) has a UCS which is about half that of Tdu_PA (Table 4.1), which would imply an average pore diameter of ~780 μm using the same K_{IC} value. This inferred diameter is larger than most of what we observed under the microscope. A possible interpretation is that wing crack growth can readily develop in a nonwelded tuff along weak interfaces (such as clast boundaries) under a significantly lower stress intensity factor (with a value of say, 0.1-0.2 MPa $m^{1/2}$).

Another micromechanical model that has been used extensively for brittle faulting is the sliding wing crack model [*Horii and Nemat-Nasser*, 1986; *Ashby and Sammis*, 1990; *Kemeny and Cook*, 1991]. The model considers sources of tensile stress concentration that are located at the tips of preexisting cracks. The applied far-field stresses induce a shear traction on the crack plane (of length $2c$), and if the resolved shear traction exceeds the frictional resistance along the closed crack, frictional slip occurs which also induces tensile stress concentrations at the two tips that may nucleate and propagate wing cracks to propagate parallel to the σ_1 direction. As wing cracks propagate to longer distances,

they interact and ultimately coalesce to result in an instability. The model predicts that the maximum and minimum principal stresses at the onset of dilatancy and peak both fall on linear trends, and therefore if mechanical data on these critical stresses are available, then the model predictions can be tested and relevant micromechanical parameters inferred [*Ashby and Sammis*, 1990; *Baud et al*., 2000; *Vajdova et al*., 2004].

However, there is a paucity of high-quality mechanical data for tuff that can be used this type of analysis. Very limited data on triaxial compression tests have been published, and they are not in a form that one can evaluate the critical stresses for the onset of dilatancy. As for our tuff samples, the brittle faulting regime falls on a very narrow pressure range and typically the amounts of dilatancy were so small that it is difficult to pick out from our data the stress at the onset of dilatancy. To circumvent this difficulty, we here adopt an analytic formulation for the UCS in the sliding wing crack model to assess the applicability of this model to tuff.

Zhu et al. [submitted, 2010b] developed recently an analytic approximation of the UCS for the sliding wing crack model:

$$\sigma_u = \frac{1.346}{\sqrt{1+\mu^2}-\mu}\ \frac{K_{IC}}{\sqrt{\pi c}}\ D_0^{-0.256} \tag{2}$$

where μ denotes the friction coefficient of the sliding crack. In the two-dimensional sliding wing crack model, the nondimensional parameter D_o which characterizes the initial damage (or crack density) is proportional to the number of preexisting cracks per unit area and the crack length squared [*Ashby and Sammis*, 1990].

For a broad range of rock types (including granite, sandstone, limestone, gabbro, gneiss and basalt), values of μ inferred from dilatancy and peak stress data are in the

range of 0.3-0.7, and of D_o in the range of 0.1-0.4. The preexisting microcracks we observed are relatively short with lengths on the order of 10 μm (Figure 4.4f). The longest have lengths of ~40 μm. Again assuming K_{IC} = 0.3 MPa $m^{1/2}$, the UCS can be estimated to be σ_u=87 MPa from (2) using c =20 μm, μ = 0.3 and D_o = 0.4. This estimate is significantly larger than the experimental measurements of 17.4 MPa and 33.4 MPa (Table 4.1). If we were to use a higher value of μ, a lower value of initial damage or a shorter crack length, the inferred UCS will be even higher. This discrepancy can be resolved only if K_{IC} has an unrealistically low value of ~0.1 MPa $m^{1/2}$, or if the preexisting sliding cracks have lengths up to 410 μm which are significantly longer than what we observed.

The implication is that between the two types of damage mechanics model, the pore-emanated cracking model is more viable than the sliding wing crack model as far as brittle failure in a nonwelded tuff is concerned. Although the sliding wing crack mechanism by itself seems unlikely to control the brittle fracture development in Alban Hills tuff, we cannot rule out that is contributes to a certain extent as a mechanism coupled to pore-emanated cracking. While our analysis illustrates how certain constraints on the micromechanics of brittle failure in a porous tuff can be obtained from microstructural and mechanical data, it also underscores the limitation when one has data on samples from only one site, especially for a material with pore space as complicated as that of tuff. Clearly more systematic studies of this nature are warranted in the future to elucidate further the brittle failure mechanics of tuff.

5.2. Inelastic Compaction and Cataclastic Pore Collapse

Our observations on inelastic compaction in Alban Hills tuff (Figure 4.7) indicate that it involves a pore collapse mechanism analogous to that in a porous limestone in two aspects. First, pore collapse tends to first initiate at the larger pores. Second, cataclasis and microcracking seem to be the dominant deformation mechanisms in the proximity of a pore that has collapsed. Relatively intense cracking would develop with a concentric halo surrounding the pore, and comminuted fragments may spall and fall into the void.

Zhu et al. [2010a] referred to this micromechanical process as "cataclastic pore collapse" and developed a model for its initiation. An externally applied stress field induces local stress concentration at the surface of a pore, and yielding initiates when the local stresses satisfy a specified failure criterion. Both the Mohr-Coulomb and Drucker-Prager yield criteria were considered. Similar to previous models of pore collapse [*Bhatt et al*., 1975; *Gurson* , 1977; *Curran and Carroll*, 1979], the pores are idealized as spherical in shape.

5.2.1. Hydrostatic Compaction

The mechanics of compaction is analyzed with reference to a representative element volume made up of a macropore embedded in an effective (porous) medium. If we first consider hydrostatic loading, the principal stresses $S_1 = S_2 = S_3 = P_c$ acts remotely on the external boundary of the element volume. It can be shown that local stresses in the vicinity of the pore are such that yielding will first occur at the spherical surface (Figure 4.9a). With reference to a cylindrical coordinate system (ρ, θ, z), the local stresses there are given by:

$$\sigma_{\rho\rho} = 0 \tag{3a}$$

$$\sigma_{\theta\theta} = \sigma_{zz} = 3P_c / 2 \tag{3b}$$

This stress state corresponds to an "unconfined compression", with a vanishing minimum principal stress. If one adopts the Mohr-Coulomb failure criterion (which is independent of the intermediate principal stress), the failure stress for the configuration (3) is identical to that for uniaxial compression. Accordingly, initial yielding (which signals the onset of cataclastic pore collapse) will occur when the maximum principal stress equals the UCS σ_u^* of the effective medium:

$$\sigma_{\theta\theta} = \sigma_{\psi\psi} = \sigma_u^* \quad \Rightarrow \quad P_c = P^* = 2\sigma_u^* / 3 \tag{4}$$

A similar analysis can be performed for the Drucker-Prager criterion, which turns out to give an identical result for a remotely applied hydrostatic loading [*Bhatt et al*., 1975; *Curran and Carroll*, 1979; *Zhu et al*., 2010a].

In most previous analyses [*Bhatt et al*., 1975; *Curran and Carroll*, 1979], it is implicitly assumed that the effective medium has a UCS (and other failure parameters) identical to those of the bulk sample, which would requires $\sigma_u^* = \sigma_u$. If indeed this assumption is valid, then (4) would imply that a plot of the pore collapse pressure *P** versus the UCS σ_u of the bulk sample falls on a linear trend with a slope of 2/3. To test this, we compile in Figure 4.9b tuff data of ours and other studies. *Lockner and Morrow* [2008] conducted a comprehensive series of measurements on nonwelded ignimbrites from Calico Hills. David Lockner (personal communication, 2009) has kindly provided us with his unpublished data. *Aversa and Evangelista* [1998] presented data on the Neaplitan fine-grained tuff. The *P** and UCS values of Mt. Helen tuff were picked by us from Figure 4.8 of the report of *Heard et al*. [1973]. Porosities for the nonwelded

ignimbrite samples compiled here range from 21.9 % to 47.3 %. For comparison, we also include limestone data that were compiled by *Zhu et al*. [2010a].

It can be seen that the tuff and limestone data all plot above the dashed line (with slope 2/3), which implies that $P^* = 2\sigma_u^* / 3 > 2\sigma_u / 3$, and therefore $\sigma_u^* > \sigma_u$. In other words, the effective medium is inferred to have a UCS that is much higher than that of the bulk sample. In light of our previous discussion of brittle failure in tuff, this implies that the effective medium is probably less porous than the bulk rock, a scenario that *Zhu et al*. [2010a] postulated for limestone using a dual porosity concept previously suggested in carbonate sedimentology [*Choquette and Pray*, 1970; *Pittman*, 1971; *Anselmetti et al*., 1998; *Baechle et al*., 2008].

The total porosity Φ is assumed to be the sum of macroporosity Φ_M and microporosity Φ_m, made up of large and small pores with average diameters *a* and *a**, respectively. The partitioning of total porosity between Φ_M and Φ_m can be related to the microstructural data in Figure 4.5c. Our observations show that there are also numerous preexisting microcracks, but it is likely that the microcrack porosity contributes little to the total porosity. The effective medium is modeled as a porous medium that contains a population of micropores and microcracks (Figure 4.10a). Since the macropores have been excluded from it, the effective medium has a porosity less than the total porosity and accordingly its UCS σ_u^* is greater that the UCS σ_u of the bulk sample which includes the macropores.

We will first analyze the effect of micropores on the UCS of the effective medium, following the approach of *Zhu et al*. [2010a]. The average micropore size *a** is assumed to relatively small in comparison to average macropore size *a* and linear dimension *b* of

the representative element volume, such that $b >> a >> a^*$. Brittle failure in the effective medium is assumed to be described by *Sammis and Ashby's* [1986] pore-emanated cracking model, and therefore its UCS σ_u^* is given by equation (1) with $r = a^*$ and, on substituting into equation (4), we obtain the following relation between the pore collapse pressure P^* and total porosity:

$$P^* = \frac{2}{3}\sigma_u^* = \frac{0.883}{\Phi_*^{0.414}} \frac{K_{IC}}{\sqrt{\pi a^*}} = \frac{0.883}{\Phi^{0.414}} S^* \tag{5a}$$

with

$$S^* = \frac{K_{IC}}{(\Phi_* / \Phi)^{0.414} \sqrt{\pi a^*}} \tag{5b}$$

where Φ_* denotes the porosity of the effective medium, which is related to the macroporosity and microporosity by $\Phi_* = \Phi_m / (1 - \Phi_M) \approx \Phi_m$. Hence this micromechanical model for cataclastic pore collapse in a dual porosity medium predicts that while there is an overall decrease of the critical pressure with increasing porosity, the compactive yield stress is also dependent on the parameter S^* which characterizes the cooperative effect of micropore size, fracture toughness and partitioning of microporosity and macroporosity.

In Figure 4.10b we plot our compiled P^* data as a function of total porosity. The data fall between two limiting curves accordingly to (5). The two Calico Hills tuff samples with lowest porosities (21.9% and 28.9%) lie on the upper curve corresponding to S^* = 81.0 MPa. Since $\pi a^* = (K_{IC} / S^*)^2 (\Phi / \Phi_*)^{0.828}$, the micropore diameter for this upper limit can be estimated to be $a^* \geq (K_{IC} / S^*)^2 / \pi = 4.4$ μm, assuming as before a K_{IC} value of 0.3 MPa $m^{1/2}$. The P^* data for the two samples with highest porosities

(Neapolitan fine-grained tuff 47% and Calico Hills tuff 51.5%) seem to fall on a plateau given by the lower limit S^*= 16.5 MPa, which implies that $a^* \geq$ 105 μm.

Between the upper and lower limits, the inferred value of S^* decreases rapidly by a factor of ~5 with porosity increasing by a factor of 2.5 (Figure 4.10b). A similar trend in porous carbonate rock with the inferred S^* value decreasing with increasing porosity was reported by *Zhu et al*. [2010a]. They also detected an approximately linear trend in the carbonate data, which is not obvious in our compiled tuff data.

Our P^* values for dry Tufo del Palatino (Tdh1_PA) and Tufo Pisolitico (Tdh1_PI) samples fall on the theoretical curve for an intermediate value of S^*=42 MPa, which implies that $a^* \geq$ 16 μm (assuming K_{IC} = 0.3 MPa m$^{1/2}$ as before), comparable in dimension to many of the micropores we observed in the vicinity of a macropore (Figure 4.7). This comparison indicates that the pore-emanated cracking model provides a viable mechanism for cataclastic pore collapse in tuff when it is treated as a dual porosity medium made up of macropores and micropores.

Microcracks were not considered to be important in the dual porosity model of *Zhu et al*. [2010a], which was formulated with a porous limestone in mind. In the case of Alban Hills tuff, the density of preexisting cracks is high, even though many of them are relatively short. We next analyze the effect of these microcracks on the UCS of the effective medium, using as before the analytic approximation (2) obtained by *Zhu et al*. [submitted, 2010b] for the sliding wing crack model. If the effective medium has a porosity that is dominated by microcracks with average length 2c, then its UCS σ_u^* is given by (2) and on substituting into (4), we obtain

$$P^* = \frac{2}{3}\sigma_u^* = \frac{0.897}{\sqrt{1+\mu^2}-\mu}\ \frac{K_{IC}}{\sqrt{\pi c}}\ D_0^{-0.256} \quad (6)$$

Since P^* values for our two dry tuff samples are 56 MPa and 60 MPa (Table 4.1), equation (4) implies that the UCS of the effective medium are 84 and 90 MPa. If we consider an effective medium made up of some of the longest preexisting microcracks (with $2c$~40 μm), then according to (2) its UCS can be estimated to be σ_u^*=87 MPa (again assuming K_{IC} = 0.3 MPa m$^{1/2}$, μ = 0.3 and D_o = 0.4). That the two estimates of σ_u^* are almost identical suggest that, at least for Alban Hills tuff, sliding wing crack growth and coalescence can also provide a viable mechanism for cataclastic pore collapse in tuff, when it is treated as a dual porosity medium made up of macropores and microcracks. As noted earlier, this represents a limiting case in that if we were to use a higher value of μ or lower value of initial damage, the inferred UCS for the sliding wing crack model will be higher than that inferred from P^*.

Our analysis of two types of mechanisms for cataclastic pore collapse has indicated that either the pore-emanated cracking or sliding wing crack model is consistent with our mechanical data and microstructural observations on Alban Hills tuff. We have assumed that the two mechanisms are decoupled, but in reality they probably operate as coupled processes that result in cataclastic damage leading to pore collapse.

5.2.2. Conventional Triaxial Compression

We compile in Figure 4.11 the peak stresses and critical stress C^* for the onset of shear-enhanced compaction of Alban Hills tuff and Neapolitan fine-grained tuff [*Aversa and Evangelista*, 1998]. There is significant scatter in the latter set of data, possibly because the samples had variable initial porosity. Overall the C^* data are qualitatively

similar in that they map out an elliptical cap in the effective stress *(P)* – differential stress (*Q*) space, that expands with decreasing porosity. The brittle strength data (in open symbols) show a positive correlation between *P* and *Q*, correspond to peak stresses that approximately follow the Mohr-Coulomb criterion.

Under nonhydrostatic loading, the local stress field in the vicinity of a pore is more complicated. Furthermore, predictions of critical yielding stresses are fundamentally different according to whether Mohr-Coulomb or Drucker-Prager criterion is adopted. We consider a remote stress field $S_1 > S_2 = S_3$ applied to the representative volume element (Figure 4.9a), corresponding to a conventional triaxial compression test in the laboratory. With reference to a cylindrical coordinate system (ρ, θ, *z*), the local stress distribution is such that initial yielding will occur first along the equator of the sphere (at *z*=0 and ρ=*a*), where the principal stresses are given by [*Timoshenko and Goodier*, 1951]

$$\sigma_1 = \sigma_{zz} = \frac{3}{2}\left[\frac{(9-5\nu)}{(7-5\nu)}(S_1 - S_3) + S_3\right], \tag{7a}$$

$$\sigma_2 = \sigma_{\theta\theta} = \frac{3}{2}\left[\frac{(5\nu-1)}{(7-5\nu)}(S_1 - S_3) + S_3\right], \tag{7b}$$

$$\sigma_3 = \sigma_{\rho\rho} = 0\,. \tag{7c}$$

Substituting the (local maximum and minimum) principal stresses (7a) and (7c) into the Mohr-Coulomb criterion, *Zhu et al*. [2010a] arrived at the following result for the critical stress state *C** at the onset of shear-enhanced compaction:

$$S_1 - S_3 = \frac{(7-5\nu)}{(9-5\nu)}\left(\frac{2}{3}\sigma_u^* - S_3\right) = \frac{(7-5\nu)}{(9-5\nu)}\left(P^* - S_3\right) \tag{8a}$$

where ν denotes Poisson's ratio of the effective medium. If we define $P = (S_1 + 2S_3)/3$ and $Q = S_1 - S_3$, then the stress state *C** can also be expressed as

$$Q = \frac{3(7-5\nu)}{10(2-\nu)}\left(P^*-P\right) \tag{8b}$$

This predicts that a plot of Q versus P falls on a straight line with a slope that falls on a narrow range of 0.9-1.05 for ν =0-0.5. However, this amazingly simple prediction of a linear yield envelope is in discrepancy with laboratory observations. In recent years, a number of studies have been conducted to investigate the inelastic compaction behavior of porous siliciclastic and carbonate rocks [e.g., *Wong et al*., 1997; *Vajdova et al*., 2004; *Bemer et al*., 2004; *Baud et al*., 2006; *Baud et al*., 2009]. To our knowledge, most of the data for the onset of inelastic compaction fall on yield caps that are approximately elliptical in shape, except for an isolated study on Bleurswiller sandstone [*Fortin et al*., 2006] which shows an apparently linear cap.

Our analysis here implies that the intermediate principal stress (7b) cannot be neglected in analyzing the development of cataclastic pore collapse. We next consider the Drucker-Prager criterion which involves all three principal stresses in (6). *Zhu et al.* [2010a] derived this quadratic relation between the remotely applied mean stress P and differential stress Q at the onset of shear-enhanced compaction:

$$\begin{aligned}&(\alpha-\beta^2\gamma^2)Q^2+[(3\beta-4\beta\gamma^2)P-2\beta\gamma(1-2\gamma)P^*]Q\\&+(1-2\gamma)(P-P^*)[(1+2\gamma)P+(1-2\gamma)P^*] = 0\end{aligned} \tag{9}$$

with $\alpha = 100(7-13\nu+7\nu^2)/[9(7-5\nu)^2]$, $\beta = 10(1+\nu)/[9(7-5\nu)]$ and $\gamma = 2\sin\phi/(3+\sin\phi)$, where ϕ denotes the angle of internal friction.

In Figure 4.12 we replot our Alban Hills tuff data for C^* in Figure 4.11, with the differential stress and mean stress at the onset of shear-enhanced compaction normalized by the critical pressure for pore collapse from hydrostatic compression experiments. For comparison, we also include data for three porous limestones presented by *Zhu et al.*

[2010a]. Yield stress data for the normalized stresses Q/P^* and P/P^* of the four rocks fall on caps very close to one another. A similar behavior was observed for porous sandstones when the yield stresses were normalized by P^* [*Wong et al.*, 1997].

For comparison, we show the theoretical predictions of (9) according to the Drucker-Prager yield criterion (for a Poisson's ratio of 0.2) and three different angles of internal fiction. *Zhu et al.* [2010a] have shown that overall the effect of Poisson's ratio on the cap is relatively small. The nonlinear caps based on Drucker-Prager criterion are in qualitative agreement with laboratory data. The cap is predicted to expand with decreasing friction angle ϕ, and the highest differential stresses are associated with the cap for ϕ=0 (corresponding to the von Mises criterion), which shows the best quantitative agreement with experimental data, albeit at somewhat lower levels. For this limiting case, the differential stress Q as a function of the mean stress P is given by:

$$\frac{Q}{P^*} = \frac{3}{20}\frac{(7-5\nu)}{(7-13\nu+7\nu^2)}\left[\sqrt{4(7-13\nu+7\nu^2)-27\left(\frac{(1-\nu)P}{P^*}\right)^2}-(1+\nu)\left(\frac{P}{P^*}\right)\right]. \qquad (10)$$

with the pore collapse pressure P^* as a function of porosity given by either (5) or (6) for an effective medium dominated by micropores or microcracks, respectively.

Our experimental data for tuff agree better with the theoretical prediction for very low values of ϕ. Just as in the limestone case that is an intriguing result. From what is known about the pressure sensitivity of brittle failure, one would expect the internal friction angle to be in the range of 10^o-45^o [*Zhu et al*., 2010a]. However, one should bear in mind that in the context of our dual porosity model, mechanical response in the effective medium made up of micropores or fine microcracks that should not be identical to that in the bulk sample involving larger macropores. Our analysis here would suggest that brittle

failure in such an effective medium with numerous micropores and fine microcracks has a pressure sensitivity significantly lower than that of the bulk sample. To be consistent with the experimentally determined yield caps, our micromechanical model would require the effective medium to fail as a cohesive and pressure insensitive material.

5.3. Weakening of Tuff in the Presence of Water

A weakening effect of water was observed at all tested pressure conditions in our block of PA tuff. Both the peak stress in the brittle regime and the onset of pore collapse *C** in the cataclastic flow regime occurred at lower differential stresses in the presence of water (Figure 4.2). Comparison of a wet and dry hydrostats for the PI block confirmed that this effect is indeed significant in the Colli Albani Tuff. More or less pronounced water weakening has also been reported by many previous studies on sandstone [*Chester and Logan*, 1986; *Rutter and Mainprice*, 1978; *Baud et al*., 2000], granite [*Hadizadeh and Law*, 1991] and porous carbonates [*Baud et al*., 2009]. Since the brittle-ductile transition occurred at relatively low pressures in both PA and PI tuff and because this transition also occurred earlier in the presence of water, the impact of water can only be consistently quantified by the ratio P^*_{wet} / P^*_{dry} which provides a scaling of the difference between the dry and wet compactive envelopes. While for PA tuff the critical pore collapse pressures for saturated and dry conditions are 41 and 60 MPa, leading to $P^*_{wet} / P^*_{dry} = 0.68$, we obtained $P^*_{wet} / P^*_{dry} = 0.50$ for the PI Tuff ($P^*_{wet} = 28\,\text{MPa}$ and $P^*_{dry} = 56\,\text{MPa}$). In comparison, *Baud et al*. [2000] obtained values ranging from 0.70 to 0.96 in porous sandstone and more recently *Baud et al*. [2009] obtained 0.72 and 0.76 for two porous carbonates. It therefore appears that the weakening effect of water is more pronounced in the tuff. On the base of two micromechanical models, *Baud et al*. [2000]

interpreted the effect of water in sandstone as mostly due to a reduction of the specific surface energy (and of the fracture toughness) and also to a reduction of the friction coefficient. If K'_{IC} and μ' are respectively the fracture toughness and the friction coefficient in the presence of water, the Hertzian fracture model developed by *Zhang et al*. [1990] predicts: $P^*_{wet} / P^*_{dry} = \left(\frac{K'_{IC}}{K_{IC}} \right)^3$. The inferred ratio K'_{IC} / K_{IC} was found for sandstone to be between 0.89 and 0.98. A consistent estimation was obtained from brittle data with a ratio μ'/μ of around 0.90 [*Baud et al*., 2000].

The effective medium models with microporosity (5) and microcracks (6) applied here to our tuff data both predict a linear relation between P^*_{wet} / P^*_{dry} and K'_{IC} / K_{IC}. For a reasonable range of μ'/μ, one can assume that $(\sqrt{1+\mu'^2} + \mu')/(\sqrt{1+\mu^2} + \mu) \sim 1$ and in first approximation both models predict that $P^*_{wet} / P^*_{dry} \approx (K'_{IC} / K_{IC})$. The fracture toughness reduction due to water is therefore according to these models way more important in Alban Hills tuff than for a sandstone. While toughness measurements in dry and wet in series of Tuff by *Tuncay* [2009] showed similar range of toughness reduction, it is likely that other factors contribute to the observed weakening. First, as there are carbonatic inclusions in our samples, the weakening can also be related to the reaction between these particles and water. Second, we observed in the starting material that tuff has many clasts and pre-existing cracks embedded in matrix. Under saturated condition, water penetrates into the pre-existing microcracks and reduce the friction between clasts embedded in matrix. As the clasts are acting as obstacles to the crack propagation and coalescence according to our microstructure observations. The lubrication between clasts

will therefore lead the propagation much easier in saturated condition, which in turn result a stronger water effect in tuff samples compared to sandstones and granite.

6. Conclusion

Our microstructural observations of intact samples of Tuff from two different depths in the Colli Albani drilling site show the geometric complexity of the pore space in these volcanic rocks, with macroporosity, microporosity and microcracks. Our new hydrostatic and triaxial compression experiments indicate that the phenomenology of deformation and failure in tuff is similar to that of sedimentary rocks. In the brittle regime, our microstructural observations emphasize the role of pores in the development of stress induced damage. As for inelastic compaction and cataclastic flow, our observations indicate that in some respects, the micromechanics in tuff is qualitatively similar to that documented recently in porous limestones, which typically involves pore collapse that initiates from stress concentrations at the periphery of the larger pores.

To interpret the compaction behavior in tuff, we extended the cataclastic pore collapse model originally formulated for a porous carbonate rock to a dual porosity medium made up of macropores and micropores or microcracks. Our analysis has indicated that either the pore-emanated cracking or sliding wing crack model is consistent with our mechanical data and microstructural observations on Alban Hills tuff. Both models suggest that the significant weakening effect of water observed in these rocks could be the result of a large decrease of the fracture toughness in presence of water.

Synthesizing published data, we observe a systematic trend for both uniaxial compressive strength and pore collapse pressure of nonwelded tuff to decrease with

increasing porosity. Such a trend did not appear when we compiled existing data on welded tuff. More mechanical and microstructural data on tuff from various sites are clearly needed get more insight on the micromechanics controlling the deformation and failure of non welded tuff.

Acknowledgments

We are grateful to Dave Lockner who kindly provided the compaction data on Calico Hills tuff before publication. We thank Kam-Biu Luk, Pat Dobson and Seiji Nakagawa for furnishing us with their failed samples of Hong Kong tuff for microstructural observations. Brian Bonner and Tom Dewers kindly provided us copies of the Lawrence Livermore and Sandia reports, respectively. We also thank Jim Quinn for invaluable assistance with SEM microscopy. We have benefited from discussions with Joe Andrews, Cecilia Cheung, Dave Lockner, Seiji Nakagawa and Robina Wong. This research was partially supported by the Office of Basic Energy Sciences, Department of Energy under grant DE-FG02-99ER14996.

References:

Andrews, D. J., T. C. Hanks, and J. W. Whitney (2007), Physical Limits on Ground Motion at Yucca Mountain, *Bulletin of the Seismological Society of America*, *97*(6), 1771-1792, doi: 10.1785/0120070014.

Anselmetti, F., S. Luthi, and G. Eberli (1998), Quantitative characterization of carbonate pore systems by digital image analysis, *AAPG Bulletin*, *82*, 1815-1836.

Ashby, M., and C. Sammis (1990), The damage mechanics of brittle solids in compression, *Pure and Applied Geophysics*, *133*, 489-521.

Atkinson, B., and P. Meredith (1987), Experimental fracture mechanics data for rocks and minerals, in *Fracture Mechanics of Rock*, edited by B. K. Atkinson pp. 477–525, Academic, London.

Avar, B., and N. Hudyma (2007), Observations on the influence of lithophysae on elastic (Young's) modulus and uniaxial compressive strength of Topopah Spring Tuff at Yucca Mountain, Nevada, USA, *Int J Rock Mech Min*, *44*(2), 266-270.

Aversa, S., and A. Evangelista (1998), The mechanical behaviour of a pyroclastic rock: Yield strength and "destructuration" effects, *Rock Mechanics and Rock Engineering*, *31*(1), 25-42.

Baechle, G., A. Colpaert, G. Eberli, and R. Weger (2008), Effects of microporosity on sonic velocity in carbonate rocks, *The Leading Edge*, *27*, 1012-1018, doi:10.1190/1.2967554.

Baud, P., A. Schubnel, and T.-f. Wong (2000), Dilatancy, compaction, and failure mode in Solnhofen limestone, *Journal of Geophysical Research*, *105*(B8), 19289-19303, doi: 10.1029/2000JB900133.

Baud, P., V. Vajdova, and T.-f. Wong (2006), Shear-enhanced compaction and strain localization: Inelastic deformation and constitutive modeling of four porous sandstones, *J. Geophys. Res.*, *111*(B12), B12401, doi: 10.1029/2005jb004101.

Baud, P., S. Vinciguerra, C. David, A. Cavallo, E. Walker, and T. Reuschlé (2009), Compaction and Failure in High Porosity Carbonates: Mechanical Data and Microstructural Observations, *Pure and Applied Geophysics*, *166*(5), 869-898, doi: 10.1007/s00024-009-0493-2.

Bemer, E., O. Vincké, and P. Longuemare (2004), Geomechanical log deduced from porosity and mineralogical content, *Oil & Gas Science and Technology*, *59*, 405-426.

Bhatt, J., M. Carroll, and J. Schatz (1975), Spherical model calculation for volumetric response of porous rocks, *Journal of Applied Mechanics*, *42*, 363-368.

Chester, F. M., and J. M. Logan (1986), Implications for mechanical properties of brittle faults from observations of the Punchbowl fault zone, California, *Pure and Applied Geophysics*, *124*, 79-106, doi: 10.1007/BF00875720.

Choquette, P., and L. Pray (1970), Geologic nomenclature and classification of porosity in sedimentary carbonates, *AAPG Bulletin*, *54*, 207-250.

Curran, J., and M. Carroll (1979), Shear stress enhancement of void compaction, *Journal of Geophysical Research*, *84*, 1105–1112, doi: 10.1029/JB084iB03p01105.

de Rita, D., and C. Giampaolo (2006), A case study—Ancient Rome was built with volcanic stone from the Roman land, *GSA Special Papers*, *408*, 127.

Dobson, P., and S. Nakagawa (2005), Summary of Rock-Property Measurements for Hong Kong Tuff Samples*Rep.*, Ernest Orlando Lawrence Berkeley NationalLaboratory, Berkeley, CA (US).

Evans, J. P., and K. K. Bradbury (2004), Faulting and fracturing of nonwelded Bishop Tuff, eastern California: Deformation mechanisms in very porous materials in the vadose zone, *Vadose Zone Journal*, *3*, 602-623.

Fortin, J., S. Stanchits, G. Dresen, and Y. Guéguen (2006), Acoustic emission and velocities associated with the formation of compaction bands in sandstone, *Journal of Geophysical Research*, *111*, B10203, doi: 10.1029/2005JB003854.

Funiciello, R., and C. Caputo (2006), Giovan Battista Brocchi's Rome: A pioneering study in urban geology, *Geological Society of America*, *411*, 199-210

Gurson, A. (1977), Continuum theory of ductile rupture by void nucleation and growth: Part I-Yield criteria and flow rules for porous ductile media, *Journal of Engineering Materials and Technology*, *99*, 2-15.

Hadizadeh, J., and R. D. Law (1991), Water-weakening of sandstone and quartzite deformed at various stress and strain rates, *Int J Rock Mech Min*, *28*, 431-439.

Heard, H., B. Bonner, A. Duba, R. Schock, and D. Stephens (1973), High Pressure Mechanical Properties Of Mt Helen, Nevada, Tuff *Rep. UCID-16261*, Lawrence Livermore National Laboratory, Livermore, CA.

Heiken, G. (2006), *Tuffs: their properties, uses, hydrology, and resources*, 131 pp., Geological Society of America, USA.

HKGeotechnicalOffice (1990), Foundation Properties of Marble and Other Rocks in the Yuen Long-Tuen Mun Area *Rep. 2/90*, HK Geotechnical Office.

Horii, H., and S. Nemat-Nasser (1986), Brittle failure in compression: splitting, faulting and brittle-ductile transition, *Philosophical Transactions for the Royal Society of London*, *319*, 337-374.

Kemeny, J., and N. Cook (1991), Micromechanics of deformation in rocks, in *Toughening mechanisms in quasi-brittle materials*, edited by S. P. Shap pp. 155-188, Klewer Academic.

Lockner, D., and C. Morrow (2008), Energy Dissipation in Calico Hills Tuff due to Pore Collapse, *Eos Trans. AGU*, *89*(53), Fall Meet. Suppl., Abstract T51A-1856.

Long, J., and R. Ewing (2004), Yucca Mountain: Earth-science issues at a geologic repository for high-level nuclear waste, *Annual Review of Earth and Planetary Sciences*, *32*, 363-401.

Mariucci, M. T., S. Pierdominici, L. Pizzino, F. Marra, and P. Montone (2008), Looking into a volcanic area: An overview on the 350 m scientific drilling at Colli Albani (Rome, Italy), *Journal of Volcanology and Geothermal Research*, *176*(2), 225-240, 10.1016/j.jvolgeores.2008.04.007.

Martin, R., P. Boyd, J. Noel, and R. Price (1994), Bulk and mechanical properties of the Paintbrush tuff recovered from borehole USW NRG-6: Data report *Rep. SAND--93-4020*, Sandia National Labs., Albuquerque, NM

Martin, R. J., P. J. Boyd, J. S. Noel, and R. H. Price (1995), Bulk and mechanical properties of the Paintbrush tuff recovered from borehole USW NRG-7/7A: Data report. *Rep. SAND--94-1996*, Sandia National Labs., Albuquerque, NM

Menéndez, B., W. Zhu, and T. Wong (1996), Micromechanics of brittle faulting and cataclastic flow in Berea sandstone, *Journal of Structural Geology*, *18*(1), 1-16, doi: 10.1016/0191-8141(95)00076-P.

Mogi, K. (1964), Deformation and fracture of rocks under confining pressure (1) Compression tests on dry rock sample, *Bull. Earthq. Res. Inst*, *42*, 491-514.

Moon, V. (1993), Geotechnical characteristics of ignimbrite: A soft pyroclastic rock type, *Engineering Geology*, *35*(1-2), 33-48.

Nimick, F. B., R. H. Price, R. G. Van Buskirk, and J. R. Goodell (1985), Uniaxial and triaxial compression test series on Topopah Spring Tuff from USW G-4, Yucca Mountain, Neveda *Rep. SAND--84-1101*, Sandia National Labs., Albuquerque, NM

Paterson, M., and T. Wong (2005), *Experimental rock deformation--The brittle field, 2nd Edition*, 348 pp., Springer-Verlag, New York.

Pittman, E. (1971), Microporosity in carbonate rocks, *AAPG Bulletin*, *55*(10), 1873–1878.

Price, R., and S. Bauer (1985), Analysis of the elastic and strength properties of Yucca Mountain tuff, Nevada, The 26th U.S. Symposium on Rock Mechanics (USRMS),1:89-96.

Russ, J. (1990), *Computer-assisted microscopy: the measurement and analysis of images*, 480 pp., Plenum Press, New York.

Rutter, E., and D. Mainprice (1978), The effect of water on stress relaxation of faulted and unfaulted sandstone, *Pure and Applied Geophysics*, *116*, 634-654.

Sammis, C., and M. Ashby (1986), The failure of brittle porous solids under compressive stress states, *Acta Metallurgica*, *34*(3), 511-526.

Schultz, R. A., and Q. Z. Li (1995), Uniaxial strength testing of non-welded Calico Hills tuff, Yucca Mountain, Nevada, *Engineering Geology*, *40*(3-4), 287-299.

Timoshenko, S., and J. Goodier (1951), *Theory of Elastic*, 567 pp., McGraw-Hill, New York.

Tuncay, E. (2009), Rock rupture phenomenon and pillar failure in tuffs in the Cappadocia region (Turkey), *Int J Rock Mech Min*, *46*, 1253-1266, doi: 10.1016/j.ijrmms.2009.01.011.

Vajdova, V., P. Baud, and T. Wong (2004), Compaction, dilatancy, and failure in porous carbonate rocks, *Journal of Geophysical Research*, *109*, B05204, doi: 10.109/2003JB002508.

Vajdova, V., W. Zhu, T.-M. N. Chen, and T. Wong (2010), Micromechanics of brittle faulting and cataclastic flow in Tavel limestone, *Journal of Structural Geology*, *in press*.

Vinciguerra, S., P. Del Gaudio, M. T. Mariucci, F. Marra, P. G. Meredith, P. Montone, S. Pierdominici, and P. Scarlato (2009), Physical properties of tuffs from a scientific borehole at Alban hills volcanic district (central Italy), *Tectonophysics*, *471*(1-2), 161-169, 10.1016/j.tecto.2008.08.010.

Wong, T.-F., C. David, and W. Zhu (1997), The transition from brittle faulting to cataclastic flow in porous sandstones: Mechanical deformation, *Journal of Geophysical Research*, *102*, 3009-3025, doi: 10.1029/96JB03281.

Zhang, J. X., T. F. Wong, and D. M. Davis (1990), Micromechanics of Pressure-Induced Grain Crushing in Porous Rocks, *Journal of Geophysical Research*, *95*, 341-352, doi: 10.1029/JB095iB01p00341.

Zhu, W., P. Baud, and T. Wong (2010a), Micromechanical basis for the Coulomb failure parameters, *Earth and Planetary Science Letters*, *submitted*.

Zhu, W., P. Baud, and T.-f. Wong (2010b), Micromechanics of cataclastic pore collapse in limestone, *Journal of Geophysical Research*, *115*(B4), B04405, doi: 10.1029/2009JB006610.

Table 4.1. Stress history of samples studied

Sample	Density, g/cm^3	Porosity[a], %	Effective Pressure, MPa	Peak Stress, MPa		Critical yield Stress, MPa	
				Differential Stress σ_1-σ_3	Effective Mean Stress $(\sigma_1+2\sigma_3)/3$-P_p	Differential Stress σ_1-σ_3	Effective Mean Stress $(\sigma_1+2\sigma_3)/3$-P_p
PA tuff (Tufo del Palatino unit)							
T0_PA	1.54	-	-	-	-	-	-
Twh1_PA	1.55	31.8	110	-	-	-	P^*=41
Twh2_PA	1.51	36.1	110	-	-	-	P^*=35
Tw1_PA	1.58	31.8	5	27.9	14.0	-	-
Tw2_PA	1.57	31.3	10	-	-	28.8	19.9
Tw3_PA	1.57	31.8	20	-	-	24.2	28.1
Tw4_PA	1.56	32.7	30	-	-	18.1	36.2
Tdu_PA	1.57	-	0	33.4	12.1	-	-
Tdh_PA	1.54	32.6	130	-	-	-	P^*=60
Td1_PA	1.56	-	5	48.4	21.5	-	-
Td2_PA	1.56	-	30	-	-	34.2	42.7
Td3_PA	1.56	-	45	-	-	23.2	53.0
PI tuff (Tufo Pisolitico di Trigoria unit)							
T0_PI	1.50	-	-	-	-	-	-
Twh_PI	1.51	35.0	40	-	-	-	P^*=28
Tdh_PI	1.53	-					P^*=56
Tdu_PI	1.50	-	0	17.4	5.8	-	-
Td1_PI	1.63	-	5	42.9	19.3	-	-
Td2_PI	1.74	-	10			25	45.04
Td3_PI	1.52	-	30	-		29.5	39.89
Td4_PI	1.50	38.6	45	-		18.8	51.28

[a] The porosity was not measured on the dry samples to avoid water effect

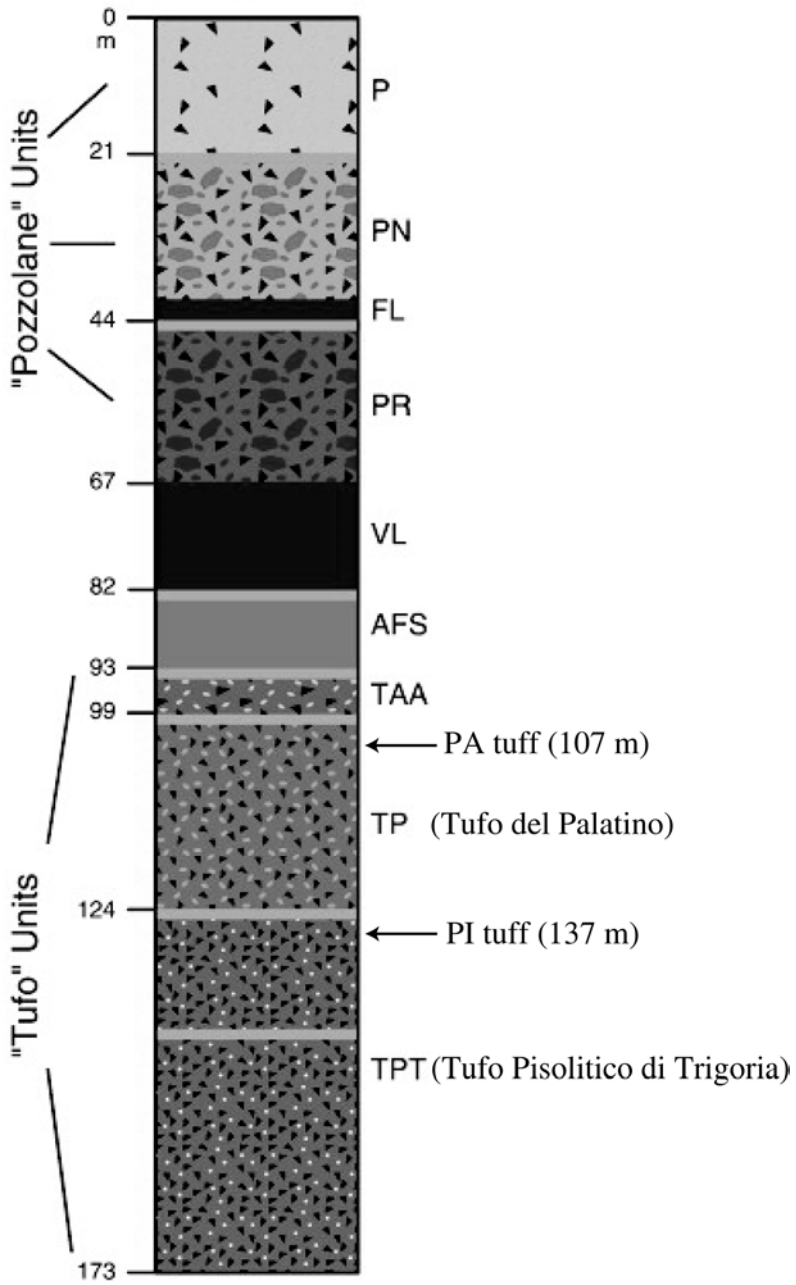

Figure 4.1. Schematic stratigraphy of volcanic units encountered by the Colli Albani borehole (after *Vincigerra et al.*, 2009). TP and TPT represent "Tufo del Palatino" and "Tufo Pisolitico di Trigoria" unit, respectively. Our samples drilled from these two units are correspondingly denoted by PA and PI tuff. The drilling depths are indicated by arrows.

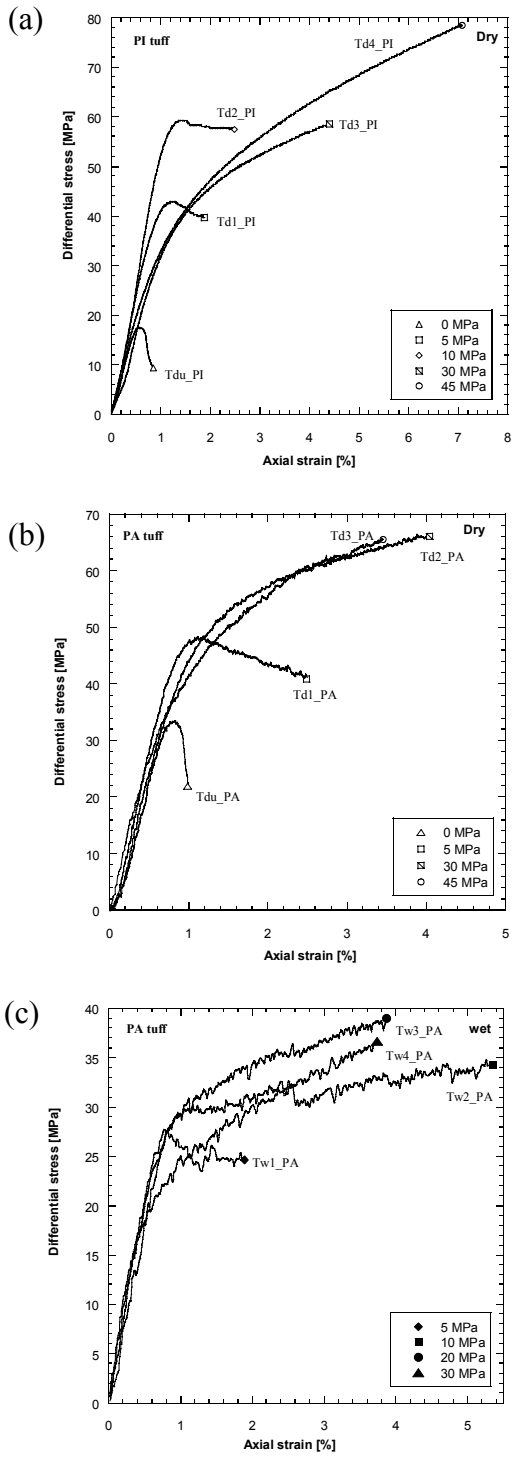

Figure 4.2. Stress-strain curves of (a) dry PI tuff (Tufo Pisolitico) with confining pressures ranging from 0 MPa to 45 MPa; (b) dry PA tuff (Tufo de Palatino) with confining pressures ranging from 0 MPa to 45 MPa, and (c) wet PA tuff (Tufo de Palatino) with effective pressures ranging from 5 MPa to 30 MPa. The samples corresponding to each curve are denoted in the plot, with symbols representing the effective pressures.

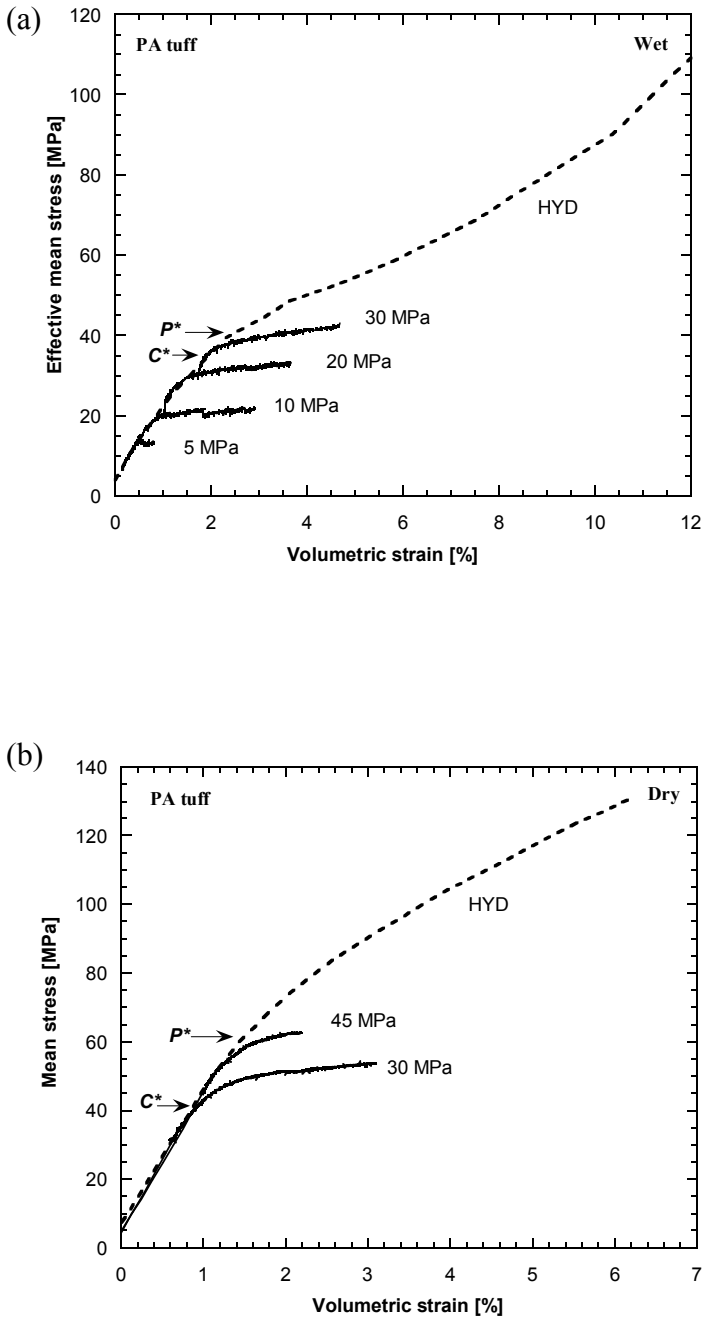

Figure 4.3. Volumetric strain versus mean stress for triaxial compression experiments on (a) wet PA tuff (Tufo de Palatine), and (b) dry PA tuff. For reference, the hydrostatic data are shown as the dashed curve. Numbers next to each curve indicate the effective pressures maintained during the experiments. The critical pore collapse pressure P^* and the onset of shear-enhanced compaction C^* at effective pressure of 30 MPa are marked by arrows.

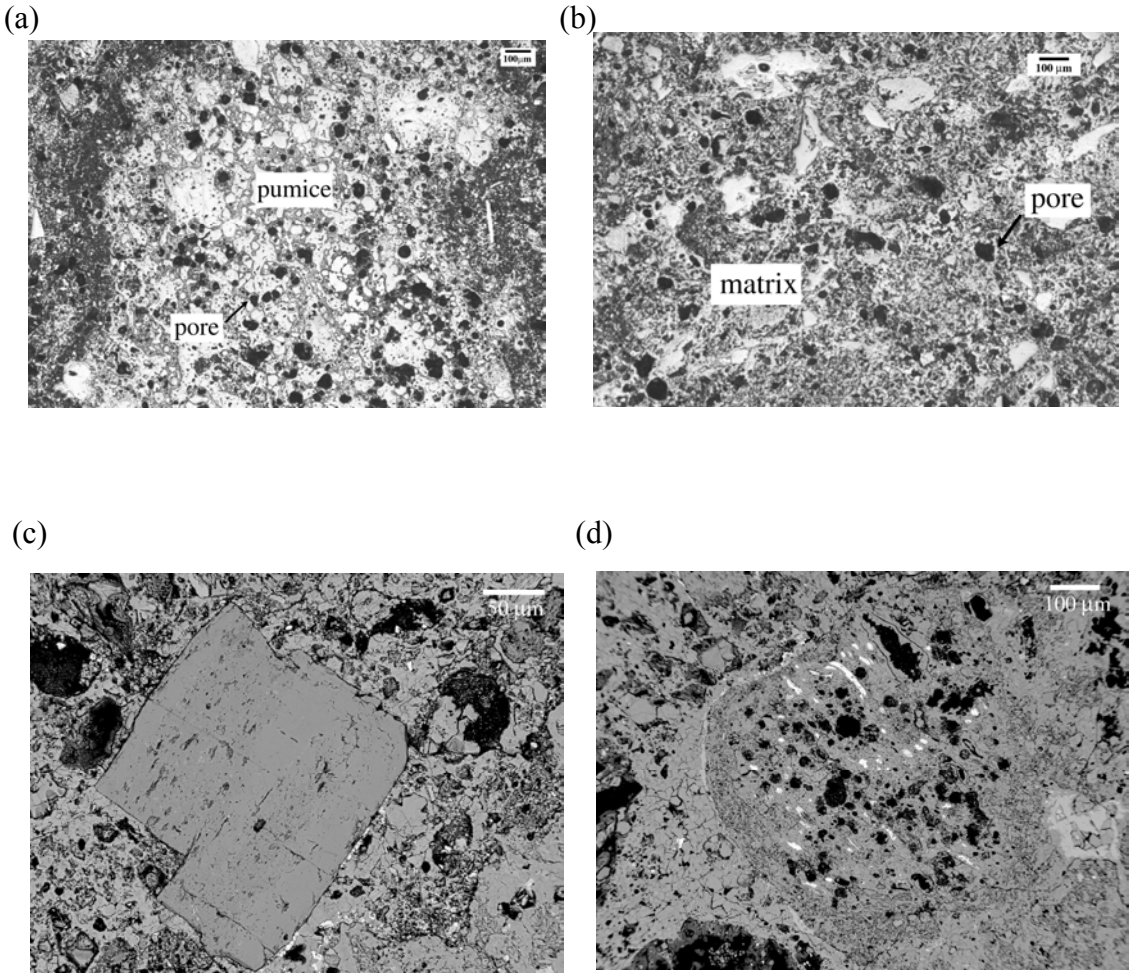

Figure 4.4. Micrographs of intact Alban Hills tuff sample. (a) A pumice and (b) interior of a lapilli observed under optical microscope. Pores are represented by the dark areas as marked in the image. Backscattered FESEM images of (c) a relatively intact shard with straight edges and sharp corners, and (d) a scoria clast in an undeformed Alban Hills tuff. Pores with dimensions up to 100 μm are shown as black areas.

(e)

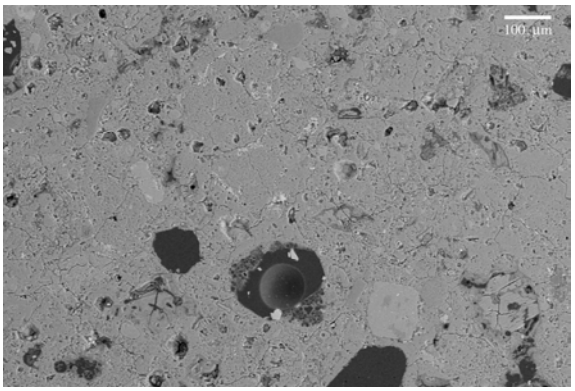

(f)

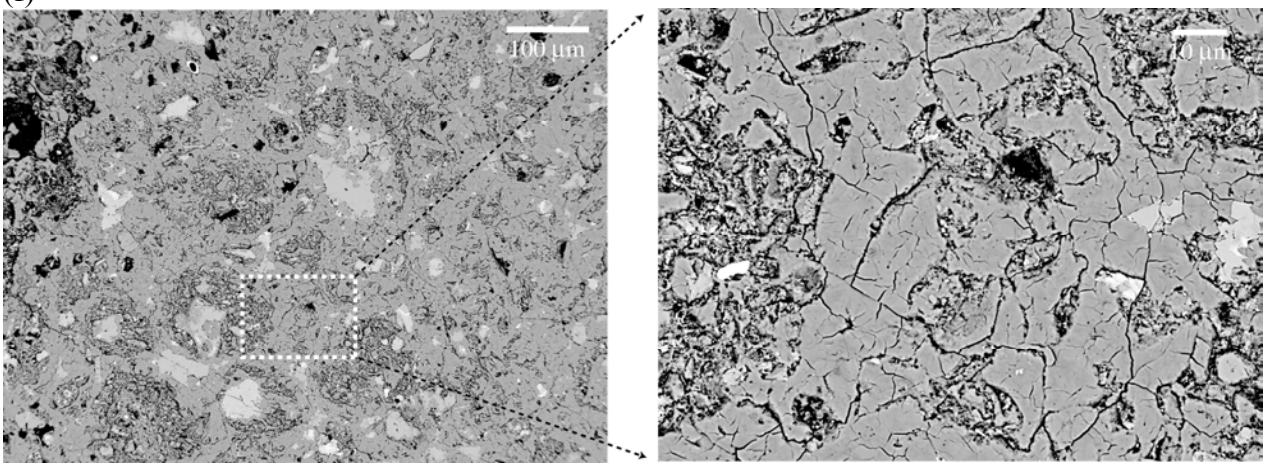

Figure 4.4. Micrographs of intact Alban Hills tuff sample.(e) Backscattered SEM images of large pores (~ 100 µm) and smaller pores (~ 10 µm) embedded in tuff matrix (f) Backscattered FESEM images of smaller pores on the order of 10 µm embedded in matrix. Numerous µm-sized pores and elongated microcracks were observed in the zoomed-in figure on the right.

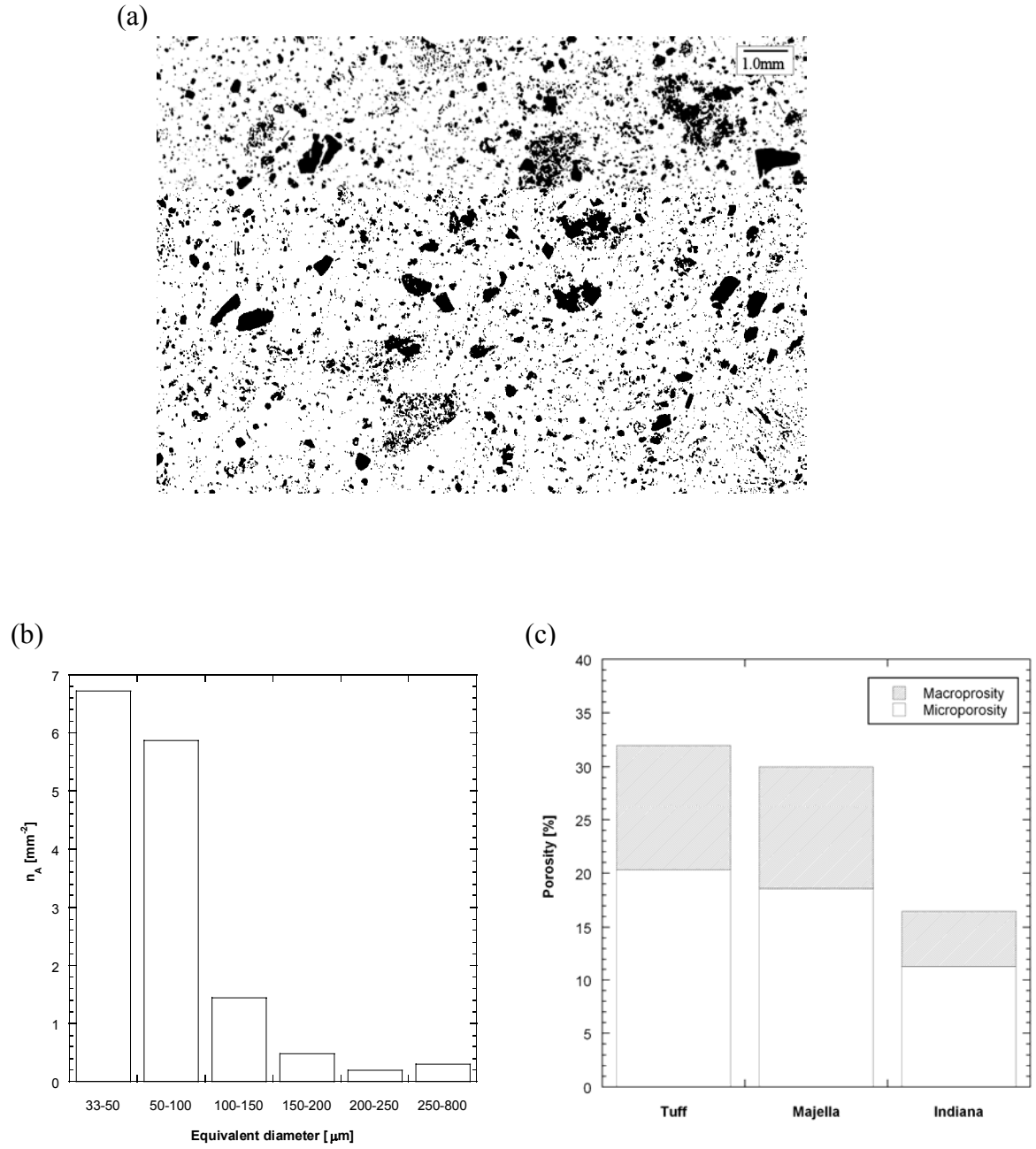

Figure 4.5. (a) Binarized image of intact Alban Hills tuff sample. Macropores resolved under optical microscope are shown in black. Isolated area with irregular shape could be plucked out grains. (b) Size distribution of pores in an undeformed Alban Hills tuff sample that can be resolved under optical microscope. The number of pores per unit area is plotted versus equivalent diameter. Only data for diameters greater than 33 μm are shown. (c) Partitioning of microporosity and macroporosity in Alban Hills tuff. For comparison, histograms of Majella and Indiana limestones (*Zhu et al*., 2010a) are also shown.

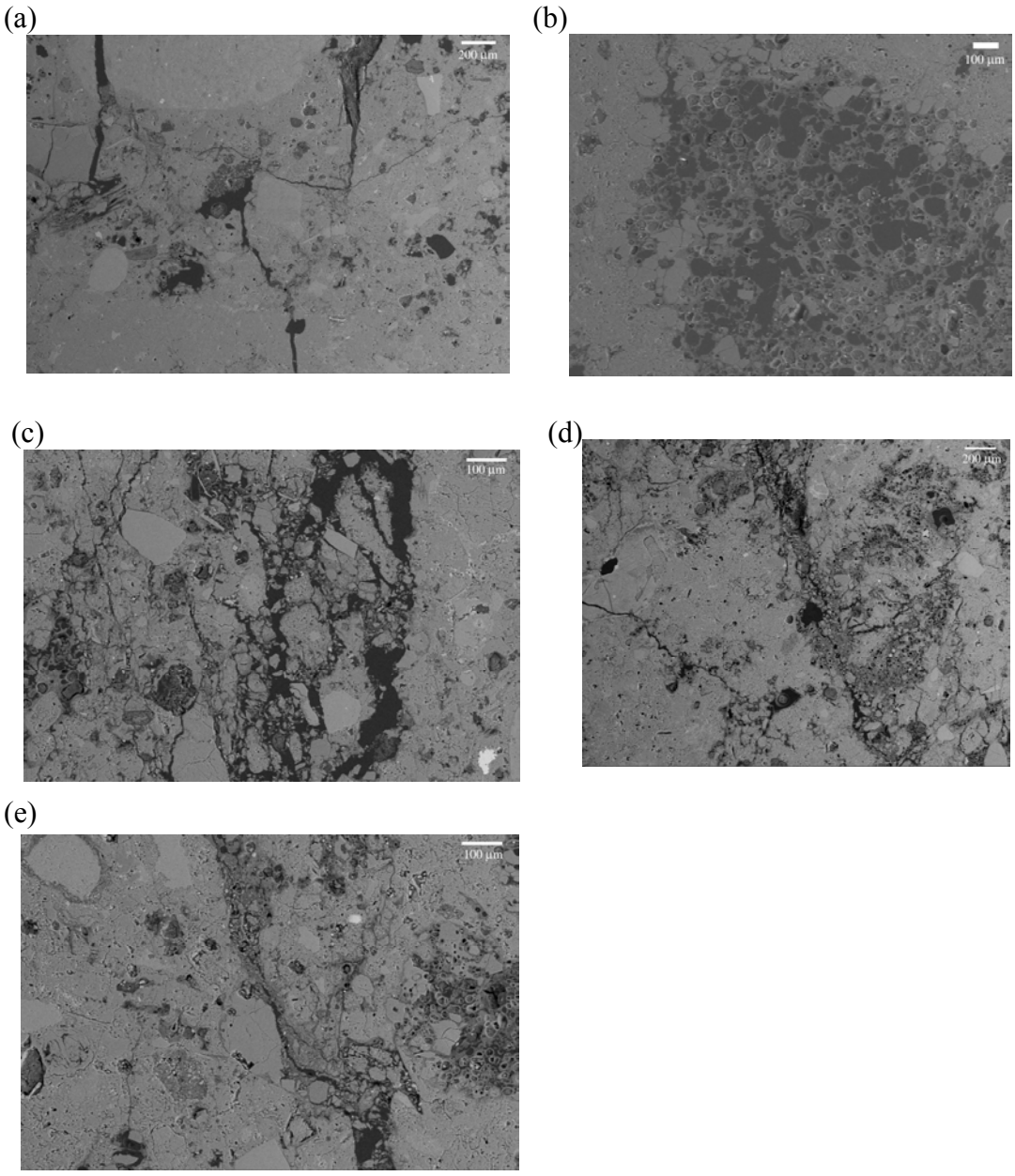

Figure 4.6. Backscattered SEM images of Alban Hills tuff samples failed in brittle regime. Direction of σ_1 is vertical. (a) Sample Tdu_PA that failed in uniaxial compression. Stress-induced microcracks were observed to emanate from relatively large pores in matrix and propagated sub-parallel to σ_1. (b) A pumice in sample Tdu_PA. Macropores embedded in the pumice were not observed to interact with wing cracks. (c) Sample Td1_PA loaded to post peak. Intense microcracking and comminution were observed in the vicinity of the shear band. (d) A macropore embedded in matrix of sample Td1_PA. Numerous stress-induced cracks sub-parallel to σ_1 had emanated from the macropore and coalesced with each other. (e) A path along which shear localization had developed in sample Td1_PA. The development was observed to bypass the lithic clasts by traversing along their boundaries.

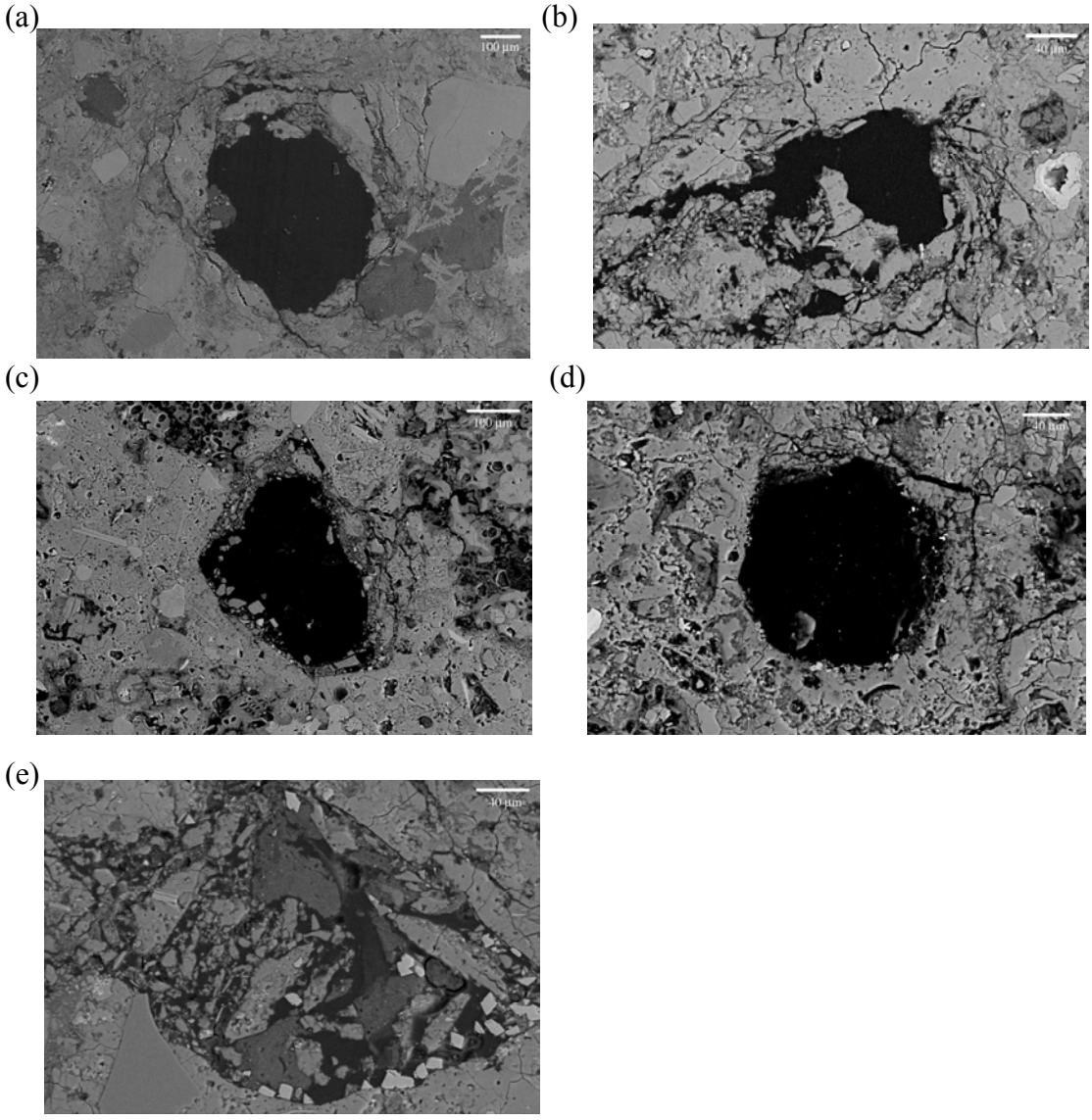

Figure 4.7. Backscatter SEM images of Alban Hills tuff samples failed by inelastic compaction. Direction of σ_1 is vertical (a) Sample Twh1_PA was hydrostatically compacted beyond the critical pore collapse pressure *P**. A macro pore in matrix surrounded by intensive cataclastic damage was observed. The damage zone had extended a distance ~ 100 μm. (b) A collapsed pore in matrix in sample Twh1_PA. The micropore, with a diameter ~ 60 μm, was about 5 times smaller than the macropore in (a). Stress-induced cracks had coalesced around the pore surface. (c) Sample Tw4_PA was stressed to beyond the compactive yield stress *C**. A macropore in matrix with a diameter ~ 250 μm was observed to collapse. A thin layer of crushed grains in the periphery of the macropore was formed by the propagation and coalescence of stress-induced microcracks. (d) A collapsed micropore with a diameter of ~ 90 μm in sample Tw4_PA. Microcracks had emanated from the micropore and coalesced around the pore circumference. (e) Collapse of spalled fragments into a macropore in sample Tw4_PA. Crushed grains had fallen into the interior of the macropore.

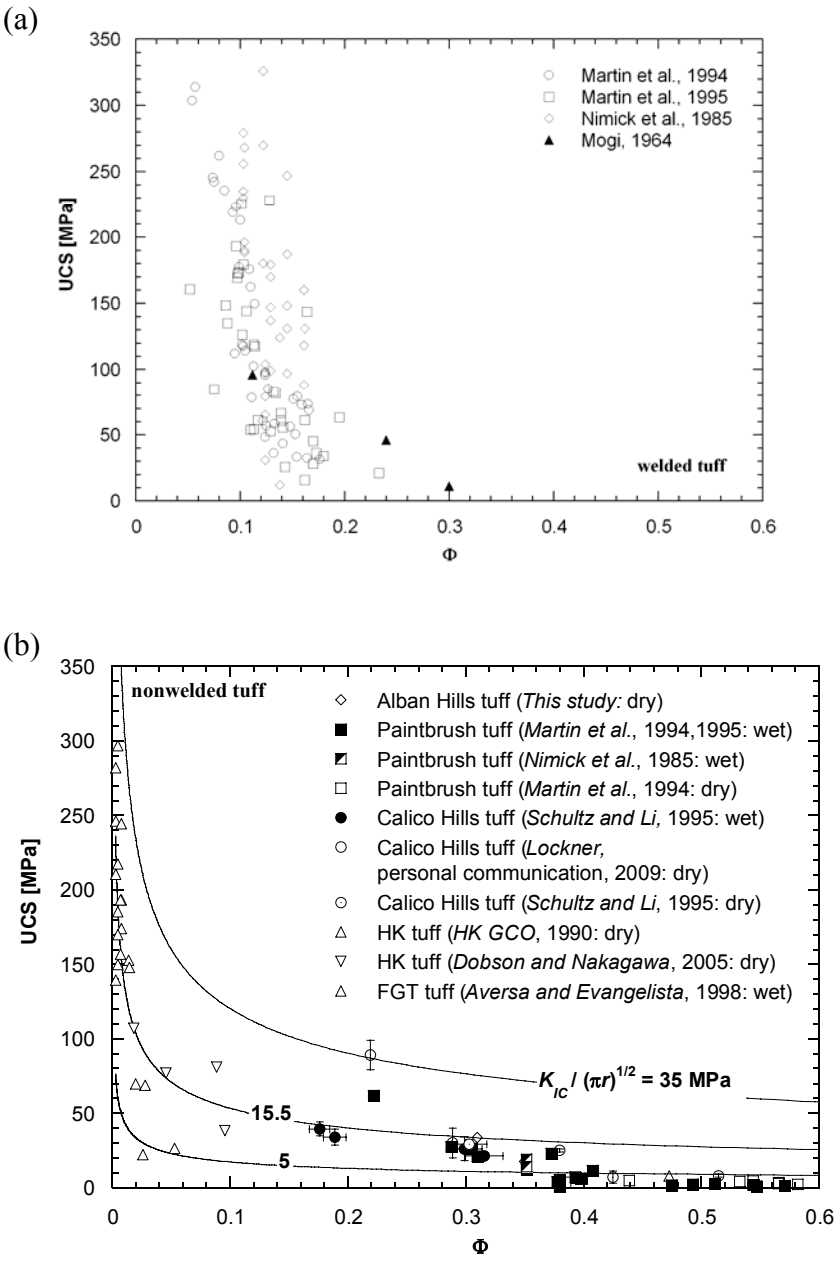

Figure 4.8. Compiled uniaxial compressive strength (UCS) data are plotted as a function of total porosity. (a) Experimental data of welded tuffs from Yucca Mountain and Japan are shown by open and solid symbols, respectively. No apparent correlations were observed between UCS and porosity for the welded tuffs. (b) Comparison of theoretical predictions with laboratory data on UCS of nonwelded tuff samples. Theoretical curves of UCS as a function of total porosity for three different values of $K_{IC}\sqrt{\pi r}$ are plotted. Most of the data can be bracketed by two limiting curves with $K_{IC}\sqrt{\pi r}$ = 5 and 35 MPa. The standard deviations of data on Calico Hills tuff are represented by error bars.

(a)

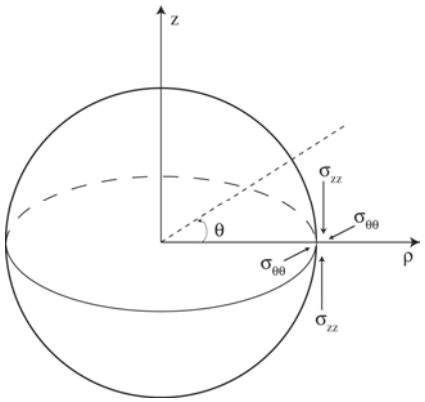

(b)

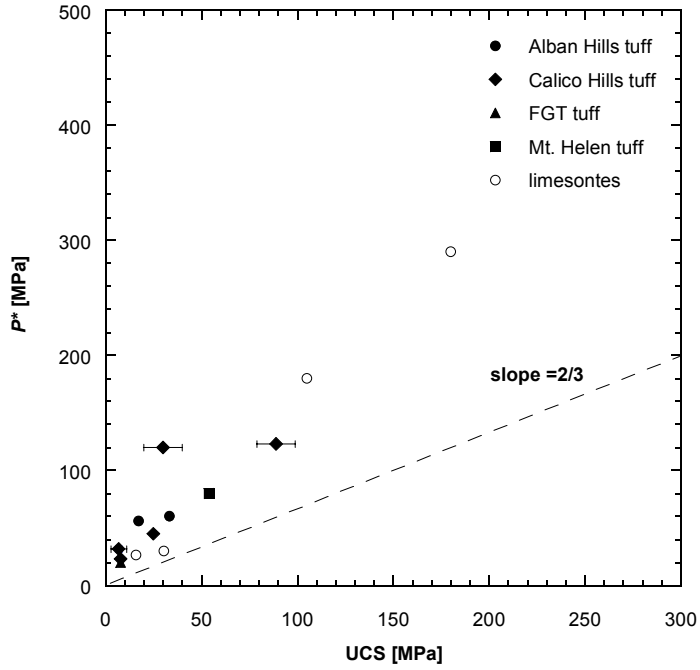

Figure 4.9. (a) Local stress field at the vicinity of the macropore. The local principal stresses σ_{zz} and $\sigma_{\theta\theta}$ act along the axial and azimuthal directions, respectively. Due to the boundary conditions in the pore surface, the radial stress is zero. (b) The critical pore collapse pressure *P** is plotted versus the uniaxial compressive strength UCS on nonwelded tuff samples. For comparison, limestone data compiled by *Zhu et al*., 2010a are also shown as open circles. The dashed line corresponds to a slope of *P** versus UCS equaled 2/3. The standard deviations of data on Calico Hills tuff are shown as error bars.

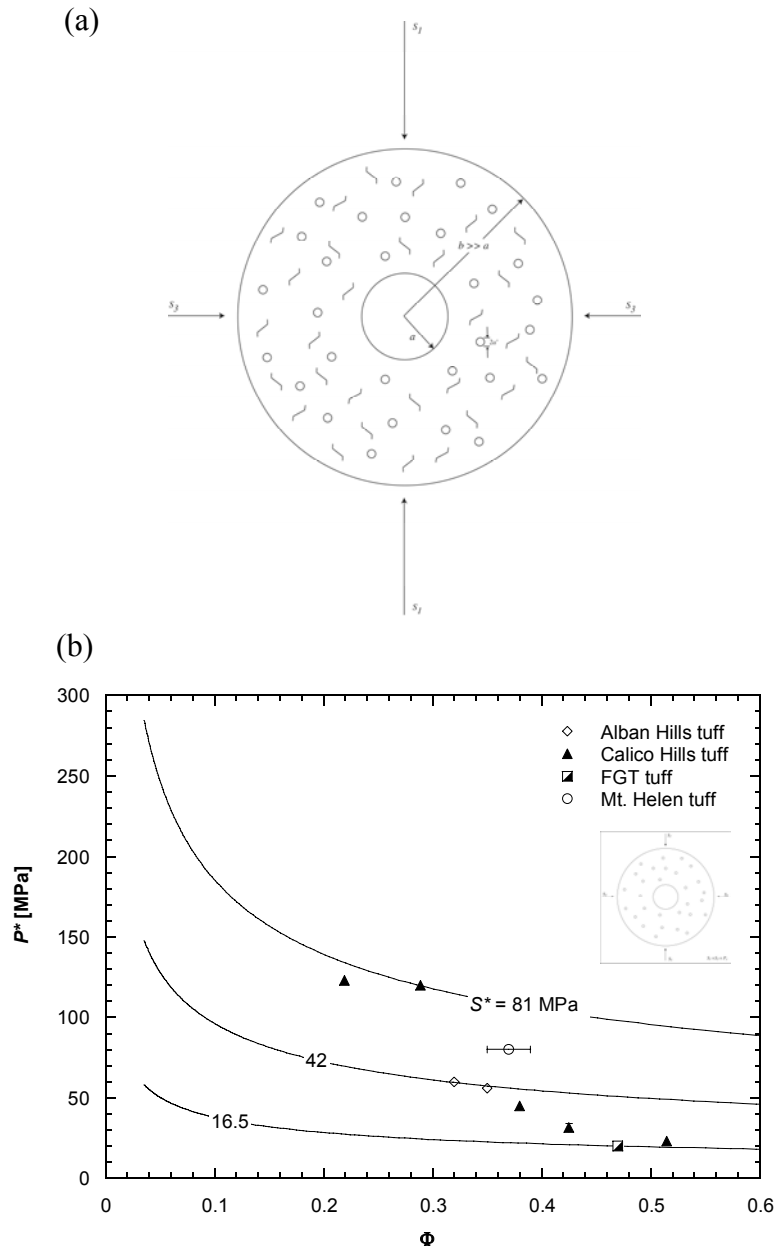

Figure 4.10. (a) Schematic diagram of a representative volume element of radius *b*. A macropore of radius *a* is surrounded by an effective medium made up of many micropores of radius *a** and pre-existing microcracks with length of *2c*. Remote principal stresses are represented by S_1, S_2, and S_3. (b) Comparison of theoretical predictions with laboratory data on critical pore collapse pressure *P** of tuff samples when adopting dual porosity model with total porosity partitioned between macropores and micropores. Theoretical curves of *P** as a function of porosity for three different values of *S** are plotted. The data are bounded by upper and lower limits of *S** = 16.5 and 81 MPa. The standard deviations of data on Mt. Helen and Calico Hills tuff are represented by error bars.

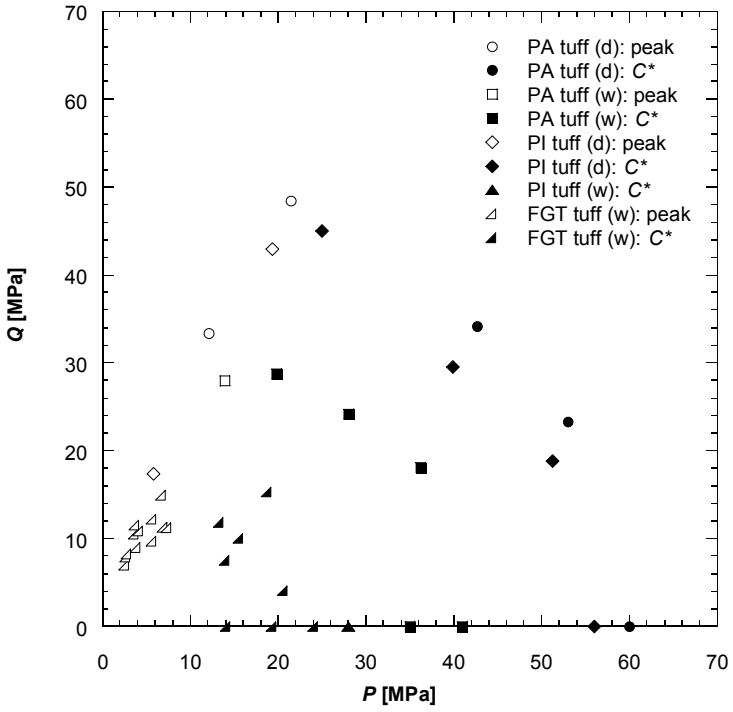

Figure 4.11. Peak stresses (open symbols) and critical stresses *C** (solid symbols) for the onset of shear-enhanced compaction are plotted in the *P* (mean stress) and *Q* (differential stress) space for Alban Hills tuff and Neapolitan fine-grained tuff (*Aversa and Evangelista*, 1998). The peak stresses seem to follow Mohr-Coulomb criterion. There is an overall trend for the yield caps (*C**) to expand with decreasing porosity.

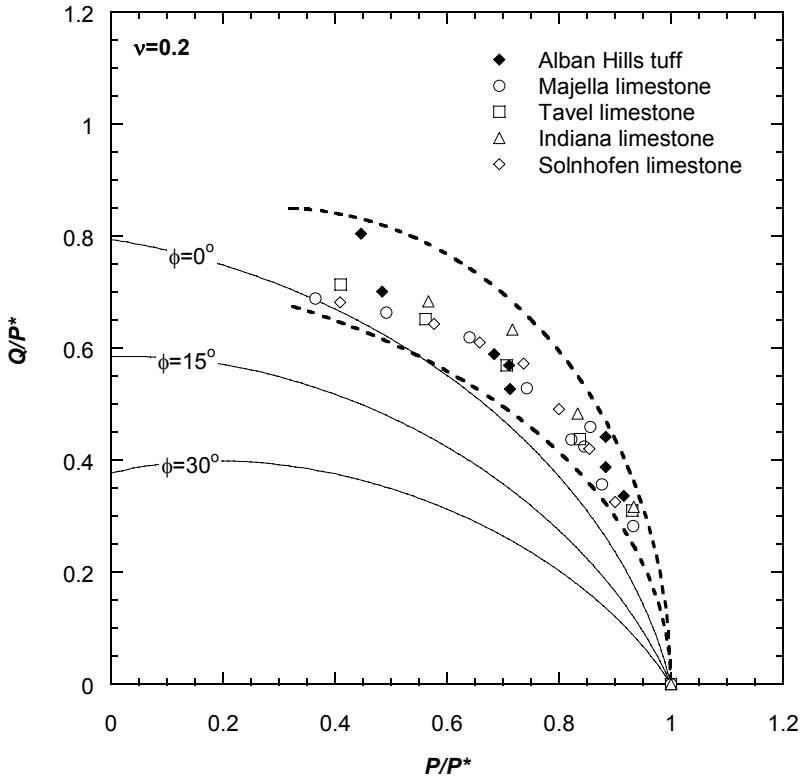

Figure 4.12. Differential stress (Q) and mean stress (P) at the onset of shear-enhance compaction normalized by the pore collapse pressure P^*. The solid diamonds represent C^* of Alban Hills tuff normalized by a P^* of 41 MPa. For comparison, three limestone data presented by *Zhu et al*., 2010a are also shown as open symbols. Normalized yield stresses of the four rocks fall on caps very close as bracketed by the dashed curves. Theoretical predictions according to the Drucker-Prager yield criterion (for a Poisson's ratio of 0.2) are plotted as solid curves. The angle of internal friction ϕ is marked on each curve.

Chapter 5

Micromechanics of dilatancy, compaction and failure mode in Mt. Etna basalt

Abstract

Understanding how the strength of volcanic rock varies with stress state, pore fluid content and pressure, damage (content and anisotropy) is fundamental to investigate the dynamics of volcanic systems. In this study, we obtained three blocks of basalt samples from Mt. Etna, Italy. Two Etna blocks with porosity of 5 % (measured by water saturation) failed in brittle failure regime with effective pressure up to 150 MPa. Shear-enhanced compaction was observed on the third block with a porosity of 8 %. The phenomenological behaviors on basalt were found to be similar to that in a porous sedimentary rock. Systematic microstructural observations were conducted to elucidate the micromechanics of brittle faulting and inelastic compaction. Wing crack model has been adopted to investigate the dilatancy and brittle failure in the compact basalt samples.

The more porous basalt was treated as a dual porosity medium that made up of macropore and preexisting cracks. Pore-emanated cracking model developed for porous carbonate rocks has been extended to porous Etna basalt, with a combination of wing crack model applied on the effective medium. The effect of water, phenocryst and porosity has been studied.

1. Introduction

As one of the planet's few continuously active volcanoes, Etna constitutes one of the most important natural volcanic laboratories. It lies on the eastern coast of Sicily in Italy, close to the boundary between the continental crust of the Hyblean Plateau and the Mesozoic oceanic crust of the Ionian basin (Figure 5.1). The physical state of the host rock has been recognized to be crucial to determine penetration of magma or steam in local fractures [*Chouet*, 1996]. Understanding how the strength of volcanic rock varies with stress state, pore fluid content and pressure, damage (content and anisotropy) is fundamental to investigate the dynamics of volcanic systems and in particular to model the progression of magma towards earth's surface that leads to eruptions. Laboratory studies under controlled conditions are therefore essential for accurate and meaningful interpretations.

The interest of mechanical studies on basaltic rocks from Mt. Etna volcano has been raised in recent years. Volcanic activities [*Azzaro et al*., 2000; *Vinciguerra et al*., 2001] indicated that the brittle failure mechanism [*Patanè et al*., 2004] has been accelerated in Mt. Etna volcano. Repeated episodes of deformation can be related to increasing damage

and a changing stress field within the volcanic edifice largely consisting of basalt [*Stanchits* et al., 2006]. As dilatancy is universally observed as a precursor to the inception of shear localization in the brittle faulting regime [*Brace*, 1978], they were observed to affect the mechanical behaviors and brittle deformation. However, there has been a paucity of data on dilatancy in Mt. Etna basalt. Mechanical behavior and failure modes on Etna basalt have not been systematically investigated either.

Previous studies on Etna basalt focused on the damage mechanics [*Vinciguerra et al*., 2001; *Vinciguerra*, 2002] and physical properties [*Heap et al*., 2009; *Vinciguerra et al*., 2005; *Stanchits et al*., 2006]. The presence of a high level of connected preexisting microcracks has been found on Etna basalt in its as-received state [*Heap et al*., 2009; *Vinciguerra et al*., 2005; *Stanchits et al*., 2006]. Seismic velocities studies implied that both the matrix and the crack population in Etna basalt are relatively isotropic [*Vinciguerra et al*., 2005]. There has been no change observed on physical and transport properties of Etna basalt by thermal stressing tests [*Heap et al*., 2009; *Vinciguerra et al*., 2005], which suggested that the microcracks can be interpreted as being of thermal origin, and the experiments under room temperature can provide analogous results to the ones under high temperatures. Besides preexisting microcracks, low-aspect ratio pores (Figure 5.2) were found in Etna basalt [*Stanchits et al*., 2006; *Adelinet et al.,* 2010], they were observed to effect bulk modulus with elevated confining pressures. Hence, to investigate the phenomenological behaviors on Etna basalt would require a priori knowledge of both cracks and pores.

In this study, we conducted a systematic suit of experiments on three blocks of Mt. Etna basalt samples under conventional triaxial compression experiment set-up. The

mechanical behavior and microstructural observation on basalt were investigated. To illustrate the water effect, we also conducted experiments at different confining pressures under both saturated and nominal dry conditions. The effects of phenocrysts and porosity on Etna basalt were investigated. The micromechanics on porous limestones and tuffs have been studied in the previous chapters. As illustrated in previous chapters, the phenomenological behaviors of limestones and tuffs are quite similar to those of clastic rocks, such as sandstones. However, the micromechanics of compaction were found to be fundamentally different. Sliding wing crack model and pore-emanated cracking model have been developed to investigate the inelastic compaction on carbonate rocks (Chapter 2) and tuff samples (Chapter 4). In this chapter, we will apply these micromechanical models to Etna basalt and assess to what extent the damage mechanics can be explained by these models.

2. Experimental procedure

2.1. Sample material and preparation

We have obtained three blocks of Mt. Etna basalt, namely EB_I, EB_II and EB_III. The EB_I block is composed of a fine-grained groundmass that takes up ~ 60 %. The phenocrysts in EB_I mainly consists of feldspar (25.08 %), pyroxene (8.54 %) and olivine(4.04 %). Cylindrical samples were ground to diameter of 18.4 mm and length of 38.2 mm. The nominal connected porosity (measure by water saturation) was found to be around 5 %, 8 % and 5 % for EB_I, EB_II and EB_III samples, respectively.

We performed a series of hydrostatic and triaxial compression experiments in a conventional triaxial set-up. In total, 11 EB_I, 4 EB_II and 5 EB_III samples were deformed and 6 physical thin sections were prepared for microstructural observations.

For a “wet” experiment the sample was first dried in vacuum at 80°C for 48 hours, then saturated with distilled water. Each sample was jacketed with copper foil with a thickness of 0.05 mm and placed between two steel end-plugs, one of which has a piezoelectric transducer (PZT-7, 5.0-mm diameter, 1-MHz longitudinal resonant frequency) on its flat surface, and the other one has a concentric hole for fluid access to the pore pressure system. Heat-shrink polyolefine tubing was used to separate the sample from confining pressure medium (kerosene). For a nominally dry test the sample was dried in vacuum at 80°C for several days. Electric resistance strain gages (TML type PFL-10-11) were attached to the copper jacket to measure the axial and transverse strains. To circumvent the breakage of strain gages, we first filled larger surface pores with an epoxy (BLH SR-4 EPY-150). The sample was then jacketed with copper foil, a hydrostatic pressure of 5 MPa was applied to “season” the copper jacket, strain gages were glued on the jacketed sample in orthogonal directions.

2.2. Mechanical deformation

The jacketed samples were stressed in the conventional triaxial configuration at room temperature. Most of the triaxial experiments were conducted under saturated conditions with a nominal pore pressure maintained at 10 MPa under fully drained conditions. Distilled water was used as pore fluid. The effective pressures (difference between confining pressure and pore pressure) were ranging from 10 MPa to 150 MPa. To compare the mechanical behaviors between wet and dry samples, 3 triaxial experiments under nominally dry conditions were conducted on EB_I samples. The confining pressure was monitored by a strain gage pressure transducer to accuracy of 0.1 MPa, and during triaxial loading it was held constant to within 1%. The axial load was measured with an

external load cell with an accuracy of 1 kN. The axial displacement was servo-controlled at a fixed rate (corresponding to a nominal strain rate of 1.0×10^{-5} s^{-1}).

For saturated experiments, adjustment of a pressure generator kept the pore pressure constant, and the pore volume change was recorded by monitoring the piston displacement of the pressure generator with a displacement transducer (DCDT). The porosity change was calculated from the ratio of the pore volume change to the initial bulk volume of the sample. The displacement was measured outside the pressure vessel with a DCDT mounted between the moving piston and the fixed upper platen. For nominally dry experiments, the volumetric strain was calculated using the relation $\varepsilon_V=2\varepsilon_\perp+\varepsilon_\parallel$, where $\varepsilon_\parallel$ and $\varepsilon_\perp$ are the strains measured in the axial and transverse directions, respectively.

The load, displacement, and strain gage signals were acquired by a 16-bit A/D converter at a sampling rate of 1 s^{-1} with resolutions of 0.3 MPa, 1μm and 10^{-5}, respectively. Uncertainty in strain was estimated to be 2×10^{-4} (when calculated from the DCDT signal) and 10^{-5} (when measured directly by the strain gages). Acoustic emission (AE) recordings were measured by a piezoelectric transducer on the flat surface of a steel spacer attached to the jacketed sample. However, during all the suites of the experiments on Mt. Etna basalt, no significant AE activity was resolved by our system. The AE data were not of use in this study.

2.3. Microstructural analysis

Microstructure of the intact and five deformed samples was studied under optical microscope and scanning electron microscopes (SEM) on thin-sections. Optical microscopy was performed using a Nikon optical polarizing microscope. For SEM

observations, the gold-coated thin-sections were studied using a LEO 1550 microscope with a voltage up to 10 KV. All SEM micrographs presented here were acquired in the backscattered electron mode.

3. Mechanical data

Table 5.1 summarizes the critical stress states on three blocks of Mt. Etna basalt in this study. The convention is adopted that compressive stresses and compactive strains (i.e. shortening and porosity decrease) are positive. The maximum and minimum principal stresses will be denoted by σ_1 and σ_3, respectively. The pore pressure will be denoted by P_p, and the difference between the confining pressure ($P_c = \sigma_1 = \sigma_3$) and pore pressure will be referred to as the "effective pressure" P_{eff}. We summarize in Figure 5.3 the mechanical data in terms of the differential stress $\sigma_1 - \sigma_3$ as a function of axial strain for Mt. Etna samples. Numbers next to each curve indicate the effective pressure maintained during the experiments.

Overall, the mechanical responses for EB_I and EB_III samples are qualitatively similar. The effective pressures conducted on EB_I and EB_III were ranging from 10 MPa to 150 MPa. In all experiments shown in Figure 5.3a and Figure 5.3c, the differential stress attained a peak, beyond which strain softening was observed and the stress dropped to a residual level. The failure modes of EB_I and EB_III are typical of the brittle faulting regime and the failed samples show macroscopic failure oriented at ~30° with respect to the σ_1 direction. The peak stress shows a positive correlation with the effective pressure and mean stress (Table 5. 1). On the other hand, the mechanical responses for EB_II samples illustrate different characteristics. The experiments on EB_II samples were conducted at effective pressures ranging from 50 MPa to 150 MPa

(Figure 5.3b). At P_{eff} = 50 MPa, the stress strain curve first increased and then a peak was reached, after that there was only a relatively small stress drop. The failed sample has a shear band oriented at an angle ~ 30° with respect to σ_1. The peak stress obtained was significantly less than the peak stresses of EB_I and EB_III at the same effective pressures. At P_{eff} = 80 MPa, shear localization was inhibited and the sample appeared to be on the transition from brittle faulting to cataclastic flow. A plateau (Figure 5.3b) on the stress-strain curve was observed with no obvious stress drop. Strain localization was not observed in the failed sample. At effective pressure larger than 80 MPa, the EB_II sample failed by cataclastic flow. As shown in Figure 5.3b, a sample typically shows an initial linear response then instead of stress drop, strain hardening was observed. The failure mode was typical of ductile failure regime (with P_{eff} = 150 MPa). There was no strain localization observed on the sample.

To illustrate the development of inelastic volume change, we show in Figure 5.4 data for the effective mean stress $(\sigma_1 + 2\sigma_3)/3$-P_p as a function of porosity reduction for Etna basalt samples deformed with confinement. Numbers next to each curve indicate the effective pressure maintained during the experiments. For reference, hydrostats for EB_I and EB_III sample were also shown as the dashed curve (Figure 5.4a, 5.4c). The hydrostatic experiments were conducted on EB_I and EB_III sample with an effective pressure up to 450 and 390 MPa, respectively. The hydrostatic response was nonlinear up to a pressure of ~ 205 for EB_I, and 174 MPa for EB_III block. The stress-strain curve became linear afterwards. An inflection point which represents the onset of pore collapse was not observed during the hydrostatic experiment on either EB_I or EB_III block. Due

to the limit quantity of samples, hydrostatic experiment was not conducted on EB_II block.

For the triaxial experiments, the overall behaviors on EB_I and EB_III samples are qualitatively the same. As shown in Figure 5.4a and 5.4c, three distinct stages on the stress-strain curves can be observed. Initially, the porosity decreased due to compaction. Then the porosity appeared to be stable with increasing effective mean stress. After that, it was followed by a reversion to a porosity increase indicating dilation of the pore space. The onset of dilatancy *C'* can be identified as the point where the volume of the triaxially compressed sample became greater than that of the hydrostatically compressed counterpart at the same mean stress. Beyond *C'* the deviatoric stress field induced the pore space to dilate. The differential stress level at *C'* for EB_I and EB_III samples showed positive pressure dependence (Table 5. 1).

As seen in Figure 5.4b, the EB_II sample showed dilation at effective pressure of 50 MPa with *C'* indicated on the curve. At elevated pressures, the samples showed behaviors of cataclastic flow regime that the triaxial curve for a given effective pressure basically coincided with each other for the hydrostatic part up to a critical stress state *C** (Figure 5.4b), beyond which there was an accelerated decrease in porosity which implies that the deviatoric stress field provided significant inelastic contribution to the compactive strain.

To illustrate the water effect on Mt. Etna basalt, we show in Figure 5.5 the comparison of mechanical behaviors on saturated and nominally dry EB_I samples. The experiments were conducted at effective pressures of 10 MPa, 50 MPa and 80 MPa. Stress-strain curves under dry and saturated conditions were plotted in solid and dashed lines, respectively. Overall the mechanical response and failure mode for dry and wet samples

are qualitatively similar at the same effective pressure; a dry sample generally obtained an appreciably higher peak stress than a saturated one. The stress drop during the strain softening was more significant for a dry sample than that of a saturated one and the post-peak behavior was less stable for a dry sample compared with a saturated sample. The slopes of the stress-strain curves of the dry and saturated samples subjected to the same confinement seemed to be more concurrence with increasing effective pressures.

4. Microstructural observations

Thin sections have been prepared on EB_I, EB_II and EB_III samples. Observed under the optical microscope, Mt. Etna basalt includes a number of phenocryst grains that are embedded in a glassy matrix. Macropores occurred as equant voids with average radius around 100 μm are shown in Figure 5.6a as black phase on intact thin section of EB_I sample (Phenocrysts and equant pores were marked by arrows). Figure 5.6b shows a SEM figure of phenocryst grain embedded in matrix. Preexisting microcracks were observed in both phenocryst (indicated by solid arrows) and matrix (indicated by dashed arrows). As shown in Figure 5.6c, many sealed or healed microcracks are presented in the matrix of an undeformed basalt sample. Some of these preexisting cracks extended over tens of microns.

4.1. Brittle faulting on EB_I and EB_III block

Under confinement, healed or sealed cracks were reopened and wing cracks can be observed in SEM observations. Figure 5.7a shows an EB_I sample stressed beyond the onset of dilatancy *C'* under effective pressure of 10 MPa. In the center a microcrack was opened up due to stress and typical wing cracks initiated from the tips. The stress-induced wing cracks oriented subparallel to σ_1 direction. It should been noted that some

micropores (diameter on the order of 10 μm) were present in the matrix as well. However no stress-induced cracks were observed to emanate from the pores, which means the microcracking from the preexisting cracks probably dominates the deformation mechanism on a brittlely failed sample. Another EB_I sample loaded beyond *C'* under effective pressure of 50 MPa was shown as a mosaic micrograph in Figure 5.7b. Under higher confinement, the crack was opened up with a certain width, stress-induced microcracks propagated sub-parallel to the maxim compression axis σ_1 as well. Compared to the sample deformed at an effective pressure of 10 MPa (Figure 5.7a), the stress-induced crack in sample deformed at 50 MPa effective pressure had propagated longer distance (Figure 5.7b).

Figure 5.7c and 5.7d are SEM images of an EB_I sample that was retrieved in the post-peak stage after significant stress drop under an effective pressure of 80 MPa. The through-going shear band sub-parallel to σ_1 direction is shown at the right corner with a width around 40 μm in Figure 5.7c. The boundary of the shear band filled with crushed grains has extended over a thickness of ~ 20 μm. In the proximity of the band, numerous stress-induced microcracks subparallel to σ_1 had propagated and coalesced. The overall pattern of shear localization seems to be controlled by the cracking from preexisting microcracks. In one of the most intensely damaged zones (Figure 5.7d), several different types of stress-induced cracks had coalesced, including cracks that had emanated from pores, as well as an array of intragranular cracks within phenocryst. It should be emphasized that in addition to the pervasive microcracking and comminution, the overall development of shear bands seems to deviate from small phenocryst grains in the matrix. As shown in Figure 5.7d, the shear band was detouring from the phenocrysts, which

means the phenocrysts were acting as obstacles to the shear band propagation. To analyze the partitioning between the phenocrysts that were gone through by the shear band and the ones that were not, we show a mosaic of the SEM figures on the shear fault on EB_I sample (Figure 5.7e). The micrographs cover an area of ~ 3.3 mm^2, with a ratio of the phenocryst gone through by the fault over the total phenocryst within a distance of 100 μm from the band equals 12 %.

Post-peak characteristics of EB_III sample are shown in Figure 5.8. The sample was deformed under effective pressure of 80 MPa. As shown in Figure 5.8a, numerous stress-induced microcracks had propagated and coalesced in the matrix. The cracks aligned sub-parallel to σ_1 direction. In Figure 5.8b we show an area in the proximity of the through-going shear band. Several stress-induced cracks were observed to propagate oriented sub-parallel to σ_1 direction, similar to what observed on EB_I sample (Figure 5.7d), the development of stress-induce crack seems to bypass phenocrysts in the matrix as well. In Figure 5.8c, we compared the shear band areas of the two blocks with the same scale bar. When subjected the same effective pressures, both EB_I and EB_III samples failed by brittle faulting with shear bands sub-parallel to σ_1 direction. However, there are at least two differences can be observed on the SEM figures. First, within a relatively equal area, the percentage of phenocryst in glassy matrix of EB_III sample (on the right) was significantly higher than that of EB_I sample (on the left). Second, the through-going shear band of EB_I sample was much wider than that of EB_III sample. It can be related to the more content of phenocrysts in EB_III block. As the extended cracks seem to bypass from the phenocrystals (Figure 5.7d, 5.8b), more obstacles in the matrix will lead

to the propagation of shear bands more difficult, which in turn results in a much narrower shear localization shown on EB_III sample.

4.2. Inelastic compaction on EB_II block

In Figure 5.9, we show samples of EB_II block that were deformed beyond *C**. In Figure 5.9a, stress-induced cracks in EB_II sample deformed at effective pressure of 80 MPa were observed. They aligned sub-parallel to σ_1 direction and deviated from the phenocrysts in a pattern akin to what observed in Figure 5.7d and 5.8b. As there are significant amount of microcracks in the starting material of Etna basalt, it is unclear whether the stress-induced cracks observed here emanate from pores or are re-opened from preexisting ones. Unlike EB_I and EB_III samples, there are more pores embedded in the EB_II block. As shown in Figure 5.9b, several collapsed pores in different sizes can been observed in the sample deformed at 80 MPa effective pressure. In a zoomed in figure, a relatively large equant pore (with a diameter around 330 μm) was collapsed with an asymmetric distribution damage. Numerous microcracks emanated from the pores and coalesced especially in the bottom part. The damage zone was about 70 μm which is relatively narrow compared to the pore size. The surrounding area beyond the damage zone seemed to be very intact.

Figure 5.9c and 5.9d are SEM images of an EB_II sample deformed at effective pressure of 150 MPa. In Figure 5.9c, a relatively equant pore was collapsed with a radius on the order of 100 μm. Intensive damage zone filled with numerous crushed grain can be observed around the circumference. The damage extended over an average thickness of 100 μm and the intensity decayed with radial distance. The area beyond the damage area seemed to be undeformed. The collapsed pore shown in Figure 5.9c has a smaller

radius while its damage zone has propagated further distance compared to the zoomed in pore in Figure 5.9b. Besides the equant pores, an elongated pore with an average radius around 300 μm is shown in Figure 5.9d. The collapsed pore was filled with crushed grains and numerous microcracks emanated from the pore and coalesced. The overall pore collapse pattern of EB_II sample deformed at 150 MPa effective pressure was far more significant than what observed in sample deformed at an effective pressure of 80 MPa. The pervasive pore collapse observation suggests that the pores rather than microcracks take the dominate role in the cataclastic flow regime.

5. Discussion

Quantitative extrapolations of the laboratory data to crustal settings would require a fundamental understanding of the micromechanics of the brittle-ductile transition, which cannot be formulated without a realistic conception of the pore geometry and defect structure. We have conducted saturated experiments on all three blocks of Etna basalt with effective pressures ranging from 10 MPa to 150 MPa. The drained conditions were maintained during all experiments which means that a reasonable amount of connected porosity was still open at relatively high pressure. To investigate the development of dilatancy and brittle faulting, we will apply a sliding wing crack model on the data of EB_I and EB_III samples. Comparisons between the three blocks of Mt. Etna basalt will be employed. The effect of water and phenocryst will be discussed. With increasing porosity, shear-enhanced compaction is possible on EB_II samples. The porosity effect will be investigated.

5.1 Dilatancy and brittle faulting failure

All experiments conducted on EB_I and EB_III samples in this study show typical of brittle failure regime. Dilatancy has been observed to arise from intragranular and intergranular cracking with a preferred orientation parallel to the maximum principal stress σ_1. Both the peak stress and dilatancy as functions of effective pressure follow an approximately linear trend (Figure 5.11a, b). A micromechanical model for brittle failure that predicts such a linear pressure dependence is the sliding crack model (Figure 5.10) [*Horii and Nemat-Nasser*, 1986; *Ashby and Sammis*, 1990; *Kemeny and Cook*, 1991; *Baud et al*., 2000a]. The model considers the growth of "wing cracks" that initiate from tensile stress concentration at the tips of preexisting cracks (with initial length 2*c* and oriented at angle γ to σ_1) undergoing frictional slip. The fracture mechanics is such that increasing the stress causes the wing crack to propagate along a curved path and ultimately to reach a stable orientation parallel to the direction of σ_1. The onset of dilatancy is corresponding to the state of the initiation of wing cracks. With the accumulation of such anisotropic cracking distributed throughout the rock, the damage will ultimately attain a critical state at which the multiplicity of cracks coalesce to develop a shear band, which corresponds to the state of peak stress. A recent study by *Zhu et al.* [2010b] has investigated the micromechanical basis for the Coulomb failure parameters with reference to the sliding crack model. They noted that the fracture toughness at the onset of dilatancy is different from the one at the stage of peak stress. Here we apply wing crack model to Mt. Etna data (EB_I and EB_III) in the same manner and followed their notation. We will use K_{IC} and K_C to denote the fracture toughness at the onset of dilatancy and at peak stress, respectively. In Figure 5.11a and 5.11b, we

summarized the application of sliding wing crack model to our data. The wing crack microparameters (the initial damage D_0, friction coefficient μ, and normalized fracture toughness $K_{IC}/(\pi c)^{1/2}$ and $K_C/(\pi c)^{1/2}$) used to fit EB_I and EB_III are complied in Table 5. 2. The friction coefficients inferred for EB_I and EB_III are 0.5 and 0.65, respectively. The higher μ value of EB_III samples suggests that the matrix of EB_III block is stronger than that of EB_I block. The initial damage D_0 for EB_I and EB_II are 0.14 and 0.18, respectively. A larger D_0 in EB_III block means the initial damage in an intact EB_III sample is higher, which may have been resulted from longer wing cracks, higher number of preexisting cracks or both. As the cracks ($2c$) in EB_III block seem to have similar length with those in EB_I block, the higher D_0 may suggest that there are probably more preexisting cracks in the EB_III block. The finding on D_0 is consistent with the inferred microcrack porosities from hydrostatic curves on EB_I and EB_III blocks (Figure 5.4). According to *Walsh's* [1965] analysis, the microcrack porosity for EB_I and EB_III are 0.6 % and 0.9 %, respectively. It suggests the EB_III block contains 1.5x more microcrack porosity than EB_I block. The normalized fracture toughness at peak stress ($K_C/(\pi c)^{1/2}$) obtained for EB_III block (55 MPa) is less than that of EB_I block (82 MPa). As mentioned before, the cracks ($2c$) in EB_III block were not observed to be twice longer than those in EB_I block, it suggests that the fracture toughness K_C of EB_I block would be 1.5x stronger than that of EB_III block.

According to *Zhu et al*. [2010b], the uniaxial compressive strength based on sliding wing crack model has been derived as:

$$\frac{\sigma_u}{K_C/\sqrt{\pi c}} = \frac{1.346}{\sqrt{1+\mu^2}-\mu} D_0^{-0.2564} \tag{1a}$$

where σ_u, K_c, c, μ and D_0 represent unconfined compressive strength, fracture toughness of peak stress, wing crack length, friction coefficient and initial damage parameter, respectively. The initial damage parameter can be expressed as: $D_0 = \pi(c\cos\gamma)^2 N_A$, where N_A is the number of sliding cracks per unit area initially present and a value of $\gamma = 45°$ is assumed in equation (1a) for all our calculations presented here. Substitute the expression of D_0 into equation (1a), the uniaxial compressive strength is given by:

$$\sigma_u = \frac{1.346K_C/\sqrt{\pi c}}{\sqrt{1+\mu^2}-\mu}(\pi(c\cos\gamma)^2 N_A)^{-0.2564} = A \cdot N_A{}^{-0.2564} c^{-1.013} \quad (1b)$$

with

$$A = \frac{1.346K_c\pi^{-0.7564}\cos\gamma^{-0.5128}}{\sqrt{1+\mu^2}-\mu}$$

Combined with Coulomb failure parameters, *Zhu et al*. [2010b] also derived an analytic approximation for the internal friction coefficient:

$\tan\varphi \approx -0.06 - \log\sqrt{D_0} + (0.90 + 0.14D_0)\mu$. Wing crack parameters can be obtained alternatively from a contour plot (Figure 5.11c). As shown in Figure11c, the contours of tanφ are generated in parameter spaces of friction coefficient μ and initial damage D_0. Using the values of μ and tanφ that respectively inferred from dilatancy and peak stress, one can locate the rock point on the contour plot, from which the corresponding value of D_0 can be read off from horizontal axis. $Kc/(\pi c)^{1/2}$ can then be inferred from the above equation (1a). In Figure 5.11c, we show the data of Mt Etna (EB_I and EB_III) and also include other rock data for reference. As seen in the plot, Etna basalt has relatively low values of D_0 and high values of μ compared to other rocks. The microparameters for EB_I and EB_III so obtained are compiled in Table 5.2. It should be noted that the

application of this contour method requires the knowledge of tanφ (inferred from peak stress data) and μ (inferred from dilatancy data). A comprehensive set of *C'* data is therefore very important to infer all the other microparameters.

5.2 Effect of water

To interpret our laboratory data on water-weakening effects in the brittle faulting regime, we adopted the modified "sliding wing crack" model and followed the same procedure as *Baud et al*. [2000b]. For a given rock the initial damage D_0 can be considered to be identical in both dry and saturated conditions. Due to environmental interaction, the fracture toughness in vacuum may be significantly higher than that in the presence of water. Along the fluid-solid interface the friction coefficient may also be reduced by lubrication due to the fluid. To account for these differences, fracture toughness of peak stress and friction coefficient are replaced with values of K_{C_d} and μ_d that are considered to be appropriate for a nominal dry rock. Following the similar process as discussed in section 5.1, we inferred the values of $K_{C\_d} / (\pi c)^{1/2}$ = 102 MPa and μ_d = 0.55 under nominal dry conditions. The ratio of K_{C_d} / K_C and μ_d / μ are therefore 1.2 and 1.1, respectively. It should be noted that dilatancy data were not measured on nominal dry EB_I block. However, with a constrained D_0 value, we consider our microparameters inferred from peak stress data are valid. Future experiments of *C'* data will provide better constraints to microparameters on nominal dry samples. We did not apply the graphical method to dry EB_I block due to the absence of dilatancy data. The microparameters obtained by sliding wing crack model are compiled in Table 5.2.

According to *Baud et al*. [2000b], the ratio of K_{C_d}/K_C was found to be from 1.02 to 1.13 on four different sandstones with porosities ranging from 11 % to 35 %. Their data also indicated the friction coefficients μ were somewhat lower in the presence of water. Based on their data in the brittle failure regime, they found the ratio of $\mu_{\_d}/\mu$ for Darley Dale and Berea sandstones were 1.12 and 1.1, respectively. Besides sandstones, the water weakening effect was also studied on igneous rocks [*Lajtai et al.*, 1987; *Bauer et al*., 1981]. *Lajtai et al.* [1987] directly measure the unconfined compressive strength and fracture toughness of Lac du Bonnet granite under nominally dry and saturated conditions. They showed that both the unconfined strength and fracture toughness were decreased ~ 10 % in the presence of water, which corresponding to a ratio of K_{C_d}/K_C around 1.1. Water-saturated data on three igneous rocks (Charcoal Granodiorite, Mt. Hood Andesite and Cuerbio Basalt) were compared to their room-dry counterparts by *Bauer et al*. [1981]. In their high temperature experiments, they illustrated that while no water effect was found on granodiorite, the water-weakening were observed on both andesite and basalt, with an average weakening factor on strength is ~ 4 on andesite and ~ 1.5 on basalt. Taken together, the chemical influence of water on the mechanical behavior of our Mt. Etna basalt samples was found to be consistent with previous studies on both sandstones and igneous rocks, which indicates that the operative mechanism of water effect could be similar as well. The weakening effect in the presence of water could be attributed from chemsorption or stress corrosion effects at crack tips that reduce fracture strengths, the lowering of critical resolved shear stresses for dislocation gliding and the reductions of the specific surface energy [*Bauer et al*., 1981; *Baud et al*., 2000b].

5.3 Effect of phenocryst

In Figure 5.12 we compiled peak stress (EB_I and EB_III) and yield stress (EB_II) data for saturated samples of Mt. Etna basalt. For comparison, peak stress data on brittle failed dry Yakuno basalt with a porosity of 7 % were also shown [*Shimada*, 2000]. The peak stress as a function of effective pressure on EB_I and EB_III blocks follows an approximately linear trend. It is of interest to compare the development of peak stress between the blocks. At lower effective pressures (10 MPa), EB_III block seems to be weaker than EB_I block. With increasing effective pressures, the strength of EB_III was increasing and was almost the same with EB_I sample at an effective pressure of 100 MPa. At 150 MPa effective pressure, EB_III sample even reached a higher strength value. As both EB_I and EB_III basalt have the same connective porosity of 5 %, the difference in content of phenocryst may play a dominate role in the development of stress. One possible explanation is that EB_III samples contain more microcrack porosity which suggests there are more preexisting cracks in the block. At low effective pressures, the larger number of preexisting cracks would result the cracks propagate and coalesce more easily, which in turn led to a lower peak stress. With increasing effective pressures many preexisting cracks would be closed due to the stress, the matrix with phenocryst would be then stronger. As shown in Figure 5.8b, the development of shear band tends to avoid phenocrysts in matrix. The more phenocrysts in matrix would therefore make a sample more difficult to develop a macroscopic band. These findings on phenocryst effect are in agreement with what inferred according to wing crack model in 5.1, where the higher μ, and D_0 values suggest that EB_III block has a stronger matrix which embedded with probably more preexisting cracks compared to EB_I basalt.

5.4 Effect of porosity

The strengths of EB_II samples are observed to be significantly weaker than those of EB_I and EB_III blocks (Figure 5.12). EB_II block has a connected porosity of 8 %, which is only 3 % more compared to the other two blocks (EB_I and EB_III). According to microstructural observations, the difference of porosity seems to mainly come from equant pores that are embedded in EB_II sample. As shown in the Figure 5.12, the mechanical behavior of EB_II sample was typical of brittle failure regime at an effective pressure of 50 MPa. When compared to EB_I and EB_III blocks subjected to the same pressure condition, EB_II block shows a much lower peak stress, which indicates the pores have significant influence on the sample strength. While shear-enhanced compaction was not observed on EB_I and EB_III samples in all experiments with effective pressure up to 150 MPa, cataclastic regime was observed on EB_II sample. It suggests that the mechanical behaviors and failure modes are very sensitive to porosity in Mt. Etna basalt.

Shimada [1991] has done microstructural observations on hydrostatic compressed Yakuno basalt at relatively high confining pressures. The samples in his study were fine-grained holocrystalline intergranular olivine basalt from Kyoto, Japan. They have a porosity of 7 % which is similar to our EB_II basalt. While pore collapse was not observed on either EB_I or EB_III blocks, collapsed pores in different sizes were identified on EB_II block (Figure 5.9). The SEM micrographs were similar to what *Shimada* found on Yakuno basalt. As shown in Figure 5.13, the pore has been collapsed with surrounding grains deformed with microcracks and crushed, filling up the pores space. However it should be noted that the experiment was conducted at a very high

confining pressure of 1950 MPa. Microstructural observations on EB_II and Yakuno basalt suggest that the inelastic compaction is associated with pores.

It is of interest to model the pore structure in basalt. *Adelinet et al*. [2010] have found that the pore structure of basalt can be characterized by a dual porosity with microcracks and equant pores on a block of basalt extracted from Iceland (Figure 5.2). The dual porosity medium was also adopted by *Zhu et al*. [2010a] to analyze the inelastic compaction in porous limestones. There are similarities in the pore structures between basalt and porous limestones. First, the pores appeared to be relatively equant and are embedded in matrix for both rocks. Second, both the pore structure can be treated as dual porosity medium to a certain degree. Based on the similarities, we considered our porous basalt as a bimodal porosity medium. As illustrated in Figure 5.14a, the representative volume element is made up of an equant pore with radius a surrounded by an effective medium made up of many preexisting cracks of length c^*. Microstructural observations suggest that brittle failure in unconfined condition on a porous rock is associated with pore-emanated cracks. A micromechanical model that captures aspects of failure process is developed recently by *Zhu et al*. [2010a], the unconfined compressive strength of the bulk sample can be expressed by:

$$\sigma_u = \frac{1.325}{\Phi^{0.414}} \frac{K_{IC}}{\sqrt{\pi a}} \tag{2}$$

According to equation (2) together with experimental data, normalized fracture toughness of EB_II block can be inferred to be 21.5 MPa. The inferred value of $K_C / (\pi a)^{1/2}$ is 3.8 and 3.0 times smaller compared with EB_I and EB_III block, respectively. As discussed before, the crack lengths in EB_I and EB_III blocks are relatively same while the fracture toughness in EB_I is probably 1.5x stronger than that in EB_III block. If we assume the

fracture toughness of EB_II block is the same with EB_III, then the average equant pore size in EB_II would be 9 times larger compared to the crack length in EB_I and EB_III block. Based on microstructural observations, the cracks in EB_I and EB_III block appeared to be on the order of 10 μm, and the equant pores in EB_II block were observed to be on the order of 100 μm. Hence to a first approximation, the inferred value of normalized fracture toughness can be considered to be in agreement with microstructural observations. However, it should be noted that the unconfined compressive strength might exhibit huge variability due to the heterogeneous characteristic of the porous EB_II block.

Under a remotely applied hydrostatic stress, the local stress field in the effective medium surrounding an equant pore is analogous to unconfined condition [*Timoshenko and Goodier*, 1951]. Brittle failure would initiates when the local stresses satisfy failure criterion. In our dual porosity model, the brittle failure is assumed to occur in an effective medium that made up solely of preexisting cracks, without any involvement of the equant pore. As the effective medium is made of microcracks, a peak stress would be reached by the propagation and coalescence of wing cracks. The uniaxial compressive strength formed by coalescence of wing cracks in a bulk sample under unconfined condition has been derived as equation (1b). If we apply the derived approximation to the brittle failure in the effective medium, then the unconfined compressive strength σ_u^* is given by:

$$\sigma_u^* = A^* \cdot N_A^{*-0.2564} c^{*-1.013} \tag{3}$$

with

$$A^* = \frac{1.346 K_c^* \pi^{-0.7564} \cos\gamma^{-0.5128}}{\sqrt{1+\mu^{*2}} - \mu^*}$$

where c^* and N_A^* denote the wing crack length and the number of cracks per unit area in the effective medium. As the fracture toughness and friction coefficient can be taken as characteristic parameters, hence they are assumed to remain the same values in the effective medium, that suggests $A^* = A$. According to *Zhu et al.* [2010a], identical predictions for the pore collapse pressure were obtained using Mohr-Coulomb or Drucker-Prager criterion:

$$P^* = \frac{2}{3}\sigma_u^* \tag{4a}$$

If we compare equation (1b) and (3) and assume K_c and μ the same in both effective medium and the bulk sample, then we will have the ratio of σ_u^* / σ_u as:

$$\frac{\sigma_u^*}{\sigma_u} = \frac{A \cdot N_A^{*-0.2564} c^{*-1.013}}{A^* \cdot N_A^{-0.2564} c^{-1.013}} = \left(\frac{N_A^*}{N_A}\right)^{-0.2564} \left(\frac{c^*}{c}\right)^{-1.013} \tag{4b}$$

By substituting equation (4b) into (4a), the critical pore collapse pressure can be illustrated as:

$$P^* = \frac{2}{3}\sigma_u \left(\frac{N_A^*}{N_A}\right)^{-0.2564} \left(\frac{c^*}{c}\right)^{-1.013} \tag{4c}$$

There are several key points should be noted. First, as discussed in 5.1, peak stress σ_u in equation (1b) is formed by the propagation and coalescence of wing cracks. While in our dual porosity model, the uniaxial compressive strength as expressed in equation (2), is obtained by the coalescence of cracks that emanated from the equant pore. Hence the σ_u in equation (4c) can not be considered as the uniaxial compressive strength of bulk medium in our representative volume element by default. Now if we consider another representative volume element as a single porosity medium that made up of solely microcracks with crack length of c (Figure 5.14b), then equation (4b) can be viewed as

the ratio of uniaxial compressive strength of the effective medium in a dual porosity model and the UCS of the bulk medium in a single porosity model. Second, as the bimodal representative volume element is made up of both pore and microcracks. The volume of the effective medium in a dual porosity model is therefore smaller compared to the bulk medium in a single porosity model, which suggests the number of cracks per unit area in effective medium (N_A^*) would be larger than that in bulk medium (N_A). However, as mentioned before the pores embedded in EB_II block only represent a small fraction of the total porosity. Hence the difference between N_A^* and N_A would be relatively small. If we further assume $N_A \approx N_A^*$, P^* would represent an upper bound value that can be expressed as:

$$P^* \approx \frac{2}{3}\sigma_u \left(\frac{c^*}{c}\right)^{-1.013} \tag{5}$$

As discussed above, σ_u and c in equation (5) represent the uniaxial compressive strength and wing crack length of bulk medium in a single porosity model (Figure 5.14b), respectively. P^* and c^* represent the critical pore collapse pressure of bulk medium and wing crack length of effective medium in a dual porosity model (Figure 5.14a), respectively. It is difficult to elucidate relationships between P^* and σ_u in two different representative volume elements. Hence a plausible assumption was made that the uniaxial compressive strength in bulk medium was assumed to have the same macroscopic values despite the fundamentally different micromechanics. Hence to a first order approximation, macroparameters P^* and σ_u in equation (5) can be taken as the critical pore collapse pressure and uniaxial compressive strength for the bulk medium in a dual porosity model. The microparameter c^* still represents the wing crack length in the effective medium in a

bimodal medium (Figure 5.14a), and c represent the crack length of bulk medium in a single porosity medium (Figure 5.14b).

In Figure 5.14c, we plot the critical pore collapse pressure as a function of uniaxial compressive strength for EB_II and Yakuno basalt. For comparisons, we also include the data on tuff samples. Due to the limit quantity of porous samples, we don't have hydrostatic data on EB_II block. The P^* is inferred to be greater than 300 MPa base on other experiments conducted on EB_II, as shown by the upper arrow in Figure 5.13c. Slopes of P^* vs. σ_u with different ratios of c^* / c are plotted as dashed lines. The assumption of $N_A \approx N_A^*$ in equation (5) implies that slopes with fixed crack length ratio represents an upper bound. A ratio of $c^* / c = 1$ suggests wing cracks have the same length in both effective medium (bimodal porosity) and the corresponding bulk medium (single porosity). As shown in Figure 5.14c, all the points on basalt and tuff locate above the slope with $c^* / c = 1$, which implies the effective medium is significantly stronger than the corresponding bulk medium. The rock data in Figure 5.14c can be bracketed by two slopes with $c^* / c = 0.5$ and $c^* / c = 0.1$, which suggests that if indeed the brittle failure in the effective medium is associated with propagation and coalescence of wing cracks, then the wing crack lengths in the effective medium are inferred to be 2x to 10x shorter than those in the corresponding bulk medium. Basalt data on EB_II and Yakuno can be approximately fitted by a slope with $c^* / c = 0.2$, that suggests the crack lengths are 5x shorter in the effective medium than those in the corresponding bulk medium.

Under higher effective pressure (150 MPa), shear-enhanced compaction was observed on EB_II sample with a porosity of 8 %. It implies that a very small increase of porosity in Etna basalt could result significant differences in failure behaviors. It also suggests that

inelastic compaction associated with pore collapse could be an important feature in volcanic environments. As the mechanical behaviors on Etna basalt are similar to those on sandstones and limestones. It is possible to observe a cap mapped by C^* data (onset of shear-enhanced compaction) in basalt similar to the elliptical curves mapped by the data of sandstones and limestones. However, we do not have enough data to defend the trend due to limit quantity on EB_II sample. As failure mode is observed to be very sensitive to porosity in Etna basalt. It might be better to conduct experiments on an even more porous block. Systematic studies on the mechanical behaviors and microstructural observations on a more porous basalt will be very useful to understand the effect of pores in the future.

5. Conclusions

In this study, we have demonstrated the mechanical behaviors and failure modes observed on Mt. Etna basalt. For EB_I and EB_III samples with a porosity of 5 %, dilatancy was observed as a precursor to the occurrence of brittle faulting in triaxial experiments conducted at effective pressures ranging from 10 MPa to 150 MPa. As a function of pressure, two primary failure modes were identified on EB_II samples with a porosity of 8 %. At relatively low pressures ($\leq$ 50 MPa), the samples failed by brittle failure similar to what observed on EB_I and EB_III block. At relatively high pressures ($\geq$ 150 MPa), the samples failed by cataclastic flow associated with shear-enhanced compaction and strain hardening. Porosity exerts significant influence over the elastic, inelastic and failure properties of Mt. Etna basalt.

Evolution of microstructural damage was described for EB_I, EB_II and EB_III samples. According to optical microscopy and SEM observations, the defect structures of the two compact basalt blocks (EB_I and EB_III) were dominated by preexisting

microcracks. In brittle faulting, wing cracks that initiated from preexisting crack tips were oriented parallel to σ_1 direction and their length increased with loading approaching the peak stress. The microcracks propagated and coalesced and ultimately formed a macroscopic shear band. Phenocrysts embedded in glassy matrix of Etna basalt seem to act as barriers to the development of crack coalescence and localization. The intensity of cataclasis was observed to decrease with distance from the shear zone. Besides shear localization, pore collapse was observed in EB_II samples that failed in cataclastic flow regime. Numerous cracks emanated from the pores and coalesced. Crushed fragments fell into relatively large cavities. At relatively high effective pressures ($\geq$ 80 MPa), the inelastic deformation seems to be dominated by pore collapse.

Wing crack model was employed to interpret the micromechanics of the samples failed by brittle regime (EB_I and EB_III block). Microparameters were inferred and evaluated on brittle failed EB_I and EB_III samples. To illustrate water effect, mechanical behaviors were compared between nominal dry and saturated samples. Our data indicated that the friction coefficients for sliding on preexisting crack surfaces were somewhat lower in the presence of water and this effect also contributed to the reduction of the brittle strength. The comparison between EB_I and EB_III samples illustrated the effect of phenocryst. The finding on phenocrysts effect is consistent with the inferred higher friction coefficient for EB_III block from sliding wing crack model. With only a few percent increase in porosity, shear-enhanced compaction was observed on EB_II block. The uniaxial strength on EB_II block was analyzed by pore-emanated cracking model. This porous block was interpreted as a dual porosity medium with porosity partitioned between equant pore and pre-exisiting cracks. As most basalt could have a

porosity similar or higher than 8 %, our data suggest compaction could be an important feature in volcanic environments. More data on porous basalt are desirable to defend a failure envelop due to the heterogeneous distribution of pores.

Acknowledgments

We are grateful to Sergio Vinciguerra who kindly provided the blocks of Mt. Etna basalt. We want to thank Jim Quinn for assistance with SEM measurements. This research was partially supported by the Office of Basic energy Sciences, Department of Energy.

References

Adelinet, M., J. Fortin, Y. Guéguen, A. Schubnel, and L. Geoffroy (2010), Frequency and fluid effects on elastic properties of basalt: Experimental investigations, *Geophys. Res. Lett.*, *37*(2), L02303, doi: 10.1029/2009gl041660.

Ashby, M., and C. Sammis (1990), The damage mechanics of brittle solids in compression, *Pure and Applied Geophysics*, *133*(3), 489-521.

Azzaro, R., M. Barbano, B. Antichi, and R. Rigano (2000), Macroseismic catalogue of Mt. Etna earthquakes from 1832 to 1998, *Acta Vulcanologica*, *12*(1/2), 3-36.

Baud, P., A. Schubnel, and T. Wong (2000a), Dilatancy, compaction, and failure mode in Solnhofen limestone, *Journal of Geophysical Research*, *105*(B8), 19289-19303, doi: 10.1029/2000JB900133.

Baud, P., W. Zhu, and T.-f. Wong (2000b), Failure mode and weakening effect of water on sandstone, *J. Geophys. Res.*, *105*(B7), 16371-16389, doi: 10.1029/2000JB900087.

Bauer, S., M. Friedman, and J. Handin (1981), Effects of water-saturation on strength and ductility of three igneous rocks at effective pressures to 50 MPa and temperatures to partial melting, The 22nd U.S. Symposium on Rock Mechanics (USRMS),p73-78.

Brace, W., B. Paulding Jr, and C. Scholz (1966), Dilatancy in the fracture of crystalline rocks, *Journal of Geophysical Research*, *71*, 3939-3954.

Chouet, B. A. (1996), Long-period volcano seismicity: its source and use in eruption forecasting, *Nature*, *380*(6572), 309-316, doi: 10.1038/380309a0.

Heap, M. J., S. Vinciguerra, and P. G. Meredith (2009), The evolution of elastic moduli with increasing crack damage during cyclic stressing of a basalt from Mt. Etna volcano, *Tectonophysics*, *471*(1-2), 153-160, doi: 10.1016/j.tecto.2008.10.004.

Horii, H., and S. Nemat-Nasser (1986), Brittle failure in compression: splitting, faulting and brittle-ductile transition, *Philosophical Transactions for the Royal Society of London*, *319*, 337-374.

Kemeny, J., and N. Cook (1991), Micromechanics of deformation in rocks, in *Toughening mechanisms in quasi-brittle materials*, edited by S. P. Shap pp. 155-188, Klewer Academic.

Lajtai, E. Z., R. H. Schmidtke, and L. P. Bielus (1987), The effect of water on the time-dependent deformation and fracture of a granite, *International Journal of Rock Mechanics and Mining Sciences & Geomechanics Abstracts*, *24*(4), 247-255.

PATANE, et al. (2004), Mt. Etna volcano: A seismological framework, in *Mt. Etna: Volcano Laboratory*, edited by A. Bonaccorso, S. Calvari, M. Coltelli and S. Falsaperla,143, pp. 147–166, American Geophysical Monograph.

Shimada, M. (1991), Comment on``The effects of pressure and porosity on the micromechanics of the brittle-ductile transition in quartzite"by Greg Hirth and Jan Tullis, *Journal of Geophysical Research*, *96*, 11877-11879.

Shimada, M. (2000), *Mechanical behavior of rocks under high pressure conditions*, 178 pp., A.A. Balkema, Netherlands.

Stanchits, S., S. Vinciguerra, and G. Dresen (2006), Ultrasonic Velocities, Acoustic Emission Characteristics and Crack Damage of Basalt and Granite, *Pure and Applied Geophysics*, *163*(5), 975-994, doi: 10.1007/s00024-006-0059-5.

Timoshenko, S., and J. Goodier (1951), *Theory of Elastic*, 567 pp., McGraw-Hill, New York.

Vinciguerra, S. (2002), Damage mechanics preceding the September-October 1989 flank eruption at Mount Etna volcano inferred by seismic scaling exponents, *Journal of Volcanology and Geothermal Research*, *113*(3-4), 391-397, doi:10.1016/S0377-0273(01)00274-8.

Vinciguerra, S., V. Latora, S. Bicciato, and R. Kamimura (2001), Identifying and discriminating seismic patterns leading flank eruptions at Mt. Etna Volcano during 1981-1996, *Journal of Volcanology and Geothermal Research*, *106*(3-4), 211-228, doi:10.1016/S0377-0273(00)00274-2.

Vinciguerra, S., C. Trovato, P. Meredith, and P. Benson (2005), Relating seismic velocities, thermal cracking and permeability in Mt. Etna and Iceland basalts, *Int J Rock Mech Min*, *42*(7-8), 900-910, doi:10.1016/j.ijrmms.2005.05.022.

Walsh, J. (1965), The effect of cracks on the compressibility of rocks, *Journal of Geophysical Research*, *70*, 381-389.

Zhu, W., P. Baud, and T.-f. Wong (2010a), Micromechanics of cataclastic pore collapse in limestone, *J. Geophys. Res.*, *115*(B4), B04405, doi: 10.1029/2009JB006610.

Zhu, W., P. Baud, and T. Wong (2010b), Micromechanical basis for the Coulomb failure parameters, *Earth and Planetary Science Letters*, *submitted*.

Table 5.1. Compilation of mechanical data on three blocks of Etna basalt samples

Effective Pressure σ_1-P_p, MPa	Onset of Dilatancy, MPa		Peak Stress, MPa		Critical Yield Stress, MPa	
	Effective Mean Stress $(\sigma_1+2\sigma_3)/3$-P_p	Differential Stress σ_1-σ_3	Effective Mean Stress $(\sigma_1+2\sigma_3)/3$-P_p	Differential Stress σ_1-σ_3	Effective Mean Stress $(\sigma_1+2\sigma_3)/3$-P_p	Differential Stress σ_1-σ_3
			EB_I			
10	24.24	42.70	104.28	280.46	-	-
20	51.51	94.79	130.49	329.08	-	-
30	63.24	98.40	163.73	399.14	-	-
50	94.38	132.39	217.54	500.41	-	-
80	137.79	173.81	267.10	560.29	-	-
100	151.43	154.18	320.19	657.53	-	-
150	256.55	317.29	401.56	753.07	-	-
			EB_II			
50	91.47	130.22	171.24	364		
80	-	-	-	-	196.12	347.25
150	-	-	-	-	287.46	411.27
200	-	-	-	-	441.99	726.97
			-	-		
			EB_III			
10	24.35	41.31	85.46	223.96	-	-
50	85.39	108.02	194.61	433.57	-	-
80	139.42	180.84	260.74	543.25	-	-
100	172.58	218.54	313.25	639.90	-	-
150	267.37	352.16	417.43	798.27	-	-

Table 5.2. Summary of parameters inferred from application of wing crack model

Rock name	μ (μ_d)	D_0	$K_C/(\pi c)^{1/2}$ ($K_{C\_d}/(\pi c)^{1/2}$), MPa	D_0 (Contour method)	$K_C/(\pi c)^{1/2}$, MPa (Contour method)
EB_I	0.5	0.14	82	0.14	80.24
EB_III	0.65	0.18	55	0.18	55.07
EB_I (dry)	(0.55)	0.14	(102)	-	-

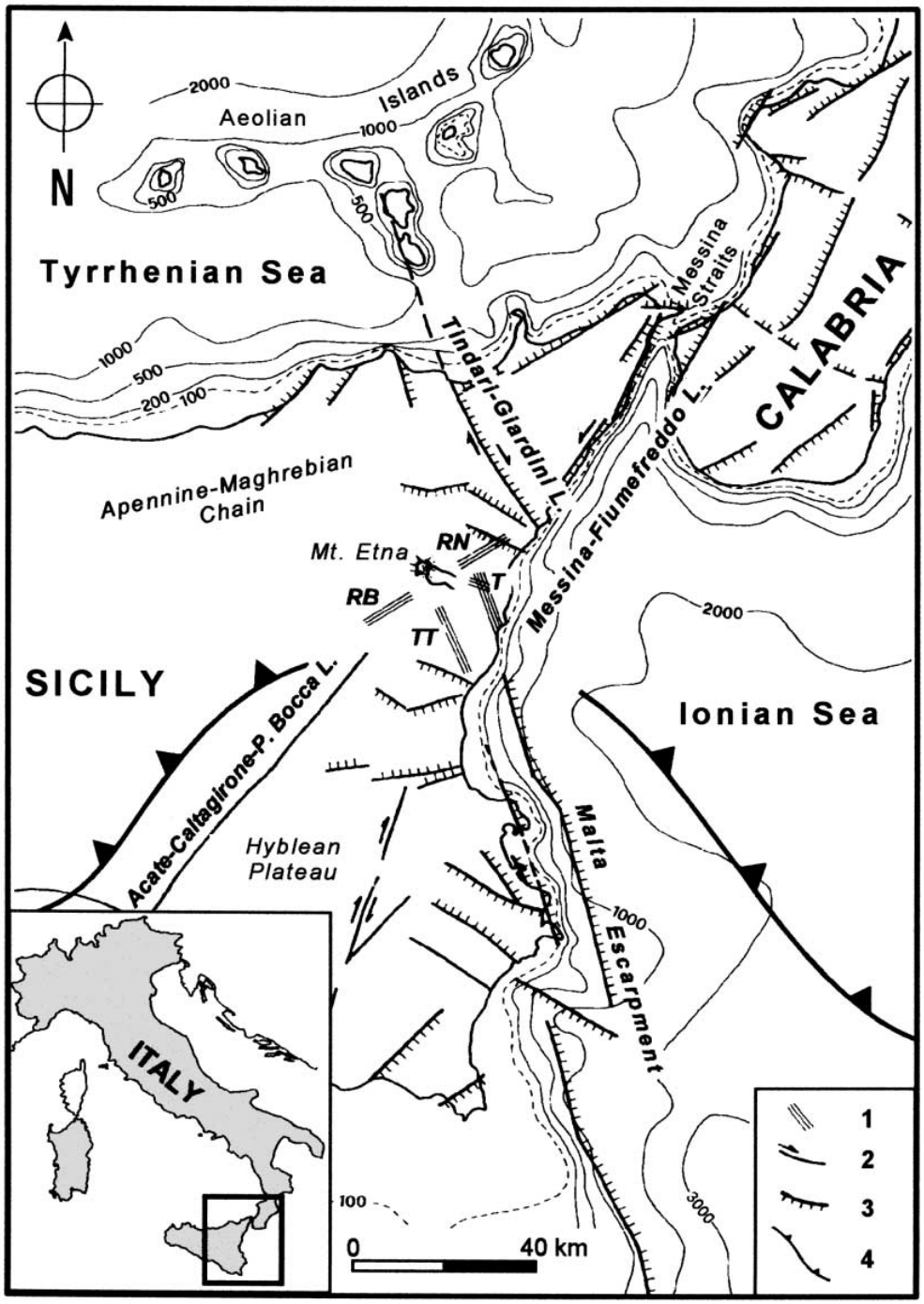

Figure 5.1. Tectonic sketch map of eastern Sicily (from *Vinciguerra et al*., 2001).

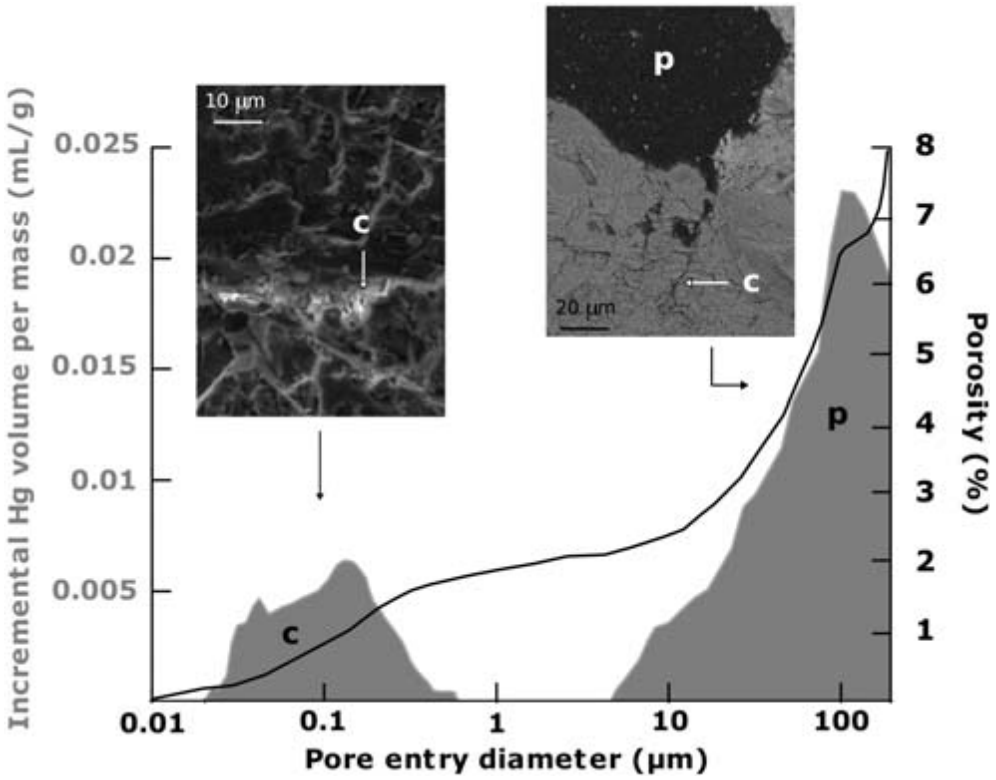

Figure 5.2. Mercury Intrusion Porosimetry data associated to electronic microscopy pictures on a block of Iceland basalt with total porosity of 8% (from *Adelinet et al*., 2010). p and c represent spherical pore and crack, respectively.

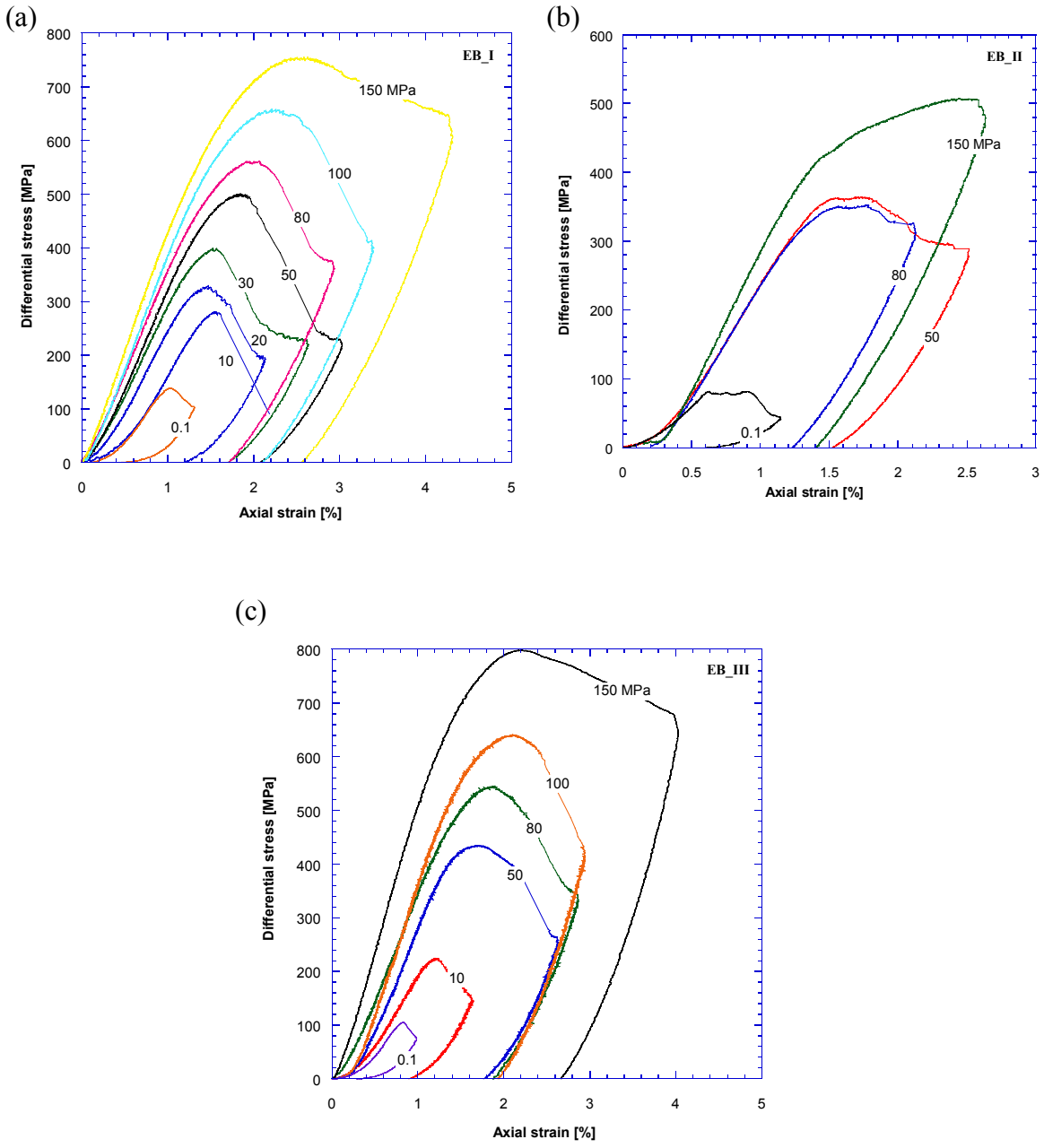

Figure 5.3. Mechanical data for wet experiments on (a) EB_I block (b) EB_II block, and (c) EB_III block of Etna basalt. Differential stress is plotted versus axial strain. Numbers next to each curve indicate the effective pressure maintained during the experiment. Samples conducted at uniaxial condition were not saturated.

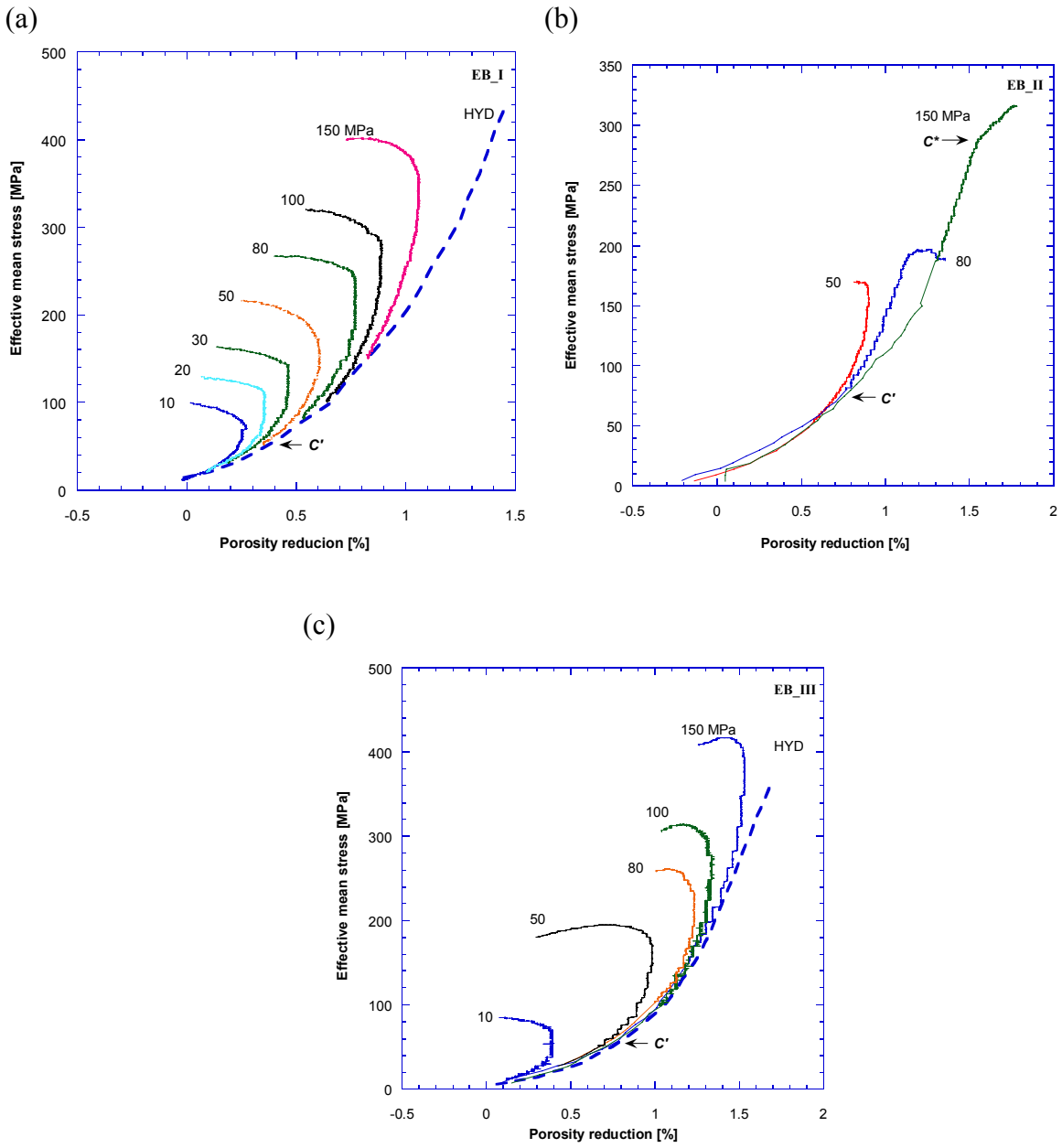

Figure 5.4. Effective mean stress is plotted as a function of porosity reduction on (a) EB_I block (b) EB_II block, and (c) EB_III block of Etna basalt. For reference, hydrostatic data are shown as the dashed curve for EB_I and EB_III blocks. The onset of dilatancy *C'* in experiment at effective pressure of 50 MPa are marked by arrows. The onset of shear-enhanced compaction C* in experiment at effective pressure of 150 MPa is marked by arrow in EB_II block.

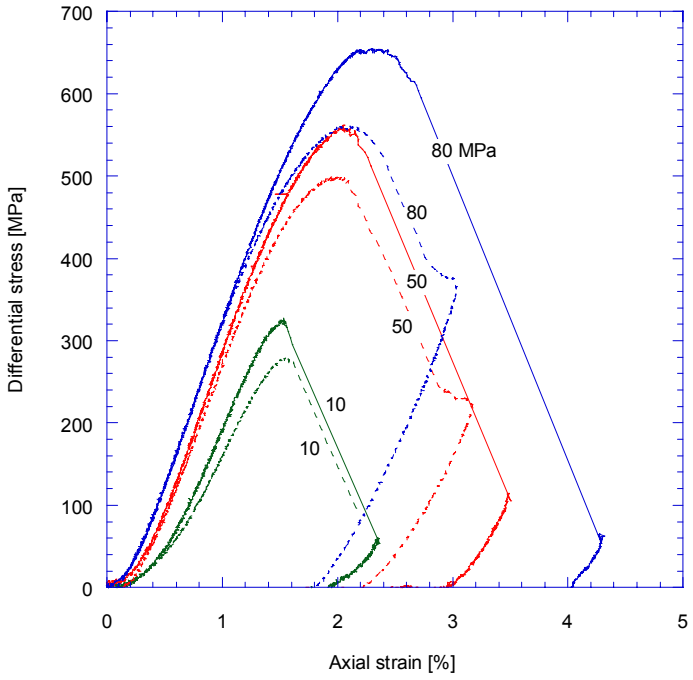

Figure 5.5. Comparison of mechanical data between nominal dry and water saturated EB_I samples. Differential stress is plotted as a function of axial strain. Numbers next to each curve indicate the effective pressure (confining pressure) maintained during the experiment. Stress-strain curves for dry and wet conditions are represented by solid and dashed line, respectively.

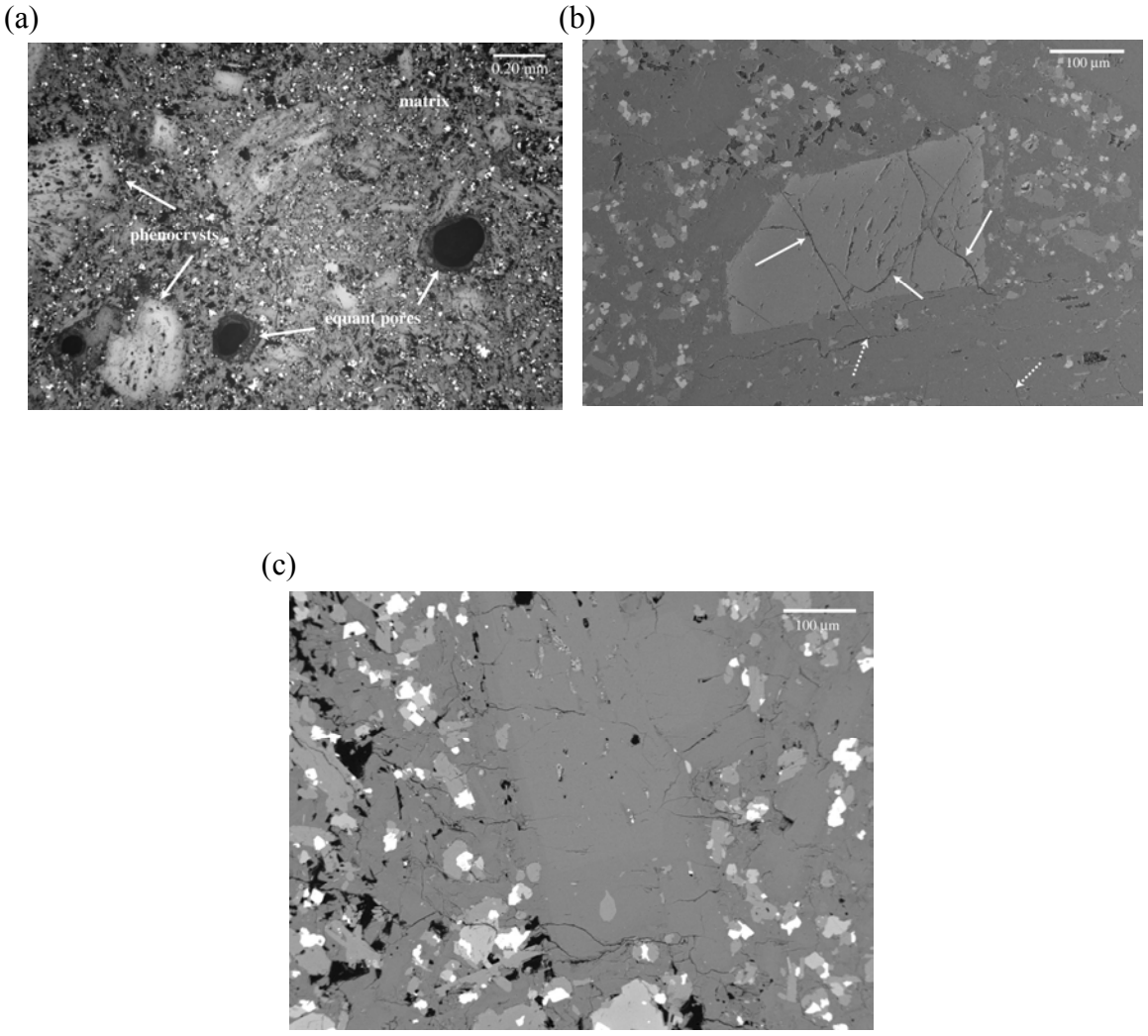

Figure 5.6. (a) Optical micrograph of intact EB_I basalt sample. Phenocrysts and equant pores are marked in the image. Macropores with radius around 100 μm were observed as shown by the dark areas. (b) Backscatter SEM image of intact EB_I sample. A phenocryst grain with sharp edges was embedded in the matrix. Preexisting microcracks within the phenocryst and in the matrix are marked by solid and dashed arrows, respectively. (c) backscatter SEM image of intact EB_I sample. Numerous healed or sealed microcracks with length around 50 μm were observed in the matrix.

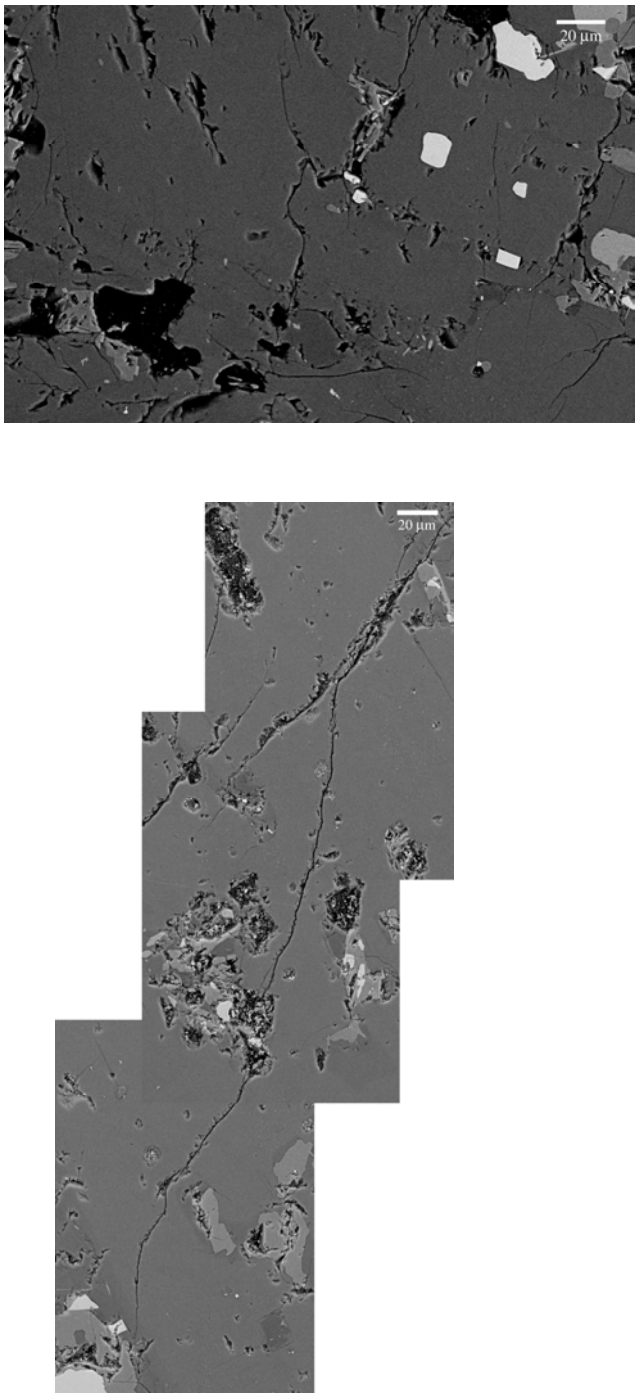

Figure 5.7. Backscatter SEM images of EB_I basalt samples failed by brittle faulting. Direction of σ_1 is vertical. (a) A sample was loaded beyond the onset of dilatancy *C'* under effective pressure of 10 MPa. Wing cracks were observed to propagate sub-parallel to σ_1. (b) A sample was stressed beyond *C'* under effective pressure of 50 MPa. Stress-induced cracks had propagated over a long distance (on the order of 100 μm) in a direction sub-parallel to σ_1.

(c)

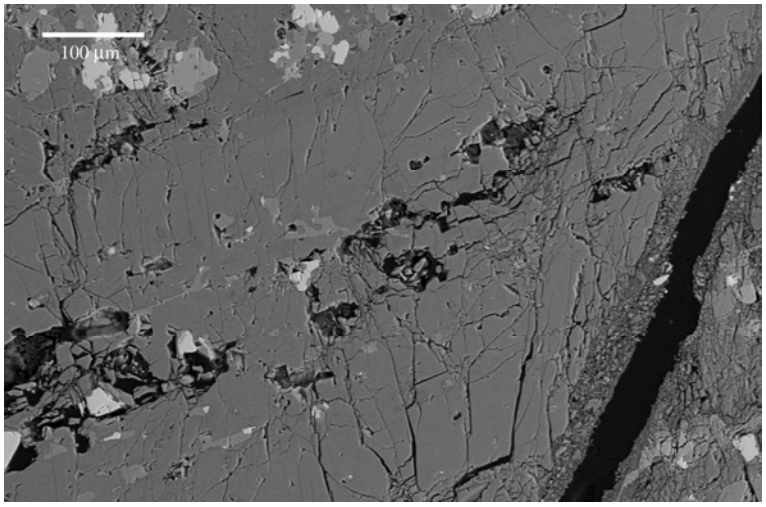

(d)

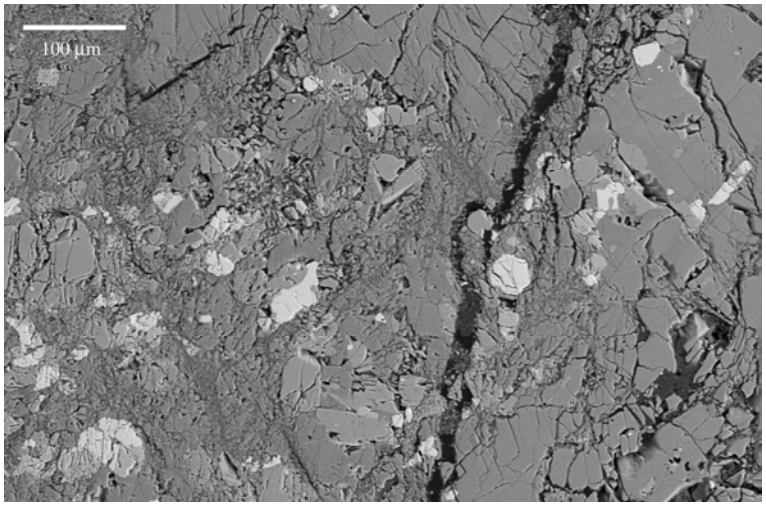

Figure 5.7. Backscatter SEM images of EB_I basalt samples failed by brittle faulting. Direction of σ_1 is vertical. (c) A sample loaded after post peak under an effective pressure of 80 MPa. Intense damage was observed in the vicinity of the shear band. Numerous microcracks propagated and coalesced sub-parallel to σ_1. (d) One of the most intensely damage zones in the same sample that loaded after post peak under an effective pressure of 80 MPa. Propagation and coalescence of stress-induced microcracks aligned sub-parallel to σ_1 were observed. The path of the development seems to bypass phenocrysts embedded in the matrix.

(e)

Figure 5.7. Backscatter SEM images of EB_I basalt samples failed by brittle faulting. Direction of σ_1 is vertical. (e) A mosaic image of the same sample that loaded after post peak under an effective pressure of 80 MPa. The micrograph covers an area of ~ 3.3 mm^2. The phenocrysts are represented by the lighter phase in the image. The number of phenocrysts that were gone through by the shear band and the ones that were not were counted.

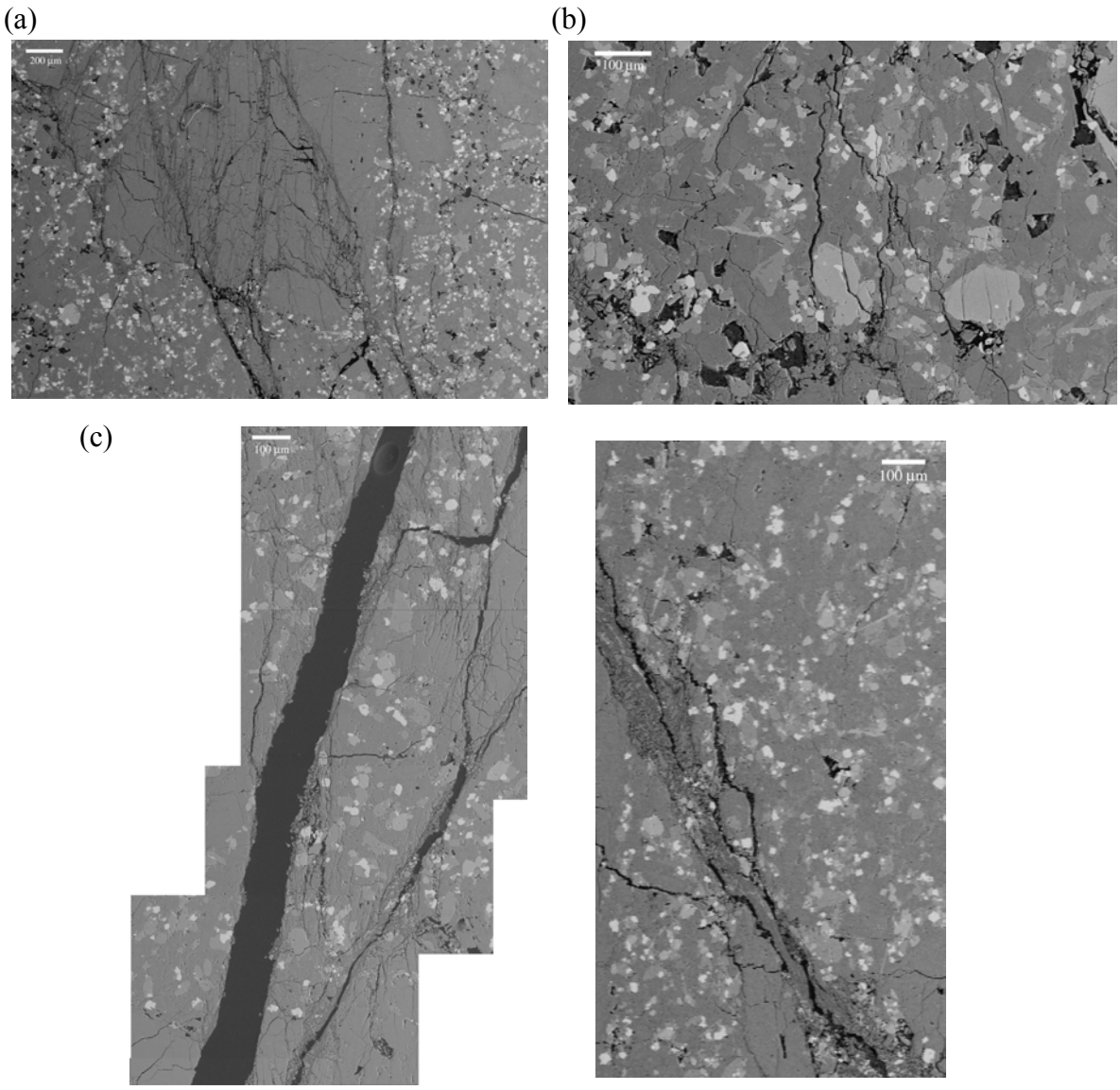

Figure 5.8. Backscatter SEM images of Etna basalt samples failed by brittle faulting. Direction of σ_1 is vertical. (a) An EB_III sample was loaded after post peak under effective pressure of 80 MPa. Numerous stress-induced microcracks were observed to propagate and coalesce in the matrix in a direction sub-parallel to σ_1. (b) The same EB_III sample that was loaded after post peak under effective pressure of 80 MPa. Microcracks were observed to extend sub-parallel to σ_1 in the incipient shear band. Development of crack propagation and coalescence seems to bypass phenocrysts embedded in the matrix. (c) Shear localizations in EB_I and EB_III samples are illustrated in the left and right images, respectively. Both samples were loaded after post peak under effective pressure of 80 MPa. Intense microcracking and comminution were observed in the vicinity of the shear bands. There were more phenocrysts embedded in the matrix in EB_III sample than EB_I sample. Shear band in EB_I was much wider than that in EB_III sample.

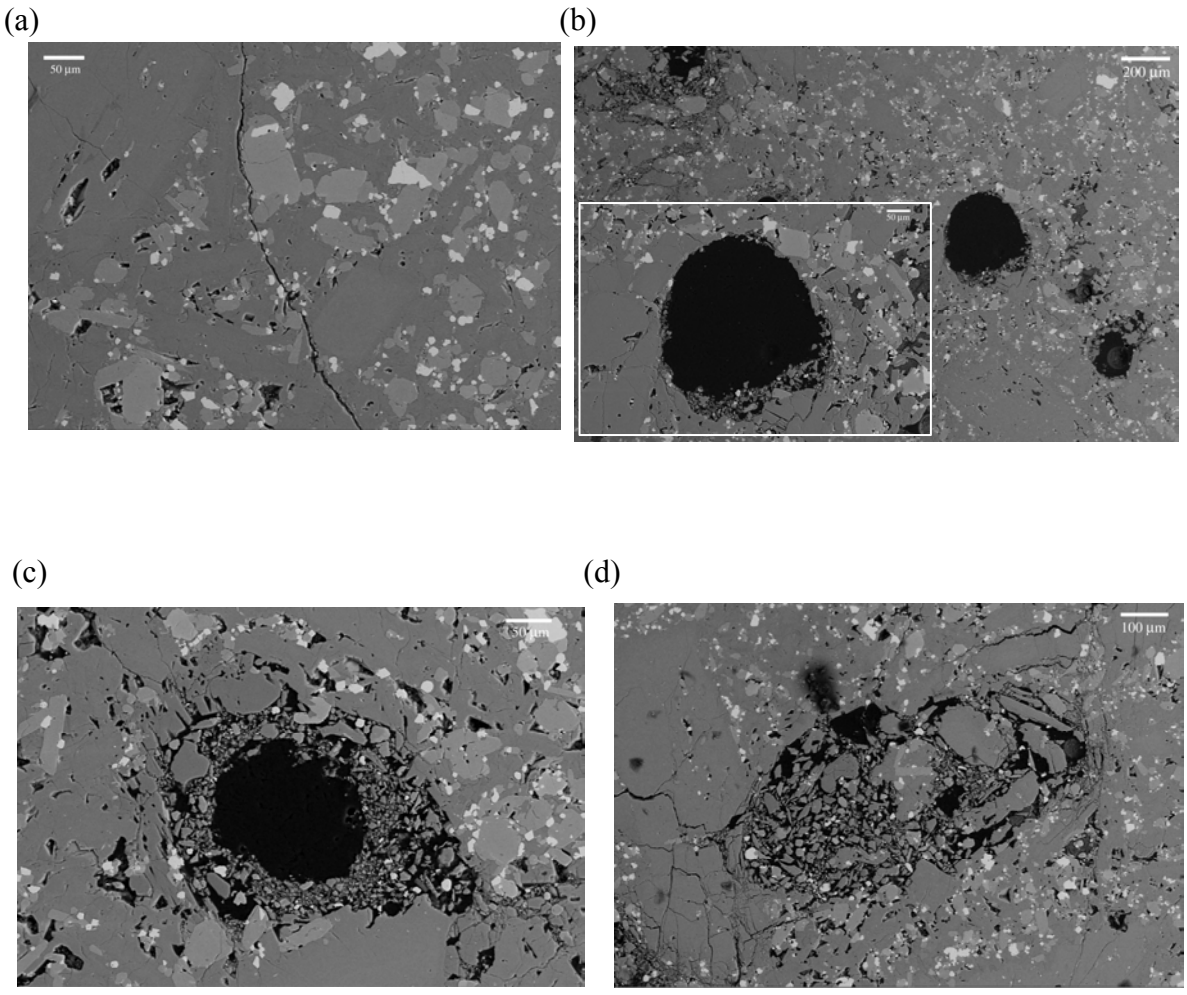

Figure 5.9. Backscatter SEM images of EB_II basalt samples failed by inelastic compaction. Direction of σ_1 is vertical. (a) A sample was loaded beyond the onset of shear-enhance compaction *C** under effective pressure of 80 MPa. A stress-induced crack was observed to propagate sub-parallel to σ_1. (b) The same EB_II sample that was loaded beyond *C** under effective pressure of 80 MPa. Macropores with a radius on the order of 100 μm were observed to collapse in the matrix. In the zoomed-in image outlined by white rectangle, numerous microcracks had emanated from the macropore and coalesced around the pore surface. (c) A sample was stressed beyond *C** under effective pressure of 150 MPa. A collapsed pore with a radius on the order of 100 μm surrounded by intensive cataclastic damage was observed. The damage zone had extended a distance ~ 100 μm. (d) The same sample that was loaded beyond *C** under effective pressure of 150 MPa. Pore collapse in an elongated macropore was observed. Crushed grains had fallen into the interior of the macropore.

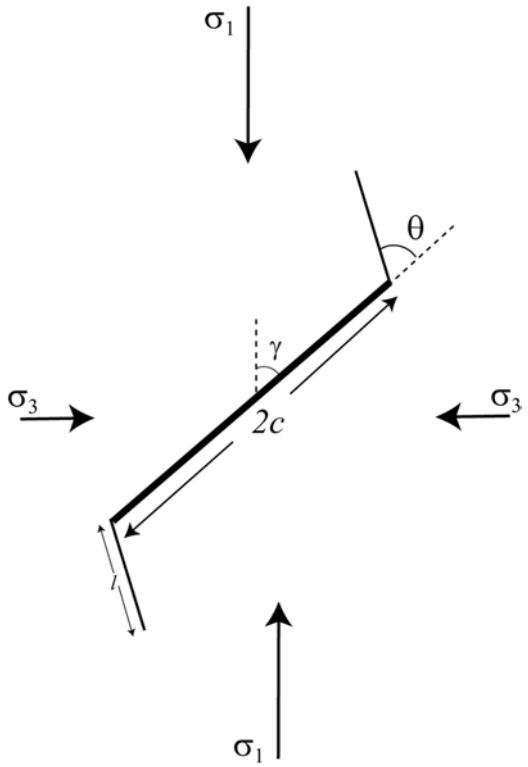

Figure 5.10. Sliding wing crack model for the development of dilatancy and instability in the brittle faulting regime. Directions of the maximum and minimum principal stresses are indicated. The sliding crack has a length of 2*c*. The sliding and wing cracks are at angles of γ and θ with respect to the σ_1 direction, respectively.

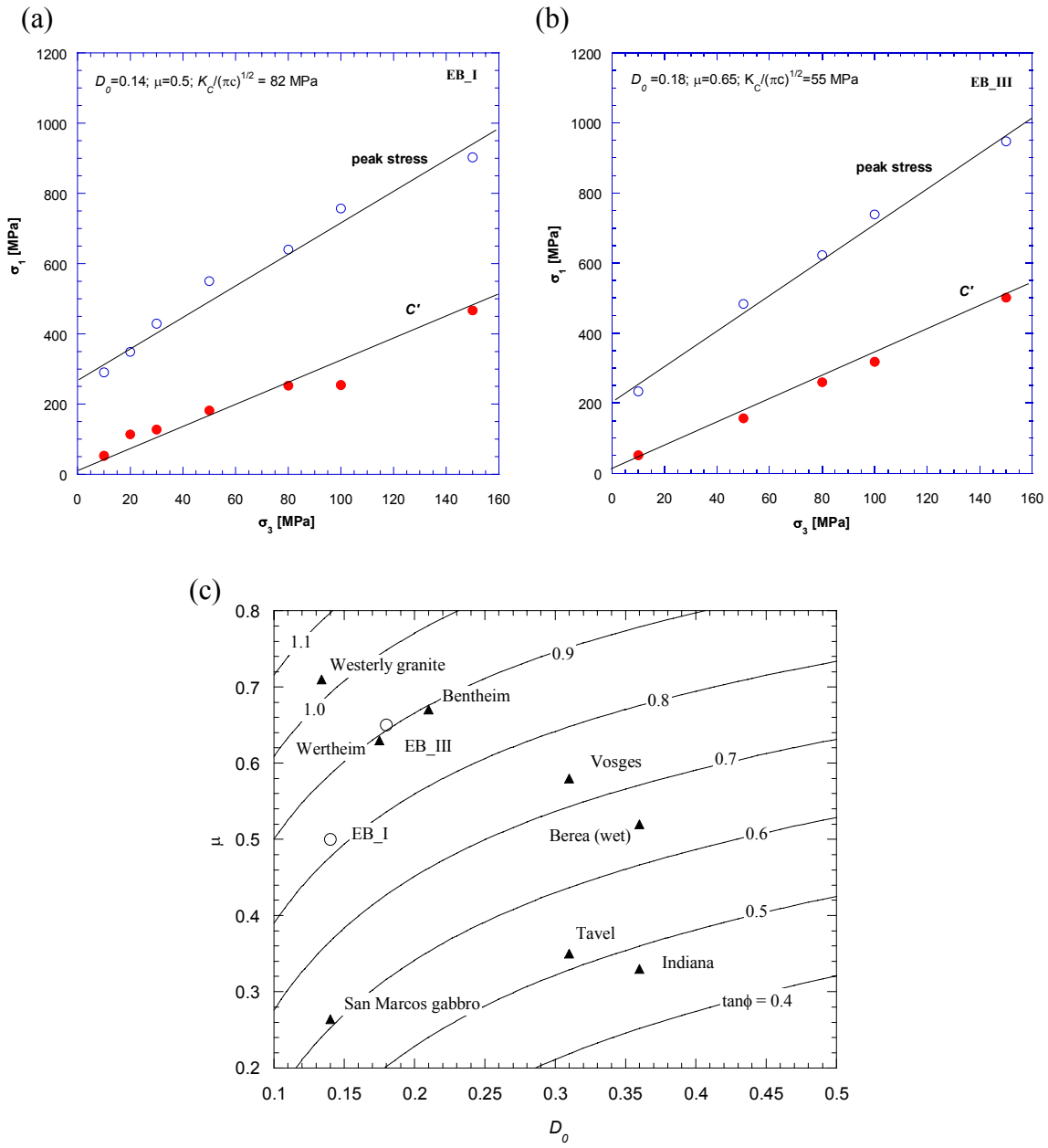

Figure 5.11. Comparison of the experimental data on brittle faulting (onset of dilatancy *C'* and the peak stress) for (a) EB_I and (b) EB_III basalt with predictions based on *Ashby and Sammis*' (1990) wing crack model. The onset of dilatancy *C'* and peak stress are represented by solid and open circles, respectively. The linear fit is shown with parameter values as indicated. (c) The solid curves represent contours of equal coefficient of internal friction (tanϕ) in the space of friction coefficient μ and initial damage D_0 according to the sliding wing crack model. EB_I and EB_III data are represented by open circles. For comparison, experimental data and inferred values of eight other rocks compiled by *Zhu et al*. (2010b) are shown as solid triangles.

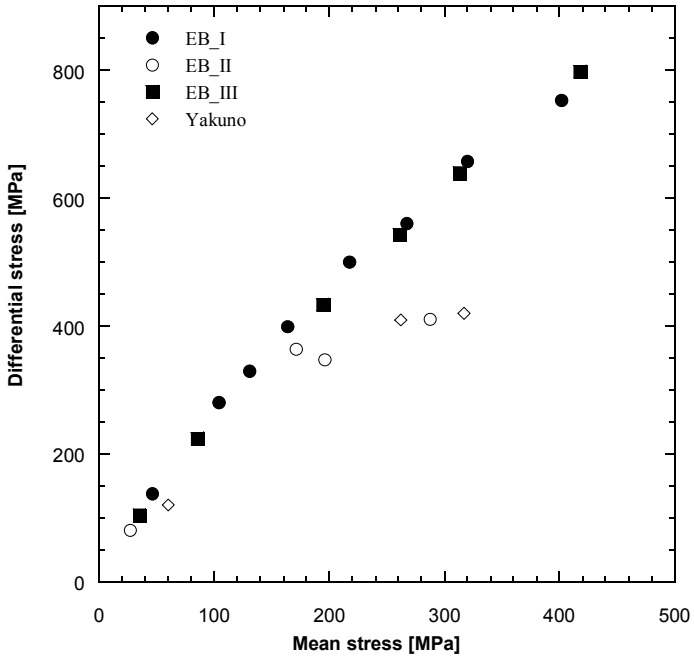

Figure 5.12. Peak stresses (EB_I, EB_II and EB_III) and yield stresses (EB_II) are plotted in the stress space. For reference, peak stress data for Yakuno basalt with a porosity of 7 % are shown as open diamonds.

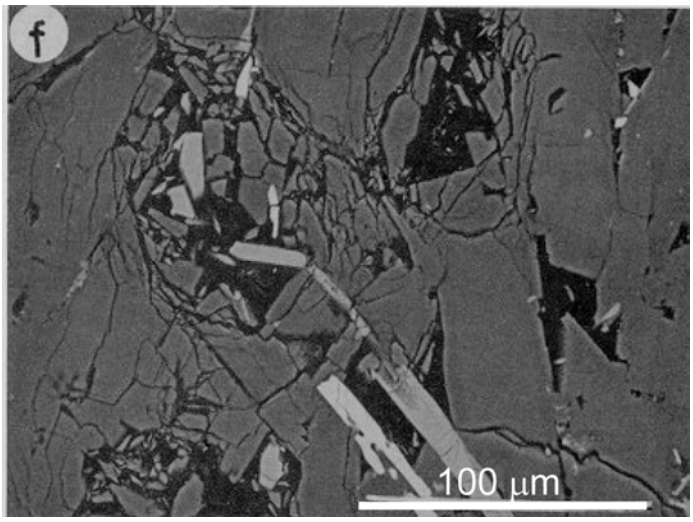

Figure 5.13. Backscatter SEM micrograph of hydrostatically compressed Yakuno basalt (*Shimada*, 1991). Pores are represented by dark areas. The sample was conducted at a confining pressure of 1950 MPa. Intensive cataclastic damage around the collapsed pores was observed.

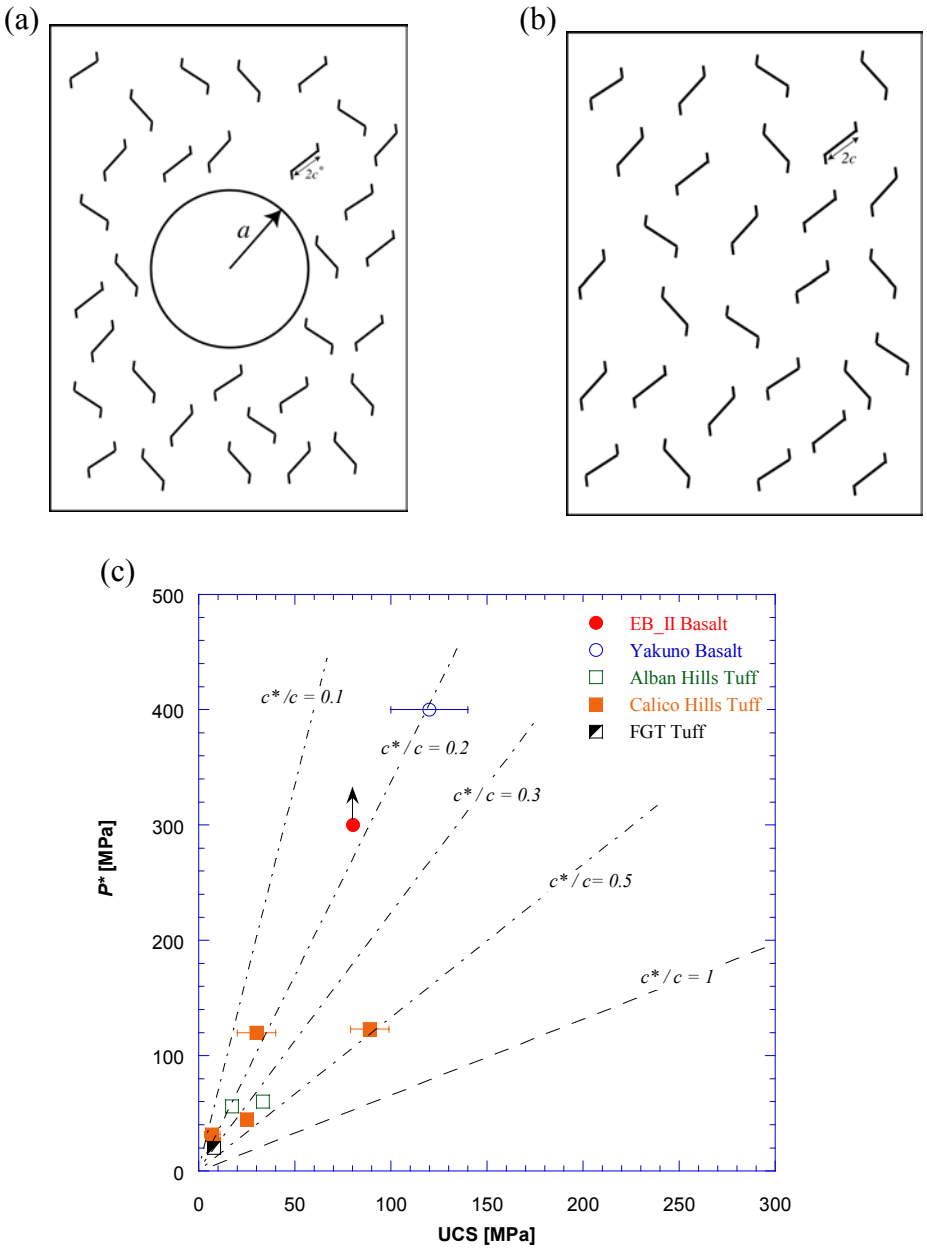

Figure 5.14. (a) Schematic diagram of a representative volume element. A macropore of radius *a* is surrounded by an effective medium made up of many microcracks with length of $2c^*$. (b) A representative volume element of a single porosity medium that numerous preexisting cracks with length of *2c* are embedded in it. (c) The critical pore collapse pressure *P** is plotted versus the uniaxial compressive strength UCS on EB_II basalt. For comparison, experimental data on Yakuno basalt (*Shimada*, 2000) and Tuffs compiled by *Zhu et al*. (in prepartion) are shown as square symbols. A ratio of c^*/c =1, which correspond to a slope of *P** versus UCS equals 2/3, is plotted in dashed line. Slopes with ratios of c^*/c ranging from 0.1 to 0.5 are plotted as dash dot lines.

Chapter 6

Summary and future work

1. Summary

We have investigated the micromechanics of porous carbonate and volcanic rocks based on laboratory experiments and microstructural observations. A suite of limestone samples, two blocks of Alban Hills tuff and three blocks of Mt. Etna basalt have been studied. All experiments were performed in conventional triaxial machine at room temperature. Distilled water was used as pore fluid and pore pressure was maintained at 10 MPa for wet experiments. Strain gages were attached in orthogonal direction for nominal dry experiments. Microstructural observations were conducted under both optical microscope and backscatter scanning electron microscopes (SEM). Numerical modeling was employed to interpret the micromechanisms.

The major conclusions of this research are summarized below:

1) Pore collapse in porous limestones was observed to initiate at the larger pores, accompanied by significant cataclasis and microcracking. Accordingly the limestone was modeled as a dual porosity medium with total porosity partitioned between macroporosity and microporosity.

2) An analytic expression has been derived for the uniaxial compressive strength associated with failure due to the propagation and coalescence of pore-emanated cracks on porous limestones. For hydrostatic loading, identical theoretical results for the pore collapse pressure P^* were obtained using the Mohr-Coulomb or Drucker-Prager criterion. For nonhydrostatic loading, the stress state at the onset of shear-enhanced compaction was predicted to fall on a linear cap according to Mohr-Coulomb criterion. Nonlinear caps in qualitative agreement with laboratory data were obtained using the Drucker-Prager criterion.

3) The micromechanical basis for the Coulomb failure parameters have been investigated. Analytic approximations were derived for the empirical failure parameters with reference to the sliding wing crack model. These expressions clarify the dependence of the uniaxial compressive strength on micromechanical parameters including the fracture toughness, friction coefficient, crack dimension and density.

4) The failure mode during triaxial loading in Alban Hills tuff is qualitatively similar to that observed in a porous sedimentary rock. Two blocks of tuff with porosity of 32 % and 35 % failed by dilatant brittle faulting at low effective pressures, and shear-enhanced compaction at high effective pressures.

5) Microstructural observations illustrates that besides macropores and micropores, there was a complex network of fine microcracks exist in the tuff matrix. Pore-emanated

cracks sub-parallel to σ_1 direction were observed in brittlely failed samples. Inelastic compaction was primarily associated with pore collapse.

6) Motivated by microstructural observations, micromechanics of brittle failure in Alban Hills tuff was analyzed by pore-emanating cracking model. The pore collapse model developed on porous limestone was extended to interpret the compaction behavior in Alban Hills tuff.

7) Dilatancy and brittle faulting were observed on two blocks of Mt. Etna basalt with porosity of 5 %. With a few percent increase in porosity, shear-enhance compaction was observed on Etna basalt with a porosity of 8%. Microstructural observations revealed the presence of thin cracks and quasi-spherical voids in intact Etna materials. The effect of water, phenocryst and porosity were investigated based on the comparison between the three blocks of Etna basalt.

2. Future work

1) The dual porosity model developed on porous limestones can capture a number of micromechanical processes, which cannot be described in a plastic pore collapse model that assume a single type of porosity. However, we have limited our applications with a couple of conditions.

a) The microporosity has been introduced as a distinct entity embedded in the effective medium. Hence, predictions of the micromechanical model hinge on geometric and mechanical attributes of the micropores are difficult to quantify. More refined microstructural observations can elucidate some of the geometric attributes, which can provide constrains to experimentally characterize the mechanical attributes (including the elastic and failure parameters).

b) The pore collapse model focuses on pore-emanated cracking, thus ignoring the role of pre-existing microcracks and their interactions with the micropores, which should be accounted for if one were to develop a more comprehensive model. It would also be useful to numerically study how the yield cap would evolve with the progressive development of pore collapse, as well as how sensitive it is to macropore geometry.

c) We have developed our pore collapse model for a nominal dry porous limestone with relatively high calcite content. Chemical effects are pervasive in a carbonate rock. To extend our results to a saturated condition, chemical effects need to be isolated from the mechanical effect. While laboratory data indicate that the brittle strength of a carbonate rock would increase with increasing dolomite and quartz contents [*Hugman and Friedman*, 1979], it is possible to extend the micromechanical model for application to these carbonate rocks.

2) The micromechanics of brittle faulting in Alban Hills tuff was analyzed by both sliding wing crack model and pore-emanated cracking model. While the pore-emanated cracking model seems to be more viable on the nonwelded tuff samples, more systematic studies of detailed microstructural observations are needed to provide further constraints on the brittle failure mechanics. The effects of micropores and microcracks on inelastic compaction were assumed as decoupled, but in reality the two types of mechanisms for cataclastic pore collapse probably operate as coupled process.

3) Shear-enhanced compaction was observed in Etna basalt with a porosity of 8%. Due to the heterogonous distribution of pores in EB_II basalt, we do not have enough data to defend the yielding stress map (onset of shear-enhanced compaction C^*). As failure mode is observed to be very sensitive to porosity in Etna basalt, it might be better

to conduct experiments on an even more porous block to investigate the inelastic compaction in more details.

References

Adelinet, M., J. Fortin, Y. Guéguen, A. Schubnel, and L. Geoffroy (2010), Frequency and fluid effects on elastic properties of basalt: Experimental investigations, *Geophys. Res. Lett.*, *37*(2), L02303, doi: 10.1029/2009gl041660.

Andrews, D. J., T. C. Hanks, and J. W. Whitney (2007), Physical Limits on Ground Motion at Yucca Mountain, *Bulletin of the Seismological Society of America*, *97*(6), 1771-1792, doi: 10.1785/0120070014.

Anselmetti, F., S. Luthi, and G. Eberli (1998), Quantitative characterization of carbonate pore systems by digital image analysis, *AAPG Bulletin*, *82*, 1815-1836.

Ashby, M., and C. Sammis (1990), The damage mechanics of brittle solids in compression, *Pure and Applied Geophysics*, *133*, 489-521.

Atkinson, B., and P. Meredith (1987), Experimental fracture mechanics data for rocks and minerals, in *Fracture Mechanics of Rock*, edited by B. K. Atkinson pp. 477–525, Academic, London.

Avar, B., and N. Hudyma (2007), Observations on the influence of lithophysae on elastic (Young's) modulus and uniaxial compressive strength of Topopah Spring Tuff at Yucca Mountain, Nevada, USA, *Int J Rock Mech Min*, *44*(2), 266-270.

Aversa, S., and A. Evangelista (1998), The mechanical behaviour of a pyroclastic rock: Yield strength and "destructuration" effects, *Rock Mechanics and Rock Engineering*, *31*(1), 25-42.

Azzaro, R., M. Barbano, B. Antichi, and R. Rigano (2000), Macroseismic catalogue of Mt. Etna earthquakes from 1832 to 1998, *Acta Vulcanologica*, *12*(1/2), 3-36.

Baechle, G., A. Colpaert, G. Eberli, and R. Weger (2008), Effects of microporosity on sonic velocity in carbonate rocks, *The Leading Edge*, *27*, 1012-1018, doi:10.1190/1.2967554.

Baud, P., A. Schubnel, and T.-f. Wong (2000a), Dilatancy, compaction, and failure mode in Solnhofen limestone, *Journal of Geophysical Research*, *105*(B8), 19289-19303, doi: 10.1029/2000JB900133.

Baud, P., S. Vinciguerra, C. David, A. Cavallo, E. Walker, and T. Reuschlé (2009), Compaction and Failure in High Porosity Carbonates: Mechanical Data and Microstructural Observations, *Pure and Applied Geophysics*, *166*(5), 869-898, doi: 10.1007/s00024-009-0493-2.

Baud, P., V. Vajdova, and T.-f. Wong (2006), Shear-enhanced compaction and strain localization: Inelastic deformation and constitutive modeling of four porous sandstones, *J. Geophys. Res.*, *111*(B12), B12401, doi: 10.1029/2005jb004101.

Baud, P., W. Zhu, and T.-f. Wong (2000b), Failure mode and weakening effect of water on sandstone, *J. Geophys. Res.*, *105*(B7), 16371-16389, doi: 10.1029/2000JB900087.

Bauer, S., M. Friedman, and J. Handin (1981), Effects of water-saturation on strength and ductility of three igneous rocks at effective pressures to 50 MPa and temperatures to partial melting, The 22nd U.S. Symposium on Rock Mechanics (USRMS),p73-78.

Bemer, E., O. Vincké, and P. Longuemare (2004), Geomechanical log deduced from porosity and mineralogical content, *Oil & Gas Science and Technology*, *59*, 405-426.

Bhatt, J., M. Carroll, and J. Schatz (1975), Spherical model calculation for volumetric response of porous rocks, *Journal of Applied Mechanics*, *42*, 363-368.

Boutéca, M., J. P. Sarda, and F. Schneider (1996), Subsidence induced by the production of fluids, *Rev I Fr Petrol*, *51*(3), 349-379.

Brace, W. (1978), Volume changes during fracture and frictional sliding: a review, *Pure and Applied Geophysics*, *116*(4), 603-614.

Brace, W., Jr B. Paulding, and C. Scholz (1966), Dilatancy in the fracture of crystalline rocks, *Journal of Geophysical Research*, *71*, 3939-3954.

Brace, W.F. (1961). Dependence of fracture strength of rocks on grain size, in Proc. 4th Symposium on Rock Mechanics, pp. 99-103, Penn. State Univ., Min. Ind. Exp. Sta. Bull. No.76.

Brace, W.F. (1964). Brittle fracture of rocks, in State of Stress in the Earth's Crust, edited by W.J. Judd, pp. 111-178, Elsevier, New York.

Brace, W.F. and R.G.I. Martin (1968). A test of the law of effective stress for crystalline rocks of low porosity, Int. J. Rock Mech. Min. Sci., 5, 415-426.

Budiansky, B. and R. J. O'Connell (1976). Elastic moduli of a cracked solid, Int. J. Solids Struct., 12, 81-97.

Byerlee, J.D. (1978). Friction of rocks, Pure Appl. Geophys., 116, 615-626.

Chang, C., M.D. Zoback, and A. Khaksar (2006). Empirical relations between rock strength and physical properties in sedimentary rocks, J. Petrol. Sci. Eng., 51, 223-237.

Chester, F. M., and J. M. Logan (1986), Implications for mechanical properties of brittle faults from observations of the Punchbowl fault zone, California, *Pure and Applied Geophysics*, *124*, 79-106, doi: 10.1007/BF00875720.

Choquette, P. W., and L. C. Pray (1970), Geologic nomenclature and classification of porosity in sedimentary carbonates, *AAPG Bulletin*, *54*, 207-250.

Choquette, P. W., and N. P. James (1986), Diagenesis in limestones - the deep burial environment, *Geosciences Canada*, *14*, 3-35.

Chouet, B. A. (1996), Long-period volcano seismicity: its source and use in eruption forecasting, *Nature*, *380*(6572), 309-316, doi: 10.1038/380309a0.

Churcher, P. L., P. R. French, J. C. Sham and L. L. Schramm (1991), Rock properties of Berea sandstone, Baker dolomite, and Indiana limestone, *Society of Petroleum Engineers*, SPE 21044.

Cotterell, B., and J.R. Rice (1980). Slightly curved or kinked cracks, Int. J. Fracture, 16, 155-169.

Curran, J., and M. Carroll (1979), Shear stress enhancement of void compaction, *Journal of Geophysical Research*, *84*, 1105–1112, doi: 10.1029/JB084iB03p01105.

Dautriat, J., N. Gland, A. Dimanov, S. Youssef, and O. Vizika (2007), Anisotropic permeabilities evolution of reservoir rocks under pressure: New experimental and numerical approaches, *http://www.earth-prints.org/bitstream/2122/2703/1/dautriat.pdf*.

Davis, R. O., and A. P. S. Selvadurai (2002), *Plasticity and Geomechanics*, 287 pp., Cambridge University Press, Cambridge, UK.

de Rita, D., and C. Giampaolo (2006), A case study—Ancient Rome was built with volcanic stone from the Roman land, *GSA Special Papers*, *408*, 127.

Dey, T. and C.Y. Wang (1981). Some mechanisms of microcrack growth and interaction in compressive rock failure, Int. J. Rock Mech. Min. Sci., 18, 199-210.

Dobson, P., and S. Nakagawa (2005), Summary of Rock-Property Measurements for Hong Kong Tuff Samples*Rep.*, Ernest Orlando Lawrence Berkeley NationalLaboratory, Berkeley, CA (US).

Dullien, F. A. L. (1992), *Porous Media: Fluid Transport and Pore Structure. (2nd ed.)*, Academic Press, San Diego.

Eberli, G. P., G. T. Baechle, F. S. Anselmetti, and M. L. Incze (2003), Factors controlling elastic properties in carbonate sediments and rocks, *The Leading Edge*, 654-666.

Evans, J. P., and K. K. Bradbury (2004), Faulting and fracturing of nonwelded Bishop Tuff, eastern California: Deformation mechanisms in very porous materials in the vadose zone, *Vadose Zone Journal*, *3*, 602-623.

Fabre, D., and J. Gustkiewicz (1997), Poroelastic properties of limestones and sandstones under hydrostatic conditions, *Int. J. Rock Mech. Min. Sci.*, *34*, 127-134.

Folk, R. L. (1980), *Petrology of Sedimentary Rocks*, 184 pp., Hemphill, Austin.

Fortin, J., S. Stanchits, G. Dresen, and Y. Guéguen (2006), Acoustic emission and velocities associated with the formation of compaction bands in sandstone, *Journal of Geophysical Research*, *111*, B10203, doi: 10.1029/2005JB003854.

Fredrich, J. T., J. G. Arguello, G. L. Deitrick, and E. P. de Rouffignac (2000), Geomechanical modeling of reservoir compaction, surface subsidence, and casing damage at the Belridge diatomite field, *Spe Reserv Eval Eng*, *3*(4), 348-359.

Fredrich, J., B. Evans, and T.-f. Wong (1990). Effects of grain size on brittle and semi-brittle strength: implications for micromechanical modelling of failure in compression, J. Geophys. Res., 95, 10907-10920.

Funiciello, R., and C. Caputo (2006), Giovan Battista Brocchi's Rome: A pioneering study in urban geology, *Geological Society of America*, *411*, 199-210

Goodman, R.E. (1989). Introduction to Rock Mechanics, 2nd ed., 2 ed., 562 pp., John Wiley and Sons, NY.

Gurson, A. (1977), Continuum theory of ductile rupture by void nucleation and growth: Part I-Yield criteria and flow rules for porous ductile media, *Journal of Engineering Materials and Technology*, *99*, 2-15.

Gurson, A. L. (1977), Continuum theory of ductile rupture by void nucleation and growth: Part I - Yield criteria and flow rules for porous ductile media, *J. Eng. Mat. Tech.*, *99*, 2-15.

Hadizadeh, J., and R. D. Law (1991), Water-weakening of sandstone and quartzite deformed at various stress and strain rates, *Int J Rock Mech Min*, *28*, 431-439.

Hadley, K. (1973). Laboratory investigation of dilatancy and motion on fault surfaces at low confining pressures, in Proc. Conf. Tectonic Problems of the San Andreas Fault System, edited by R. L. Kovach and A. Nur, pp. 427-435.

Handin, J. (1969). On the Coulomb-Mohr failure criterion, J. Geophys. Res., 74, 5343-5348.

Handin, J., and R. V. Hager (1957), Experimental deformation of sedimentary rocks under confining pressure: tests at room emperature on dry samples, *AAPG Bulletin*, *41*, 1-50.

Handin, J., R.V. Hager, M. Friedman and J. N. Feather (1963). Experimental deformation of sedimentary rock under confining pressure: pore pressure effects, Bull. Am. Asso. Petrol. Geol., 47, 717-755.

Heap, M. J., S. Vinciguerra, and P. G. Meredith (2009), The evolution of elastic moduli with increasing crack damage during cyclic stressing of a basalt from Mt. Etna volcano, *Tectonophysics*, *471*(1-2), 153-160, doi: 10.1016/j.tecto.2008.10.004.

Heard, H., B. Bonner, A. Duba, R. Schock, and D. Stephens (1973), High Pressure Mechanical Properties Of Mt Helen, Nevada, Tuff *Rep. UCID-16261*, Lawrence Livermore National Laboratory, Livermore, CA.

Heiken, G. (2006), *Tuffs: their properties, uses, hydrology, and resources*, 131 pp., Geological Society of America, USA.

Hickman, S., and M. D. Zoback (2004). Stress orientations and magnitudes in the SAFOD pilot hole, Geophys. Res. Lett., 31, L15S12, doi:10.1029/2004GL020043.

HKGeotechnicalOffice (1990), Foundation Properties of Marble and Other Rocks in the Yuen Long-Tuen Mun Area *Rep. 2/90*, HK Geotechnical Office.

Holtz, R.D. and W. D. Kovacs (1981). Introduction to Geotechnical Engineering, 733 pp., Prentice-Hall, Englewood Cliffs, NJ.

Horii, H., and S. Nemat-Nasser (1986), Brittle failure in compression: splitting, faulting and brittle-ductile transition, *Philosophical Transactions for the Royal Society of London*, *319*, 337-374.

Horn, H.M. and D. U. Deere (1962). Frictional Characteristics of minerals, Geotechnique, 12, 319-335.

Hugman, R. H. H., and M. Friedman (1979), Effects of texture and composition on mechanical behavior of experimentally deformed carbonate rocks, *AAPG Bulletin*, *63*, 1478-1489.

Jaeger, J.C., N.G. W. Cook, and R.W. Zimmerman (2007). Fundamentals of Rock Mechanics, 4th ed., 475 pp., Blackwell, Oxford.

Keith, B. D., and E. D. Pittman (1983), Bimodal porosity in oolitic reservoir: effect on productivity and log response, Rodessa Limestone (Lower Cretaceous), East Texas Basin, *AAPG Bulletin*, *67*, 1391-1399.

Kemeny, J., and N. Cook (1991), Micromechanics of deformation in rocks, in *Toughening mechanisms in quasi-brittle materials*, edited by S. P. Shap pp. 155-188, Klewer Academic.

Klein, E. (2002). Micromécanique des Roches Granulaires Poreuses: Expérimentation et Modélisation, 158 pp, Université Louis Pasteur de Strabourg, Strasbourg, France.

Knackstedt, M. A., S. Latham, M. Madadi, A. Sheppard, and T. Varslot (2009), Digital rock physics: 3D imaging of core material and correlations to acoustic and flow properties, *The Leading Edge*, *January*, 28-33.

Kranz, R. L. (1983), Microcracks in rocks, a review, *Tectonophysics*, *100*, 449-480.

Lajtai, E. Z., R. H. Schmidtke, and L. P. Bielus (1987), The effect of water on the time-dependent deformation and fracture of a granite, *International Journal of Rock Mechanics and Mining Sciences & Geomechanics Abstracts*, *24*(4), 247-255.

Lambe, T.W., and R.V. Whitman (1969). Soil Mechanics, 553 pp., John Wiley, NY.

Lézin, C., F. Odonne, G. J. Massonnat, and G. Escadeillas (2009), Dependence of joint spacing on rock properties in carbonate strata, *AAPG Bulletin*, *93*, 271-290.

Lion, M., M. Skoczylasa, and B. Ledesert (2005), Effects of heating on the hydraulic and poroelastic properties of bourgogne limestone, *Int. J. Rock Mech. Min. Sci.*, *42*, 508-520.

Lockner, D., and C. Morrow (2008), Energy Dissipation in Calico Hills Tuff due to Pore Collapse, *Eos Trans. AGU*, *89*(53), Fall Meet. Suppl., Abstract T51A-1856.

Long, J., and R. Ewing (2004), Yucca Mountain: Earth-science issues at a geologic repository for high-level nuclear waste, *Annual Review of Earth and Planetary Sciences*, *32*, 363-401.

Lønøy, A. (2006), Making sense of carbonate pore systems, *AAPG Bulletin*, *90*, 1381-1405.

Lucia, F. J. (1995), Rock-fabric/petrophysical classification of carbonate pore space for reservoir characterization, *AAPG Bulletin*, *79*, 1275-1300.

Mariucci, M. T., S. Pierdominici, L. Pizzino, F. Marra, and P. Montone (2008), Looking into a volcanic area: An overview on the 350 m scientific drilling at Colli Albani (Rome, Italy), *Journal of Volcanology and Geothermal Research*, *176*(2), 225-240, 10.1016/j.jvolgeores.2008.04.007.

Martin, R. J., P. J. Boyd, J. S. Noel, and R. H. Price (1995), Bulk and mechanical properties of the Paintbrush tuff recovered from borehole USW NRG-7/7A: Data report. *Rep. SAND--94-1996*, Sandia National Labs., Albuquerque, NM

Martin, R., P. Boyd, J. Noel, and R. Price (1994), Bulk and mechanical properties of the Paintbrush tuff recovered from borehole USW NRG-6: Data report *Rep. SAND--93-4020*, Sandia National Labs., Albuquerque, NM

Mavko, G., T. Mukerji, and J. Dvorkin (1998). The Rock Physics Handbook: Tools for Seismic Analysis in Porous Media, 329 pp., Cambridge University Press, Cambridge.

Menéndez, B., W. Zhu, and T. Wong (1996), Micromechanics of brittle faulting and cataclastic flow in Berea sandstone, *Journal of Structural Geology*, *18*(1), 1-16, doi: 10.1016/0191-8141(95)00076-P.

Mitchell, J.K.(1993). Fundamentals of Soil Behavior, 2nd Edition, 437 pp., John Wiley, NY.

Mogi, K. (1964), Deformation and fracture of rocks under confining pressure (1) Compression tests on dry rock sample, *Bull. Earthq. Res. Inst*, *42*, 491-514.

Moon, V. (1993), Geotechnical characteristics of ignimbrite: A soft pyroclastic rock type, *Engineering Geology*, *35*(1-2), 33-48.

Moore, D.E. and D. A. Lockner (1995). The role of microcracking in shear-fracture propagation in granite, J. Struct. Geol., 17, 95-114.

Nemat-Nasser, S. (1985). Discussion of geometric probability approach to the characterization and analysis of microcracking in rocks, Mech. Mater., 4, 277-281.

Nimick, F. B., R. H. Price, R. G. Van Buskirk, and J. R. Goodell (1985), Uniaxial and triaxial compression test series on Topopah Spring Tuff from USW G-4, Yucca Mountain, Neveda *Rep. SAND--84-1101*, Sandia National Labs., Albuquerque, NM

PATANE, et al. (2004), Mt. Etna volcano: A seismological framework, in *Mt. Etna: Volcano Laboratory*, edited by A. Bonaccorso, S. Calvari, M. Coltelli and S. Falsaperla,143, pp. 147–166, American Geophysical Monograph.

Paterson, M., and T.-f. Wong (2005), *Experimental rock deformation--The brittle field, 2nd Edition*, 348 pp., Springer-Verlag, New York.

Pettijohn, F. J. (1975), *Sedimentary Rocks, 3rd ed.*, 628 pp., Harper & Row, New York.

Pittman, E. D. (1971), Microporosity in carbonate rocks, *AAPG Bulletin*, *55*, 1873-1878.

Price, R., and S. Bauer (1985), Analysis of the elastic and strength properties of Yucca Mountain tuff, Nevada, The 26th U.S. Symposium on Rock Mechanics (USRMS),1:89-96.

Ramamurthy, T. (2001), Shear strength response of some geological materials in triaxial compression, *Int. J. Rock Mech. Min. Sci.*, *38*, 683-697.

Rawling, G.C., P. Baud and T.-f. Wong (2002). Dilatancy, brittle strength and anisotropy of foliated rocks: Experimental deformation and micromechanical modeling, J. Geophys. Res., 107, 2234, doi:10.1029/2001JB000472.

Russ, J. (1990), *Computer-assisted microscopy: the measurement and analysis of images*, 480 pp., Plenum Press, New York.

Rutter, E., and D. Mainprice (1978), The effect of water on stress relaxation of faulted and unfaulted sandstone, *Pure and Applied Geophysics*, *116*, 634-654.

Sammis, C. G., and M. F. Ashby (1986), The failure of brittle porous solids under compressive stress states, *Acta metall.*, *34*, 511-526.

Schultz, R. A., and Q. Z. Li (1995), Uniaxial strength testing of non-welded Calico Hills tuff, Yucca Mountain, Nevada, *Engineering Geology*, *40*(3-4), 287-299.

Segall, P. (1989), Earthquakes Triggered by Fluid Extraction, *Geology*, *17*(10), 942-946.

Shimada, M. (1991), Comment on``The effects of pressure and porosity on the micromechanics of the brittle-ductile transition in quartzite"by Greg Hirth and Jan Tullis, *Journal of Geophysical Research*, *96*, 11877-11879.

Shimada, M. (2000), *Mechanical behavior of rocks under high pressure conditions*, 178 pp., A.A. Balkema, Netherlands.

Stanchits, S., S. Vinciguerra, and G. Dresen (2006), Ultrasonic Velocities, Acoustic Emission Characteristics and Crack Damage of Basalt and Granite, *Pure and Applied Geophysics*, *163*(5), 975-994, doi: 10.1007/s00024-006-0059-5.

Tapponier, P., and W. F. Brace (1976), Development of stress-induced microcracks in Westerly granite, *Int. J. Rock Mech. Min. Sci. & Geomech. Abstr*, *13*, 103-112.

Timoshenko, S., and J. Goodier (1951), *Theory of Elastic*, 567 pp., McGraw-Hill, New York.

Tondi, E., M. Antonellini, A. Aydin, L. Marchegiani, and G. Cello (2006), The role of deformation bands, stylolites and sheared stylolites in fault development in carbonate grainstones of Majella Mountain, Italy, *J. Struct. Geol.*, *28*, 376-391.

Tuncay, E. (2009), Rock rupture phenomenon and pillar failure in tuffs in the Cappadocia region (Turkey), *Int J Rock Mech Min*, *46*, 1253-1266, doi: 10.1016/j.ijrmms.2009.01.011.

Underwood, E. E. (1970), *Quantitative Stereology*, 274 pp., Addison Wesley, Reading.

Vajdova, V., P. Baud, and T. Wong (2004), Compaction, dilatancy, and failure in porous carbonate rocks, *Journal of Geophysical Research*, *109*, B05204, doi: 10.109/2003JB002508.

Vajdova, V., W. Zhu, T.-M. N. Chen, and T. Wong (2010), Micromechanics of brittle faulting and cataclastic flow in Tavel limestone, *Journal of Structural Geology*, *in press*.

Vinciguerra, S. (2002), Damage mechanics preceding the September-October 1989 flank eruption at Mount Etna volcano inferred by seismic scaling exponents, *Journal of Volcanology and Geothermal Research*, *113*(3-4), 391-397, doi:10.1016/S0377-0273(01)00274-8.

Vinciguerra, S., C. Trovato, P. Meredith, and P. Benson (2005), Relating seismic velocities, thermal cracking and permeability in Mt. Etna and Iceland basalts, *Int J Rock Mech Min*, *42*(7-8), 900-910, doi:10.1016/j.ijrmms.2005.05.022.

Vinciguerra, S., P. Del Gaudio, M. T. Mariucci, F. Marra, P. G. Meredith, P. Montone, S. Pierdominici, and P. Scarlato (2009), Physical properties of tuffs from a scientific borehole at Alban hills volcanic district (central Italy), *Tectonophysics*, *471*(1-2), 161-169, 10.1016/j.tecto.2008.08.010.

Vinciguerra, S., V. Latora, S. Bicciato, and R. Kamimura (2001), Identifying and discriminating seismic patterns leading flank eruptions at Mt. Etna Volcano during 1981-1996, *Journal of Volcanology and Geothermal Research*, *106*(3-4), 211-228, doi:10.1016/S0377-0273(00)00274-2.

Vincké, O., M. J. Boutéca, J. M. Piau, and D. Fourmaintraux (1998), Study of the effective stress at failure, in *Poromechanics, A Tribute to Maurice A. Biot*, edited by J.-F. Thimus, Y. Abousleiman, A. H.-D. Cheng, O. Coussy and E. Detournay, pp. 635-639, A. A. Balkema, Rotterdam.

Walsh, J. (1965), The effect of cracks on the compressibility of rocks, *Journal of Geophysical Research*, *70*, 381-389.

Wardlaw, N. C., M. McKellar and Y. Li (1988), Pore and throat size distributions determined by mercury porosimetry and by direct observation, *Carbonates and Evaporites*, *3*, 1-15.

Wardlaw, N. C., Y. Li and D. Forbes (1987), Pore-Throat size correlation from capillary pressure curves, *Transport in Porous Media*, *2*, 597-614.

Wong, R.H.C., K.T. Chau, and P. Wang (1996). Microcracking and grain size effect in Yuen Long marbles, Int. J. Rock Mech. Min. Sci., 33, 479-485.

Wong, T.-f. (1990), Mechanical compaction and the brittle-ductile transition in porous sandstones, in *Deformation Mechanisms, Rheology and Tectonics*, edited by R. J. Knipe and R. H. Rutter, pp. 111-122, Geol. Society Special Publication Vol. 54, London.

Wong, T.-f. (1982). Micromechanics of faulting in Westerly granite, Int. J. Rock Mech. Min. Sci., 19, 49-64.

Wong, T.-f., (1990). A note on the propagation behavior of a crack nucleated by a dislocation pile-up, J. Geophys. Res., 95, 8639-8646.

Wong, T.-f., C. David, and B. Menéndez (2004), Mechanical compaction, in *Mechanics of Fluid-Saturated Rocks*, edited by Y. Guéguen and M. Boutéca, pp. 55-114, Elsevier Academic Press, Amsterdam.

Wong, T.-F., C. David, and W. Zhu (1997), The transition from brittle faulting to cataclastic flow in porous sandstones: Mechanical deformation, *Journal of Geophysical Research*, *102*, 3009-3025, doi: 10.1029/96JB03281.

Zhang, J. X., T.-f. Wong, and D. M. Davis (1990), Micromechanics of Pressure-Induced Grain Crushing in Porous Rocks, *Journal of Geophysical Research*, *95*, 341-352, doi: 10.1029/JB095iB01p00341.

Zhu, W., P. Baud, and T.-f. Wong (2010b), Micromechanical basis for the Coulomb failure parameters, *Earth and Planetary Science Letters*, *submitted*.

Zhu, W., P. Baud, and T.-f. Wong (2010a), Micromechanics of cataclastic pore collapse in limestone, *J. Geophys. Res.*, *115*(B4), B04405, doi: 10.1029/2009JB006610.